



Fermi National Accelerator Laboratory

FN-508

A Study of Nonlinear Dynamics in the Fermilab TEVATRON

Nikolitsa Merminga
Fermi National Accelerator Laboratory
P.O. Box 500, Batavia, Illinois 60510

and

The University of Michigan
Ann Arbor, Michigan 48109

January 1989

* A dissertation submitted in partial fulfillment of the requirements for the degree of Doctor of Philosophy (Physics), The University of Michigan, Ann Arbor, Michigan, 1989.



Operated by Universities Research Association, Inc., under contract with the United States Department of Energy

A STUDY OF NONLINEAR DYNAMICS IN THE FERMILAB TEVATRON

by

Nikolitsa Merminga

A dissertation submitted in partial fulfillment
of the requirements for the degree of
Doctor of Philosophy
(Physics)
in The University of Michigan
1989

Doctoral Committee:

Professor Lawrence Jones, Co-chairman
Donald Edwards, Physicist, Fermilab, Co-chairman
Professor Robert Lewis
Professor David Winter
Leo Michelotti, Physicist, Fermilab

© Nikolitsa Merminga 1989
All Rights Reserved

*Αφιερωμένο
στη μάνα μου
και
στον πατέρα μου*

ACKNOWLEDGEMENTS

It is a great pleasure to sincerely thank my Dissertation Committee members: Professors Jones, Lewis, Winter and in particular Professor Terwilliger, of the University of Michigan, for their support. I would also like to thank the members of the PhD in Accelerator Physics Committee of the Fermi National Accelerator Laboratory for allowing me the opportunity to participate in their program.

The expertise and assistance of my FNAL collaborators Dave Finley, Rod Gerig, Norman Gelfand, Mike Harrison, Rol Johnson and particularly Mike Syphers — whom I thank for carefully reading my thesis — has always been appreciated.

I would like to thank my CDG collaborators Dave Johnson, Jack Peterson, Lindsay Schachinger, Chris Saltmarsh and Tjet Sun for always being very helpful and hospitable in my visits there. Alex Chao and Richard Talman have been invaluable to me throughout this work, for their insightful conversation and support. Above all from Berkeley, Steve Peggs, whom, despite the fact that he has constantly given me hard times, I like to thank for everything he taught me, and above all: ‘Often wrong, never in doubt!’

I also want to thank Phil Morton of SLAC for his support.

Outside the E778 collaboration, thanks must go to King-Yuen (Bill) Ng and Sateesh Mane for always being very helpful to me, and to Jim MacLachlan for reading and commenting on my thesis.

To Leo Michelotti I am grateful for being able to count on his presence whenever I had a question.

Above all, it is Don Edwards who resides in the heart of this work. He introduced me to accelerator physics, taught me the scientific methods and provided direction throughout the entire work. His support has always been patient, his encouragement and understanding unlimited, his guidance subtle, and his teaching insightful.

TABLE OF CONTENTS

DEDICATION	ii
ACKNOWLEDGEMENTS	iii
LIST OF FIGURES	vii
LIST OF TABLES	xii
LIST OF APPENDICES	xiii
CHAPTER	
I. INTRODUCTION	1
History of High Energy Physics Accelerators	
Motivation of Thesis	
Structure of Thesis	
II. SINGLE PARTICLE DYNAMICS IN THE PRESENCE OF A SEXTUPOLE FIELD	8
Beam Shape Distortions — Distortion Functions	
Second Order Tuneshifts	
One Dimensional Nonlinear Resonance	
III. GENERAL REMARKS ON THE EXPERIMENTS	33
Sextupoles Used in E778	
Phase Space Measurements	
Preliminary Steps for the Experiments	
Experimental Procedures	
IV. THE SMEAR EXPERIMENT	51
The Perturbative Approach	
Tracking Calculations	
The Experiment	
Analysis	
Results	

V. THE INJECTION EXPERIMENT	112
The Experiment	
Results	
VI. RESONANCE ISLANDS	125
Island Width and Island Tune	
Simulation	
The Experiment	
Analysis	
Results	
VII. THE DYNAMIC APERTURE EXPERIMENT	160
The Experiment	
Analysis	
Results	
VIII. CONCLUDING REMARKS	169
APPENDICES	172
BIBLIOGRAPHY	199

LIST OF FIGURES

<u>Figure</u>	
1.1	Poincaré plot generated by numerically tracking particles of various amplitudes. 6
2.1	Schematic representation of the phase space structure of the third integer resonance. 32
3.1	Tevatron layout during E778. 34
3.2	Power supplies connecting the E778 sextupoles. 36
3.3	Vector diagram showing a strong driving term for the resonance $3\nu_x = 58$ due to the 16 E778 sextupoles. \mathcal{R} denotes the resultant of the 16 vectors s_1 to s_{16} 37
3.4	(a) and (c) are the output of two neighboring BPMs for 1024 turns. The Fourier transforms are shown in (b) and (d); the fractional part of the tune is .34. 39
3.5	Phase space plot constructed from data similar to that shown in Fig. 3.4. Normalized coordinates have been employed on purpose in order to obtain the characteristic circle of the simple harmonic motion. 40
3.6	Phase space plot from experimental data for betatron oscillation of amplitude close to third-integer resonance separatrix. 41
3.7	Waveform generator for the chromaticity measurements. 45
3.8	Experimental data of the closed orbit. 48
3.9	Measurements of tune versus sextupole current. 49
4.1	Smear versus phase advance, around the machine, as predicted from perturbation calculation. 54
4.2	Smear versus amplitude, from perturbation calculation. 56
4.3	Smear versus sextupole strength, from perturbation. 57

4.4	Smear versus sextupole excitation for $\nu = 19.42$, as predicted from EVOL tracking.	61
4.5	Smear versus amplitude for $\nu = 19.42$ and 30 amperes, as predicted from EVOL tracking.	62
4.6	Tune versus amplitude from single particle EVOL simulation.	64
4.7	The standard Fermilab BPM front end electronics were used to record the above turn-by-turn data of the centroid of the beam.	69
4.8	Peak-sensing front end electronics were used to record these turn-by-turn data.	70
4.9	Flow diagram of TEVEX.	74
4.10	Typical example of TEVEX.CMD, the file which contains the values of the control parameters.	75
4.11	Raw position data before and after filtering of the synchrotron oscillations. The title indicates that this dataset was recorded with a kicker strength of 5 kV, sextupole excitation of 15 amps and tune of 19.39.	76
4.12	Ranges of data that are relevant to the analysis by TEVEX.	78
4.13	Position of the centroid of the beam and smear plotted as functions of turn number. The determination of smear deteriorates as the beam decoheres.	79
4.14	Typical TEVEX.OUT file; the analysis has been performed at level 0. . .	82
4.15	Typical TEVEX.OUT for analysis performed at level 3.	87
4.16	Raw beam intensity data, in least significant bits (LSB) for 4000 turns. Zero intensity corresponds to 2048 bits. The calibration constant is $-134 \text{ LSB}/10^{10}$ particles.	88
4.17	Typical graphical output of TEVEX for analysis performed at level 0. . .	90
4.18	Typical graphical output of TEVEX for analysis performed at level 3. . .	91
4.19	Smear versus sextupole excitation, for low emittance data.	93
4.20	Smear versus sextupole excitation for high emittance data.	95
4.21	Smear versus sextupole excitation; comparison between predictions of perturbation theory and experimental data.	96

4.22	Smear versus sextupole excitation; comparison between predictions from perturbation theory and tracking calculations.	97
4.23	Smear versus kicker strength for low emittance data.	98
4.24	Smear versus kicker strength for high emittance data.	99
4.25	Decoherence time versus sextupole strength for low emittance and a kick of 5kV.	101
4.26	Decoherence time versus sextupole strength, high emittance, 5kV kick. .	102
4.27	Decoherence time versus sextupole strength, low emittance, 8 kV kick. .	103
4.28	Decoherence time versus sextupole strength, high emittance, 8 kV	104
4.29	Decoherence time versus sextupole strength, low emittance, 10 kV	105
4.30	Decoherence time versus sextupole strength, high emittance, 10 kV	106
4.31	Experimental data illustrating the dependence of tune on the amplitude. The smooth curve is a fit to the data.	107
4.32	Simulation of two experimental conditions in phase space at kicker location immediately after beam deflection. The dotted line represents the limit of stability. The dots represent the particle distribution. . . .	109
4.33	Fraction of surviving particles as a function of the horizontal tune. . . .	110
5.1	First-turn data taken with the sextupoles turned off, (a) without, (b) with a steering error of 4 kV, and (c) their difference.	113
5.2	Difference between first-turn data taken by injecting the beam on the closed orbit and off the closed orbit. The sextupole excitation is 45 amps.	115
5.3	Overlay of Fig. 5.1(c) and Fig. 5.2.	116
5.4	Display frame data, at 0 amps and a tune of 19.42, (a) without and (b) with a steering error. The difference is illustrated in (c). Another such difference, with the sextupoles powered to 45 amps is illustrated in (d). .	117
5.5	Flying wire data from the Tevatron at C48. The sextupole excitation was 45 amps and the tune 19.38. In (a) there was no steering error; in (b) there was a steering error of 4 kV. Profiles (1) were taken .25 secs after injection, and profiles (2) were taken 9 secs later.	119

5.6	Fraction of beam lost between injection into the Tevatron and 5 secs later, versus sextupole excitation.	120
5.7	Beam intensity in the Main Ring and Tevatron as a function of time for a sextupole excitation of 45 amps and a tune of 19.42.	121
5.8	Plot obtained from the scintillation counters associated with the flying wires, illustrating that the time structure of the losses contains a component at the synchrotron frequency.	123
5.9	Summary of the results on the losses after the RF was turned off, and the cavities cooled.	124
6.1	Contours of the Hamiltonian describing motion under the action of a fifth-order resonance. The sextupole excitation is 25 amperes and the initial tune 19.415.	128
6.2	Action-angle representation of single particle tracking using EVOL. The sextupole excitation is 25 amperes, the kick amplitude is 5.25 mm and the initial tune 19.415.	132
6.3	Relative position of the kicked beam with respect to the five stable islands.	134
6.4	A magnified view of the previous plot.	135
6.5	Raw BPM turn-by-turn output, for (a) 4000 turns and (b) 500 turns, with sextupole strength of 25 amps. The capture efficiency is given by amplitude (2) / amplitude (1).	137
6.6	Experimental phase space plot, for 4000 turns, starting right before the kick.	138
6.7	Experimental phase space plot of the same data as in Fig. 6.6, taken some seconds later.	139
6.8	A different representation of the data of the previous plot where successive points are now joined by straight lines. This plot confirms the 2/5 identification.	140
6.9	Typical TEVEX output including the persistent signal analysis.	144
6.10	Typical graphical output of TEVEX in the case of persistent signal analysis.	145
6.11	Kick amplitude versus base tune, corresponding to maximum capture efficiency. Data have been obtained from EVOL simulations.	146

6.12	Island tune versus resonance amplitude, from single particle EVOL tracking.	147
6.13	Phases of the five islands versus tune as predicted from EVOL.	148
6.14	Phases of the five islands from experimental data.	150
6.15	Capture efficiency versus tune using EVOL, for 4 different kick amplitudes.	151
6.16	Resonant response of the capture fraction as a function of the tune. The curve only guides the eye. The different symbols differentiate a course and a fine scan.	152
6.17	Maximum persistent response versus kick amplitude, for the experimental data (crosses) and from simulated data (rhombs). The dashed line is a theoretical fit to the data.	153
6.18	The beam on the left has been kicked while sextupole SF22 was turned off.	154
6.19	The beam on the right has been kicked while sextupole SF26 was turned off.	156
6.20	The beam on the left has been kicked while sextupole SF28 was turned off.	157
6.21	The beam on the left has been kicked in the presence of a phase error. .	158
6.22	The beam on the left has been kicked in the presence of a phase error and of one of the sextupole (SF22) being turned off.	159
7.1	Phase space trajectories close to the dynamic aperture.	161
7.2	Beam intensity versus time for a sextupole excitation of 30 amps.	162
7.3	Beam profiles taken using the wire profile technique, at the location HC48.	164
7.4	Dynamic aperture at HC48. The circles represent the experimental data points while the dashed line was obtained from tracking calculations using TEAPOT and ART.	166
7.5	Dynamic aperture at HA17. The smooth curve is a fit to the simulated results for off-momentum particles.	167
F.1	Tevatron F4 to Sun 3/140 (Fig) cabling.	195
F.2	Links among the Suns and the Schottky and noise devices.	196
F.3	Part of the ceiling of the service building F4.	197

LIST OF TABLES

Table

4.1	Summary of the accelerator conditions at which low emittance data were taken, in the smear experiment.	67
4.2	Summary of the conditions at which high emittance data were taken in the smear experiment.	68
4.3	Amplitude-dependent tunes shift as calculated from perturbation theory and from single particle tracking. The agreement between the two methods of calculation is very good.	108
6.1	A summary of multiparticle EVOL simulation performed for the study of the resonance islands.	136
6.2	A summary of the experimental conditions at which data were taken for the study of the nonlinear resonance islands.	142

LIST OF APPENDICES

Appendix

A.	Smear due to horizontal-vertical coupling	173
B.	Derivation of the expression for the amplitude	177
C.	Derivation of the expression for the phase advance	179
D.	Derivation of decoherence due to nonlinearity	180
E.	TEVEX Subroutines	184
F.	E778 Hardware	194

CHAPTER I

INTRODUCTION

This thesis describes a beam dynamics experiment (E778) performed in the Fermilab Tevatron. Experiment E778 was motivated by the desire to reduce uncertainties in the design of the 40 TeV center-of-mass energy Superconducting Super Collider (SSC) [1].

Controlled nonlinear elements added in the Tevatron, created the nonlinear environment anticipated in the SSC. Observations were made which are applicable to areas of physics much broader than accelerator physics, since they relate to the phase-space description of nonlinear oscillations. Those features are described in this work. The subject of this thesis, then, is the study, both experimental and theoretical, of a Hamiltonian system and its Poincaré map, an object described later.

The new element of this study is the experimental demonstration of theoretically predicted phase-space features, in particular the new state of the accelerator, with particles captured on nonlinear resonance islands.

There have been two experimental runs to date, in May 1987 [2] and in February 1988 [3,4,5,6], and there are plans for continuing studies. The work described here is the cumulative effort of many individuals. My contribution was restricted to participating in the data acquisition and data analysis. One of the simulation codes (ART) was written by me. I am also responsible for the theoretical discussion and

derivations using the canonical Hamiltonian formalism.

In order to put the significance of this work into its historical and scientific context, a brief overview of high energy physics accelerators is presented first. Next the motivation for this study is discussed, and much of the terminology is introduced when the structure of the thesis is explained.

History of High Energy Physics Accelerators

Some of the fundamental questions of high energy physics lead to the understanding of the marvelous complexity of the physical world in basic terms. High energy physics is both a theoretical and an experimental science, but its progress is largely paced by the technology of its accelerator and detectors. Accelerators are instruments for producing the reactions that reveal the basic material entities and their interactions.

The history of accelerators is one of generations. Each generation corresponds to the invention of a new device, which is subsequently replaced by another, more powerful innovation. The electrostatic accelerators, typical example of which is the Van de Graaff machine, were followed by the cyclotron which was based on the concept of time varying accelerating fields. Next, the weak focusing notion as a mechanism for beam confinement was introduced through the betatron, an accelerator based on electromagnetic induction. The synchrocyclotron took the lead next and the concept of longitudinal phase space stability was introduced.

In 1952 a new idea was advanced by Courant, Livingston and Snyder (suggested two years earlier by Christofilos but not published): the alternating-gradient focusing, or strong-focusing [11]. This technique allowed particles to circulate in the machine, called synchrotron, for millions of orbits. The combination of the strong-focusing concept and the phase stability led to controlled acceleration to high energies.

The storage ring is now the highest energy accelerator. The largest energy in

the center of mass, 1.8 TeV, is currently achieved in the Tevatron, located at Fermi National Accelerator Laboratory (Fermilab). The Tevatron, with its one-kilometer radius, is a proton-antiproton collider, like CERN's $S\bar{p}\bar{p}S$ collider. The proposed SSC will be a proton-proton collider. Its design energy is 22 times larger than that of the Tevatron and its circumference is 53 miles.

Motivation of Thesis

The bending magnets of the SSC, approximately 8000, represent a significant fraction of the total project cost. The magnet cost grows with the size of the aperture provided for the beam. Hence a critical parameter in the optimization of the SSC design is the 'magnet aperture' [7]. In order to optimize the SSC design, the aperture-size must be chosen (a) to minimize the cost and (b) to provide a high confidence level in achieving the design performance goal. If the chosen aperture is too large, the design will not be cost effective. Too small an aperture will cause difficulties in operation. The value chosen for the aperture in the SSC Conceptual Design Report [1] is based on accelerator theory, past experience and extensive computer simulations. Due to the great importance of this result, an experimental study of the aperture was suggested in order to evaluate the design as well as to improve the criteria for the determination of a magnet aperture. The Tevatron was chosen for this experimental study for reasons that will soon be described.

In the SSC the effective aperture will be determined by nonlinearities in the magnetic field [1,7]. By intentionally adding nonlinear elements into the Tevatron, one could "mock up" some nonlinear features anticipated for the SSC. Experiment E778 addressed the question of studying the particle motion under the influence of controlled nonlinearities in the Tevatron.

Structure of Thesis

The one-degree-of-freedom equation of motion of a particle in a storage ring, in the presence of sextupole magnets, is given by

$$\frac{d^2 X}{ds^2} + K(s)X = -\epsilon(s)X^2, \quad (1.1)$$

where $X(s)$ is the horizontal deviation of the particle from the closed orbit. Here s is the longitudinal particle coordinate, which advances from 0 to C , the circumference, as the particle completes one revolution of the accelerator.

Particles execute ‘betatron’ oscillations about the closed orbit with linear focusing due to quadrupole fields of strength $K(s)$ given by

$$K(s) = \frac{B'_y}{B\rho}. \quad (1.2)$$

The product $B\rho$ is called the magnetic rigidity of the particle and it is proportional to the particle’s momentum,

$$B\rho = \frac{p}{e}, \quad (1.3)$$

e being the charge of the electron and ρ the radius of curvature. ($B\rho$) can be calculated from

$$B\rho = \frac{10}{2.9979} p_{\text{GeV}/c} \quad \text{Tesla} - \text{meters}. \quad (1.4)$$

The quadrupole strength $K(s)$ alternates sign in an alternating-gradient accelerator such as the Tevatron. The number of betatron oscillations in one turn is called the tune, ν : about 19.4 for the Tevatron. (Occasionally the symbol Q will also be used to denote the tune.)

The nonlinear term on the right hand side of (1.1) is due to sextupole fields of strength $\epsilon(s)$. It can sometimes be treated perturbatively. Both $K(s)$ and $\epsilon(s)$ are periodic functions of s with period C .

The concept of phase space is closely related, both theoretically and experimentally, to the analysis of these oscillations. The coordinate X and the slope $P \equiv dX/ds$

form the phase space. An observer, stationed at a fixed point in the accelerator observing the horizontal motion of a particle can plot the phase space point X_t, P_t for successive turns t , to obtain a Poincaré plot. After a simple transformation, these points are given by

$$X_t = A_t \cos \Phi_t \quad (1.5)$$

and

$$P_t = -A_t \sin \Phi_t, \quad (1.6)$$

where $A_t^2/2, \Phi_t = 2\pi\nu t$ are the ‘action-angle’ variables. When the amplitude A_t is sufficiently small, it does not deviate from its average value A , and the phase space point moves on a circle on the X, P plot. When nonlinearities become important, the phase space point falls on a smooth, yet distorted, curve. From here on, the terms phase space plot and Poincaré plot will be used interchangeably.

The expected phase space structure can be calculated by numerical tracking of particles. This is illustrated in Fig. 1.1 where particles of various amplitudes have been tracked through an accurate representation of the Tevatron. Most of the features have been demonstrated and measured during E778. In order to link the various features of the phase space to the specific experiments the E778 collaboration performed, the qualitative phase space behavior at various amplitudes is considered next.

At sufficiently small amplitudes the motion is still linear to a good approximation and the one-degree-of-freedom trajectories are circles. At larger amplitudes deviation from circularity due to the nonlinearities becomes apparent. To quantify the magnitude of the distortion a parameter called ‘smear’ is defined as the root mean square (rms) deviation from a circle. In experiment E778 the smear was measured for a variety of accelerator conditions and compared with both numerical and analytical calculations. These measurements constitute the Smear Experiment. Along with the corresponding theoretical predictions, they form the subject of the Chapter IV.

The correlation between the smear and such accelerator performance measures as

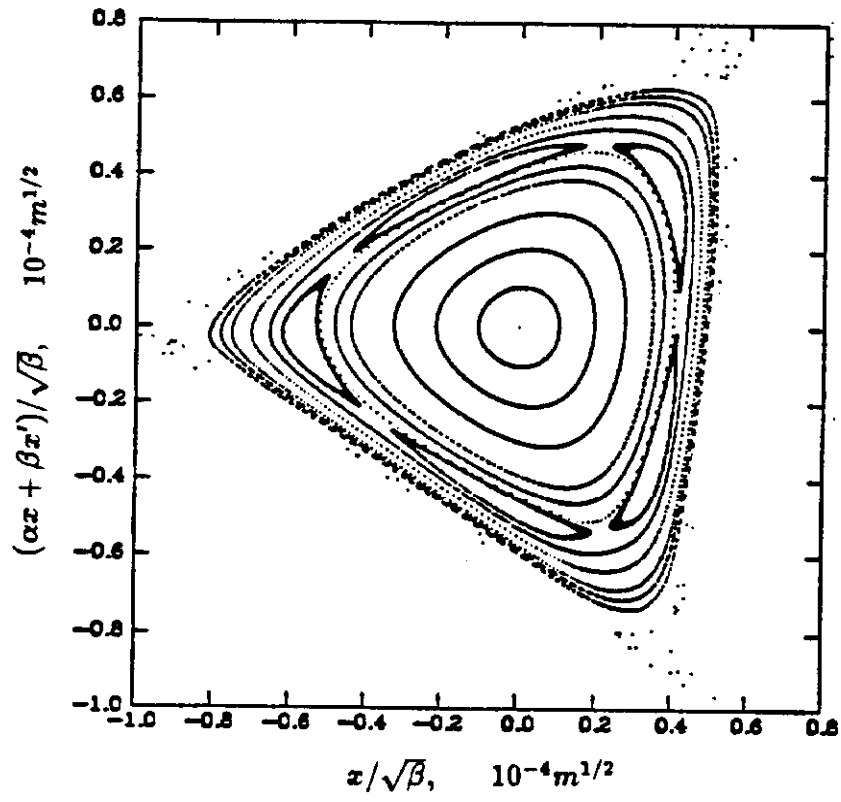


Figure 1.1: Poincaré plot generated by numerically tracking particles of various amplitudes.

injection efficiency and particle lifetime was also studied. This second experiment is the Injection Experiment and it is described in Chapter V.

At intermediate amplitudes, one finds a very interesting feature of the nonlinear motion, namely the five-beaded necklace, conventionally called the $n=5$ resonance island chain. Fundamental quantities associated with this structure are calculated and compared with experimental results. This experiment will be referred to as the Resonance Island Experiment and it is analyzed in Chapter VI.

Finally, at large amplitudes the regularity is lost and the motion becomes chaotic. The largest regular contour is sometimes called the 'dynamic aperture' of the accelerator. It decreases with the increase of the magnitude of nonlinearities. In E778 the dynamic aperture was measured for various conditions. These results are compared with the prediction from short-term tracking calculations. These measurements comprise the Dynamic Aperture Experiment, the analysis of which is given in Chapter VII.

Chapter II is devoted to a theoretical discussion of the concepts investigated experimentally in E778, while Chapter III contains general remarks on the experimental aspect of this study. Most of the lengthy and tedious derivations have been put in the Appendices. Thus, the general reader need not be distracted with their mathematical details.

Before the end of this introduction, two more remarks are in order. First, nonlinearities were introduced into the Tevatron in the form of already installed sextupole magnets. Second, the study described in this thesis is a purely one-degree-of-freedom one: horizontal. Already existing plans for continuation of this experiment include studies in both transverse planes.

CHAPTER II

SINGLE PARTICLE DYNAMICS IN THE PRESENCE OF A SEXTUPOLE FIELD

Hamiltonian concepts are important in analysing phase space motion. The Hamiltonian leading to (1.1) is

$$H_1(X, P; s) = \frac{1}{2} [P^2 + K(s)X^2] + \frac{1}{3}\epsilon(s)X^3. \quad (2.1)$$

In the case of E778 where the nonlinearities were introduced in the form of sextupole magnets, $\epsilon(s)$ is the normal sextupole strength

$$\epsilon(s) = \frac{B_y'''}{2(B\rho)}. \quad (2.2)$$

A canonical transformation is performed next to 'normalized' coordinates x, p , in terms of which the linear part of the motion is reduced to a simple harmonic oscillator. This is called a Floquet transformation. The new coordinates and momenta are given in terms of the old ones through the relations

$$x = \sqrt{\frac{\beta_0}{\beta}} X \quad (2.3)$$

and

$$p = \sqrt{\frac{\beta}{\beta_0}} P - \frac{\alpha}{\beta_0} \sqrt{\frac{\beta_0}{\beta}} X. \quad (2.4)$$

Here β is the horizontal beta function at the point x . Also known as the 'Courant-Snyder amplitude function', the beta function is usually a periodic function of s and

its square root is proportional to the amplitude of the betatron oscillation. The beta function at a reference point is denoted by β_0 above. The parameter α is defined by

$$\alpha \equiv -\frac{1}{2}\beta', \quad (2.5)$$

where prime denotes differentiation with respect to s . Together with β and a third parameter γ defined by

$$\gamma \equiv \frac{1 + \alpha^2}{\beta}, \quad (2.6)$$

they form the so called lattice parameters. They are also referred to as Courant-Snyder parameters collectively.

The new Hamiltonian becomes

$$H_2 = \frac{R}{2\beta} \left(\beta_0 p^2 + \frac{x^2}{\beta_0} \right) + \frac{RB_y''}{6B\rho} \left(\frac{\beta}{\beta_0} \right)^{3/2} x^3, \quad (2.7)$$

where the independent variable s has been changed to the more convenient $\theta = s/R$, R being the average radius of the storage ring.

So the Hamiltonian now is that of a simple harmonic oscillator with the addition of a small nonlinear term due to sextupoles. It is well known that action-angle coordinates are very useful for studying this problem. Hence the action-angle variables I, a are defined here by

$$x = \sqrt{2I\beta_0} \cos [\psi(\theta) - \nu\theta + a] \quad (2.8)$$

and

$$\beta_0 p = -\sqrt{2I\beta_0} \sin [\psi(\theta) - \nu\theta + a], \quad (2.9)$$

where

$$\beta_0 p = \frac{dx}{d\psi}, \quad (2.10)$$

and it is denoted by x' below. The betatron tune is denoted by ν and $\psi(\theta)$ defined by

$$\psi(s) = \int_{s_0}^s \frac{ds'}{\beta(s')} \quad (2.11)$$

is the Floquet phase at the location θ , or the betatron phase at θ . The amplitude of the motion will be denoted by \mathcal{A} and is defined by

$$\mathcal{A} = \sqrt{2I\beta_0} \quad (2.12)$$

and the phase ϕ is defined by

$$\phi = \psi(\theta) - \nu\theta + a. \quad (2.13)$$

Then Eqs (2.8) and (2.9) take the form

$$x = \mathcal{A} \cos \phi \quad (2.14)$$

and

$$x' = -\mathcal{A} \sin \phi. \quad (2.15)$$

The new Hamiltonian, in terms of action-angle variables, reads

$$H_3 = \nu I + \frac{RB_y''}{6(B\rho)} \left(\frac{\beta}{\beta_0} \right)^{3/2} (2I\beta_0)^{3/2} \cos^3(\psi - \nu\theta + a). \quad (2.16)$$

The final goal is to come up with a set of coordinates in terms of which the Hamiltonian assumes the form

$$H(a, I) = \nu_1 I + \nu_2 I^2 + \nu_3 I^3 + \dots, \quad (2.17)$$

that is, H is a function of the action only, independent of angle. This can be accomplished via a series of canonical transformations [8]. The purpose of each of these transformations is to defer the angular dependence to higher order. As expected the coefficients $\nu_1, \nu_2, \nu_3, \dots$ are of order 0, 2, 4, ... in the small perturbation parameter which is proportional to the sextupole strength.

It is demonstrated in this chapter that applying these transformations to first order results in the distortions of the beam shapes, which are relevant to the smear experiment. Eventually these formulæ will be used to derive expressions for the smear which will be compared with experimental and tracking calculations.

Furthermore, it is shown that a second order Moser transformation leads to the expressions for the variation of tune with amplitude (the term ‘amplitude-dependent tuneshift’ will also be used) due to nonlinearities. Comparison with experimental and simulated results will also be given.

A third order Moser transformation of the Hamiltonian (2.16) will be demonstrated next. This derivation will lead to an expression which describes a system under the action of a nonlinear resonance. It serves as the theoretical model for the description of the nonlinear resonance island region of the phase space. Expressions of the ‘island width’ and the ‘island tune’ (to be defined below) will be derived and compared with single particle tracking results.

It should be noted that several theoretical models [14,15,16,17,18] exist to describe the resonance island part of the phase space. The Moser transformation approach was chosen because it is a traditional and rather pedagogical one.

Finally at large amplitudes, near the boundary of stability, the phase space topology can be described reasonably accurately by a model which assumes only the existence of the third integer resonance. The details of this description will be given in the last section of this chapter.

In reality large amplitudes exhibit chaotic behavior. This is illustrated in Fig. 1.1 by the dots outside the dynamic aperture. Understanding of the chaotic region though is beyond the scope of this thesis.

Beam Shape Distortions — Distortion Functions

Following tradition [15,16,17], the canonical Hamiltonian formalism is used to derive the lowest order beam shape distortions due to sextupoles in the horizontal plane. The final formulæ are expressed in terms of ‘distortion functions’, a term introduced by Collins [20]. The idea of distortion functions is the following. As shown above, a judicious transformation of the variables forced the formulæ describing the

linear part of a betatron motion to be identical to that for simple harmonic motion. The idea of distortion functions is to account approximately for extra perturbing effects by allowing the amplitude \mathcal{A} and the phase ϕ of (2.14) and (2.15), to be ‘distorted’ by the addition of small s -independent terms $\delta\mathcal{A}$ and $\delta\phi$. To first order in the strength of the nonlinear perturbation (the sextupole strength here), the motion is described by

$$x \sim (\mathcal{A} + \delta\mathcal{A}) \cos(\phi + \delta\phi). \quad (2.18)$$

In the accelerator physics context distortion functions have been derived independently by various authors [20,9,10,15,22,8].

Only an outline of the derivations of beam shape distortions will be presented here. More detailed discussion can be found in references [21,22,23].

In Eq. (2.16), note that the expression

$$\frac{RB_y''}{6(B\rho)} \left(\frac{\beta}{\beta_0} \right)^{3/2} e^{i(\psi - \nu\theta)} \quad (2.19)$$

is a periodic function of θ , hence it can be expanded into harmonics, to get

$$H_3(a, I) = \nu I + (2I)^{3/2} \beta_0^{1/2} \sum_m [3A_{1m} \sin(a - m\theta) + A_{3m} \sin(3a - m\theta)], \quad (2.20)$$

where

$$A_{1m} = \frac{i}{24\pi} \sum_k s_k e^{i(\psi - \nu\theta + m\theta)_k} \quad (2.21)$$

and

$$A_{3m} = \frac{i}{24\pi} \sum_k s_k e^{i(3\psi - 3\nu\theta + m\theta)_k}. \quad (2.22)$$

The summation above is over all the sextupoles in the ring, which are assumed to have infinitesimal length ℓ_k and strengths

$$s_k = \left(\frac{\beta_x^3}{\beta_0} \right)_k^{1/2} \frac{(B_y''\ell)_k}{2(B\rho)}. \quad (2.23)$$

In principle one could now solve the equations of motion obtained from the Hamiltonian H_3 to first order and calculate the beam shape. However, I am going to

proceed by making a Moser transformation from (a, I) to (b, J) so that the J 's become constants of the motion up to first order in s_k . The generating function of this transformation is

$$G_3(a, J; \theta) = aJ - (2J)^{3/2} \beta_0^{1/2} \sum_m \left(\frac{3A_{1m}}{m - \nu} \cos q_{1m} + \frac{A_{3m}}{m - 3\nu} \cos q_{3m} \right), \quad (2.24)$$

where $q_{1m} = a - m\theta$ and $q_{3m} = 3a - m\theta$. By definition, the new Hamiltonian is

$$H_4 = \nu J + \Delta H_4|_{\text{ext}}, \quad (2.25)$$

where $\Delta H_4|_{\text{ext}}$ does not contain any zeroth or first order terms in s_k . The first order changes in I and a are given by

$$\delta I = I - J = \frac{\partial G_3}{\partial a} - J \quad (2.26)$$

and

$$\delta a = a - b = a - \frac{\partial G_3}{\partial J}. \quad (2.27)$$

Explicitly they are

$$\delta I = (2I)^{3/2} \beta_0^{1/2} \sum_m \left(\frac{3A_{1m}}{m - \nu} \sin q_{1m} + \frac{3A_{3m}}{m - 3\nu} \sin q_{3m} \right) \quad (2.28)$$

and

$$\delta a = 3(2I)^{1/2} \beta_0^{1/2} \sum_m \left(\frac{A_{1m}}{m - \nu} \cos q_{1m} + \frac{A_{3m}}{m - 3\nu} \cos q_{3m} \right). \quad (2.29)$$

These are related to the changes in amplitudes and phases through the relations

$$\delta \mathcal{A} = \left(\frac{\beta_0}{2I} \right)^{1/2} \delta I \quad (2.30)$$

and

$$\delta \phi = \delta a. \quad (2.31)$$

Before the calculation of the changes in the amplitude and phase, notice that when ν or 3ν equals an integer, in Eqs (2.28) and (2.29) the solutions diverge. These are in fact the first-order resonances for the sextupoles. When the tune is close to

a particular resonance, then the resonance term dominates in the sum and one can safely disregard the rest of the terms. This is the way to handle the situation near a resonance. I shall return to this point soon.

For the time being, a situation far away from resonances is assumed and the summations over m in (2.28) and (2.29) are performed. Using the formula

$$\sum_{m=-\infty}^{\infty} \frac{e^{i(m\theta + b)}}{m - \nu} = \begin{cases} -\frac{\pi}{\sin \pi \nu} e^{i[b + \nu(\theta - \pi)]} & 0 < \theta < 2\pi \\ -\pi(\cot \pi \nu) e^{ib} & \theta = 0 \end{cases} \quad (2.32)$$

one arrives at

$$\delta \mathcal{A} = \mathcal{A}^2 [(A_1 \sin \phi - B_1 \cos \phi) + (A_3 \sin 3\phi - B_3 \cos 3\phi)] \quad (2.33)$$

and

$$\delta \phi = \mathcal{A} [3(A_1 \cos \phi + B_1 \sin \phi) + (A_3 \cos 3\phi + B_3 \sin 3\phi)], \quad (2.34)$$

where A_1 , B_1 , A_3 and B_3 are the Collins' distortion functions defined by

$$B_1(\psi) = \frac{1}{2 \sin \pi \nu} \sum_k \frac{s_k}{4} \cos(|\psi_k - \psi| - \pi \nu) \quad 0 \leq |\psi_k - \psi| \leq 2\pi \nu$$

$$A_1(\psi) = B_1'(\psi) \quad 0 < |\psi_k - \psi| < 2\pi \nu \quad (2.35)$$

$$B_3(3\psi) = \frac{1}{2 \sin 3\pi \nu} \sum_k \frac{s_k}{4} \cos 3(|\psi_k - \psi| - \pi \nu) \quad 0 \leq |\psi_k - \psi| \leq 2\pi \nu$$

$$A_3(3\psi) = B_3'(3\psi) \quad 0 < |\psi_k - \psi| < 2\pi \nu.$$

The prime denotes differentiation with respect to the argument. The distortion functions defined above are lattice functions due to the presence of sextupoles, much the same way β and α are lattice functions due to the presence of normal quadrupoles. They are periodic functions of the ring. Notice that at a sextupole of strength s_k , A_1 jumps by $s_k/4$ while B_1 remains continuous but exhibits a cusp. Another property

of the distortion functions is the following. If B, A are the distortion functions at location ψ , then the distortion functions at location $\psi' = \psi + \alpha$ are given by

$$B' = \frac{1}{2 \sin \pi \nu} \cos (\psi + \alpha - \psi_k - \pi \nu) \quad (2.36)$$

and

$$A' = -\frac{1}{2 \sin \pi \nu} \sin (\psi + \alpha - \psi_k - \pi \nu), \quad (2.37)$$

where it is assumed for simplicity that there is only one sextupole at location ψ_k , with $\psi_k < \psi, \psi'$. From here one concludes that

$$\begin{pmatrix} B' \\ A' \end{pmatrix} = \begin{pmatrix} \cos \alpha & \sin \alpha \\ -\sin \alpha & \cos \alpha \end{pmatrix} \begin{pmatrix} B \\ A \end{pmatrix}, \quad (2.38)$$

which implies a rotation of the vector (B, A) by an angle α .

Finally, taking into account an average dipole effect that sextupoles have on a charged particle which leads to a distortion of the ideal closed orbit, one obtains

$$\delta \mathcal{A} = \mathcal{A}^2 [-(A_1 \sin \phi - B_1 \cos \phi) + (A_3 \sin 3\phi - B_3 \cos 3\phi)] \quad (2.39)$$

and

$$\delta \phi = \mathcal{A} [(A_1 \cos \phi + B_1 \sin \phi) + (A_3 \cos 3\phi + B_3 \sin 3\phi)]. \quad (2.40)$$

The distorted beam shape in the horizontal phase space are given by

$$x = \delta x + (\mathcal{A} + \delta \mathcal{A}) \cos (\phi + \delta \phi) \quad (2.41)$$

and

$$x' = \delta x' - (\mathcal{A} + \delta \mathcal{A}) \sin (\phi + \delta \phi), \quad (2.42)$$

where

$$\delta x = -2\mathcal{A}^2 B_1 \quad (2.43)$$

and

$$\delta x' = -2\mathcal{A}^2 A_1. \quad (2.44)$$

Second Order Tuneshifts

Nonlinearities cause variation of the frequency with amplitude. The first order perturbation does not produce any such tuneshifts. The reason is that the first order term in the perturbation Hamiltonian is of the form x^3 . Since $\cos^3 \phi$ averages to zero, there is no resultant shift in the tune to first order and hence one must seek higher approximations. The lowest contribution to the tuneshift comes from the second order.

From the generating function G_3 of Eq. (2.24),

$$(2I)^{3/2} = (2J)^{3/2} + 9(2J)^2 \beta_0^{1/2} \sum_m \left(\frac{A_{1m}}{m - \nu} \sin q_{1m} + \frac{A_{3m}}{m - 3\nu} \sin q_{3m} \right). \quad (2.45)$$

The second order terms in the Hamiltonian is

$$\begin{aligned} \Delta H_4|_{\text{sext}} = & \sum_{m'} (3A_{1m'} \sin q_{1m'} + A_{3m'} \sin q_{3m'}) \times \\ & \times 9\beta_0(2J)^2 \sum_m \left(\frac{A_{1m}}{m - \nu} \sin q_{1m} + \frac{A_{3m}}{m - 3\nu} \sin q_{3m} \right). \end{aligned} \quad (2.46)$$

Since the betatron tunes are defined per revolution, one must average over θ to obtain

$$\Delta H'_4|_{\text{sext}} = \frac{9}{2} \beta_0 (2J)^2 \sum_m \left(\frac{3A_{1m}^2}{m - \nu} + \frac{A_{3m}^2}{m - 3\nu} \right). \quad (2.47)$$

Summation over the harmonics leads to the following result

$$\sum_m \frac{A_{1m}^2}{m - \nu} = -\frac{1}{72\pi} \sum_k (B_1 s)_k \quad (2.48)$$

and

$$\sum_m \frac{A_{3m}^2}{m - 3\nu} = -\frac{1}{72\pi} \sum_k (B_3 s)_k. \quad (2.49)$$

Here B_1 and B_3 are the distortion functions previously defined by (2.35). Recalling that the tuneshift is given by

$$\Delta\nu = \frac{\partial \Delta H'_4}{\partial J}, \quad (2.50)$$

the second order tuneshift due to sextupoles is

$$\Delta\nu = -\frac{1}{4\pi} \mathcal{A}^2 \sum_k (3B_1 s + B_3 s)_k. \quad (2.51)$$

There are two remarks to be made on this expression. First the parabolic dependence of tune on the amplitude is characteristic to sextupole-induced nonlinearities. Second the effect of nonlinearity is to make the tune change with increasing amplitude. It is demonstrated later that this behavior is followed by experimental data. Finally these two properties of the tuneshift are first responsible for the phenomenon of the ‘decoherence’ of the beam (to be described later) and second, they lead to the formation of the nonlinear resonance islands, a concept I am introducing next.

One Dimensional Nonlinear Resonance

Sextupole-Generated 2/5 Resonance Islands

In this section attempt is made to understand intuitively the origin of the $n=5$ resonance island chain. Furthermore, a mathematical derivation is presented demonstrating how a Hamiltonian describing the motion of a particle in the presence of a sextupole field can lead to a new Hamiltonian representing motion along the contours of the 5 resonance islands.

The concept of resonance enters as follows. Suppose that the base tune (the tune with the nonlinearities set equal to zero) is just above $1/5$. (Since the number of complete cycles, and hence the integer part of the tune, are undetectable, the ‘fractional tune’ will often replace the tune.) After 5 turns around the accelerator a particle will return close to where it started. It was shown above that the effect of the nonlinearity is to make the tune change with increasing amplitude, so there is one amplitude, A_R , for which the tune is exactly $1/5$ and the repetition is perfect.

Furthermore there is a frequency entrainment effect causing all nearby amplitudes to “lock-on” to exactly the same tune of $1/5$. This accounts for the islands, illustrated in Fig. 1.1. The centers of these islands are called stable fixed points since a particle starting near one stays near forever. The topology of the structure also requires 5 unstable fixed points between the islands. The maximum separation (in amplitude) of the curves forming the boundary of the island is sometimes called the island width.

The particle moves steadily along a regular oval curve, circulating around the fixed point in much the same way that a small amplitude particle circulates around the origin. An island tune Q_I is defined as the average number of revolutions around the island per turn around the accelerator. In reality the particle jumps from the regular curve of one island to the corresponding regular curve on the next island, returning to a somewhat displaced position on its original curve after 5 turns. Tunes near $2/5$ or $3/5$ or $4/5$ lead to much the same story. For example, with the tune near $2/5$, the case investigated experimentally in E778, the particle jumps 2 islands at a time but still returns to its original island after 5 turns.

The next goal is to derive a Hamiltonian representing motion at a tune $2/5$, or actually $97/5$, if the integer part of the Tevatron tune (19) is included. The equation of motion of a particle of tune $97/5$ is expected (from Eq. (2.8)) to contain a term of the form $\cos[\psi - \frac{97}{5}\theta + a]$, or, $\cos[5a - 97\theta + \phi_0]$, or $\cos[5a + \dots]$, where ϕ_0 is some constant phase. From the Hamiltonian (2.16), such a term can only appear in third order in the sextupole strength [25]: indeed first order terms are of the form

$$\cos^3 a \sim \cos a + \cos 3a, \quad (2.52)$$

second order terms come from $\cos^3 a \times \cos^3 a$ and are of the form

$$\cos 4a + \cos 2a + \text{constant} \quad (2.53)$$

and only third order terms can be of the form

$$\cos^3 a \times \cos^3 a \times \cos^3 a \sim \cos 5a + \dots \quad (2.54)$$

I shall follow up this argument and proceed by constructing a Hamiltonian which is exact up to third order. However, the reader should be aware that the idea of the term $\cos[5a + \dots]$ appearing in third order in perturbation is not commonly accepted. The interesting notion of *interference of resonances*, introduced by Michelotti [26,27], suggests that the 2/5 resonance is due to an interference between the 1/3 resonance appearing at first order in the perturbation expansion, and the 1/2 resonance, which appears at second order. Plans exist for further investigation of this idea by comparison with experimental and tracking data.

The generating function G_3 of Eq. (2.24) was constructed so as the Hamiltonian H_3 be exact up to second order in s_k . Hence one more transformation is needed that will give rise to a Hamiltonian H_4 , which is exact up to third order.

The generating function G_3 from Eq. (2.24),

$$G_3(a, J, \theta) = aJ - (2J)^{3/2} \beta_0^{1/2} \sum_m \left(\frac{3A_{1m}}{m - \nu} \cos q_{1m} + \frac{A_{3m}}{m - 3\nu} \cos q_{3m} \right) \quad (2.55)$$

implies

$$I = \frac{\partial G_3}{\partial a}, \quad (2.56)$$

$$b = \frac{\partial G_3}{\partial J} \quad (2.57)$$

and

$$H_3(b, J) = H_2(b, J) + \frac{\partial G_3}{\partial \theta}. \quad (2.58)$$

Explicitly,

$$I = J + (2J)^{3/2} \beta_0^{1/2} Q(a), \quad (2.59)$$

where

$$Q(a) = \sum_m \left[\frac{3A_{1m}}{m - \nu} \sin q_{1m}(a) + \frac{3A_{3m}}{m - 3\nu} \sin q_{3m}(a) \right] \quad (2.60)$$

and $q_{im}(a) = ia - m\theta + \alpha_{im}$ with $i=1,3$. From here one can calculate the term $(2I)^{3/2}$ by expanding (2.59) in powers of J

$$(2I)^{3/2} = (2J)^{3/2} + 3(2J)^2 \beta_0^{1/2} Q(a) + \frac{3}{2} (2J)^{5/2} \beta_0 Q^2(a) + \dots \quad (2.61)$$

The new angle variable b can be calculated from Eq. (2.57)

$$b = a - 3(2J)^{1/2}\beta_0^{1/2}Q_1(a) \quad (2.62)$$

where

$$Q_1(a) = \sum_m \left[\frac{3A_{1m}}{m-\nu} \cos q_{1m}(a) + \frac{A_{3m}}{m-3\nu} \cos q_{3m}(a) \right]. \quad (2.63)$$

The next step is to solve Eq. (2.62) for a . This can be done recursively. To a first approximation a is set equal to b in Q_1 and hence a is given by

$$a = b + 3(2J)^{1/2}\beta_0^{1/2}Q_1(b). \quad (2.64)$$

Hence the new Hamiltonian (2.58) becomes

$$\begin{aligned} H_3(b, J) = & \nu J + \\ & 3(2J)^2\beta_0 \sum_m \left(\frac{3A_{1m}}{m-\nu} \sin q_{1m} + \frac{3A_{3m}}{m-3\nu} \sin q_{3m} \right) \times \\ & \sum_{m'} (3A_{1m'} \sin q_{1m'} + A_{3m'} \sin q_{3m'}) \\ & + \frac{3}{2}(2J)^{5/2}\beta_0^{3/2} \sum_m \left(\frac{3A_{1m}}{m-\nu} \sin q_{1m} + \frac{3A_{3m}}{m-3\nu} \sin q_{3m} \right) \times \\ & \sum_{m'} \left(\frac{3A_{1m'}}{m'-\nu} \sin q_{1m'} + \frac{3A_{3m'}}{m'-3\nu} \sin q_{3m'} \right) \times \\ & \sum_{m''} (3A_{1m''} \sin q_{1m''} + A_{3m''} \sin q_{3m''}). \end{aligned} \quad (2.65)$$

Notice that in the above expression

$$\sin q_{im} = \sin (ia - m\theta + \alpha_{im}) \quad i = 1, 3. \quad (2.66)$$

With the use of Eq. (2.64), Eq. (2.66) becomes — for $i=1$,

$$\begin{aligned} \sin q_{1m} = & \sin [(b - m\theta + \alpha_{1m}) - 3(2J)^{1/2}\beta_0^{1/2}Q_1(b)] \\ = & \sin (b - m\theta + \alpha_{1m}) \cos [3(2J)^{1/2}\beta_0^{1/2}Q_1(b)] \\ & - \cos (b - m\theta + \alpha_{1m}) \sin [3(2J)^{1/2}\beta_0^{1/2}Q_1(b)]. \end{aligned} \quad (2.67)$$

Then using the first equality of Eq. (2.67)

$$\begin{aligned}
H_3(b, J) = & \nu J + \\
& + 3(2J)^2 \beta_0 \sum_m \left\{ \frac{3A_{1m}}{m - \nu} \sin [q_{1m}(b) + 3(2J)^{1/2} \beta_0^{1/2} Q_1(b)] \right. \\
& + \left. \frac{3A_{3m}}{m - 3\nu} \sin [q_{3m}(b) + 9(2J)^{1/2} \beta_0^{1/2} Q_1(b)] \right\} \times \\
& \sum_{m'} \{ 3A_{1m'} \sin [q_{1m'}(b) + 3(2J)^{1/2} \beta_0^{1/2} Q_1(b)] \\
& + A_{3m'} \sin [q_{3m'}(b) + 9(2J)^{1/2} \beta_0^{1/2} Q_1(b)] \} \\
& + \frac{3}{2} (2J)^{5/2} \beta_0^{3/2} \sum_m \left\{ \frac{3A_{1m}}{m - \nu} \sin [q_{1m}(b) + 3(2J)^{1/2} \beta_0^{1/2} Q_1(b)] \right. \\
& + \left. \frac{3A_{3m}}{m - 3\nu} \sin [q_{3m}(b) + 9(2J)^{1/2} \beta_0^{1/2} Q_1(b)] \right\} \times \\
& \sum_{m'} \left\{ \frac{3A_{1m'}}{m' - \nu} \sin [q_{1m'}(b) + 3(2J)^{1/2} \beta_0^{1/2} Q_1(b)] \right. \\
& + \left. \frac{3A_{3m'}}{m' - 3\nu} \sin [q_{3m'}(b) + 9(2J)^{1/2} \beta_0^{1/2} Q_1(b)] \right\} \times \\
& \sum_{m''} \{ 3A_{1m''} \sin [q_{1m''}(b) + 3(2J)^{1/2} \beta_0^{1/2} Q_1(b)] \\
& + A_{3m''} \sin [q_{3m''}(b) + 9(2J)^{1/2} \beta_0^{1/2} Q_1(b)] \}, \tag{2.68}
\end{aligned}$$

where

$$q_{im}(b) = ib - m\theta + \alpha_{im} \quad i = 1, 3. \tag{2.69}$$

If only the first order terms in the sextupole strength, which enters in $Q_1(b)$, are kept and use of the second of the equalities of (2.67) is made, one arrives at

$$\sin q_{1m} \simeq \sin (b - m\theta + \alpha_{1m}) - 3(2J)^{1/2} \beta_0^{1/2} Q_1(b). \tag{2.70}$$

The same expansion is valid for $\sin q_{3m}$. Taking this into consideration, H_3 becomes

$$\begin{aligned}
H_3(b, J) = & \nu J + \\
& 9(2J)^2 \beta_0 \sum_m \left\{ \frac{A_{1m}}{m - \nu} \sin q_{1m}(b) + \frac{A_{1m}}{m - \nu} 3(2J)^{1/2} \beta_0^{1/2} Q_1(b) \cos q_{1m}(b) \right. \\
& + \left. \frac{A_{3m}}{m - 3\nu} \sin q_{3m}(b) + \frac{A_{3m}}{m - 3\nu} 9(2J)^{1/2} \beta_0^{1/2} Q_1(b) \cos q_{3m}(b) \right\} \times \\
& \sum_{m'} \{ 3A_{1m'} \sin q_{1m'}(b) + 3A_{1m'} 3(2J)^{1/2} \beta_0^{1/2} Q_1(b) \cos q_{1m'}(b) \\
& + A_{3m'} \sin q_{3m'}(b) + A_{3m'} 9(2J)^{1/2} \beta_0^{1/2} Q_1(b) \cos q_{3m'}(b) \}
\end{aligned}$$

$$\begin{aligned}
& + A_{3m'} \sin q_{3m'}(b) + A_{3m'} 9(2J)^{1/2} \beta_0^{1/2} Q_1(b) \cos q_{3m'}(b) \} \\
& + \frac{9}{2} (2J)^{5/2} \beta_0^{3/2} \sum_m \left\{ \frac{3A_{1m}}{m-\nu} \sin q_{1m}(b) + \frac{3A_{3m}}{m-3\nu} \sin q_{3m}(b) \right\} \times \\
& \sum_{m'} \left\{ \frac{A_{1m'}}{m'-\nu} \sin q_{1m'}(b) + \frac{A_{3m'}}{m'-3\nu} \sin q_{3m'}(b) \right\} \times \\
& \sum_{m''} \{ 3A_{1m''} \sin q_{1m''}(b) + A_{3m''} \sin q_{3m''}(b) \}. \tag{2.71}
\end{aligned}$$

In the above, all terms contributing to powers of J higher than $5/2$ have been ignored, because only contributions to 5th order resonance ($\sim I^{5/2}$) are of interest.

Grouping the terms of equal powers of J together, one gets

$$\begin{aligned}
H_3(b, J) = & \nu J + \\
& 9(2J)^2 \beta_0 \sum_{m, m'} \left\{ \frac{3A_{1m}A_{1m'}}{m-\nu} \sin q_{1m} \sin q_{1m'} + \frac{A_{1m}A_{3m'}}{m-\nu} \sin q_{1m} \sin q_{3m'} \right. \\
& + \frac{3A_{3m}A_{1m'}}{m-3\nu} \sin q_{3m} \sin q_{1m'} + \left. \frac{A_{3m}A_{3m'}}{m-3\nu} \sin q_{3m} \sin q_{3m'} \right\} \\
& + 9(2J)^{5/2} \beta_0^{3/2} \sum_{m, m', m''} \left\{ \frac{27A_{1m}A_{1m'}A_{1m''}}{(m-\nu)(m''-\nu)} \cos q_{1m''} \cos q_{1m'} \sin q_{1m} \right. \\
& + \frac{9A_{1m}A_{1m'}A_{3m''}}{(m-\nu)(m''-3\nu)} \cos q_{3m''} \cos q_{1m'} \sin q_{1m} \\
& + \frac{27A_{1m}A_{3m'}A_{1m''}}{(m-\nu)(m''-\nu)} \sin q_{1m} \cos q_{3m'} \cos q_{1m''} \\
& + \frac{9A_{1m}A_{3m'}A_{3m''}}{(m-\nu)(m''-3\nu)} \cos q_{3m''} \cos q_{3m'} \sin q_{1m} \\
& + \frac{27A_{1m}A_{1m'}A_{1m''}}{(m-\nu)(m''-\nu)} \cos q_{1m''} \sin q_{1m'} \cos q_{1m} \\
& + \frac{9A_{1m}A_{1m'}A_{3m''}}{(m-\nu)(m''-3\nu)} \cos q_{1m} \sin q_{1m'} \cos q_{3m''} \\
& + \frac{9A_{1m}A_{3m'}A_{1m''}}{(m-\nu)(m''-\nu)} \cos q_{1m} \sin q_{3m'} \cos q_{1m''} \\
& + \frac{3A_{1m}A_{3m'}A_{3m''}}{(m-\nu)(m''-3\nu)} \cos q_{1m} \sin q_{3m'} \cos q_{3m''} \\
& + \frac{27A_{3m}A_{1m'}A_{1m''}}{(m-3\nu)(m''-\nu)} \sin q_{3m} \cos q_{1m'} \cos q_{1m''} \\
& + \frac{9A_{3m}A_{1m'}A_{3m''}}{(m-3\nu)(m''-3\nu)} \sin q_{3m} \cos q_{1m'} \cos q_{3m''} \\
& + \left. \frac{27A_{3m}A_{3m'}A_{1m''}}{(m-3\nu)(m''-\nu)} \sin q_{3m} \cos q_{3m'} \cos q_{1m''} \right\}
\end{aligned}$$

$$\begin{aligned}
& + \frac{9A_{3m}A_{3m'}A_{3m''}}{(m-3\nu)(m''-3\nu)} \sin q_{3m} \cos q_{3m'} \cos q_{3m''} \\
& + \frac{81A_{3m}A_{1m'}A_{1m''}}{(m-3\nu)(m''-\nu)} \cos q_{3m} \sin q_{1m'} \cos q_{1m''} \\
& + \frac{27A_{3m}A_{1m'}A_{3m''}}{(m-3\nu)(m''-3\nu)} \cos q_{3m} \sin q_{1m'} \cos q_{3m''} \\
& + \frac{27A_{3m}A_{3m'}A_{1m''}}{(m-3\nu)(m''-\nu)} \cos q_{3m} \sin q_{3m'} \cos q_{1m''} \\
& + \frac{9A_{3m}A_{3m'}A_{3m''}}{(m-3\nu)(m''-3\nu)} \cos q_{3m''} \sin q_{3m'} \cos q_{3m} \Big\} \\
& + \frac{9}{2}(2J)^{5/2}\beta_0^{3/2} \sum_{m,m',m''} \Big\{ \frac{9A_{1m}A_{1m'}A_{1m''}}{(m-\nu)(m'-\nu)} \sin q_{1m} \sin q_{1m'} \sin q_{1m''} \\
& + \frac{3A_{1m}A_{1m'}A_{3m''}}{(m-\nu)(m'-\nu)} \sin q_{1m} \sin q_{1m'} \sin q_{3m''} \\
& + \frac{9A_{1m}A_{3m'}A_{1m''}}{(m-\nu)(m'-3\nu)} \sin q_{1m} \sin q_{3m'} \sin q_{1m''} \\
& + \frac{3A_{1m}A_{3m'}A_{3m''}}{(m-\nu)(m'-3\nu)} \sin q_{1m} \sin q_{3m'} \sin q_{3m''} \\
& + \frac{9A_{3m}A_{1m'}A_{1m''}}{(m-3\nu)(m'-\nu)} \sin q_{3m} \sin q_{1m'} \sin q_{1m''} \\
& + \frac{3A_{3m}A_{1m'}A_{3m''}}{(m-3\nu)(m'-\nu)} \sin q_{3m} \sin q_{1m'} \sin q_{3m''} \\
& + \frac{9A_{3m}A_{3m'}A_{1m''}}{(m-3\nu)(m'-3\nu)} \sin q_{3m} \sin q_{3m'} \sin q_{1m''} \\
& + \frac{3A_{3m}A_{3m'}A_{3m''}}{(m-3\nu)(m'-3\nu)} \sin q_{3m} \sin q_{3m'} \sin q_{3m''} \Big\}. \tag{2.72}
\end{aligned}$$

With the use of the trigonometric identity

$$\sin A \sin B = \frac{1}{2}[\cos(A+B) - \cos(A-B)], \tag{2.73}$$

the terms which are proportional to J^2 in (2.72) are rewritten, to give

$$\begin{aligned}
H_3(b, J) = & \nu J + \\
& \frac{9}{2}(2J)^2\beta_0 \sum_{m,m'} \Big\{ \frac{3A_{1m}A_{1m'}}{m-\nu} \cos [-(m-m')\theta + (\alpha_{1m} - \alpha_{1m'})] - \frac{3A_{1m}A_{1m'}}{m-\nu} \cos Q_1 \\
& + \frac{A_{1m}A_{3m'}}{m-\nu} \cos Q_2 - \frac{A_{1m}A_{3m'}}{m-\nu} \cos Q_3 + \frac{3A_{3m}A_{1m'}}{m-3\nu} \cos Q_4 - \frac{3A_{3m}A_{1m'}}{m-3\nu} \cos Q_5 \\
& + \frac{A_{3m}A_{3m'}}{m-3\nu} \cos [-(m'-m)\theta + (\alpha_{3m'} - \alpha_{3m})] - \frac{A_{3m}A_{3m'}}{m-3\nu} \cos Q_6 \Big\}
\end{aligned}$$

$$+9(2J)^{5/2}\beta_0^{3/2} \sum_{m,m',m''} \{\dots\} + \frac{9}{2}(2J)^{5/2}\beta_0^{3/2} \sum_{m,m',m''} \{\dots\}. \quad (2.74)$$

The terms proportional to $J^{5/2}$ remain the same as in Eq. (2.72). The quantities Q_1 to Q_6 are defined as follows

$$Q_1 = 2b - (m + m')\theta + (\alpha_{1m} + \alpha_{1m'}), \quad (2.75)$$

$$Q_2 = 2b - (m' - m)\theta + (\alpha_{3m'} - \alpha_{1m}), \quad (2.76)$$

$$Q_3 = 4b - (m + m')\theta + (\alpha_{1m} + \alpha_{3m'}), \quad (2.77)$$

$$Q_4 = 2b - (m - m')\theta + (\alpha_{3m} - \alpha_{1m'}), \quad (2.78)$$

$$Q_5 = 4b - (m + m')\theta + (\alpha_{3m} + \alpha_{1m'}), \quad (2.79)$$

and

$$Q_6 = 6b - (m + m')\theta + (\alpha_{3m} + \alpha_{3m'}). \quad (2.80)$$

The last Moser transformation is performed now, from (b, J) to (a, I) such that the new Hamiltonian is exact up to 3rd order in the sextupole strength. To avoid proliferation of the notation the new variables are called (a, I) again. The generating function for this transformation is given by

$$\begin{aligned} G_4(b, I; \theta) = & bI + \\ & \frac{9}{2}(2I)^2\beta_0 \sum_{m,m'} \left\{ -\frac{3A_{1m}A_{1m'}}{(m-\nu)[(m+m')-2\nu]} \sin Q_1 \right. \\ & + \frac{A_{1m}A_{3m'}}{(m-\nu)[(m'-m)-2\nu]} \sin Q_2 - \frac{A_{1m}A_{3m'}}{(m-\nu)[(m'+m)-4\nu]} \sin Q_3 \\ & + \frac{3A_{3m}A_{1m'}}{(m-3\nu)[(m-m')-2\nu]} \sin Q_4 - \frac{3A_{3m}A_{1m'}}{(m-3\nu)[(m+m')-4\nu]} \sin Q_5 \\ & \left. - \frac{A_{3m}A_{3m'}}{(m-3\nu)[(m+m')-6\nu]} \sin Q_6 \right\} \\ & - \frac{9}{2}(2I)^2\beta_0 \sum_{m,m',m \neq m'} \left\{ -\frac{3A_{1m}A_{1m'}}{(m-\nu)(m-m')} \sin [-(m-m')\theta + (\alpha_{1m} - \alpha_{1m'})] \right. \\ & \left. - \frac{A_{3m}A_{3m'}}{(m-3\nu)(m'-m)} \sin [-(m'-m)\theta + (\alpha_{3m'} - \alpha_{3m})] \right\}. \quad (2.81) \end{aligned}$$

From the above generating function the old action J is given by

$$J = \frac{\partial G_4}{\partial b}. \quad (2.82)$$

Since only terms of order $J^{5/2}$ are of interest, the following approximations are true

$$(2J)^2 \simeq (2I)^2, \quad (2.83)$$

$$(2J)^{5/2} \simeq (2I)^{5/2} \quad (2.84)$$

and

$$a \simeq b. \quad (2.85)$$

The new Hamiltonian is given by

$$H_4(a, I) = H_3(a, I) + \frac{\partial G_4}{\partial \theta}. \quad (2.86)$$

If one keeps only the terms which give rise to terms of the form $\sin(5a + \dots)$, because those are the ones contributing to the 5th order resonance, and if one writes explicitly the expressions for the q_{im} 's, $i=1,3$ and collects all the similar terms together, one arrives at

$$\begin{aligned} H_4(a, I) = & \nu I + \frac{9}{2}(2I)^2 \beta_0 \sum_m \left[\frac{3A_{1m}^2}{m - \nu} + \frac{A_{3m}^2}{m - 3\nu} \right] \\ & + \frac{9}{4}(2I)^{5/2} \beta_0^{3/2} \left\{ 117S_1 + \frac{69}{2}S_2 + 51S_3 - \frac{27}{2}S_4 \right\}, \end{aligned} \quad (2.87)$$

where

$$S_1 = \sum_{m, m', m''} \frac{A_{1m} A_{1m'} A_{3m''}}{(m - \nu)(m'' - 3\nu)} \sin [5a - (m + m' + m'')\theta + (\alpha_{1m} + \alpha_{1m'} + \alpha_{3m''})],$$

$$S_2 = \sum_{m, m', m''} \frac{A_{1m} A_{3m'} A_{1m''}}{(m - \nu)(m'' - \nu)} \sin [5a - (m + m' + m'')\theta + (\alpha_{1m} + \alpha_{3m'} + \alpha_{1m''})],$$

$$S_3 = \sum_{m, m', m''} \frac{A_{1m} A_{3m'} A_{3m''}}{(m - \nu)(m'' - 3\nu)} \sin [5a - (m + m'' - m')\theta + (\alpha_{3m'} + \alpha_{3m''} - \alpha_{1m})],$$

and

$$S_4 = \sum_{m, m', m''} \frac{A_{3m} A_{1m'} A_{3m''}}{(m - 3\nu)(m'' - 3\nu)} \sin [5a - (m - m' + m'')\theta + (\alpha_{3m} + \alpha_{3m''} - \alpha_{1m'})].$$

The next step is to perform the summations over the harmonics. First, the coefficient of the term which is quadratic in the action I ,

$$c = 18\beta_0 \sum_m \left[\frac{3A_{1m}^2}{m - \nu} + \frac{A_{3m}^2}{m - 3\nu} \right] \quad (2.88)$$

can be expressed [21] as

$$c = -\frac{\beta_0}{4\pi} \sum_k (3B_1 s + B_3 s)_k, \quad (2.89)$$

where B_1 and B_3 are the distortion functions previously defined in (2.35).

In fact, it can be easily shown [21] that this coefficient c is simply related to the amplitude-dependent tuneshift due to the sextupoles. Indeed the tuneshift due to sextupoles is given by

$$\Delta\nu = 2Ic. \quad (2.90)$$

Hence cI^2 is the detuning term due to sextupoles.

Next I am going to calculate the triple sums of S_1 , S_2 , S_3 and S_4 , and express the S_i 's in a closed form. The way to calculate S_1 is demonstrated and the results for the other three sums are given. First S_1 is written as

$$S_1 = \text{Im} \left\{ \sum_{m,m',m''} \frac{A_{1m} A_{1m'} A_{3m''}}{(m - \nu)(m'' - 3\nu)} e^{i[5a - (m + m' + m'')\theta + (\alpha_{1m} + \alpha_{1m'} + \alpha_{3m''})]} \right\}$$

or

$$S_1 = \text{Im} \left\{ \sum_{m,m',m''} \frac{(A_{1m} e^{i\alpha_{1m}})(A_{1m'} e^{i\alpha_{1m'}})(A_{3m''} e^{i\alpha_{3m''}})}{(m - \nu)(m'' - 3\nu)} e^{i[5a - (m + m' + m'')\theta]} \right\}.$$

The expressions

$$A_{im} e^{i\alpha_{im}} \quad i = 1, 3$$

are given in Eqs (2.21) and (2.22). From the above sum, only the slowly varying terms will be kept, that is, terms of the form $e^{i(5a - 97\theta)}$, since the tune of the machine is close to 19.40.

Hence the above triple sum - over m , m' and m'' - is actually constrained by the condition

$$m + m' + m'' = 97. \quad (2.91)$$

Then S_1 becomes

$$S_1 = \text{Im} \left\{ \sum_{m, m', m''} \frac{(A_{1m} e^{i\alpha_{1m}})(A_{1m'} e^{i\alpha_{1m'}})(A_{3m''} e^{i\alpha_{3m''}})}{(m - \nu)(m'' - 3\nu)} e^{i(5a - 97\theta)} \right\}.$$

In the following m' is substituted for $(97 - m - m'')$, so S_1 becomes

$$S_1 = \text{Im} \left\{ \sum_{m, m''} \frac{(A_{1m} e^{i\alpha_{1m}})(A_{1(97-m-m'')} e^{i\alpha_{1(97-m-m'')}})(A_{3m''} e^{i\alpha_{3m''}})}{(m - \nu)(m'' - 3\nu)} e^{i(5a - 97\theta)} \right\}.$$

Substituting Eqs (2.21) and (2.22) above leads to

$$S_1 = \text{Im} \left\{ \left(\frac{i}{24\pi} \right)^3 \sum_{k1, k2, k3} s_{k1} s_{k2} s_{k3} e^{i(\psi - \nu\theta + 97\theta)_{k2}} e^{i(5a - 97\theta)} \times \sum_m \frac{e^{i[\psi_{k1} - \nu\theta_{k1} + m(\theta_{k1} - \theta_{k2})]}}{m - \nu} \sum_{m''} \frac{e^{i[3\psi_{k3} - 3\nu\theta_{k3} + m''(\theta_{k3} - \theta_{k2})]}}{m'' - 3\nu} \right\}.$$

The two sums over m and m' above can be calculated using formula (2.32). The result is

$$S_1 = \text{Im} \left\{ -\frac{i}{(24)^3 \pi \sin \pi \nu \sin 3\pi \nu} \times \sum_{k1, k2, k3} s_{k1} s_{k2} s_{k3} e^{i[(\psi_{k1} + \psi_{k2} + 3\psi_{k3}) - 5\delta\theta_{k2} - 4\pi\nu]} \right\}, \quad (2.92)$$

where

$$\delta = \nu - \frac{97}{5}, \quad (2.93)$$

or

$$S_1 = -\frac{1}{(24)^3 \pi \sin \pi \nu \sin 3\pi \nu} \times \sum_{k1, k2, k3} s_{k1} s_{k2} s_{k3} \times \cos [(5a - 97\theta) + (\psi_{k1} + \psi_{k2} + 3\psi_{k3}) - 5\delta\theta_{k2} - 4\pi\nu]. \quad (2.94)$$

Similarly

$$S_2 = -\frac{1}{(24)^3 \pi (\sin \pi \nu)^2} \times \sum_{k1, k2, k3} s_{k1} s_{k2} s_{k3} \times \cos [(5a - 97\theta) + (\psi_{k1} + \psi_{k3} + 3\psi_{k2}) - 5\delta\theta_{k2} - 2\pi\nu], \quad (2.95)$$

$$S_3 = \frac{1}{(24)^3 \pi \sin \pi \nu \sin 3\pi \nu} \times \sum_{k_1, k_2, k_3} s_{k_1} s_{k_2} s_{k_3} \times \cos [(5a - 97\theta) + (3\psi_{k_2} - \psi_{k_1} + 3\psi_{k_3}) - 5\delta\theta_{k_2} - 2\pi\nu], \quad (2.96)$$

and

$$S_4 = \frac{1}{(24)^3 \pi (\sin 3\pi \nu)^2} \times \sum_{k_1, k_2, k_3} s_{k_1} s_{k_2} s_{k_3} \times \cos [(5a - 97\theta) + (3\psi_{k_1} - \psi_{k_2} + 3\psi_{k_3}) - 5\delta\theta_{k_2} - 6\pi\nu]. \quad (2.97)$$

So the Hamiltonian now has the following form

$$\begin{aligned} H_4(a, I) = & \nu I - \frac{\beta_0 I^2}{4\pi} \sum_k (3B_1 s + B_3 s)_k \\ & + \frac{9}{4} (2I)^{5/2} \beta_0^{3/2} \frac{1}{(24)^3 \pi} \sum_{k_1, k_2, k_3} s_{k_1} s_{k_2} s_{k_3} \left\{ -117 \frac{\cos [(5a - 97\theta) + \delta_1]}{\sin \pi \nu \sin 3\pi \nu} \right. \\ & - \frac{69 \cos [(5a - 97\theta) + \delta_2]}{2 (\sin \pi \nu)^2} + 51 \frac{\cos [(5a - 97\theta) + \delta_3]}{\sin \pi \nu \sin 3\pi \nu} \\ & \left. - \frac{27 \cos [(5a - 97\theta) + \delta_4]}{2 (\sin 3\pi \nu)^2} \right\}. \end{aligned} \quad (2.98)$$

In short the above expression can be written as

$$H_4(a, I) = \nu I + cI^2 + I^{5/2} [\epsilon_1 \cos (5a - 97\theta) + \epsilon_2 \sin (5a - 97\theta)], \quad (2.99)$$

where

$$c = -\frac{\beta_0}{4\pi} \sum_k (3B_1 s + B_3 s)_k, \quad (2.100)$$

$$\begin{aligned} \epsilon_1 = & \frac{9}{4} 2^{5/2} \beta_0^{3/2} \frac{1}{(24)^3 \pi} \sum_{k_1, k_2, k_3} s_{k_1} s_{k_2} s_{k_3} \times \\ & \left\{ -117 \frac{\cos \delta_1}{\sin \pi \nu \sin 3\pi \nu} - \frac{69 \cos \delta_2}{2 (\sin \pi \nu)^2} \right. \\ & \left. + 51 \frac{\cos \delta_3}{\sin \pi \nu \sin 3\pi \nu} - \frac{27 \cos \delta_4}{2 (\sin 3\pi \nu)^2} \right\}, \end{aligned} \quad (2.101)$$

and

$$\epsilon_2 = -\frac{9}{4} 2^{5/2} \beta_0^{3/2} \frac{1}{(24)^3 \pi} \sum_{k_1, k_2, k_3} s_{k_1} s_{k_2} s_{k_3} \times$$

$$\left\{ -117 \frac{\sin \delta_1}{\sin \pi \nu \sin 3\pi \nu} - \frac{69}{2} \frac{\sin \delta_2}{(\sin \pi \nu)^2} + 51 \frac{\sin \delta_3}{\sin \pi \nu \sin 3\pi \nu} - \frac{27}{2} \frac{\sin \delta_4}{(\sin 3\pi \nu)^2} \right\}. \quad (2.102)$$

The various angles are defined as follows

$$\delta_1 = (\psi_{k1} + \psi_{k2} + 3\psi_{k3}) - 5\delta\theta_{k2} - 4\pi\nu, \quad (2.103)$$

$$\delta_2 = (\psi_{k1} + \psi_{k3} + 3\psi_{k2}) - 5\delta\theta_{k2} - 2\pi\nu, \quad (2.104)$$

$$\delta_3 = (3\psi_{k2} - \psi_{k1} + 3\psi_{k3}) - 5\delta\theta_{k2} - 2\pi\nu, \quad (2.105)$$

$$\delta_4 = (3\psi_{k1} - \psi_{k2} + 3\psi_{k3}) - 5\delta\theta_{k2} - 6\pi\nu. \quad (2.106)$$

The above Hamiltonian can be written as

$$H_4(a, I) = \nu I + cI^2 + \epsilon_0 I^{5/2} \cos [(5a - 97\theta) + \phi_0] \quad (2.107)$$

with

$$\epsilon_0 = \sqrt{\epsilon_1^2 + \epsilon_2^2} \quad (2.108)$$

and

$$\phi_0 = \arctan \left(-\frac{\epsilon_2}{\epsilon_1} \right). \quad (2.109)$$

Hence, starting from the sextupole Hamiltonian, a new form has been derived which describes a system under the action of the resonance 97/5. Eventually (in Chapter VI) these expressions will be used to derive the island tune and the island width.

It is already clear that the above model of the *isolated* nonlinear resonance, namely the model which assumes a particle moving under the action of a single resonance, is incomplete when used to describe the situation of the resonance island experiment of E778. One can see from Fig. 1.1 that the phase space is heavily influenced by the presence of the third integer resonance (to be discussed next). As a result of this, the five islands are distributed along a triangular contour, characteristic of the

third integer resonance. However, the above calculation is still useful in a twofold way. First, it provides an insight of how sextupoles give rise to 2/5 resonance islands. Second, it demonstrates the degree of accuracy of the model.

The Third Integer Resonance

In the same way as before, when the tune is very close to a third integer,

$$\nu = \frac{58}{3} + \delta, \quad (2.110)$$

the Hamiltonian H_3

$$H_3 = \nu I + (2I)^{3/2} \beta_0^{1/2} \sum_m [3A_{1m} \sin(a - m\theta) + A_{3m} \sin(3a - m\theta)] \quad (2.111)$$

is dominated by the term

$$A_{3,58} \sin(3a - 58\theta). \quad (2.112)$$

Hence the Hamiltonian describing motion near a sextupole-induced third integer resonance is

$$H_T = \nu I + (2I)^{3/2} \beta_0^{1/2} A_{3,58} \sin(3a - 58\theta). \quad (2.113)$$

Transformation to the rotating system in phase space, yields the new invariant Hamiltonian

$$H_T = \delta I_1 + (2I_1)^{3/2} \beta_0^{1/2} A_{3,58} \sin(3a_1) = \text{constant}, \quad (2.114)$$

where δ is defined by Eq. (2.110).

For δ nonzero the motion in phase space is shown in Fig. 2.1. The curves shown correspond to four different values of the invariant H_T . At small amplitudes the circles are distorted and are described well by the first order perturbation theory as shown earlier in this Chapter.

For larger amplitudes the curves approach a triangular shape with three unstable fixed points at the points of the triangle. The fixed points of the motion can be found

by solving the equations

$$\frac{\partial H_T}{\partial I_1} = 0, \quad \frac{\partial H_T}{\partial a_1} = 0 \quad (2.115)$$

which lead to

$$a_1 = \frac{\pi}{3}, \quad a_1 = \frac{3\pi}{3}, \quad a_1 = \frac{5\pi}{3}, \quad (2.116)$$

and

$$I_{1R} = \left(\frac{2\delta}{3A_{3,58}} \right)^2. \quad (2.117)$$

Here I_{1R} is the action from the origin to the fixed points. Finally, at sufficiently large amplitude the motion is unbounded.

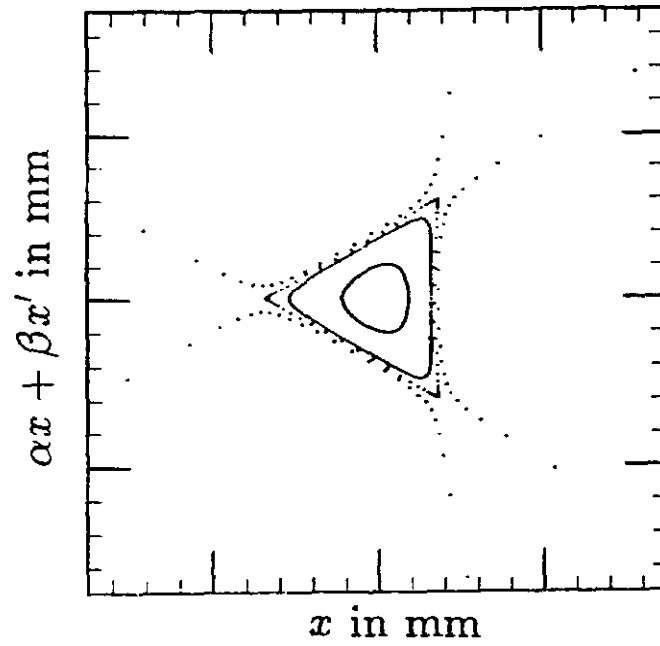


Figure 2.1: Schematic representation of the phase space structure of the third integer resonance.

CHAPTER III

GENERAL REMARKS ON THE EXPERIMENTS

For the experimental study of the Hamiltonian system described above the Tevatron was chosen. The Tevatron, the world's first superconducting proton synchrotron, is approximately circular with a four-mile circumference which is mostly occupied by dipole and quadrupole magnets. The ring is divided into six equally spaced intervals, called sectors.

There are two reasons for choosing the Tevatron for E778. First it is a proton accelerator with excellent linear behavior as was reaffirmed as part of this experiment. (The linearity of the Tevatron was first demonstrated in 1983.) Second, a substantial number of sextupole magnets were already installed in the Tevatron and could be used as sources of nonlinearity. The position of the sextupoles (given below), the kicker magnet (E17), the beam position monitors used in the first run (E24 and E26) and the beam position monitors used in the second run (F42 and F44), are shown in a layout of the Tevatron in Fig. 3.1. Also the 6 sectors are clearly marked. The function of each of the above devices will be explained shortly.

Sextupoles Used in E778

Some initial studies of the perturbation of the motion by nonlinearities were made in the Tevatron [28] in 1985. Then, eight superconducting sextupoles were used to

excite the resonance at the betatron oscillation tune of $19 \frac{1}{3}$. For E778, sixteen additional sextupoles were commissioned. Together with the eight previously used magnets, the total number of sextupoles is sixteen normal ones at stations 22, 24, 26, 28, 32, 34, 36, 38 in C and F sectors and eight skew sextupoles at stations 12, 14, 16, 18, 23, 27, 37, 43 in D sector (see Fig. 3.1). The skew sextupoles were not used in the studies performed up to now.

The normal sextupoles are powered in pairs by 8 supplies, so one can have a variety of configurations. For E778 it was elected to power them as shown in Fig. 3.2. This particular $(+ - + - \dots)$ configuration produces a strong driving term for $3\nu_x = 58$ as one can see from the vector diagram of Fig. 3.3. Fig. 3.3 is a graphical representation of the contributing terms to the summations

$$\sum_k s_k e^{i(3\psi - 3\nu\theta + m\theta)_k}, \quad (3.1)$$

where $m = 58$ for the Tevatron. The sum is over all sixteen sextupoles. Near the third integer resonance $3\nu - 58 \approx 0$, so the above sum is given to a good approximation by

$$\sum_{k=1}^{16} s_k e^{i(3\psi)_k}. \quad (3.2)$$

The phase advance between two adjacent E778 sextupoles is 68° . Fig. 3.3 illustrates the sixteen vectors representing the individual terms of (3.2) as well as their resultant.

The integrated field of each sextupole is

$$\int \vec{B} \cdot d\vec{\ell} = 44.45 \text{ kG-inch at } 1'' \text{ and } 50 \text{ amperes} \quad (3.3)$$

or

$$\frac{B''_v \ell}{2} = 44.45 \text{ kG/in at } 50 \text{ amperes.} \quad (3.4)$$

By varying the current through the sextupoles one could adjust the magnitude of the nonlinearity. In most cases all sixteen sextupoles had the same strength.

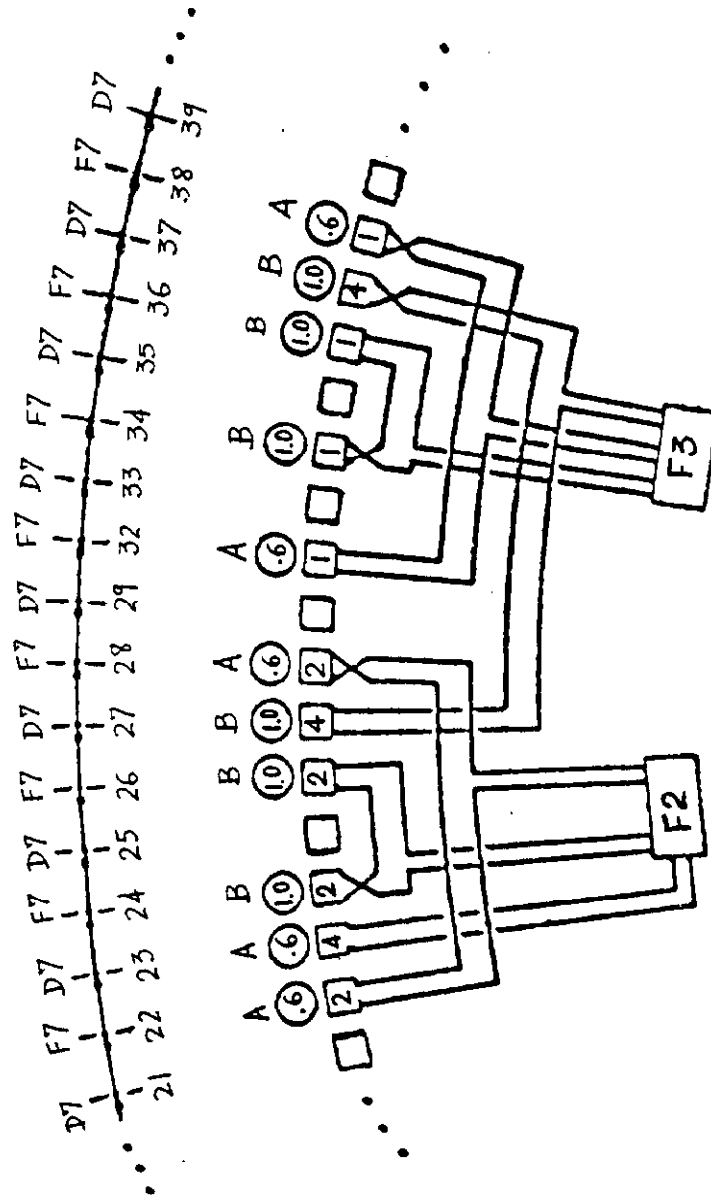


Figure 3.2: Power supplies connecting the E778 sextupoles.

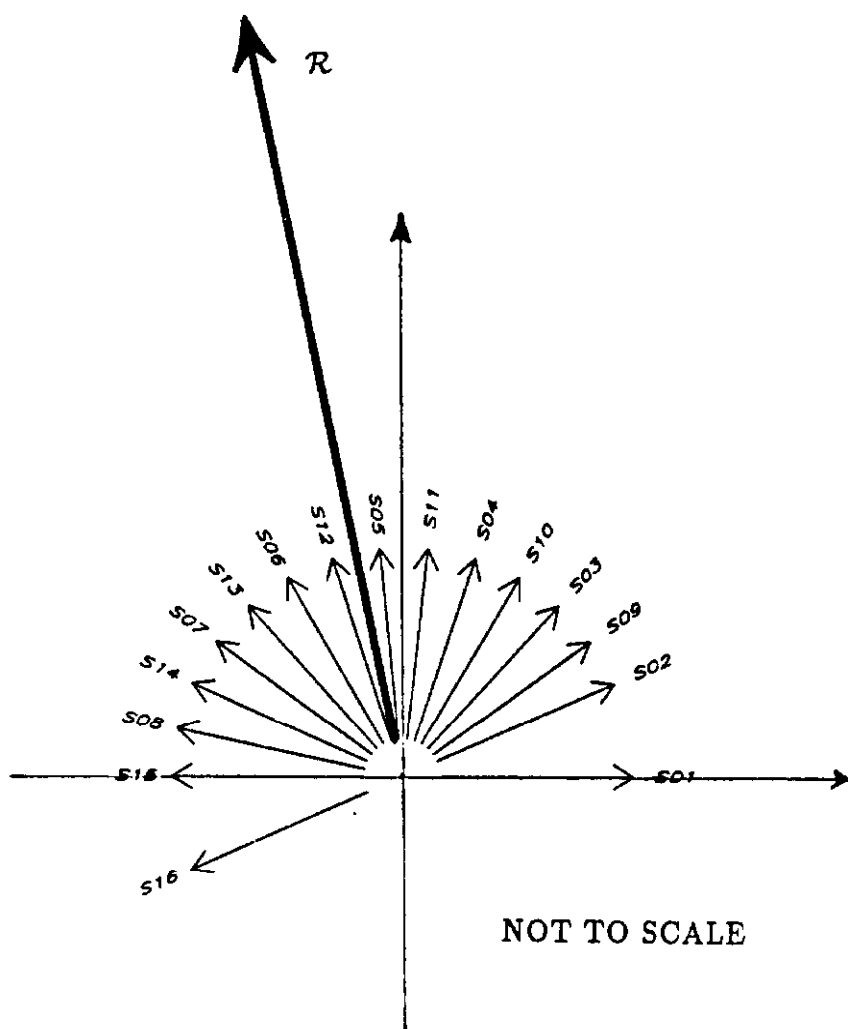


Figure 3.3: Vector diagram showing a strong driving term for the resonance $3\nu_x = 58$ due to the 16 E778 sextupoles. R denotes the resultant of the 16 vectors s_1 to s_{16} .

Phase Space Measurements

The original beam position monitor (BPM) system in the Tevatron was capable of recording the motion of the centroid of the beam for 1024 turns. (An upgrade for this experiment [29] extended the capability to the million turn level.) Fig. 3.4(a) and (c) are plots of turn-by-turn data from the Tevatron as recorded by two neighboring position monitors (E24 and E26) in the horizontal plane. The Tevatron injection kicker magnet, located at E17, has fired 50 turns after the beginning of the plot inducing a coherent betatron oscillation. The fact that the amplitude does not decrease significantly, is an indication of near linearity, as will be shown later. Fig. 3.4(b) and (d) display the Fourier transforms of the two position signals and give the fractional part of the betatron tune. These data were recorded during the 1985 studies.

The positions at two neighboring monitors, together with a knowledge of the intervening optics assumed linear, can be used to generate an experimental phase space plot like the one shown on Fig. 3.5 [28]. This figure displays data similar to Fig. 3.4 in normalized phase space coordinates: the horizontal axis is displacement from the closed orbit, x , and the vertical axis is $\beta x' + \alpha x$, where x' is the angle with respect to the unperturbed orbit, dx/ds , and β , α are the conventional Courant-Snyder parameters. In these coordinates the phase space plot is the familiar circle of the simple harmonic motion. In the presence of nonlinearities arranged in such a way as to excite the $1/3$ resonance the circle is deformed into the triangle characteristic of this resonance. Fig. 3.6 is the experimental verification of this case. It displays data taken during the above mentioned studies of 1985, where only 8 sextupoles were used and the small amplitude tune was very close to the third integer resonance (19.34). The same kicker as above (injection kicker) produced an initial amplitude so that a particle at the centroid would perform stable motion close to the separatrix.

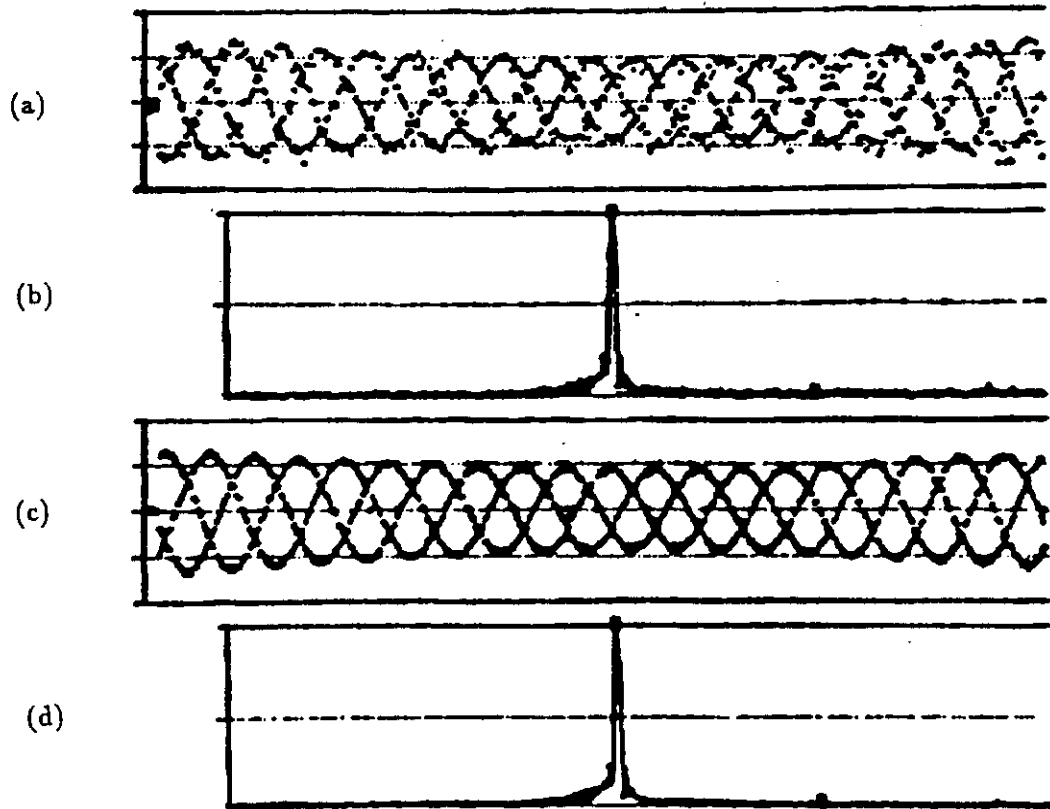


Figure 3.4: (a) and (c) are the output of two neighboring BPMs for 1024 turns. The Fourier transforms are shown in (b) and (d); the fractional part of the tune is .34.

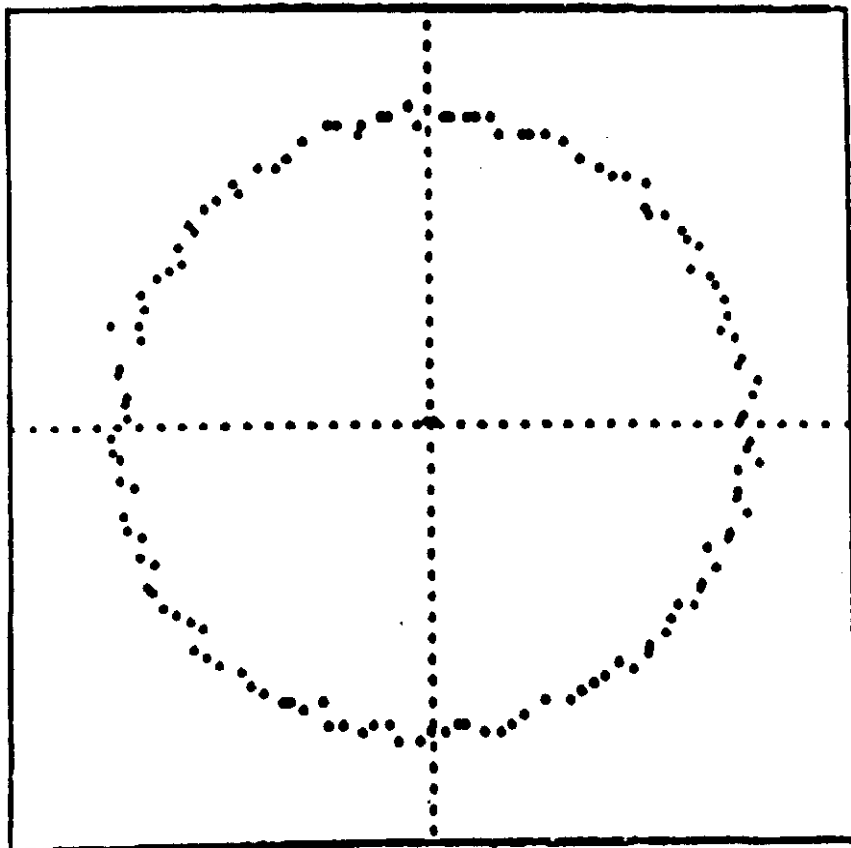


Figure 3.5: Phase space plot constructed from data similar to that shown in Fig. 3.4. Normalized coordinates have been employed on purpose in order to obtain the characteristic circle of the simple harmonic motion.

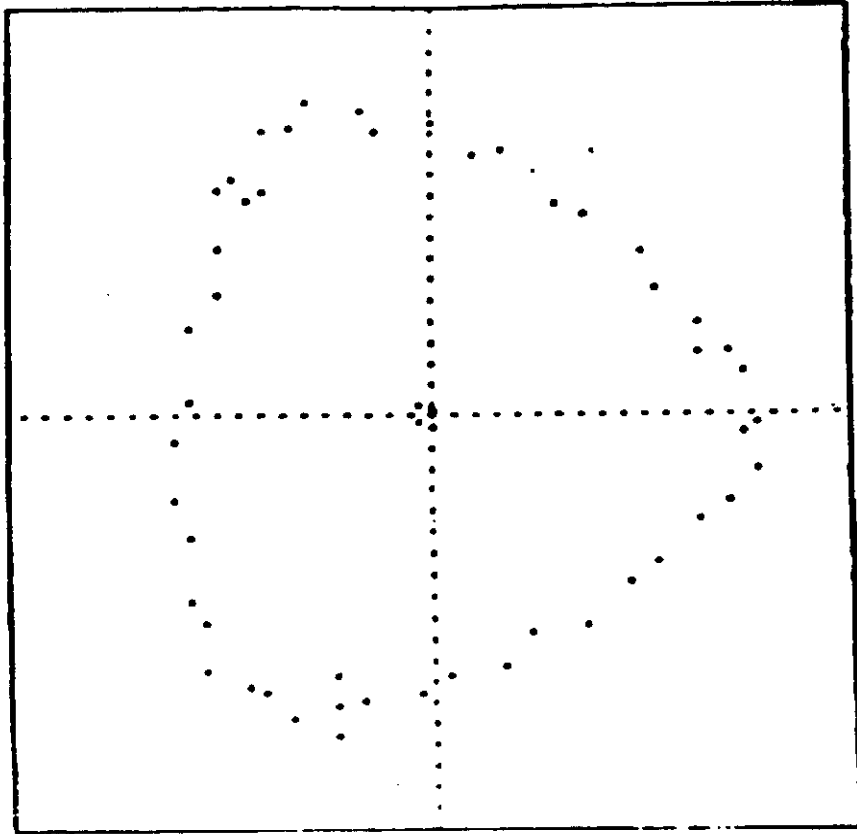


Figure 3.6: Phase space plot from experimental data for betatron oscillation of amplitude close to third-integer resonance separatrix.

Preliminary Steps for the Experiments

There were several steps preliminary to the measurements. First, all the experiments were carried out in the standard fixed-target optics lattice of the Tevatron. Two different cycle modes were employed:

1. For the smear, a standard cyclic mode of operation was employed with the energy held constant at 150 GeV.
2. The resonance island experiment was done under storage conditions in order to see long-time effects.

After setting the appropriate cycle structure and basic optics proton beams of good quality were established: the transverse emittance was smaller than 15π mm-mrad and the longitudinal emittance was equal to .3 eV-sec. The definition of emittance used throughout this work is the 95% normalized emittance and is given by

$$\epsilon = -\frac{6\pi\sigma^2}{\beta}\gamma, \quad (3.5)$$

where β is the beta function, γ is the relativistic parameter and σ is the rms beam size.

Further emittance reduction was accomplished [30] with the use of the fixed target collimators at D17. The collimation is capable of reducing the emittance to approximately 2π mm-mrad or less. Specifically, the collimators are first aligned and positioned at about 20 mm from the center of the beam pipe. Then an orbit distortion at D17 steers the beam at the collimators and as a result 90% of the beam is removed. The function of the time bump is to steer the beam towards the collimators and back to the center. The alternative, which would be to move the collimators further in, would result in the undesirable aperture reduction. With sufficiently low Booster intensity (1×10^{12}) a Tevatron intensity of about 2×10^{10} was achieved after collimation, which is approximately 10^9 particles per bunch (ppb). The resultant emittances were $\epsilon_H \simeq 2\pi$ mm-mrad, $\epsilon_V \simeq 8\pi$ mm-mrad and $\sigma_p/p \simeq 1 \times 10^{-4}$ where

σ_p/p is the rms momentum spread of the beam. The initial values of the emittances were approximately 10π mm-mrad in both planes and $\sigma_p/p \simeq 1.8 \times 10^{-4}$. Notice that there is no vertical collimation.

The main mode of operation was to inject up to 20 bunches with a single-bunch intensity of $2 - 3 \times 10^9$.

The following discussion concerns the smear introduced by linear coupling. It is demonstrated in the Appendix that linear coupling introduces a smear in the horizontal direction of order $K^2/(\nu_x - \nu_y)^2$, where K is the coupling constant and ν_x, ν_y are the horizontal and vertical tunes respectively. That is,

$$s_{cx} \sim \frac{K^2}{(\nu_x - \nu_y)^2}. \quad (3.6)$$

On the other hand the smear in the vertical direction due to coupling, s_{cy} , is

$$s_{cy} \sim \frac{K}{(\nu_x - \nu_y)}. \quad (3.7)$$

The asymmetry between s_{cx} and s_{cy} originates from the special choice of the initial conditions. (See Appendix.)

Hence, as long as the analysis involves only the horizontal motion, the smear due to coupling can be ignored to a good approximation, provided the coupling is sufficiently small. However, in a two degree-of-freedom treatment the contribution to the smear from coupling is an order of the expansion parameter larger than in the one degree-of-freedom case and should be taken into account.

Since this smear is caused by linear fields and not by nonlinearities, one wishes to minimize it by controlling the coupling constant to $K \leq .001$ with the use of a skew quadrupole circuit which is controlled through an application program written specifically for E778 [33]. Moreover the tunes are separated by $\sim .06$ by setting $\nu_y = .46$ and $\nu_x \simeq .40$. With the values of K, ν_x and ν_y given here, the smear s_{cx} turns out to be

$$s_{cx} \sim \frac{(.001)^2}{(.06)^2} = .02\%; \quad (3.8)$$

indeed very small.

Chromaticity compensation was performed to better than 2 to 3 units. In order to optimize the compensation process an “automatic” chromaticity measurement method was implemented [34,35]. The principle of the method is given here. Start from the definition of chromaticity ξ ,

$$\delta\nu = \xi \frac{\delta p}{p} \quad (3.9)$$

and recall that

$$\frac{\delta p}{p} = -\frac{1}{\eta} \frac{\delta f_{RF}}{f_{RF}}, \quad (3.10)$$

where f_{RF} is the RF frequency, and η is the so-called momentum dispersion function defined by

$$\eta \equiv \frac{1}{\gamma_t^2} - \frac{1}{\gamma^2}. \quad (3.11)$$

By combining (3.9) and (3.10) one gets

$$\xi = -\eta \frac{\delta\nu}{\frac{\delta f_{RF}}{f_{RF}}}. \quad (3.12)$$

In the high energy limit where $\gamma \gg \gamma_t$, (3.12) becomes

$$\xi = -\frac{1}{\gamma_t^2} \frac{\delta\nu}{\frac{\delta f_{RF}}{f_{RF}}}. \quad (3.13)$$

For the Tevatron, $\gamma_t^2 = 351$.

Thus by changing the RF frequency by a known amount and determining the resulting tune change, one can calculate the chromaticity of the machine. In practice the change in the RF frequency was produced by a waveform generator and had the form of Fig. 3.7. The amplitude of the waveform was 1 Volt or 53.1 Hz. The position of the centroid of the beam was recorded for every turn during the intervals AB and CD of Fig. 3.7. From the Fourier analysis of this information, $\delta\nu = \nu_{AB} - \nu_{CD}$ was extracted and the chromaticity was calculated from (3.13).

Waveform generator for chromaticity measurements

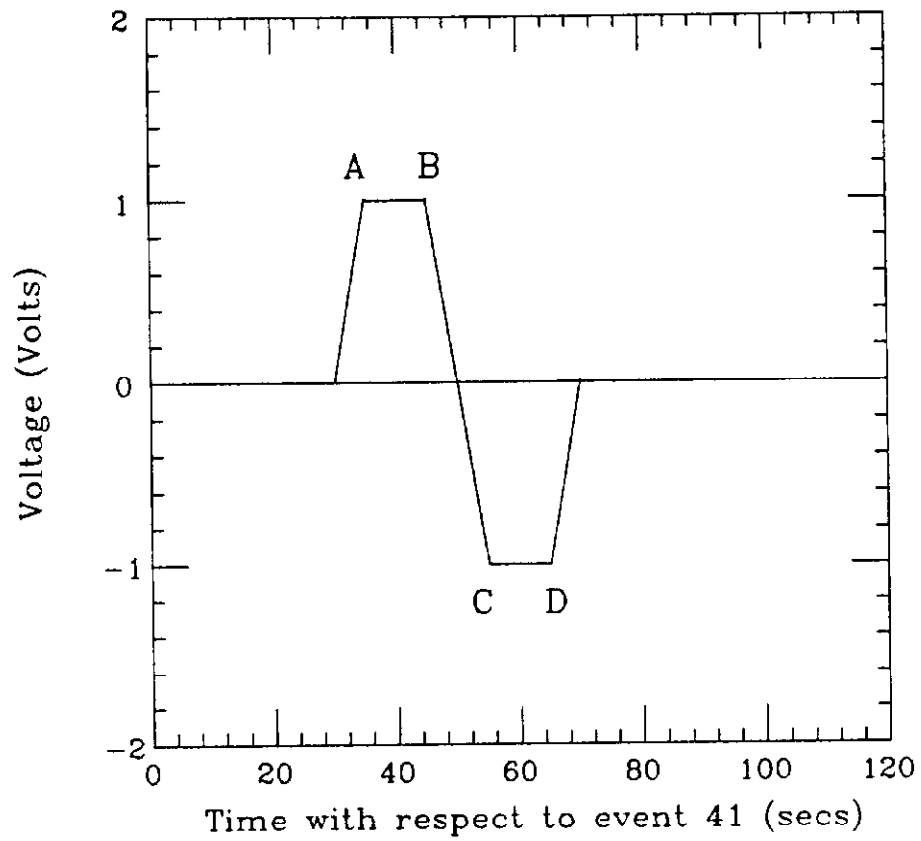


Figure 3.7: Waveform generator for the chromaticity measurements.

The closed orbit had to be adjusted at the nonlinearities in order to minimize the tuneshifts and other off-center effects. The tuneshift due to an off-centered orbit at the E778 sextupoles can be calculated as follows [36]. The tuneshift due to a gradient error is given by

$$\Delta\nu = \frac{1}{4\pi}\beta \left(\frac{B'\ell}{B\rho} \right), \quad (3.14)$$

where β is the beta function at the location of the error, namely the sextupole location in this case. From

$$B = \frac{1}{2}B''x^2 \implies B' = B''x \quad (3.15)$$

and

$$\Delta\nu = \frac{1}{2\pi}\beta \left(\frac{B''\ell}{2B\rho} \right) x, \quad (3.16)$$

where x denotes the displacement of the closed orbit from the center of the sextupoles.

For the E778 sextupoles

$$\frac{B''\ell}{2B\rho} = .35/\text{m}^2 \text{ at } 50 \text{ A} \quad (3.17)$$

or

$$\frac{B''\ell}{2B\rho} = .007/\text{m}^2 \quad \text{per ampere.} \quad (3.18)$$

So

$$\frac{\Delta\nu}{I} = \frac{1}{2\pi}\beta x \left[\left(\frac{B''\ell}{2B\rho} \right) / I \right] = (.000113/\text{mm A}) \times \sum_{i=1}^{18} (\pm)x_i, \quad (3.19)$$

where β at the sextupoles is 100m and the sum extends over all E778 sextupoles. The plus/minus sign takes care of the sextupole polarity. The deviation of the closed orbit from the design orbit, expressed in mm, as a function of the longitudinal coordinate s , is plotted in Fig. 3.8. The letters C, D, F,... on the horizontal axis mark the beginning of the each of the 6 sectors. The table just above the plot, contains the raw beam position data used to make the closed orbit plot, at each of the 18 quadrupole locations (left column) in each sector (top row). Recall that the E778 sextupoles are located at positions 22, 24, 26, 28, 32, 34, 36, 38 of the C and F sectors. This

information yields

$$\sum_{i=1}^{16} (\pm)x_i = +3.99\text{mm}. \quad (3.20)$$

So, one should expect

$$\Delta\nu/I = .0005/\text{amp}. \quad (3.21)$$

In fact this result can be compared with measurements of tune versus sextupole current, taken during the E778 run and plotted on Fig. 3.9. The slope of the curve of Fig. 3.9 is .0007 / amp. Considering the uncertainties in the determination of the tune as well as the errors in the beta functions at the sextupoles, this result is in reasonable agreement with the above calculation.

Finally the coherent synchrotron oscillations at injection had to be minimized. At the injection energy of 150 GeV, a phase locking mechanism ensures the matching of the two buckets from the Main Ring and the Tevatron. Once the phase is locked, one can adjust the energy so as to minimize the coherent synchrotron oscillations.

Experimental Procedures

All measurements were carried out at the Tevatron injection energy of 150 GeV. A different experimental procedure was followed in each of the four experiments mentioned in the Introduction. The first type of experiment consisted of injecting a beam of protons into the Tevatron, then ramping the sextupoles up to the desired setting in 10 seconds. After a further 10 second delay, a coherent betatron oscillation was induced by firing the kicker. The displacement of the centroid of the beam and the beam intensity were recorded by the Tevatron BPMs through the Tevatron's two-minute cycle. This is the technique employed during the smear experiment.

For the injection experiment, the sextupoles were powered when the beam was injected into the Tevatron and measurements were performed with intentional injection steering errors. The recorded data include: the BPM readings during the first turn,

```

DISPLAY FRAME      7.014
FILE 140 02/20/88 0337:
E778 CLOSED ORBIT

      (MM)      02/22/88 1353
      C      D      E      F      A      B
11      1.24      8.23      3.33      1.42      -.1      -1.89
13      1.03      .78      -2.28      -1.15      -.69      -1.49
15      .42      -1.42      -12.95      -3.01      -1.07      1.21
17      -.8      -2.64      -4.34      -1.72      NOBEAM      -.05
19      -2.81      -1.35      -4.99      .46      .27      -1.49
22      -.45      .28      -.1      1.6      -1.33      -3.01
24      1.77      1.95      3.46      -.46      -1.58      -1.11
26      .58      .07      2.85      -2.25      -1.32      .31
28      -1.89      -2.52      -.55      -2.3      .22      1.14
32      -3.29      -2.09      -2.87      -1.16      1.76      -1.72
34      -3.58      -.2      1.26      .01      -1.83
36      1.43      1.75      2.31      .33      -1.49      -.39
38      .99      1.38      .98      -1.99      -1.49      -.21
42      .06      -1.22      -2.25      -2.53      -.59      .9
44      -1.3      -3.68      -3.86      -.66      1.38      -1.12
46      -1.45      -2.75      -1.5      NOBEAM      .68      -1.38
48      4.87      7.24      1.14      1.39      2.85      -2.01
49      6.99      7.22      1.89      .4      -1.5      -1.4

```

```

RHS (MM) = 2.654    DP/P (%) = .0037    MOM CORR RMS = 2.691

```

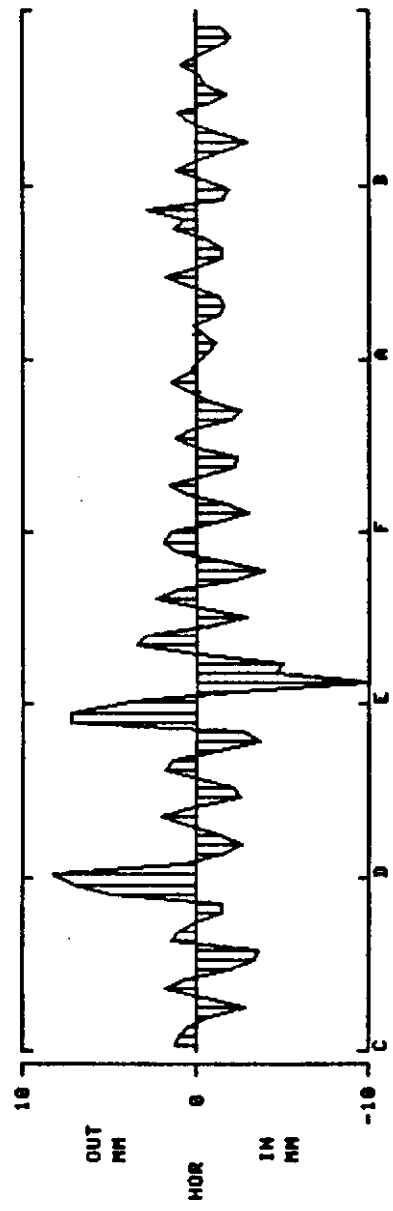


Figure 3.8: Experimental data of the closed orbit.

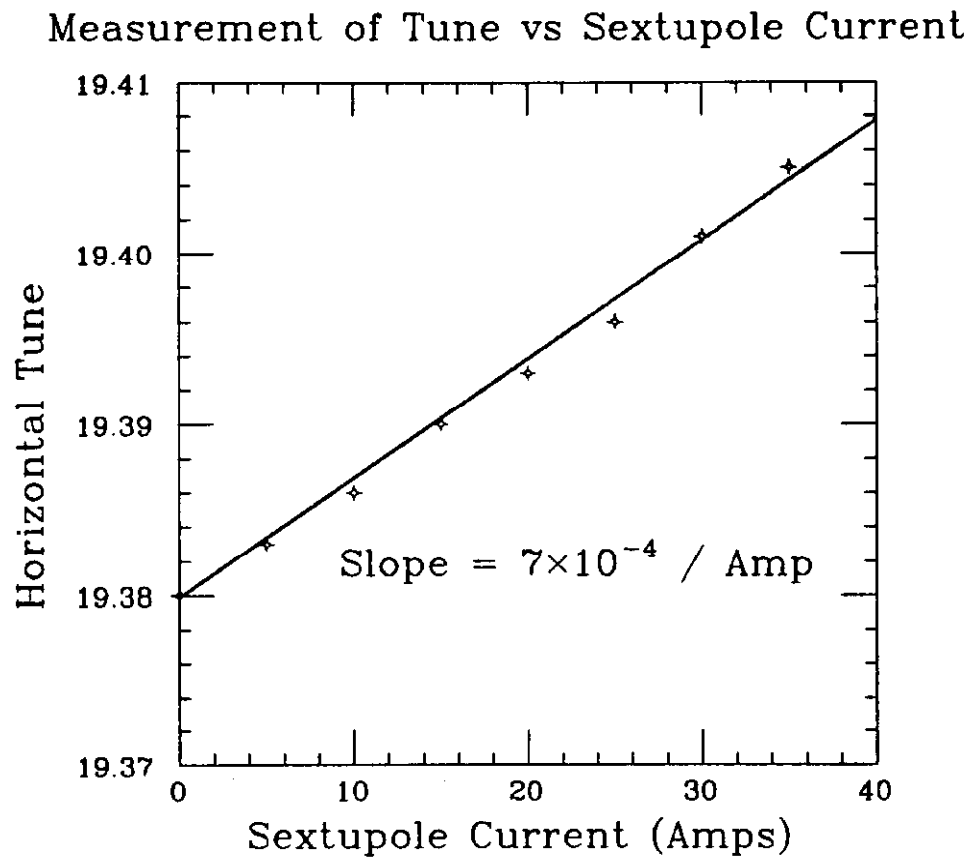


Figure 3.9: Measurements of tune versus sextupole current.

the closed orbit shortly after injection, turn-by-turn data at injection, beam profiles at injection and 9 seconds later and beam intensity versus time.

The third variety of measurements was associated with the study of resonance islands. The procedure was similar to the first one, but here the accelerator conditions were adjusted in order to enhance the capture of particles on the islands.

In the last type of measurements, the emittance of the beam was slowly increased by adding noise into the transverse dampers until particles were lost. Using the Tevatron flying wires the beam size was measured as a function of the sextupole excitation. The limiting beam size was taken to be a measure of the dynamic aperture (when it was less than the physical aperture).

CHAPTER IV

THE SMEAR EXPERIMENT

The principal aim of the smear experiment was to determine if the smear is predictable from the nonlinear tracking calculations, which are important in projecting the performance of existing and future accelerators. The reliability of single and multi-particle tracking calculations in predicting other quantities, such as the decoherence time of the beam, the variation of tune with the amplitude and the fraction of ‘surviving’ particles (to be defined later), was equally relevant.

This chapter is structured as follows. A theoretical discussion of the subject is presented first, followed by the experimental aspect of it. The chapter is concluded with the presentation of the results of this study. In particular, I start with a derivation of the smear and the variation of the tune with the amplitude using the formalism developed in Chapter II. A discussion on the tracking codes used to simulate the experimental conditions follows. The details of the experimental procedure are given next. Then, the code used for the analysis of both the experimental and the simulated data is described in detail. Finally, the results of the analysis of the data are presented and compared with the theoretical predictions from both tracking and perturbation calculations.

The Perturbative Approach

The formalism developed in Chapter II is used to derive expressions for the horizontal smear and the nonlinear tunes shift due to a distribution of normal sextupoles in the ring.

Smear

Consider the situation where the only nonlinearities in the ring are due to normal sextupoles. Let also this derivation be confined to the horizontal plane. Then, to first order in perturbation, the distortion of the horizontal amplitude \mathcal{A} at phase advance, ψ is given by

$$\delta\mathcal{A}(\psi) = \mathcal{A}^2\{[-A_1(\psi)\sin\phi + B_1(\psi)\cos\phi] + [A_3(\psi)\sin 3\phi - B_3(\psi)\cos 3\phi]\} \quad (4.1)$$

as shown in Chapter II, Eq. (2.39). Here ϕ is the betatron phase and A_1, B_1, A_3, B_3 are the Collins distortion functions defined by Eqs (2.35).

The single particle smear can be written by definition as

$$s = \frac{\sqrt{\langle\mathcal{A}^2\rangle - \langle\mathcal{A}\rangle^2}}{\langle\mathcal{A}\rangle} \quad (4.2)$$

or

$$s = \left(\frac{\langle(\delta\mathcal{A})^2\rangle}{\mathcal{A}^2} \right)^{1/2}, \quad (4.3)$$

where $\langle \rangle$ denotes the average over many turns or equivalently over the betatron phase ϕ . From Eq. (4.1) one gets

$$s^2(\psi) = \frac{1}{2}\mathcal{A}^2\{A_3^2(\psi) + B_3^2(\psi) + A_1^2(\psi) + B_1^2(\psi)\}. \quad (4.4)$$

If the distortion functions are put into arrays

$$R_1(\psi) = \begin{pmatrix} B_1(\psi) \\ A_1(\psi) \end{pmatrix} \quad R_3(\psi) = \begin{pmatrix} B_3(\psi) \\ A_3(\psi) \end{pmatrix}, \quad (4.5)$$

then the smear is related to the norms of these vectors by

$$s^2(\psi) = \frac{1}{2} \mathcal{A}^2 \{|R_1|^2 + |R_3|^2\}. \quad (4.6)$$

Recall from Eq. (2.38) that the vectors $R_1(\psi + \Delta\psi)$ and $R_3(\psi + \Delta\psi)$ are given by the vectors $R_1(\psi)$ and $R_3(\psi)$ rotated through angles $\Delta\psi$ and $3\Delta\psi$ respectively if there is no sextupole between the two points, ψ and $\psi + \Delta\psi$,

$$\begin{pmatrix} B_p \\ A_p \end{pmatrix}_{\psi + \Delta\psi} = \begin{pmatrix} \cos p\Delta\psi & \sin p\Delta\psi \\ -\sin p\Delta\psi & \cos p\Delta\psi \end{pmatrix} \begin{pmatrix} B_p \\ A_p \end{pmatrix}_{\psi}, \quad (4.7)$$

with p being 1 or 3. In passing through a thin sextupole of length $\ell_k \rightarrow 0$ and strength s_k defined by (2.23), the B_p 's are continuous, while the A_p 's jump by $s_k/4$. Thus the smear is a constant between two sextupoles but will have a jump when a sextupole is crossed. Indeed Fig. 4.1 is the picture one obtains by plotting the smear as given by (4.6) as a function of the phase advance around the machine. Sixteen sextupoles clustered in two groups of eight located at phase advances in the neighborhood of $4.5 \times 2\pi$ and $14.5 \times 2\pi$ cause these jumps in the smear.

Further insight can be obtained if one writes explicitly the definition of the distortion functions at any point ψ between 0 and $2\pi\nu$, where ν is the horizontal tune:

$$\begin{aligned} B_1(\psi) &= \frac{1}{2 \sin \pi\nu} \sum_k \frac{s_k}{4} \cos(\psi'_k - \psi - \pi\nu), \\ A_1(\psi) &= \frac{1}{2 \sin \pi\nu} \sum_k \frac{s_k}{4} \sin(\psi'_k - \psi - \pi\nu), \\ B_3(\psi) &= \frac{1}{2 \sin 3\pi\nu} \sum_k \frac{s_k}{4} \cos 3(\psi'_k - \psi - \pi\nu), \\ A_3(\psi) &= \frac{1}{2 \sin 3\pi\nu} \sum_k \frac{s_k}{4} \sin 3(\psi'_k - \psi - \pi\nu). \end{aligned} \quad (4.8)$$

The summations above are over each sextupole at phase advance ψ'_k which is related to the Floquet phase ψ_k by

$$\psi'_k = \begin{cases} \psi_k & \text{if } \psi_k \geq \psi, \\ \psi_k + 2\pi\nu & \text{if } \psi_k < \psi, \end{cases} \quad (4.9)$$

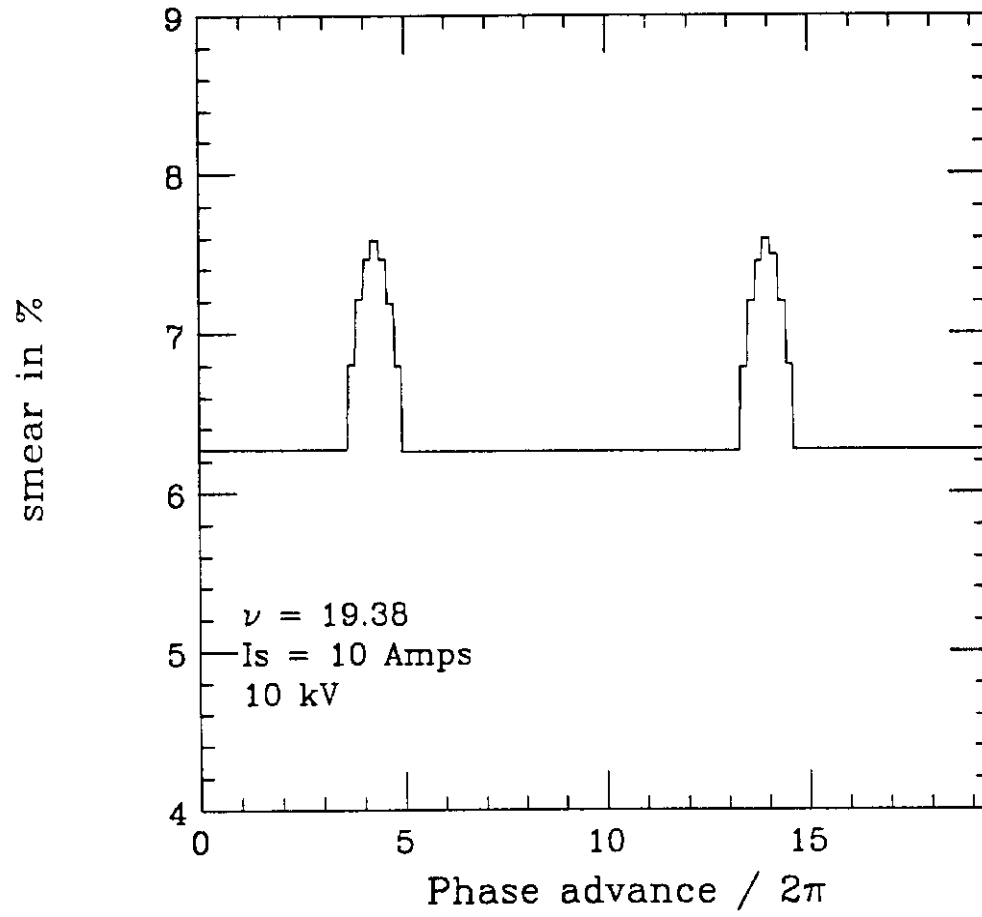


Figure 4.1: Smear versus phase advance, around the machine, as predicted from perturbation calculation.

Then

$$B_1^2(\psi) + A_1^2(\psi) = \frac{1}{64 \sin^2 \pi \nu} \sum_{kk'} s_k s_{k'} \cos(\psi'_k - \psi'_{k'}) , \quad (4.10)$$

or

$$|R_1(\psi)| = \frac{1}{8 |\sin \pi \nu|} \left| \sum_k s_k e^{i\psi'_k} \right| . \quad (4.11)$$

Similarly,

$$|R_3(\psi)| = \frac{1}{8 |\sin 3\pi \nu|} \left| \sum_k s_k e^{i3\psi'_k} \right| . \quad (4.12)$$

From (4.6) and (4.11), (4.12) one can conclude that to first order in the sextupole strength s_k , the smear is proportional to the amplitude of the particle \mathcal{A} . Fig. 4.2 and 4.3 display the smear as a function of the amplitude and the sextupole strength respectively. In both cases the smear has been calculated using (4.6), (4.11) and (4.12) for the 16-sextupole configuration used during E778. The results of the above calculation of the smear, for the experimental conditions at which data were taken will be displayed at the end of this chapter. Then these results will be compared with the values of smear extracted from the data and from tracking calculations.

Finally a generalized expression for the horizontal smear due to all multipoles can be found in reference [37]. In the same reference a two degree of freedom calculation yields the smear due to sextupoles.

Tune versus Amplitude

In Chapter II an expression was derived for the single particle amplitude dependent tuneshift due to sextupoles. This is

$$\Delta\nu = -\frac{1}{4\pi} \mathcal{A}^2 \sum_k (3B_1 s + B_3 s)_k, \quad (4.13)$$

where B_1 and B_3 are given by Eqs (2.35).

In Chapter IV it will be demonstrated that tuneshifts calculated from (4.13) agree remarkably well with the single particle tracking predictions [38]. However it is of

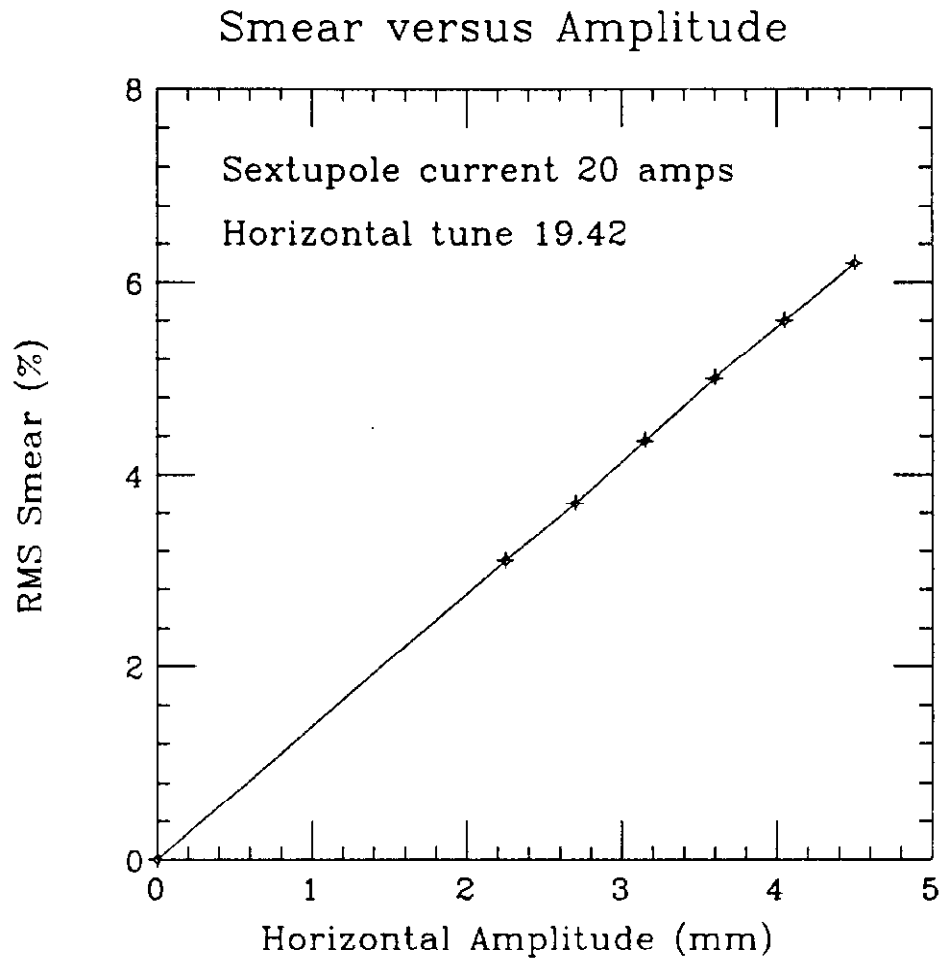


Figure 4.2: Smear versus amplitude, from perturbation calculation.

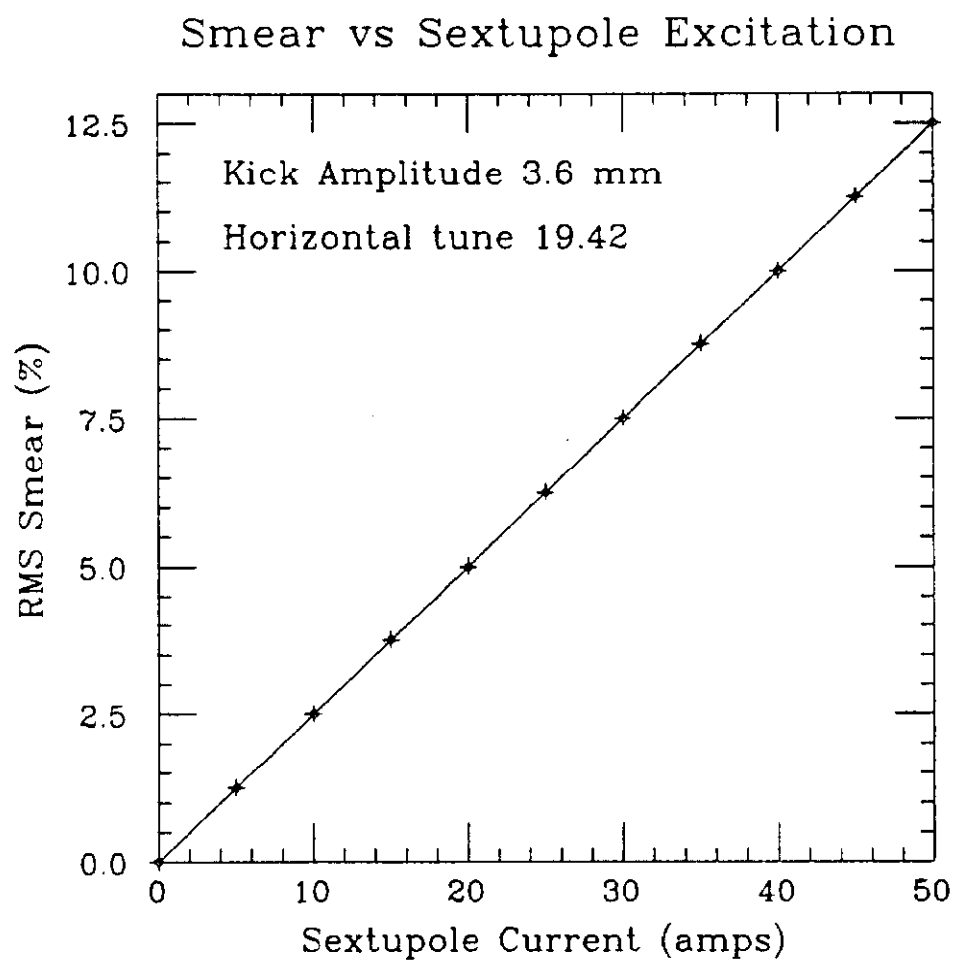


Figure 4.3: Smear versus sextupole strength, from perturbation.

interest to examine the effect of the single particle tuneshift on the motion of the centroid of the whole beam. Particles of a finite-sized beam are at different amplitudes and hence, in the presence of nonlinearities, oscillate at different frequencies. So even though the amplitude of the centroid of the beam is large right after the beam is kicked, it eventually becomes smaller as the various particles occupy more area in the phase space, until it vanishes completely. Assuming first that the beam size is significantly smaller than the kick amplitude, secondly a parabolic dependence of the tune on the amplitude and thirdly a gaussian distribution of particles in the beam, the expression for the amplitude at turn N is given by [40]

$$\mathcal{A}(N) \sim e^{-(Q_g N)^2/2}, \quad (4.14)$$

where $Q_g = 4\pi\Delta\nu$, $\Delta\nu$ being the single particle tuneshift. A proof is given in the Appendix. In this model, the decoherence time R , of the beam, expressed in number of turns, is defined by

$$R = \frac{1}{4\pi\Delta\nu}. \quad (4.15)$$

The decoherence time as derived from these perturbative considerations, is compared to that from tracking and experimental data in the last section of this chapter.

Tracking Calculations

Another way of predicting the values of the smear and the decoherence time of the beam in the presence of nonlinearities is by numerically simulating the environment of the beam and then tracking its motion for a number of turns. Then an algorithm must be developed for the extraction of the relevant quantities out of the motion of the particles in the beam. In this section the various simulation codes used in E778 are described. The discussion of the algorithm is presented in the ‘Analysis’ section.

Three different simulation codes were used initially for tracking calculations: TEAPOT [41], ART [42] and EVOL [43]. They have been used both as single and

multi-particle codes depending on the type of calculation needed. They all simulated more or less exactly the motion of a number of particles in the Tevatron, for the same set of parameters the experimental data were taken. The results of the calculations were analyzed the same way the experimental data were. All three codes generated almost identical data, so only one of them, EVOL, was chosen for copious production of simulated smear-data.

A description of the main characteristics of the three programs is now in order. The *realistic* Tevatron lattice—including magnet field errors and the chromaticity correction sextupoles in the Tevatron—served as TEAPOT's input; it was then translated into a similar lattice containing only thin elements. Tracking into that lattice is exact. TEAPOT's output included the position and the slope of the centroid of the beam at several locations in the ring, for every turn. These calculations were repeated for 512 turns.

Both ART and EVOL, as opposed to TEAPOT, assumed a lattice which is otherwise linear except for the sixteen special sextupoles used to control the nonlinearities in the Tevatron. This assumption was justified on the basis of the relative magnitude of the sextupole strengths and the harmonic content of the chromaticity-correction sextupoles: The current needed for chromaticity corrections in the Tevatron is of the order of 1 ampere while the current passing through the E778 sextupoles was an order of magnitude higher—from 10 to 50 amperes. Moreover the transfer constant, defined as the field strength per ampere, of the chromaticity sextupoles is 50% lower than that of the E778 sextupoles. Finally, the chromaticity sextupoles have been arranged in a way that does not excite any resonances, as opposed to the E778 sextupoles. For these reasons the sixteen special sextupoles dominate, and neglecting the chromaticity-correction sextupoles is a successful approximation.

The main difference between ART and EVOL lies on the way the initial distribution of particles is defined. ART starts with a randomly generated gaussian

distribution of particles in a linear environment. The horizontal emittance of the beam, as measured experimentally, is used to calculate the rms beam size. Hence the rms of ART's gaussian distribution is given by the σ as calculated from the emittance. As the sextupole strengths change adiabatically from zero towards their final settings, the particles find themselves moving in the slowly varying nonlinear environment. As a result, the shape of the distribution changes. Thus, tracking begins with a deformed-gaussian distribution of particles. This model simulates the process of injecting the beam in a linear machine and subsequently ramping the sextupole magnets to their final settings while the beam particles circulate in the machine.

In EVOL on the other hand, the initial distribution of particles is two-dimensional: a distribution in amplitude and in phase. A number of particles are uniformly distributed within a range of values of the amplitude, however there is a different weight associated with each particle. Similar is the phase assignment to each particle.

Both ART and EVOL typically use approximately 600 particles and track their motion for up to 500 turns. The position and the slope of the centroid of the distribution are recorded at the end of each turn, at the locations of the two beam position monitors and the location of the kicker.

Results from extensive EVOL tracking calculations as compared to the experimental data will be shown in the last section of this chapter. Now though, I would like to display some examples of the kind of calculations one can perform with tracking codes. First in Fig. 4.4 the smear is plotted as a function of the sextupole excitation for a tune of 19.42.

In Fig. 4.5 smear versus amplitude particle is displayed for a tune of 19.42 and 30 amperes in the sextupoles. Single particle EVOL tracking has generated the data for these calculations.

Also in Fig. 4.6 the tune, as calculated from single particle EVOL tracking, is displayed as a function of the particle amplitude for a variety of conditions. Notice

Smear vs Sextupole Excitation

Single Particle EVOL tracking

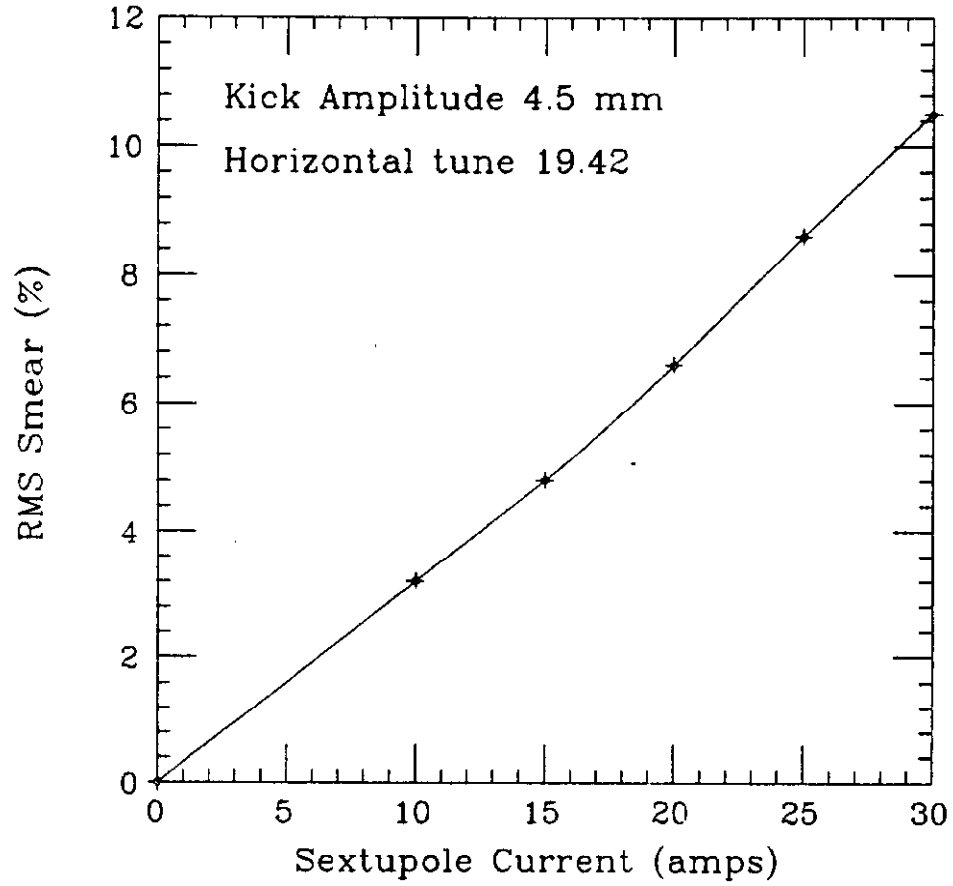


Figure 4.4: Smear versus sextupole excitation for $\nu = 19.42$, as predicted from EVOL tracking.

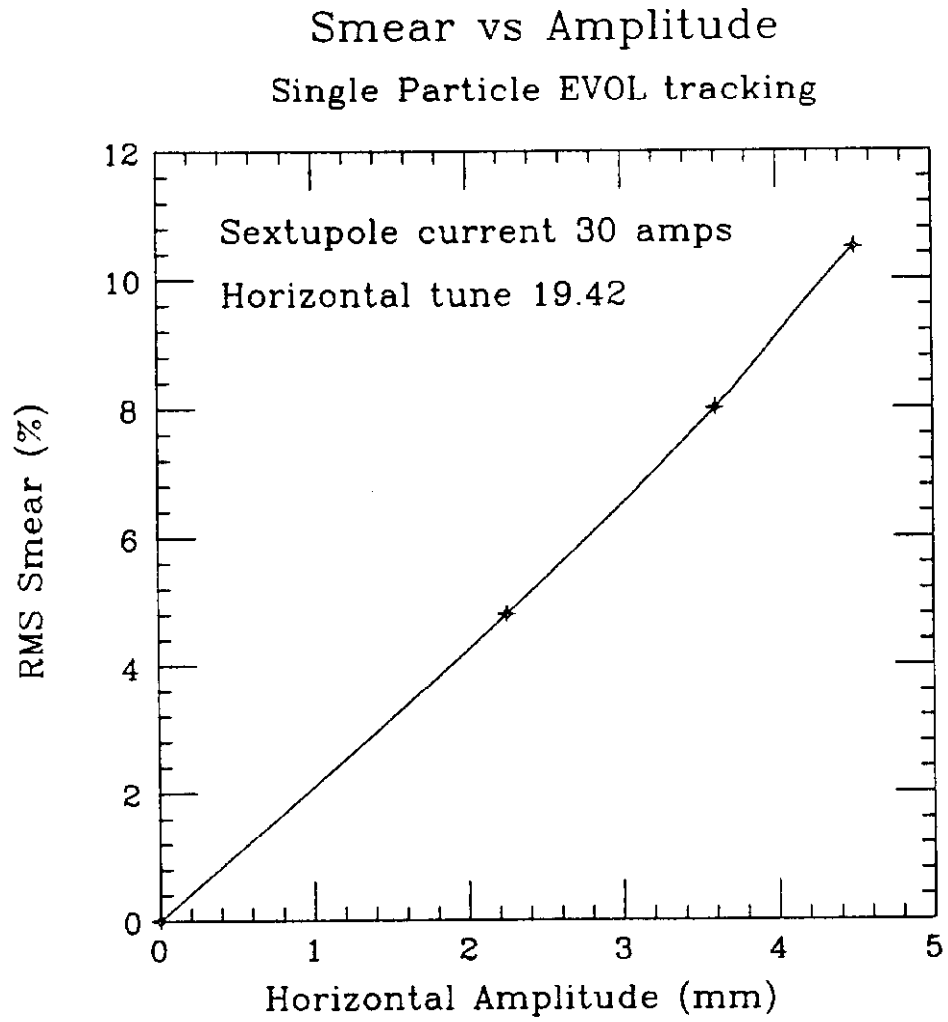


Figure 4.5: Smear versus amplitude for $\nu = 19.42$ and 30 amperes, as predicted from EVOL tracking.

the characteristic parabolic (at least for small amplitudes) shape of the curves as predicted from analytical considerations.

The Experiment

The real test of the validity of the above predictions comes from their agreement with the experimental observations. A description of the experiment is given first.

The experimental sequence started with the injection of a low emittance proton beam into the Tevatron. In the next ten seconds the sextupoles were ramped up to their final setting. Ten seconds later the kicker fired and the centroid beam position was recorded for up to half a million turns in each of the two adjacent BPMs located at stations F42 and F44. For the majority of the data the recording was restricted to 64,000 turns, corresponding to more than one second of real time.

Measurements were made at various values of four different parameters: the sextupole excitation, the horizontal tune, the kicker strength and the beam emittance. The sextupole excitations varied from 0 to 50 amperes in steps of 5 amperes. Another, perhaps more general way to determine the sextupole strength, is to specify the 'resonance width' of the third-order resonance, i.e., the width of that range of the tune ν over which the motion is unstable. For a beam of *physical* (as opposed to normalized, which is multiplied by the relativistic parameter γ) emittance ϵ , the resonance width can be defined by equating the beam emittance to the stable area, and is given by [12,13]

$$\Delta\nu = \frac{A}{2\pi} \left(\frac{\beta_0 \epsilon}{3\sqrt{3}} \right)^{1/2}. \quad (4.16)$$

Here β_0 is the beta function at the reference point and A is a measure of the strength of the sextupole configuration and is given by

$$A = \sum_k s_k \cos(3\nu_0 \phi'_k), \quad (4.17)$$

Tune vs Amplitude

Single particle EVOL tracking

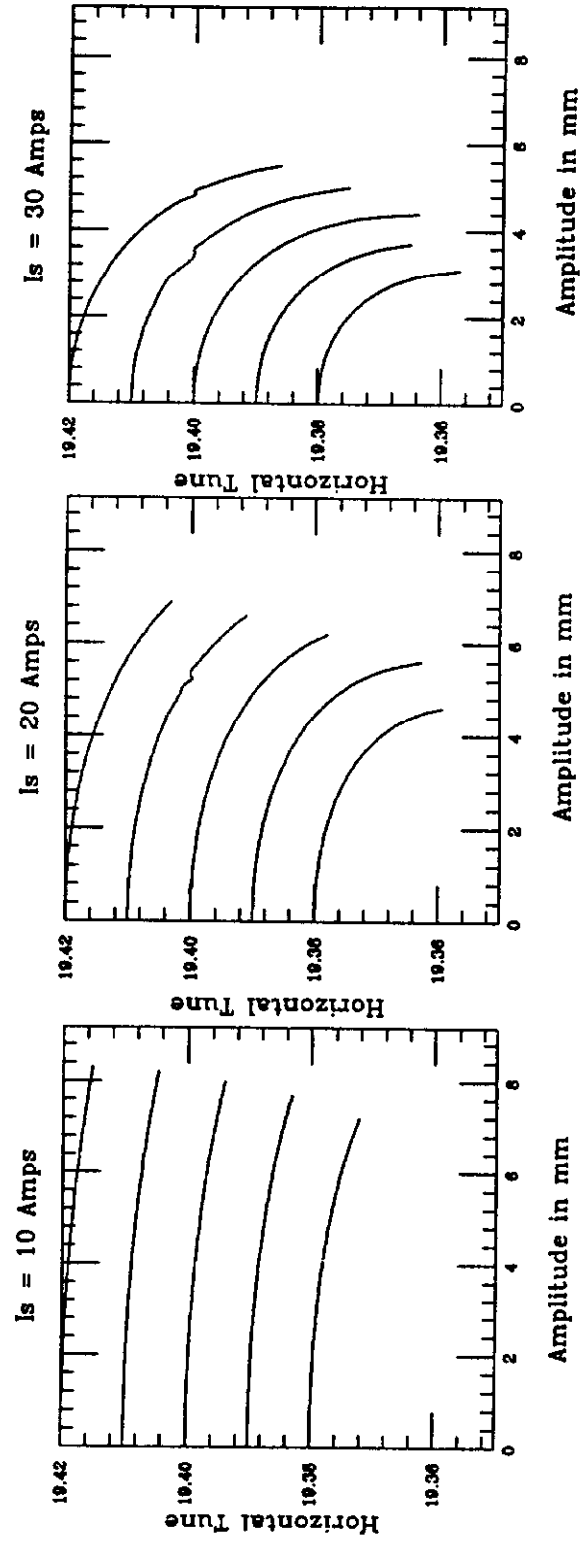


Figure 4.6: Tune versus amplitude from single particle EVOL simulation.

where ϕ'_k is defined by

$$\phi'_k = \frac{1}{\nu} \int_0^s \frac{ds'}{\beta(s')} \quad (4.18)$$

and $\nu_0 = 19 \frac{1}{3}$ in the case of Tevatron. When the current through the E778 sextupoles is 50 amperes, A is

$$A \simeq 346 \text{ m}^{-1}. \quad (4.19)$$

In this computation, I have used the proximity of ν to ν_0 . At a reference point with beta function of 100 m, and a beam of *normalized* emittance equal to 10π mm-mrad, the width of the third-order resonance is

$$\text{Resonance width } \Delta\nu = .107, \quad \text{for 50 amperes.} \quad (4.20)$$

The second parameter varied during the smear measurements was the horizontal tune which assumed 5 different values from 19.38 to 19.42 in steps of .01 while the vertical tune was set to 19.46. The kicker strength was 5, 8 or 10 kilovolts. At the HF42 BPM, the maximum horizontal displacement, x_1 in meters, is related to the kicker strength D in kV, by

$$x = 0.48 \times 10^{-5} D \sqrt{\beta_1 \beta_k}, \quad (4.21)$$

where β_1 is the beta function in meters at the location of HF42 and β_k is the beta function at the location of the kicker E17, so

$$x = 0.48 \times 10^{-5} D \sqrt{100.2 \times 82.8}. \quad (4.22)$$

Measured at the kicker, the maximum angle, p_k in radians, maximum displacement x_k in meters and initial kick strength, D in kV, are ideally related by

$$p_k = 0.48 \times 10^{-5} D = \frac{x_k}{82.8}. \quad (4.23)$$

Hence the corresponding oscillation amplitudes at the bare Tevatron were 2.19, 3.50 and 4.37 mm.

Measurements were taken at two different ranges of the horizontal emittance. At the low range the emittance varied from 1.5π to 3.7π while at the high range it was between 7.8π and 10.9π . Table 4.1 summarizes the conditions at which low emittance data were taken during the smear experiment. The degree to which the value of smear as predicted from multiparticle EVOL simulation and from the experimental data, is shown on the same table. Three asterisks imply agreement better than 20%. Two asterisks imply agreement between 20% and 30%, while agreement worse than 30% is denoted by one asterisk. The question mark is used for situations where one could not extract a value for the smear. The same notation has been employed for Table 4.2, which summarizes the conditions at which high emittance data were taken. In both tables, the second column displays the kicker voltage in kV while the top row displays the sextupole excitation in amperes.

Two sets of front end electronics were used for the data recording. The first, the standard Tevatron BPM front end, gave direct horizontal, vertical and intensity signals. The second is a peak-sensing circuit which gives signals from the separate plates of two horizontal and one vertical pickup. A more detailed description of the instrumentation including diagrams of the hardware configuration is given in reference [29].

Fig. 4.7 displays the four channels of information as recorded by the standard BPM front end. The top plot on the left is the centroid of the beam recorded by the HF42 position monitor, while the one right below it, is the signal recorded by the HF44 monitor. The top right plot displays the signal from the VF43 monitor and the one below it displays the beam intensity recorded by the I.45 intensity monitor. Fig. 4.8 shows the same dataset recorded by the peak-sensitive circuit. The top left plot displays the signal from one of the plates of the HF42 BPM, while the top right displays the signal from one of the plates of the HF44 BPM. The bottom left plot shows the signal from the left plate of the VF45 BPM while the signal from the right

LOW EMITTANCE DATA												
ν_z	kV/ I_s	0	5	10	15	20	25	30	35	40	45	50
.38	5			***	***	***	***	***				
.39	5	*		**	?	***	***	***				
.40	5				***	***	***	?				
.41	5		?	***	***	***	***	***	***	?		**
.42	5				**	***	***	***		***	***	
.38	8			***	***	***	***	***				
.39	8	*		***	***	***	***	***				
.40	8				***	***	***	***				
.41	8				***	***	***	?				
.42	8				***	***	***	***		?		
.38	10			***	***	***						
.39	10				***	***	***	***				
.40	10				***	***	***	***				
.41	10				***	***		?				
.42	10				***	***	***	?				

Table 4.1: Summary of the accelerator conditions at which low emittance data were taken, in the smear experiment.

HIGH EMITTANCE DATA												
ν_x	kV/ I_s	0	5	10	15	20	25	30	35	40	45	50
.38	5			***		***		***				
.39	5	*	?	***		***		?				
.40	5			?	?	?	?	?				
.41	5			***		***		?	?			
.42	5			?		***		***		***	?	***
.38	8			***		***		*				
.39	8			***		***		***				
.40	8			***		***		***				
.41	8			?		***		?				
.42	8			?		***		***		?		
.38	10			***		***		*				
.39	10			***		***		**				
.40	10			***		***		***				
.41	10			***		?		***				
.42	10			***		***		?				

Table 4.2: Summary of the conditions at which high emittance data were taken in the smear experiment.

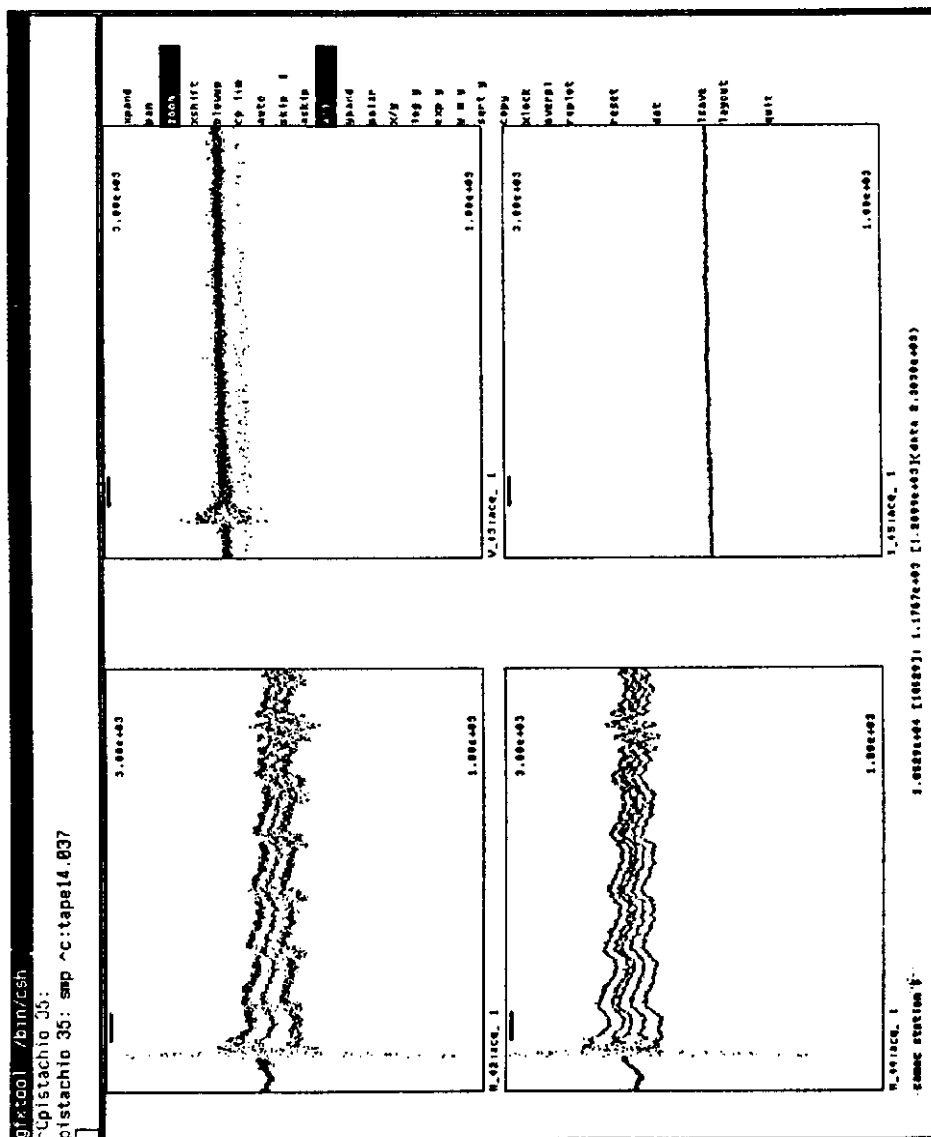


Figure 4.7: The standard Fermilab BPM front end electronics were used to record the above turn-by-turn data of the centroid of the beam.

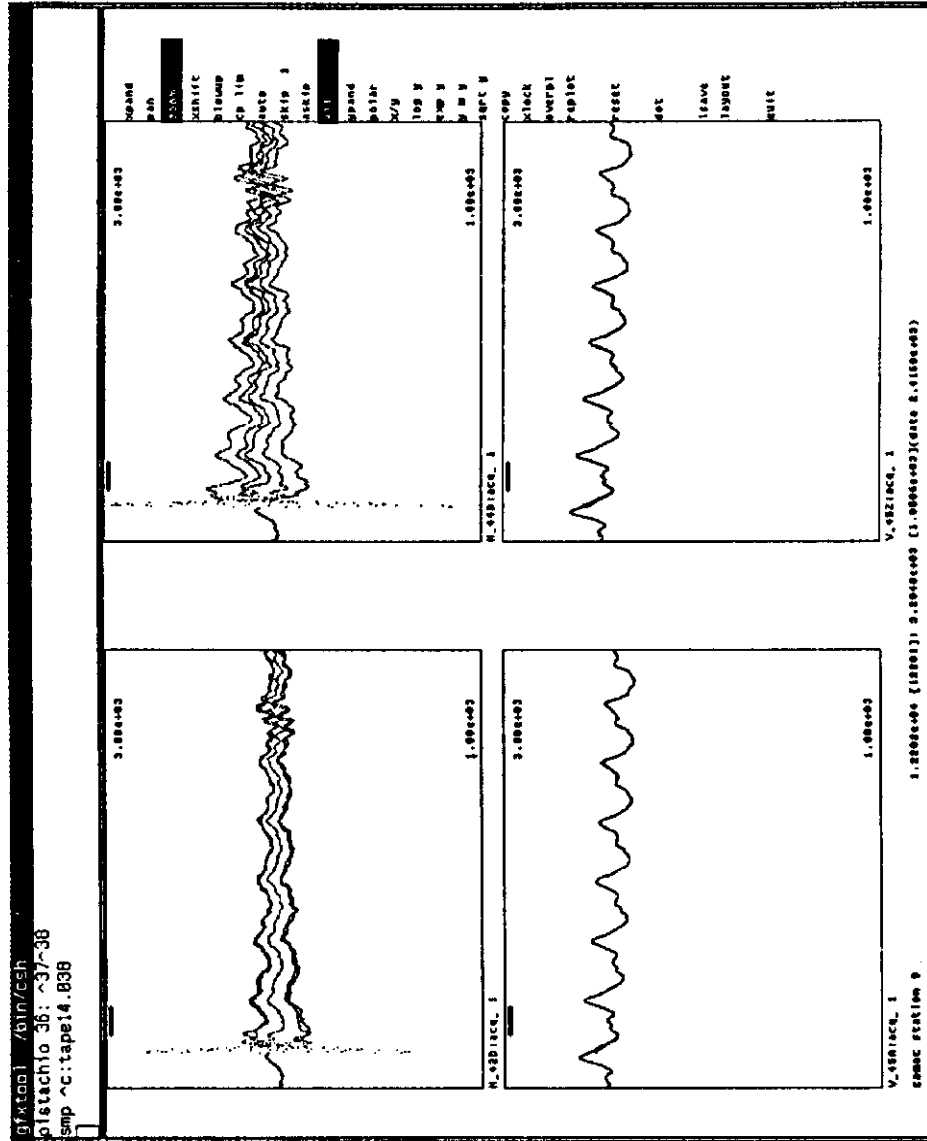


Figure 4.8: Peak-sensing front end electronics were used to record these turn-by-turn data.

plate of VF45 is plotted on the bottom right plot. All these signals are plotted as functions of turn number.

Finally, only the data recorded by the standard Tevatron BPMs have been analyzed. The question of calibration of the signals from the Tevatron beam position and intensity monitors has been previously [44] addressed.

Analysis

This section is devoted to the detailed description of TEVEX, the code originally written by Peggs [39], and used almost exclusively for the analysis of both the experimental and the simulated data. The underlying principle of TEVEX is given first, followed by the flow diagram and a general explanation of it. A detailed derivation of the formulæ used in this section is given in the Appendix.

The Principle of TEVEX

The program TEVEX has been developed to analyze both experimental and simulated data of transverse nonlinear phenomena. The basic input for TEVEX is x_1 and x_2 , the positions of the centroid of the beam at two different locations of the accelerator, for a number of machine turns. For the experimental data this information is provided by the recordings of the two BPMs. TEVEX output includes the values of quantities which characterize the nonlinear motion, such as the smear, the tune of the machine and the decoherence rate. The program displays these quantities as a function of the number of turns used for their calculation.

Several definitions are now in order. The smear is defined, as before, as the fractional rms deviation of the amplitude. The amplitude in TEVEX is defined as the geometric mean of the amplitudes at the locations of the two BPMs. The tune in TEVEX is defined as the number of phase-space oscillations divided by the number

of revolutions.

A choice of the level of sophistication of the analysis is available, which determines the procedure followed for the analysis of the data. Thus, at the zeroth level the raw data together with the design values of the beta functions and the phase advances are combined to give an expression for the amplitude from which the smear is calculated. Similarly, from the same information one can derive an expression for the phase advance and hence the tune of the machine.

The next level 1 calculates the average closed orbit offsets at the two BPMs and then subtracts them from the BPM recordings. The analysis otherwise remains the same as before.

The beta functions and the phase advance are not really precisely known. The principle of TEVEX is that they should also be extracted from the data. This is done at the second level of the analysis. The equation of an ellipse in the x_1, x_2 space can be written in terms of the following four parameters: the two closed orbit offsets, the ratio of the beta functions at the two BPMs and the phase advance between the BPMs. The data are fitted to this ellipse so as to minimize the rms deviation of the amplitude—the smear. The four parameters above are determined as a result of the fit. They are subsequently used for the calculation of the smear, the tune, etc.

At the last level 3 the multi-particle aspect of the analysis is addressed. The presence of a finite-sized beam in a nonlinear environment gives rise to an apparent amplitude damping due to the decoherence of the particle motion. TEVEX assumes a gaussian model [40] for the decoherence. The standard deviation of the gaussian curve, which is defined in TEVEX to be the decoherence time, is the fifth parameter to be determined by a minimization fit. Now the data are fitted to the ellipse as before, but there is also a gaussian factor multiplying the equation for the ellipse. The fit determines the five parameters which are then used again to process the data.

At the end a summary of the results is reported and graphical outputs are avail-

able.

In the following the discussion will be restricted to the horizontal plane only, even though TEVEX provides a limited two-degree of freedom analysis.

Program Organization

The flow diagram of TEVEX is given in Fig. 4.9. I shall follow this diagram and explain the physical meaning of each structure. TEVEX first obtains the 'global control parameters' supplied by the user. These parameters control the format of the input data, the filtering of input and output data, the persistent signal analysis, the discrete Fourier transform analysis, the resonance analysis, the fitting procedure and the graphical output. The design lattice parameters are also included. The file which contains this information is called TEVEX.CMD. The exact file is shown in Fig. 4.10 with typical values of the various parameters. The comments included in the file explain briefly the meaning of each parameter.

Next, TEVEX reads the phase space information which consists of the positions of the centroid of the beam at two locations (BPMs for the experimental data) for a number of turns. TEVEX has the capability of analyzing data coming from a variety of sources. Specifically, it analyzes experimental data taken during the 1987 E778 run and stored in the form of ASCII files, data stored in the shared memory, simulated data from EVOL and simulated data from TEAPOT. Finally there is a version of TEVEX which runs only with shared memory on UNIX V on the SUN Workstations.

A filtering of undesirable frequencies, for example the self-induced synchrotron frequency, from the raw position and intensity data can be done next. The user specifies the region of tune values to be filtered. Fig. 4.11 shows the effect of filtering the synchrotron frequency from raw position data.

At this point the user chooses the level of the analysis. Once the analysis level has been chosen, the range of data to be analyzed is determined either automatically or

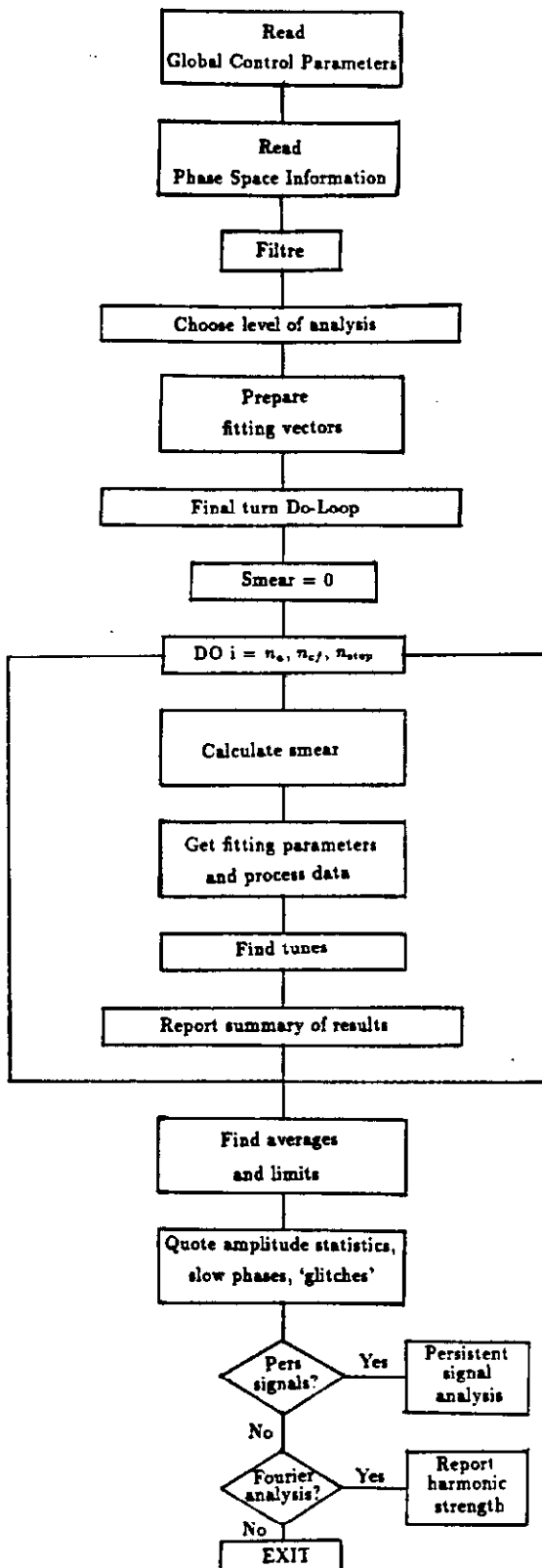


Figure 4.9: Flow diagram of TEVEX.

```

@ 12 @.2          ifmt, ihead, bnoise
f f 3 @ 4@ 4@ 1 @ BATCH FAST level nt(strt,fs,ff,fi) next
5kv15a.files      infils
t .0005 .005      FILTER, qmin, qmax
f 300 500         PERSIG, npsmin, npsmax
f .35 .45 .00 1.1 DODFT, ftl, ftr, ftmin, ftmax
3 1 1 .1          maxhar, iq1, iq2, senhar
1 2 5 @.1         NSTROB, numer, norder, dfitol
99.64 28.36 94.83 29.94 67.84 beta(x1,y1,x2,y2), ficell
-1.9 @.53 -1.9 @.53 alfa(x1,y1,x2,y2)
.0 1 100          bitsiz, npstrt, npfin
1 2000 -2000 1.5 @.99 @.2d-11 man, itmx, itw, pfin, pfac, ftol
t t t t t t      XlvT, AXvT, AXvFIX, SvT, QXvT, FITvT
-----
*** input control *****
IFMT = 0          specifies the input format to be read:      IHEAD = 8 or 12
      1          E77B ascii files                          any IHEAD
      2          E77B shared memory                        try IHEAD = 16
      3          EVOL (x1,x2,y1,y2) mm                      IHEAD = 5
      4          TPOT-TeVbpm (x1,x2,x1,x2) metres           try IHEAD = 7
      5          TEAPOT (x,x',y,y') metres                 any IHEAD
IHEAD number of header lines stripped off the input file(s)
BNOISE 1st real data must rise above this noise (mm) eg @.2

*** fast pass default values *****
BATCH if TRUE (.and.FAST) input filenames are read from INFILS
FAST if TRUE, invokes the default values in the array...
IFAST(1-6), instead of prompting the user, for a fast pass. If @ is
input for the "NTnnnn" values, 2,3,4 & 5, a full scan is
invoked (eg, 97, 1024, 1024, 1).
INFILS contains BATCH input filenames - on a line by itself

*** filtering input and output data *****
FILTRE = TRUE turns on a frequency filter of X1 & X2 raw data from
QMIN, QMAX frequencies between QMIN, QMAX. (about 600 for
TeV synch period)

*** persistent signal measurement *****
PERSIG = TRUE turns on the persistent signal analysis
NPSMIN, MAX post-decoherence range for persistent signal measurement

*** Discrete Fourier Transform parameters *****
DODFT = TRUE turns on the DFT (turn off if speed is important)
FTL, FTR are the Left & Right margins for the DFT plots
FTMIN is the lower bound of the DFT plots (log IF ftmin > @.0)
FTMAX is the upper vertical bound of the DFT plot
MAXHAR is the maximum harmonic order plotted
IQ1, IQ2 specifies which horz(vert) tune to use for Q1{Q2}, in
harmonic analysis
      = 0          (# of phase space turns) / (# of machine turns)
      1          highest peak in the appropriate DFT
      2          second highest peak in the DFT
SENHAR is the threshold DFT response to signify a harmonic peak

*** slow phase parameters *****
NSTROB plot only every NSTROB'th turn on some graphs - lock on?
NUMER, NORDER the slow phase is measured as Fi - Qres*(Turn number)
where the resonance tune is Qres = NUMER / NORDER
DFITOL tolerance for BPM glitches/phase discontinuities (twopi)

*** idealised lattice parameters *****
BETA(X1,Y1,X2,Y2) are the design betas at the monitors
FICELL is the phase advance per cell, in degrees

ALFA(X1,Y1,X2,Y2) are the design alphas at the monitors

*** test data parameters *****
BITSIZ is the assumed bit size of the BPMs (millimetres)
NPSTRT,NPFIN are the start and finish particles whose coordinates are
summed

*** fitting control *****
MAN = @ (1) turns off(on) some manual control of the optimisation
ITMX is the maximum number of HYDRA steps before quitting
ITW is the number of HYDRA steps per write
PFIN multiplies single coordinates of the initial matrix
PFAC is the multiplier used when shaking up the solution
FTOL is the goal tolerance

*** graphical output control *****
XlvT = T if X1 BPM data is plotted versus turn T (uses NSKIP)
AXvT = T if amplitude AX is plotted versus turn number
AXvFIX = T if amplitude AX is plotted versus phase FIX
SvT = T if Smeas is plotted versus last turn number fitted
QXvT = T if tune QX is plotted versus last turn number fitted
FITvT = T to plot FIT parameters versus last turn number fitted

```

Figure 4.10: Typical example of TEVEX.CMD, the file which contains the values of the control parameters.

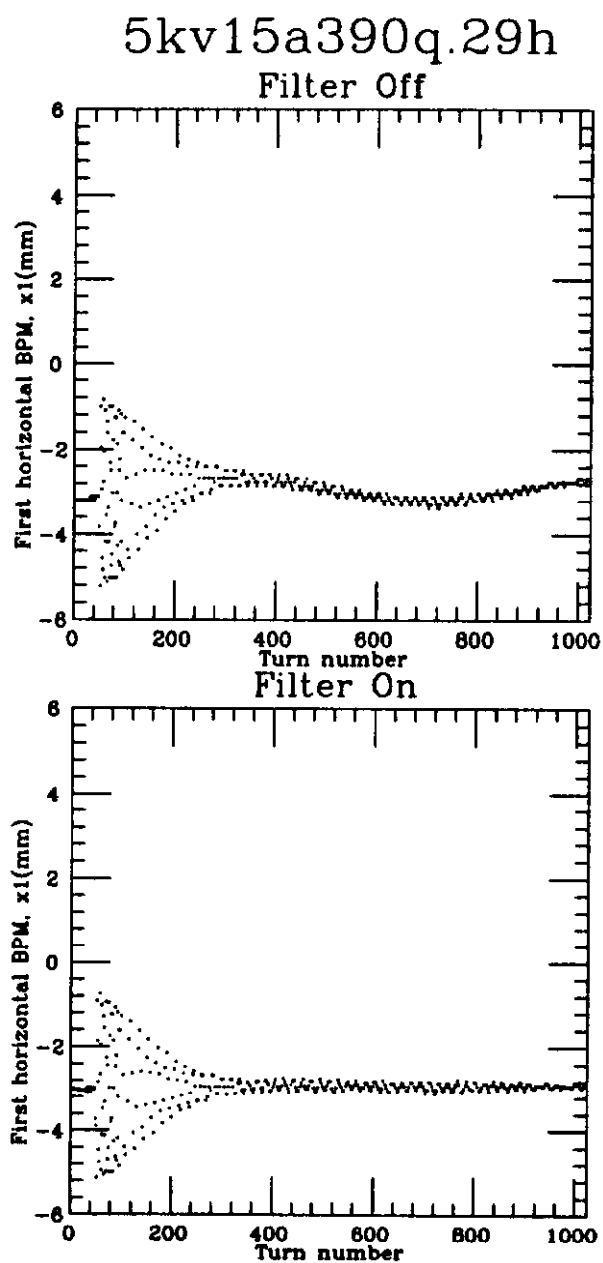


Figure 4.11: Raw position data before and after filtering of the synchrotron oscillations. The title indicates that this dataset was recorded with a kicker strength of 5 kV, sextupole excitation of 15 amps and tune of 19.39.

by the user. Let n_i denote the turn number on which data start, and n_f denote the turn number on which data finish. Suppose that the analysis starts at turn number n_a , which is usually the kick time, with $n_a \geq n_i$. Also let n_{ci} and n_{cf} denote the first and last turn number at which the quantities of interest, e.g. smear, may be calculated. Notice that n_{ci} must be greater than $n_a + 5$ because at least five data points are needed to determine the five parameters from the fit described above. At this point the ranges of the tracking data, the analysis and the calculation are determined. These various ranges of data are shown in Fig. 4.12. The displacement of the centroid of the beam as a function of turn number for 200 turns is plotted in Fig. 4.13(a). Exactly below is Fig. 4.13(b) which displays the smear corresponding to the same data as a function of the number of turns used for its calculation. So, for example, the value of the smear at the n -th turn is obtained by processing data from turn number n_a to n . Similarly the value of the smear at the $(n + 1)$ -th turn is obtained from data between n_a and $(n + 1)$ turns.

The average values of the digitized data as well as their limits are calculated next in the range between the first turn used for the analysis n_a , and the last turn used for the calculations, n_{cf} .

The final step before the calculations start is to prepare the vector with the fitting parameters for each one of the four levels of the analysis.

From now on I shall concentrate on one level of analysis at a time since the calculational techniques can be quite different for different levels.

Level 0

The purpose is to calculate the smear and the horizontal tune of the machine for every turn, from the recordings of the two BPMs.

Again as before, suppose that tracking data start on turn n_i and finish on turn

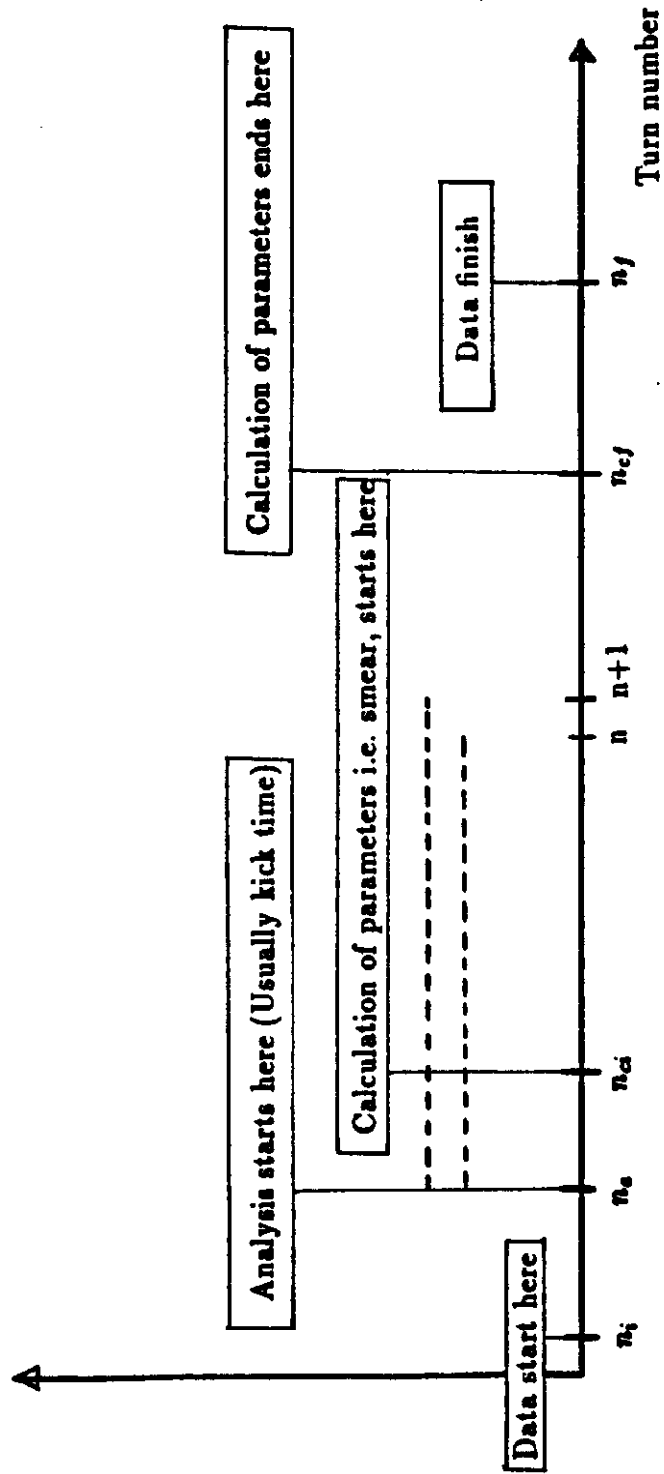


Figure 4.12: Ranges of data that are relevant to the analysis by TEVEX.

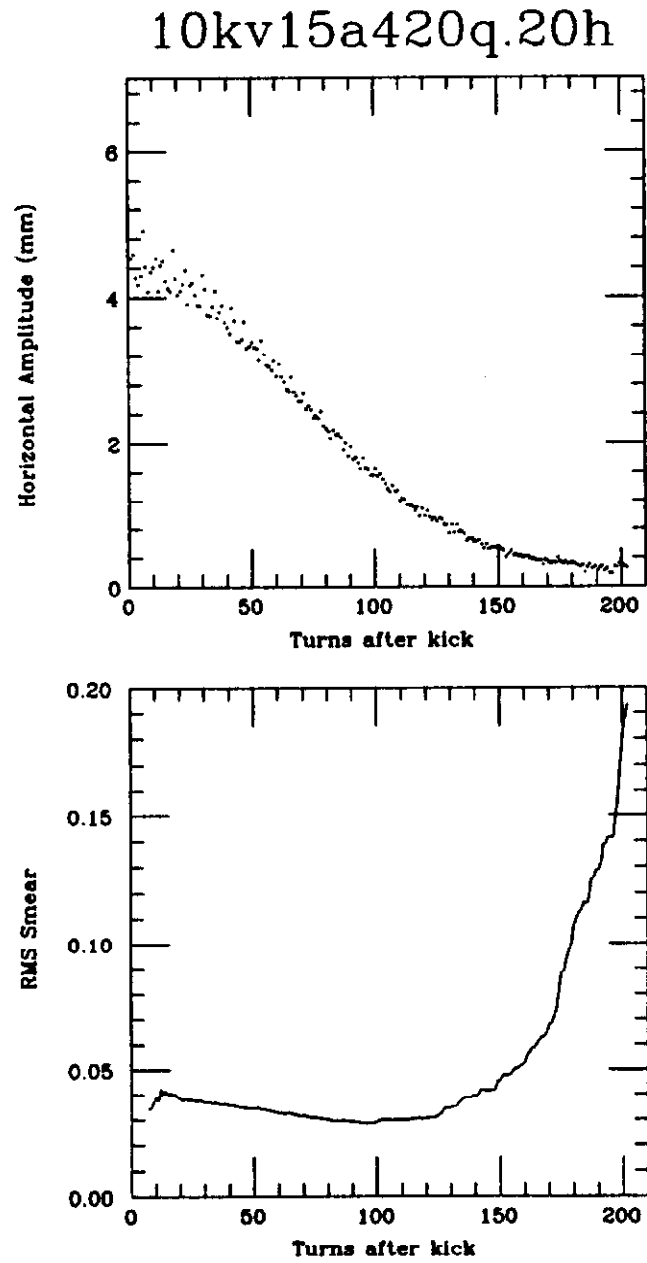


Figure 4.13: Position of the centroid of the beam and smear plotted as functions of turn number. The determination of smear deteriorates as the beam decoheres.

n_f , and the analysis starts at the kick time which occurs on turn n_a . The goal is to calculate the smear and the tune at turn n , starting from turn number n_{ci} and ending at turn number n_{cf} . By definition

$$\text{smear}(n) = \frac{\sqrt{\langle a_x^2 \rangle - \langle a_x \rangle^2}}{\langle a_x \rangle}, \quad (4.24)$$

where the average is calculated over the range (n_a, n) . The amplitude a_x is defined in TEVEX to be the geometric mean of the amplitudes at the two BPMs. That is

$$a_x^2 = a_{x1} a_{x2}, \quad (4.25)$$

and is given by the expression

$$a_x(n) = \sqrt{c_{11}x_1^2(n) + c_{12}x_1(n)x_2(n) + c_{22}x_2^2(n)}, \quad (4.26)$$

where the various coefficients are defined by

$$c_{11} = \frac{1}{\sin^2(\phi_{\text{cell}})} \sqrt{\frac{\beta_{x2}}{\beta_{x1}}}, \quad (4.27)$$

$$c_{22} = \frac{1}{\sin^2(\phi_{\text{cell}})} \sqrt{\frac{\beta_{x1}}{\beta_{x2}}}, \quad (4.28)$$

$$c_{12} = -2 \frac{\cos(\phi_{\text{cell}})}{\sin^2(\phi_{\text{cell}})}. \quad (4.29)$$

Here β_{x1} and β_{x2} are the design horizontal beta functions at the locations of the two BPMs. ϕ_{cell} is the design phase advance between the two BPMs. Notice that the two BPMs used in E778 were one cell apart, hence the subscript of ϕ . The proof of (4.26)-(4.29) is given in the Appendix. At this level the values of the beta functions and the phase advance are the design values.

The next goal is to calculate the tune at turn n . In TEVEX the tune Q_x is defined to be

$$Q_x(n) = \frac{1}{2\pi} \frac{\phi(n) - \phi(n_i)}{n - n_i}, \quad (4.30)$$

where $\phi(n)$ is the phase advance in the middle of the two BPMs, at turn n . $\phi(n)$ is computed in TEVEX from the formula

$$\phi(n) = \arctan \frac{(x_{\beta 1} + x_{\beta 2}) / \cos(\phi_{\text{cell}}/2)}{(x_{\beta 2} - x_{\beta 1}) / \sin(\phi_{\text{cell}}/2)}, \quad (4.31)$$

where $x_{\beta 1}$ and $x_{\beta 2}$ are given by

$$x_{\beta i} = \frac{x_i}{\sqrt{\beta_{xi}}} \quad i = 1, 2 \quad (4.32)$$

and x_1, x_2 are the recordings of the two BPMs. A proof of (4.31) is given in the Appendix. Recall that at this level the design values of the beta functions and the phase advance are used.

At the end of the calculation TEVEX reports a summary of the results. A separate line for each turn of the analysis is written out containing the following information: the turn number n , the amplitude $a_x(n)$, the smear $s(n)$, the tune $Q_x(n)$, the average closed orbit offset at the first BPM $x_{1\text{off}}$, the average closed orbit offset at the second BPM $x_{2\text{off}}$, the value of the beta function at the first BPM β_{x1} , the value of the beta function at the second BPM β_{x2} , the phase advance between the two BPMs ϕ_{cell} and the decoherence rate $R(n)$ which has no value at this level and becomes different from zero at the third level. The closed orbit offsets are also zero at this level while the values of the two beta functions and the value of the phase advance are equal to the design values and hence constant for every turn n .

A typical TEVEX output of the analysis of experimental data is presented in Fig. 4.14. The analysis was performed at level 0. The global control parameters assumed the values shown in Fig. 4.10. The corresponding graphical output is given later.

Level 1

The analysis at level 1 is very similar to the analysis at level 0, the only difference being that now the average closed orbit offsets are subtracted from x_1 and x_2 .


```

>>> THE FOLLOWING PARAMETERS ARE SET IN tevox.cmd <<<
----- Input file format parameters -----
format, #headers, initial noise = 0 12 0.20000
----- Fast pass default values -----
BATCH FAST level nt(st,fs,ff,fi) next = F F 3 0 40 40 1 0
infiles : 5kv15a.files
----- Input and output filters -----
FILTER, qmin, qmax = T 0.00050 0.00500
----- Persistent signal analysis -----
PERSIG npsmin npsmax = F 300 500
----- Discrete Fourier Transform parameters -----
DODFT, dftL, dftR, dftMIN, dftMAX = F 0.35000 0.45000 0.00000 1.10000
Max harmonic, Q1/2 choice, threshold = 3 1 1 0.10000
----- Slow Phase Parameters -----
Nstrob, Numer, Norder, DftTol = 1 2 5 0.10000
----- Idealised lattice parameters -----
beta(x1,y1,x2,y2), phase per cell = 99.64 28.36 94.83 29.94 67.84
alpha(x1,y1,x2,y2) = -1.900 0.530 -1.900 0.530
----- Test data parameters -----
BPM LSB, 1st & last particles = 0.00000 1 100
----- Fitting control parameters -----
manual ctrl, max iters, iters/write = 1 2000 -2000
initial & shake factors, tolerance = 1.50000 0.99000 0.200-11
----- Graphical output control -----
X1vT, AXvT, AXvFIX, SvT, QXvT, FITvT = T T T T T T
Horizontal file:[e778.may11]5kv15a390q.29h *****

FILE 29 5KV 15A .39 .48 DATA 05/11/87 2142
Detector 1 = T:HPE24 Data Timing: 29.9990
Detector 2 = T:HPE26 Data Timing: 29.9990
T:HPE24 T:HPE26
13616 12591 12681 14136 8224 12594 12852
13600 22091 12576 16693 8224
13102 8249 13358 8246 16708
16724 8224 8224 8224
29.99900 29.99900
-2.95198 -1.79139
0 0

First data line : 1 -3.21000 -2.06000 0.00000 0.00000
Real data starts: 49 -3.84000 -4.02000 0.00000 0.00000

LEVEL = 0 *****

Tracking data appears to start on turn 49 and finish on turn 1024
ntstbt, ntfini, ntfinf, ntfini= 49 1 140 1

NTFIN Ax mm. SMEAR Qx Xoff(1,2) mm. BetaX(1,2) m. Fix d. Rdec
55 4.5714 0.3303 0.35464 0.0000 0.0000 99.64 94.83 67.840 0.0000+00
56 1.3501 0.4166 0.42277 0.0000 0.0000 99.64 94.83 67.840 0.0000+00
57 5.2501 0.3997 0.37943 0.0000 0.0000 99.64 94.83 67.840 0.0000+00
58 2.9776 0.3904 0.35205 0.0000 0.0000 99.64 94.83 67.840 0.0000+00
59 3.2874 0.3752 0.39588 0.0000 0.0000 99.64 94.83 67.840 0.0000+00
60 4.9782 0.3622 0.37285 0.0000 0.0000 99.64 94.83 67.840 0.0000+00
61 1.1358 0.4194 0.42171 0.0000 0.0000 99.64 94.83 67.840 0.0000+00
62 4.8994 0.4047 0.46258 0.0000 0.0000 99.64 94.83 67.840 0.0000+00
63 3.7412 0.3893 0.43977 0.0000 0.0000 99.64 94.83 67.840 0.0000+00
64 2.4843 0.3923 0.48295 0.0000 0.0000 99.64 94.83 67.840 0.0000+00
65 5.1404 0.3845 0.44223 0.0000 0.0000 99.64 94.83 67.840 0.0000+00
66 1.6771 0.4066 0.42046 0.0000 0.0000 99.64 94.83 67.840 0.0000+00
67 4.3868 0.3939 0.44393 0.0000 0.0000 99.64 94.83 67.840 0.0000+00
68 4.2752 0.3821 0.42850 0.0000 0.0000 99.64 94.83 67.840 0.0000+00
69 1.7821 0.3983 0.44741 0.0000 0.0000 99.64 94.83 67.840 0.0000+00
70 5.2534 0.3935 0.43099 0.0000 0.0000 99.64 94.83 67.840 0.0000+00

*
*
*

137 4.3557 0.3696 0.42106 0.0000 0.0000 99.64 94.83 67.840 0.0000+00
138 2.5290 0.3695 0.41727 0.0000 0.0000 99.64 94.83 67.840 0.0000+00
139 3.1304 0.3679 0.42219 0.0000 0.0000 99.64 94.83 67.840 0.0000+00
140 3.9706 0.3656 0.41872 0.0000 0.0000 99.64 94.83 67.840 0.0000+00

Min(X1,X2), max(X1,X2), <X1>, <X2> (mm) = -5.2300 0.0000 -3.0462 -1.8267
X Amplitude: min, max (mm) = 0.0000 5.3534

** WARNING ** Phase advances out of tolerance (0.1000) ?? GLITCHY DATA ??
Turn Amp(mm) Old fi(2pi) New fi(2pi) Old<slowfi> New<slowfi> Dsfi(adjusted)
81 1.136 0.8430 0.8021 -0.0137 0.7917 0.7750
77 2.902 0.9058 0.8992 0.7988 0.6040 -0.1898
93 4.702 0.7869 0.7662 0.6075 1.4113 0.7792
110 1.367 0.8362 0.8218 1.3946 2.2004 0.7951
124 4.367 0.7718 0.7767 2.2083 2.0114 -0.2126
126 2.787 0.8876 0.7245 2.2041 2.0067 -0.1995
128 1.012 0.8336 0.8358 2.1986 2.0030 -0.2028

EXIT with only summary graphics *****

```

Figure 4.14: Typical TEVEX.OUT file; the analysis has been performed at level 0.

Specifically at this level the amplitude a_x defined by (4.25) is given by the expression

$$a_x(n) = \sqrt{c_{11}(x_1(n) - x_{1\text{off}})^2 + c_{12}(x_1(n) - x_{1\text{off}})(x_2(n) - x_{2\text{off}}) + c_{22}(x_2(n) - x_{2\text{off}})^2}. \quad (4.33)$$

Here $x_{1\text{off}}$ and $x_{2\text{off}}$ are the average values of x_1 and x_2 in the range between the first turn used in the analysis, n_a , and the last turn used for the calculations, n_{cf} . The coefficients c_{ij} , $i,j=1,2$, are defined in (4.27), (4.28) and (4.29) and again the beta functions as well as the phase advance assume their design values.

The calculation of the horizontal tune at turn n involves the phase advance $\phi(n)$ which has been defined in (4.31) in terms of $x_{\beta 1}$ and $x_{\beta 2}$. As expected $x_{\beta 1}$ and $x_{\beta 2}$ are now given by the expressions

$$x_{\beta i} = \frac{x_i - x_{i\text{off}}}{\sqrt{\beta_{xi}}} \quad i = 1, 2. \quad (4.34)$$

Otherwise the tune calculation remains unchanged.

Finally the values of the average closed orbit offsets are reported in the final summary of the results. At this level their values remain constant throughout the range where the calculations are performed.

Level 2

At this level the calculation of smear and tune is substantially different from the calculations of the previous two levels. Since neither the beta functions at the two BPMs nor the phase advance between them are known, an attempt is made to extract this important information from the data. This is realized in the TEVEX analysis performed at a level greater than 1.

At level 2 the amplitude as defined by (4.33), and hence the smear, can be viewed

as a function of the components of the following 4-dimensional vector

$$v_{\text{in}} = \begin{pmatrix} x_{1\text{off}} \\ x_{2\text{off}} \\ \phi_{\text{cell}}/2 \\ \sqrt{\beta_{x1}/\beta_{x2}} \end{pmatrix}. \quad (4.35)$$

The parameters $x_{1\text{off}}$ and $x_{2\text{off}}$ are defined as in level 1 analysis, while ϕ_{cell} , β_{x1} and β_{x2} are initialized to their design values.

A new vector v_{out} ,

$$v_{\text{out}} = \begin{pmatrix} x_{1\text{off}}|_f \\ x_{2\text{off}}|_f \\ \phi_{\text{cell}}/2|_f \\ \sqrt{\beta_{x1}/\beta_{x2}}|_f \end{pmatrix} \quad (4.36)$$

is computed such that the smear expressed in terms of these new components is a minimum. This multidimensional minimization is accomplished by the *downhill simplex method* [45] of Nelder and Mead. The $|_f$ denotes that these are fitted parameters. The above procedure is repeated for every single turn of the data and hence a new fitting vector v_{out} is calculated for every turn. The new coefficients are now used to process the data, that is to compute the smear and tune for every turn. Thus, the calculation of the smear is straightforward since it involves precisely the 4 new coefficients which minimize it.

In order to calculate the phase advance - and hence the tune - one needs to know the value of each beta function separately. However only the value of the ratio of the two betas is known. To circumvent this problem the product of the two variable betas is constrained to be equal to the design product of the two betas and thus each beta is calculated separately. It has been demonstrated, by experience, that this hypothesis is reasonably accurate. Note also that the phase advance between the two BPMs and the closed orbit offsets entering the tune calculation are given by the appropriate

components of v_{out} .

The final summary reports the values of the same physical quantities as before but now the fitting parameters have taken the place of the design values. Only the decoherence rate, $\text{rdec}(n)$, continues to be 0 for every turn n .

Level 3

Multi-particle considerations have not yet been taken into account. In the previous three levels of analysis the measured amplitude has been considered as a constant in time. This is clearly not true. It was shown earlier that nonlinearities give rise to amplitude-dependent tunes, which in turn cause an apparent damping of the amplitude. It is shown in the Appendix that, under certain assumptions, the expression for the amplitude at turn n contains a decoherence factor of gaussian form and is given by

$$a_{\mathbf{x}}(n) = e^{-\frac{n^2 R^2}{2}} \sqrt{c_{11}x_1'^2(n) + c_{12}x_1'(n)x_2'(n) + c_{22}x_2'^2(n)}, \quad (4.37)$$

where

$$x_i'(n) = x_i(n) - x_{\text{ioff}}(n) \quad i = 1, 2. \quad (4.38)$$

Also recall that equation (4.37) defines the decoherence rate R in units of inverse turn number. So now the amplitude and hence the smear, can be considered as functions of the components of a 5-dimensional vector, v_{in}

$$v_{\text{in}} = \begin{pmatrix} x_{1\text{off}} \\ x_{2\text{off}} \\ \phi_{\text{cell}}/2 \\ \sqrt{\beta_{x1}/\beta_{x2}} \\ R^2/2 \end{pmatrix}. \quad (4.39)$$

As in level 2, one tries to determine a set of new coefficients, v_{out} , such that the smear is a minimum. Using these new coefficients the smear can be computed as well as the tune and also the decoherence rate. Fig. 4.15 displays the TEVEX output of data analysis performed at the 3rd level. Same data as before (Fig. 4.14) are analyzed and the same TEVEX.CMD file is used (Fig. 4.10). The corresponding graphical output will be given at the end of the next section.

Finally, there are cases where the variation of amplitude with time does not follow a gaussian behavior. This is the circumstance of the persistent signals, for example, to which I shall come back.

Analysis after the 'Final Turn Do-Loop'

At this stage, the major part of the analysis has been completed. Information of statistical nature on the beam intensity, the amplitude, the 'slow phase' and the Fourier spectrum is calculated and reported next.

The beam intensity was recorded by the Tevatron intensity monitors (I.45) for a number of turns. Fig. 4.16 shows raw beam intensity data for 4000 turns. However synchrotron oscillations significantly affected the signal and any reliable intensity measurement requires filtering of the synchrotron motion. Hence the calculation of the beam intensity before the kick occurs is done in TEVEX by averaging over one synchrotron period before the kick. Similarly the beam intensity after the kick is calculated as the average over one synchrotron period, 100 turns after the kick. Finally TEVEX quotes the maximum and minimum intensity values for a given dataset.

Next is a report on the amplitude statistics. The average, maximum and minimum values of the two BPM signals as well as the minimum and maximum values of the amplitude are reported.

```

>>> THE FOLLOWING PARAMETERS ARE SET IN tevex.cmd <<<
----- Input file format parameters -----
format, $headers, initial noise = 0 12 0.20000
----- Fast pass default values -----
BATCH FAST level nt(st,fs,ff,fi) next = F F 3 0 40 40 1 0
infiles : 5kv15a.files
----- Input and output filters -----
FILTER, qmin, qmax = T 0.00050 0.00500
----- Persistent signal analysis -----
PERSIG npsmin npsmax = F 300 500
----- Discrete Fourier Transform parameters -----
DODFT, dftL, dftR, dftMIN, dftMAX = F 0.35000 0.45000 0.00000 1.10000
Max harmonic, Q1/2 choice, threshold = 3 1 1 0.10000
----- Slow Phase Parameters -----
Nstrob, Numer, Norder, DfiTol = 1 2 5 0.10000
----- Idealised lattice parameters -----
beta(x1,y1,x2,y2), phase per cell = 99.64 28.36 94.83 29.94 67.84
alpha(x1,y1,x2,y2) = -1.900 0.530 -1.900 0.530
----- Test data parameters -----
BPM LSB, 1st & last particles = 0.00000 1 100
----- Fitting control parameters -----
manual ctrl, max iters, iters/write = 1 2000 -2000
initial & shake factors, tolerance = 1.50000 0.99000 0.200-11
----- Graphical output control -----
X1vT, AXvT, AXvFIX, SvT, QXvT, FITvT = T T T T T T
Horizontal file: [e778.may11]5kv15a390q.29h *****

FILE 29 5KV 15A .39 .46 DATA 05/11/87 2142
Detector 1 = T:HPE24 Data Timing: 29.9990
Detector 2 = T:HPE26 Data Timing: 29.9990
T:HPE24 T:HPE26
13018 12591 12081 14136 8224 12594 12852
13600 22091 12576 16693 8224
13102 8249 13358 8246 16708
16724 8224 8224 8224
29.99900 29.99900
-2.95198 -1.79139
0 0

First data line : 1 -3.21000 -2.06000 0.00000 0.00000
Real data starts: 49 -3.84000 -4.02000 0.00000 0.00000

LEVEL = 3 *****

Tracking data appears to start on turn 49 and finish on turn 1024
ntatrt, ntfini, ntfinf, ntfini= 49 1 140 1

NTFIN Ax mm. SMEAR Qx Xoff(1,2) mm. BetaX(1,2) m. Fix d. Rdec
55 1.9652 0.0065 0.38875 -3.1496 -1.9167 108.43 87.14 71.907 0.813D-01
56 2.0999 0.0290 0.38617 -3.0978 -1.9085 111.39 84.82 70.374 0.558D-01
57 2.1757 0.0357 0.38562 -3.1321 -1.9301 109.71 86.13 69.287 0.297D-01
58 2.1544 0.0348 0.38628 -3.1260 -1.9203 108.45 87.13 69.469 0.183D-01
59 2.0427 0.0342 0.38688 -3.1297 -1.9077 108.46 87.12 68.541 0.292D-01
60 1.9831 0.0341 0.38735 -3.1114 -1.9055 107.11 88.21 68.358 0.349D-01
61 2.0052 0.0326 0.38741 -3.1101 -1.9047 107.13 88.20 68.300 0.345D-01
62 2.1109 0.0354 0.38697 -3.1212 -1.9216 105.56 89.51 68.122 0.271D-01
63 2.1444 0.0377 0.38691 -3.1230 -1.9096 104.58 90.35 68.886 0.197D-01
64 2.0720 0.0366 0.38649 -3.1212 -1.9108 104.74 90.21 68.992 0.186D-01
65 1.9509 0.0367 0.38676 -3.1082 -1.9086 103.90 90.95 69.258 0.219D-01
66 1.9806 0.0356 0.39679 -3.1095 -1.9079 103.06 90.69 69.330 0.222D-01
67 2.0375 0.0353 0.38714 -3.1107 -1.9143 103.41 91.38 69.472 0.204D-01
68 2.0970 0.0367 0.38761 -3.1177 -1.9086 103.44 91.35 70.095 0.171D-01
69 2.0864 0.0360 0.38690 -3.1105 -1.9089 104.12 90.75 70.116 0.149D-01
70 2.0849 0.0366 0.38681 -3.1167 -1.9127 104.27 90.62 69.831 0.131D-01

*
*
*

137 1.3040 0.0439 0.38766 -3.0204 -1.7965 103.11 91.84 69.006 0.107D-01
138 1.4129 0.0442 0.38766 -3.0192 -1.7937 102.84 91.88 68.949 0.106D-01
139 1.2783 0.0441 0.38754 -3.0197 -1.7923 102.90 91.83 68.877 0.107D-01
140 1.2282 0.0442 0.38788 -3.0168 -1.7927 102.74 91.96 68.777 0.107D-01

Min(X1,X2), max(X1,X2), <X1>, <X2> (mm) = -5.2300 0.0800 -3.0462 -1.8267
X Amplitude: min, max (mm) = 0.0132 3.0516

The largest non-noisy phase discontinuity was
Turn Amp(mm) Old fi(2pi) New fi(2pi) Old<slowfi> New<slowfi> Dsfi(adjusted)
94 1.872 0.6990 0.6795 -0.4803 -0.5466 -0.0140
EXIT with only summary graphics *****

```

Figure 4.15: Typical TEVEX.OUT for analysis performed at level 3.

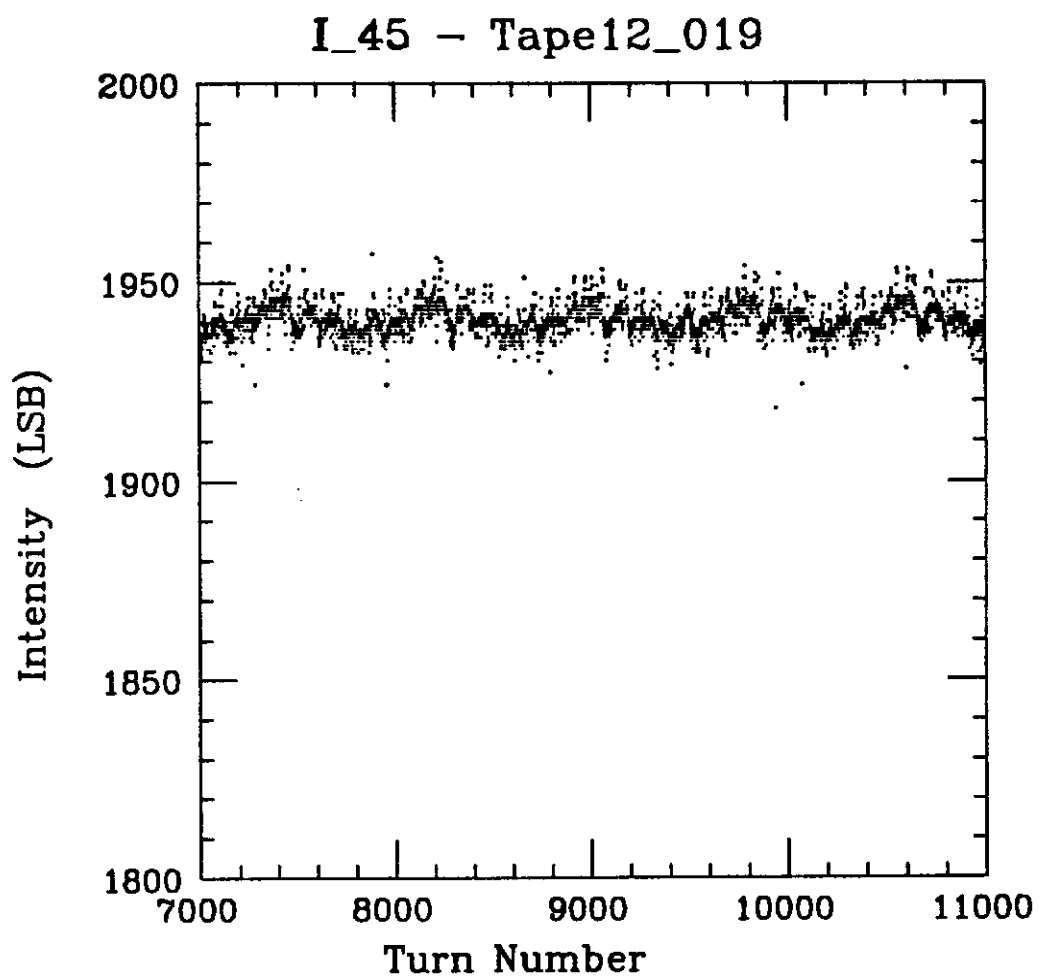


Figure 4.16: Raw beam intensity data, in least significant bits (LSB) for 4000 turns. Zero intensity corresponds to 2048 bits. The calibration constant is $-134 \text{ LSB}/10^{10} \text{ particles}$.

The slow phase is a parameter defined by

$$\phi_{\text{sl}}(n) = \phi(n) - \frac{m'}{n'}n, \quad (4.40)$$

where m'/n' is the nearest resonance. Similarly the 'slow tune' is defined as

$$q_{\text{sl}}(n) = \frac{\phi_{\text{sl}}(n + n') - \phi_{\text{sl}}(n)}{n'}. \quad (4.41)$$

It has already been mentioned that in most of the analysis performed $m'/n' = 2/5$. TEVEX calculates the slow phase as a function of turn number. It also computes the average of the slow phase and the slow tune over n' turns and the change in the average slow phase from turn to turn is recorded.

This last piece of information is used for a search of discontinuities in the slow phase. Any phase jumps greater than a pre-specified tolerance level — 0.1 — is reported in the output file as a warning for non-reliable data. The biggest phase jump is always reported independently of its magnitude.

At this point TEVEX proceeds with the analysis of the persistent signals. These new computational techniques though will be developed in the resonance island chapter.

The last calculation TEVEX performs is a discrete Fourier transform of the BPM signals. This is followed by a report on the strengths of the two harmonics on either side of the peak.

The analysis of a given dataset has been completed here and the user is given four options: to quit the analysis by obtaining a summary graphical output, to quit the analysis and obtain detailed graphical outputs, to return for new analysis of the same dataset or to return for analysis of a new dataset.

If the first option is chosen and if the analysis was performed at the zeroth level, then the graphical output looks like Fig. 4.17. In fact this is the graphical output corresponding to the text output of Fig. 4.14. The graphical output which corresponds to the text of Fig. 4.15, where the analysis level was 3, is shown in Fig. 4.18. The

[e778.may11]5kv15a390q.29h L0

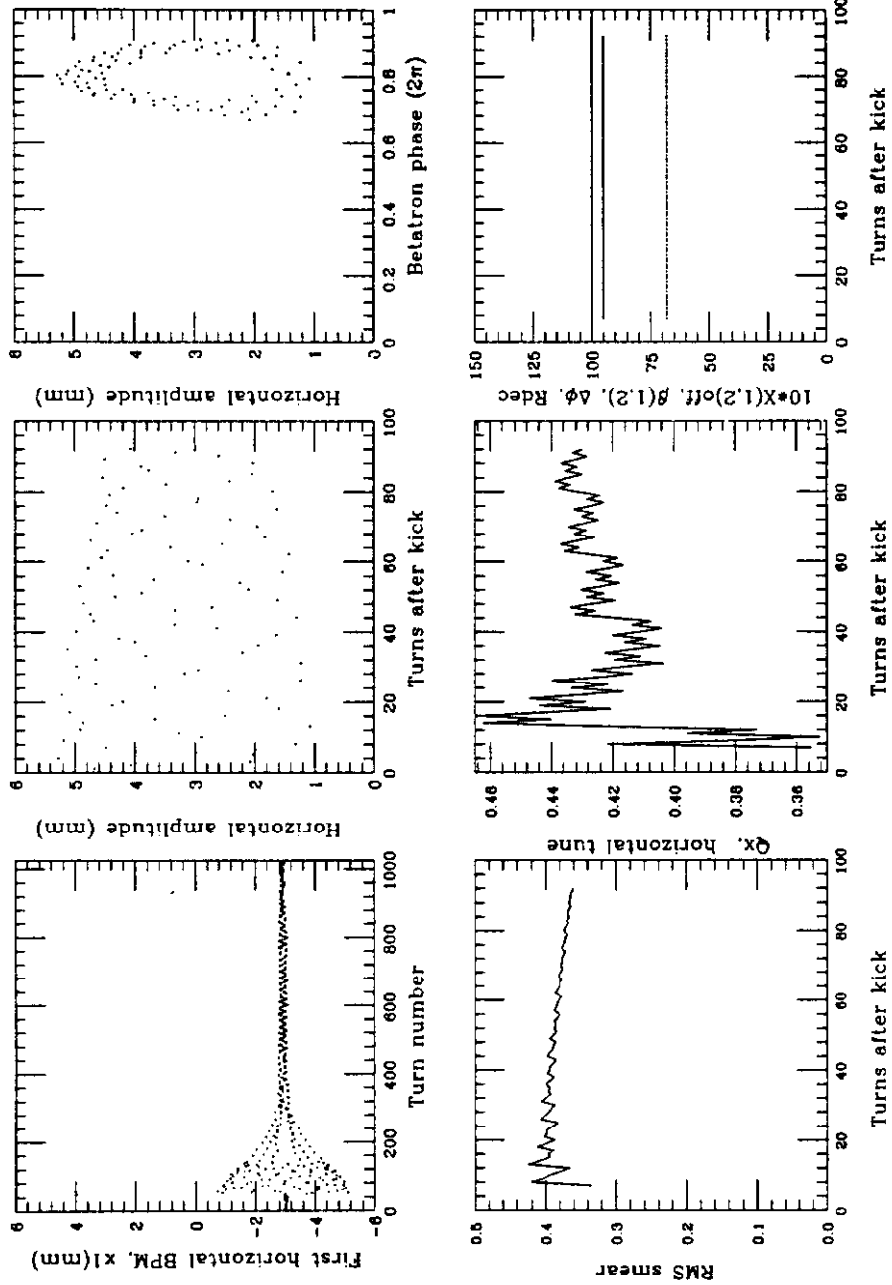


Figure 4.17: Typical graphical output of TEVEX for analysis performed at level 0.

[e778.may11]5kv15a390q.29h L3

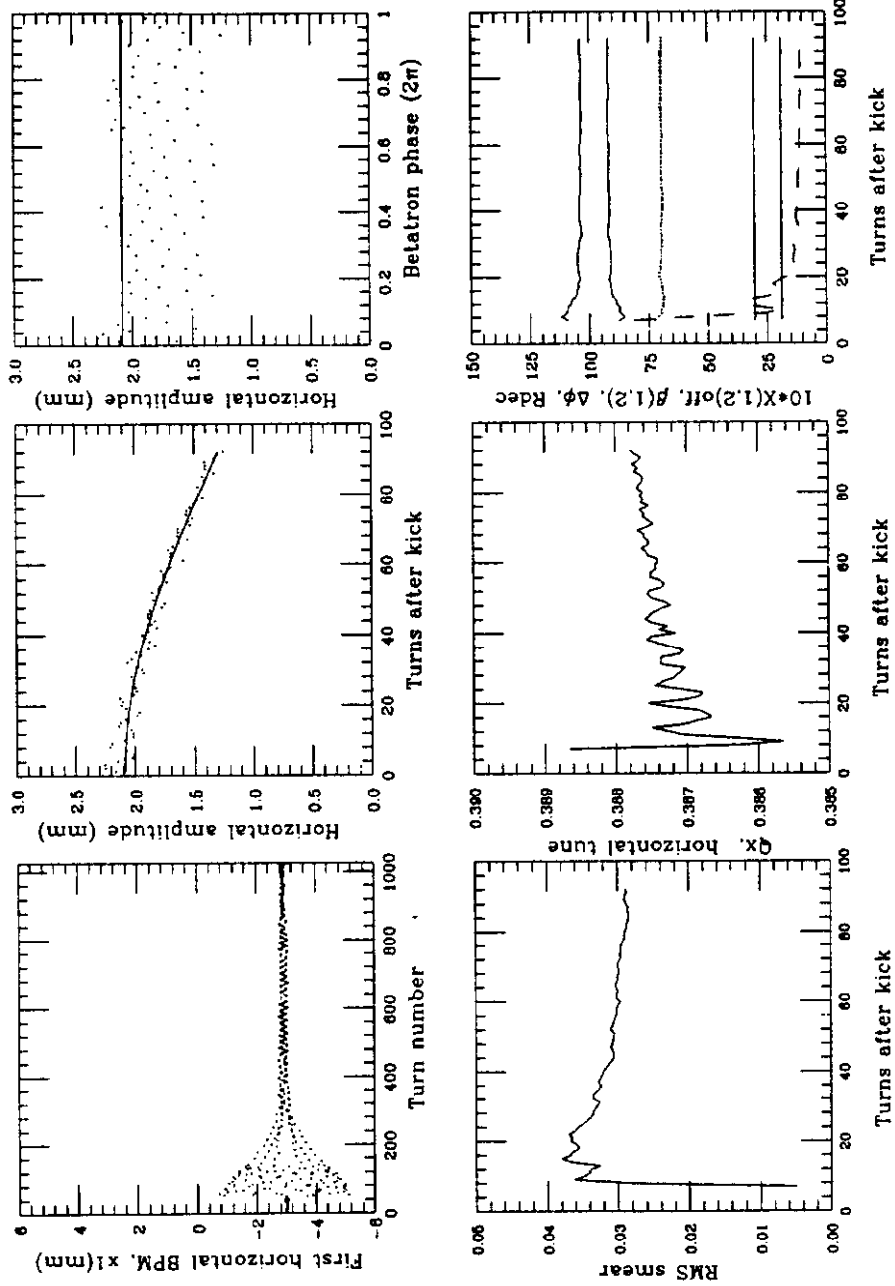


Figure 4.18: Typical graphical output of TEVEX for analysis performed at level 3.

first plot of these 6-plot graphs displays the first horizontal BPM recordings, x_1 as a function of the turn number. The amplitude as a function of turn number is plotted on the second graph. The amplitude as a function of the phase advance (expressed in units of 2π) is next on the third plot. It is essentially an action-angle representation of the data. The lower left and middle plots display the smear and tune respectively as functions of the number of turns used for their calculations. Finally the fitting parameters, x_{1off} , x_{2off} , β_1 , β_2 , ϕ_{cell} and decoherence rate R , are plotted against turn number on the sixth graph.

If the second option was chosen, then a number of different graphs are created. For the same data used above, analyzed at the third level, the following graphical output option is presented: Beam current versus time, horizontal discrete Fourier transform, horizontal phase versus turn number, horizontal slow phase versus turn number, horizontal displacement from the second BPM, x_2 , versus turn number, and x_1 versus x_2 . It was mentioned before that TEVEX is a two-degree-of-freedom code; as such, capability exists for graphical representation of the same quantities as above but on the vertical plane.

Results

The results of the three-fold study described above—experiment, tracking calculations and analytical calculations—are presented here.

In Fig. 4.19 smear is plotted against the sextupole excitation expressed in amperes, for five different tune values (19.38 to 19.42). The three curves in each of the five plots correspond to the three different kicker strengths. The dashed lines represent prediction from tracking calculations while the solid lines correspond to the experimental data. All these data were taken with a low emittance beam (emittance ranged from 1.5π to 3.7π). The agreement between experimental and tracking results is very good.

Low Emittance ($1.5\pi - 3.7\pi$)

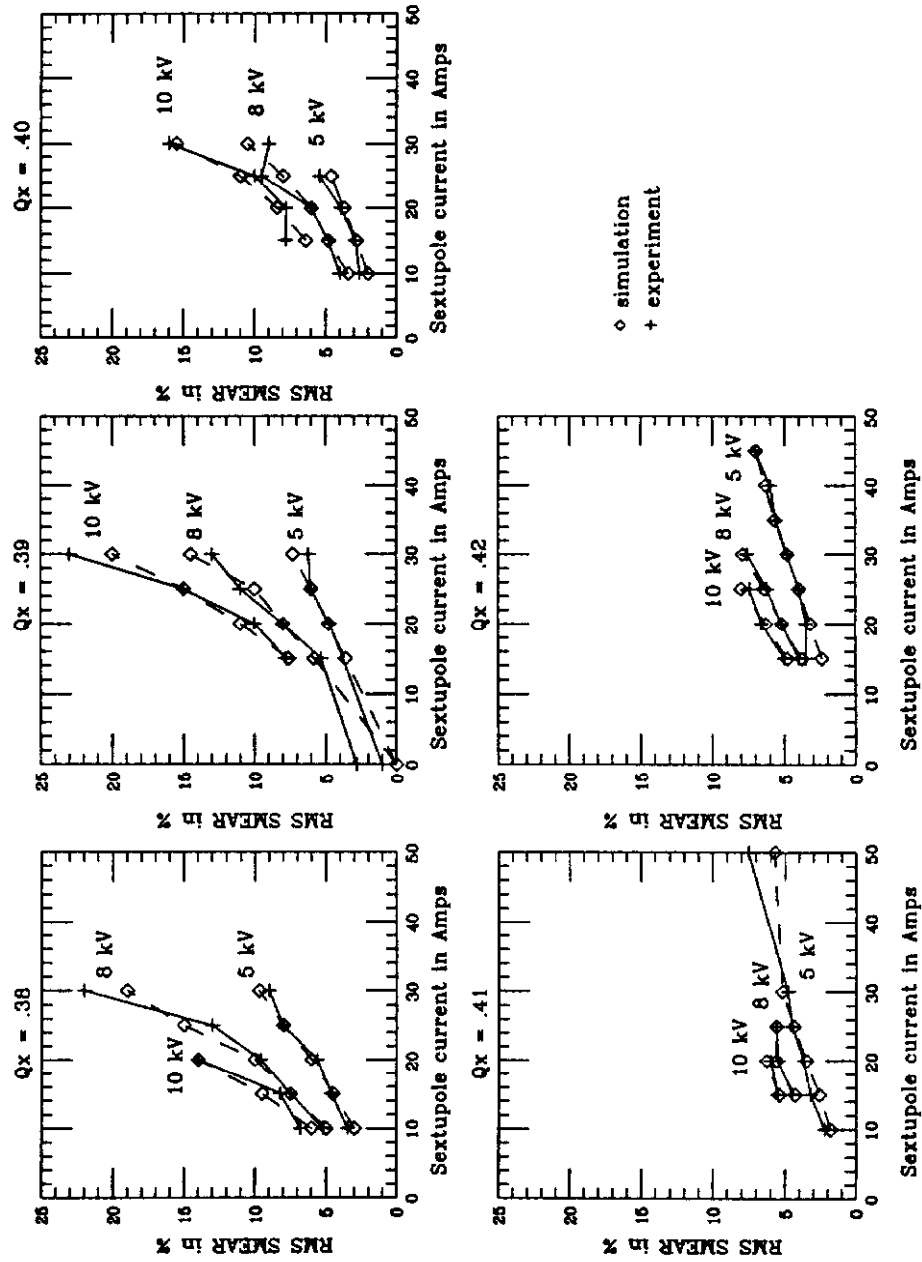


Figure 4.19: Smear versus sextupole excitation, for low emittance data.

Fig. 4.20 illustrates the same quantities as before, the only difference being the beam emittance which ranged from 7.8π to 10.9π here. The agreement between experimental and simulated data is still good, but somewhat worse than for the low emittance beam data. This is due to the fact that higher emittance beam decoheres faster because of the wider spread of amplitudes in phase space. The smear, on the other hand, is extracted before the beam decoheres. Hence for a higher emittance beam the smear has to be extracted from a fewer number of turns which is frequently not adequate for an accurate determination of its value.

A comparison between the predictions of perturbation theory —the smear has been calculated using the previously derived formulæ (4.6) and (4.11), (4.12)— and experimental data for a low emittance beam is in Fig. 4.21. Again the three different curves in each of the five plots correspond to 5, 8 and 10 kV of the kicker strength. Notice that even though the agreement is very good for low current - low kicker amplitude data points, the agreement deteriorates as one moves to higher currents and kick amplitudes. Obviously perturbation theory does not faithfully describe the situation in these regime of the data. The nonlinearities are too strong to be handled perturbatively. On the other hand, one could argue that the disagreement is due to the fact that the perturbative calculations stopped at first order in the sextupole strength. Perhaps the agreement would be better had they been continued to second order. Similar remarks can be made for Fig. 4.22 which compares perturbation and tracking calculations. Also notice that in the perturbative calculations, the smear varies linearly with the sextupole strength as expected from Eqs (4.6) and (4.10).

The smear as a function of the kicker strength expressed in kV, is plotted for various conditions and for low and high emittance beam in Fig. 4.23 and Fig. 4.24 respectively. The previous comments can presumably explain any disagreement between simulated and experimental data. The most noticeable feature of these plots is the linearity of the smear as a function of the kick amplitude, in agreement with

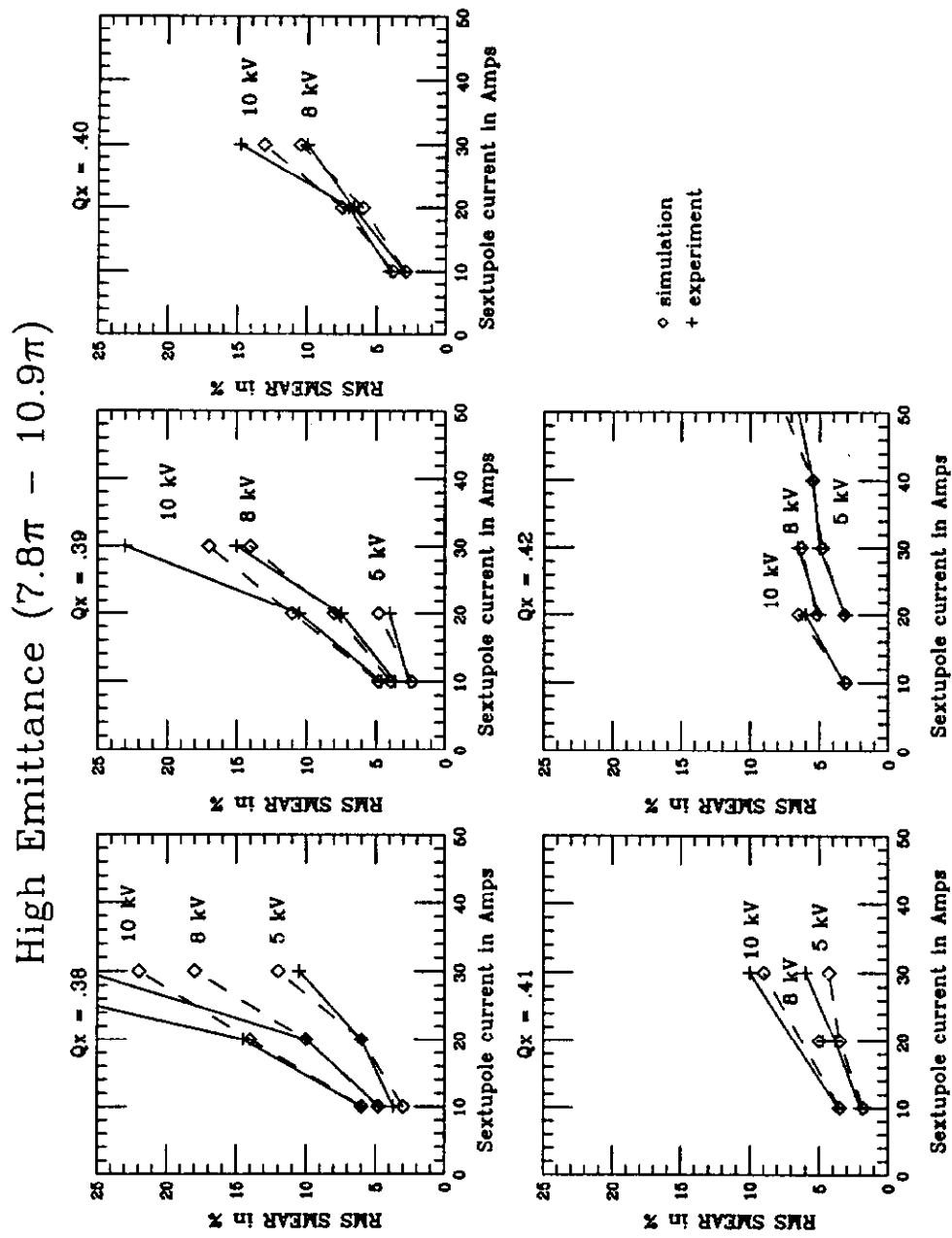


Figure 4.20: Smear versus sextupole excitation for high emittance data.

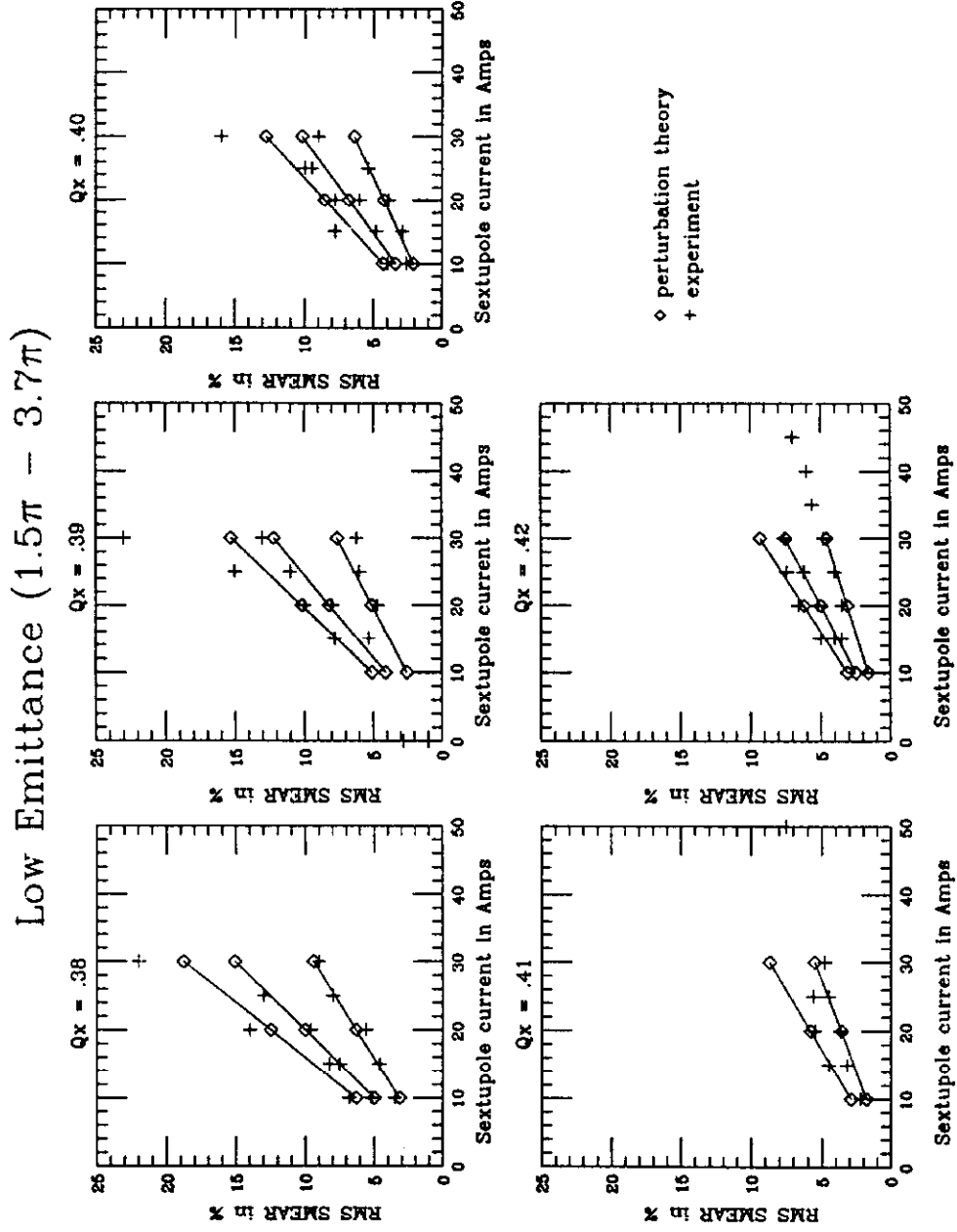


Figure 4.21: Smear versus sextupole excitation; comparison between predictions of perturbation theory and experimental data.

Single Particle Smear

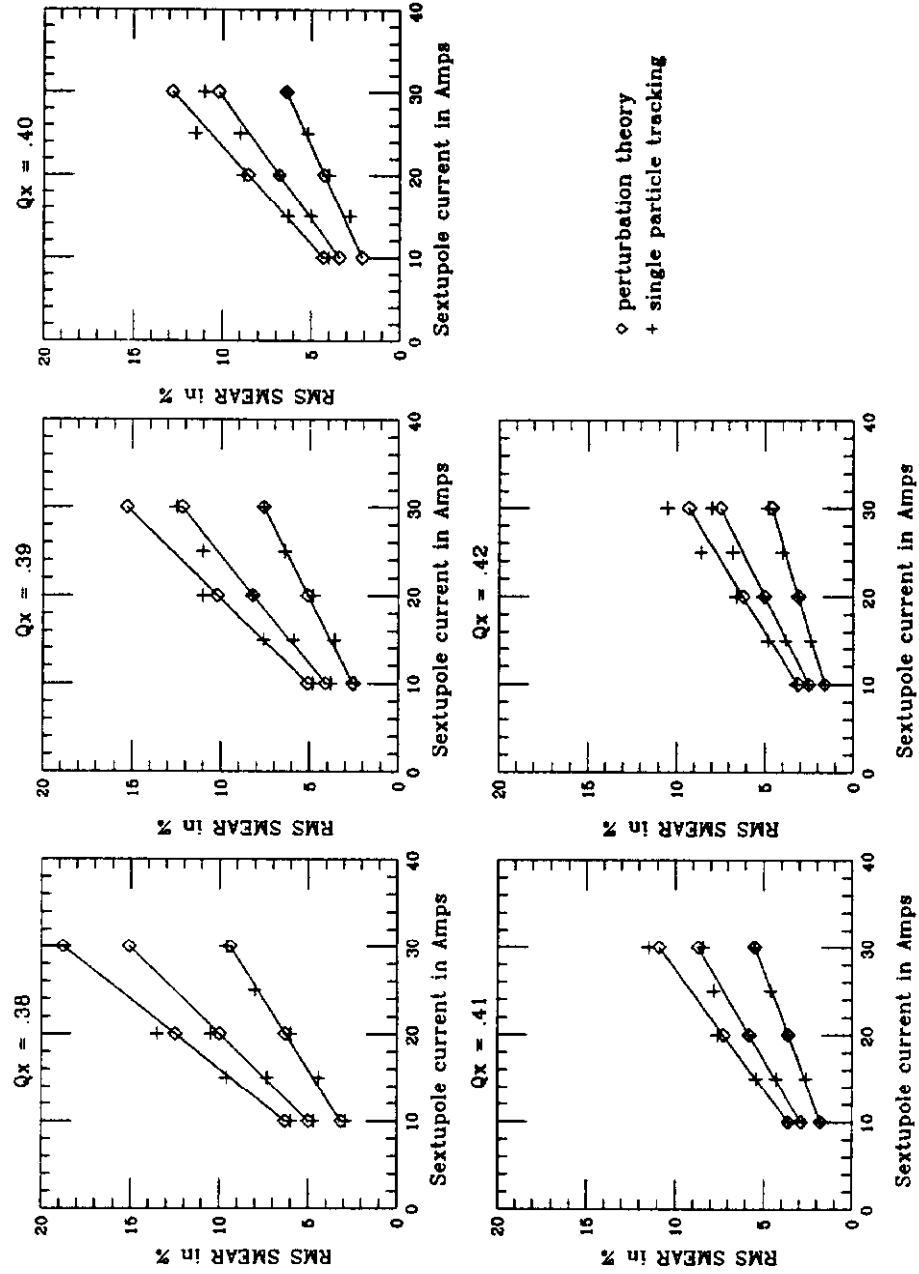


Figure 4.22: Smear versus sextupole excitation; comparison between predictions from perturbation theory and tracking calculations.

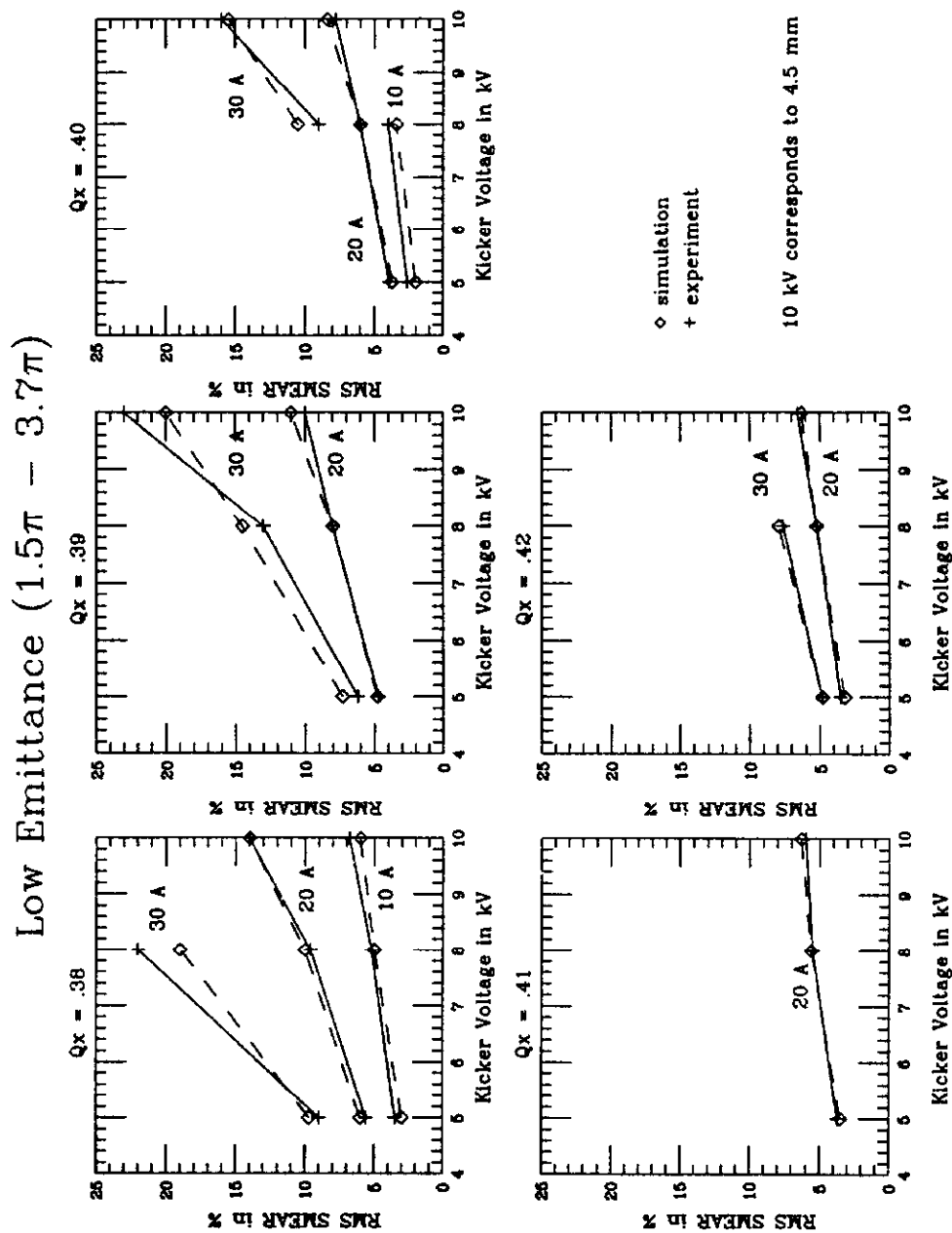


Figure 4.23: Smear versus kicker strength for low emittance data.

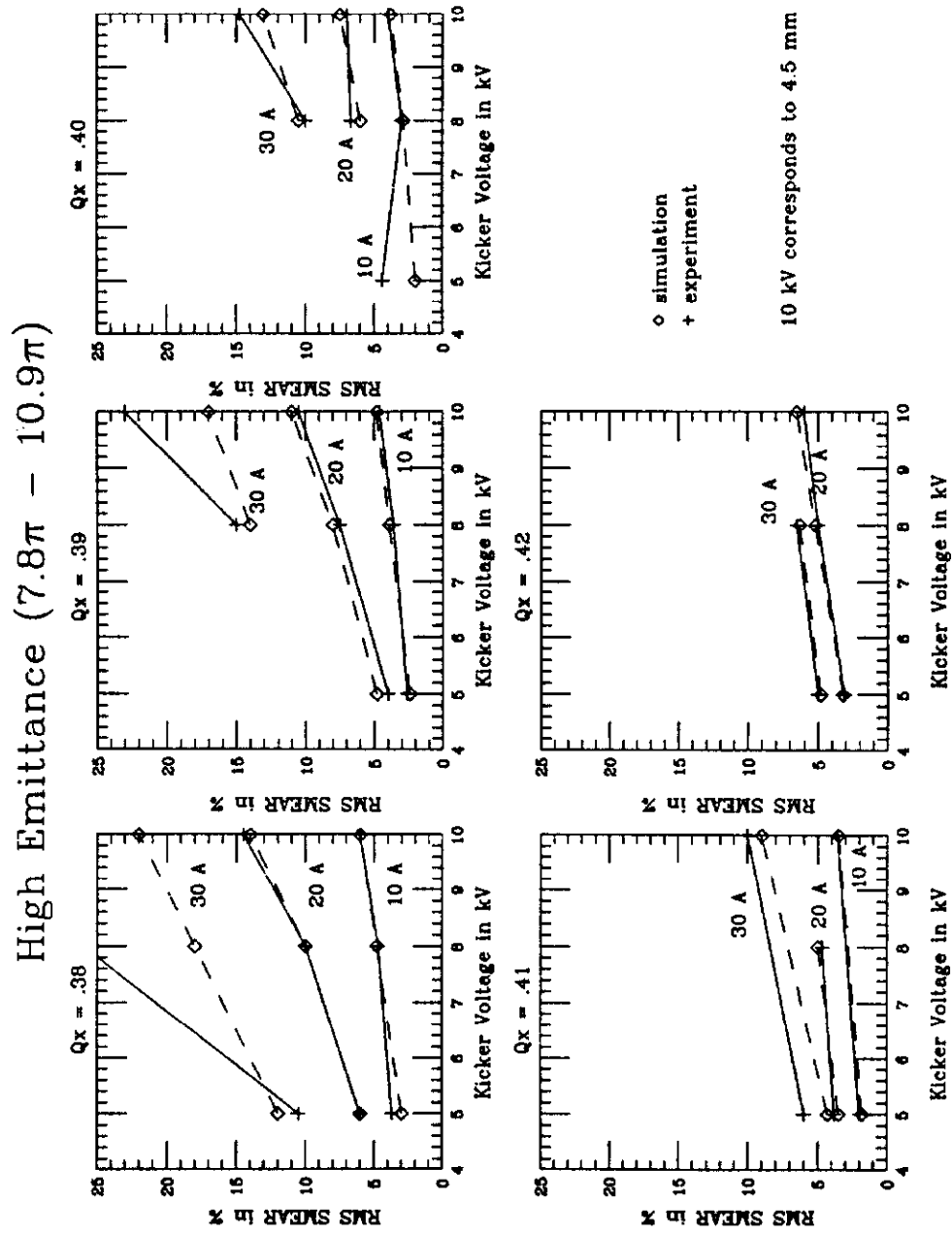


Figure 4.24: Smear versus kicker strength for high emittance data.

the analytical formula.

Results on the ability to predict the decoherence time are presented next. Fig. 4.25 and Fig. 4.26 illustrate the decoherence time as function of the sextupole excitation for experimental (data points) and simulated (solid curves) data, for various values of the tune, kicker strength of 5 kV, and low and high emittance respectively. The decoherence time is measured in number of turns. Figs 4.27 and 4.28 display the same quantities but at 8 kV kicker strength and finally Figs 4.29 and 4.30 are the 10 kV analogues. There are two major points of observation in these three sets of data. The first is that the disagreement between tracking calculations and experimental data is bigger for the low kick amplitude than for the 8 and 10 kV cases. The second point is related to the consistently observed disagreement between tracking calculations and observation at low sextupole excitation (10 amperes). The conjecture is that both points can be explained as follows. There exist residual nonlinearities in the Tevatron (chromaticity-correction sextupoles) which have not been taken into account in the simulation. These nonlinearities have a relatively stronger effect when they are superimposed on relatively weak controlled nonlinearities (low current). The effect is negligible when compared to a highly nonlinear situation. Moreover the decoherence time extracted from the experimental data is shorter than that from simulation as expected according to this argument.

Table 4.3 displays the tuneshift as calculated using Eq. (4.13) and as extracted from the curves of Fig. 4.6 for a 5 kV kick. The agreement is remarkably good. The dependence of the tune on the amplitude is checked for the experimental data, in Fig. 4.31. The tune offset is plotted against the strength of the kicker magnet, expressed in kV. The smooth curve, an extrapolation into the origin assuming the theoretically predicted curvature, agrees with the differently measured zero amplitude value, whose error bar is an estimate of the relative uncertainty of the two methods.

A strong deflection of the beam, in the presence of strong nonlinearities, can place

Low Emittance ($1.5\pi - 3.7\pi$) - 5 kV

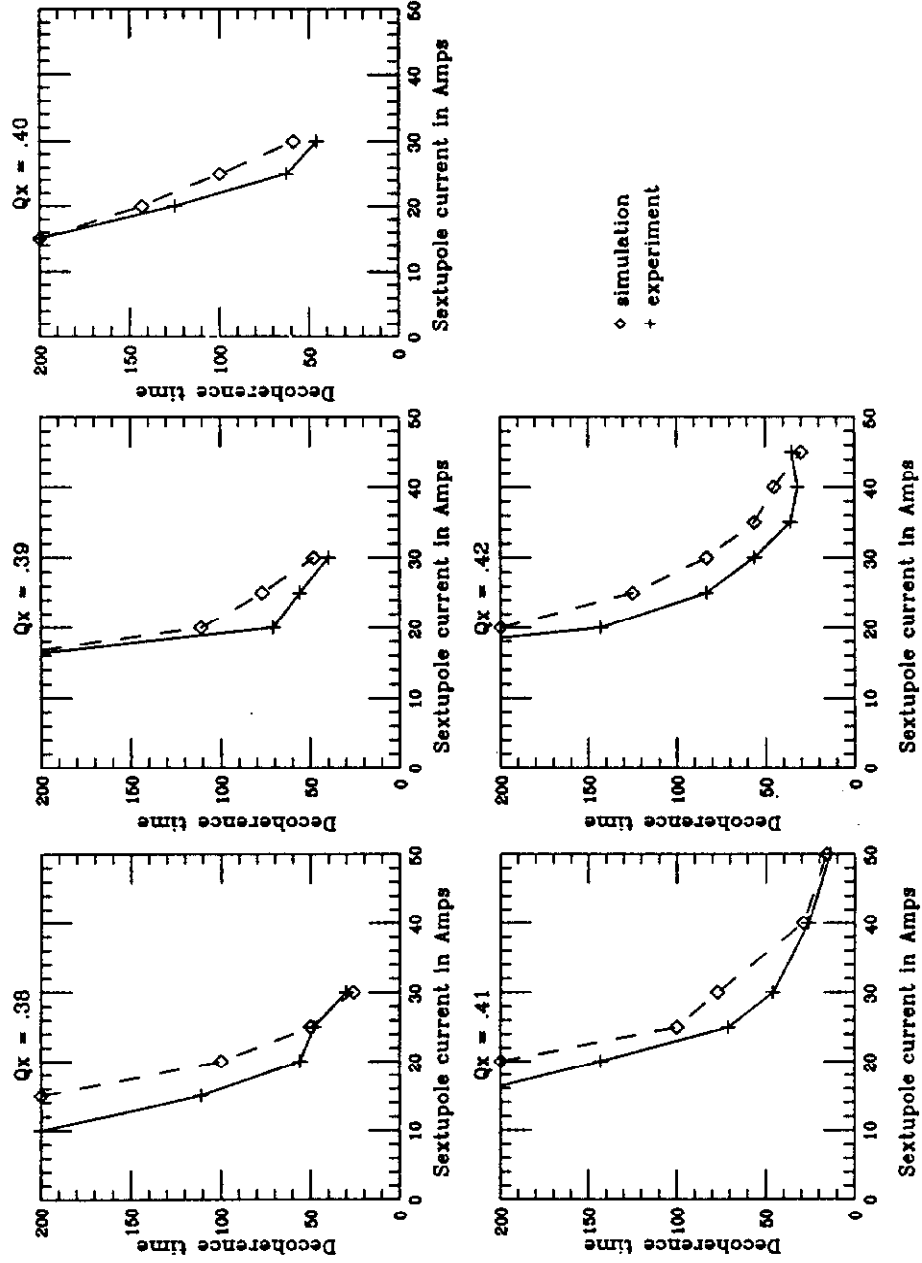


Figure 4.25: Decoherence time versus sextupole strength for low emittance and a kick of 5kV.

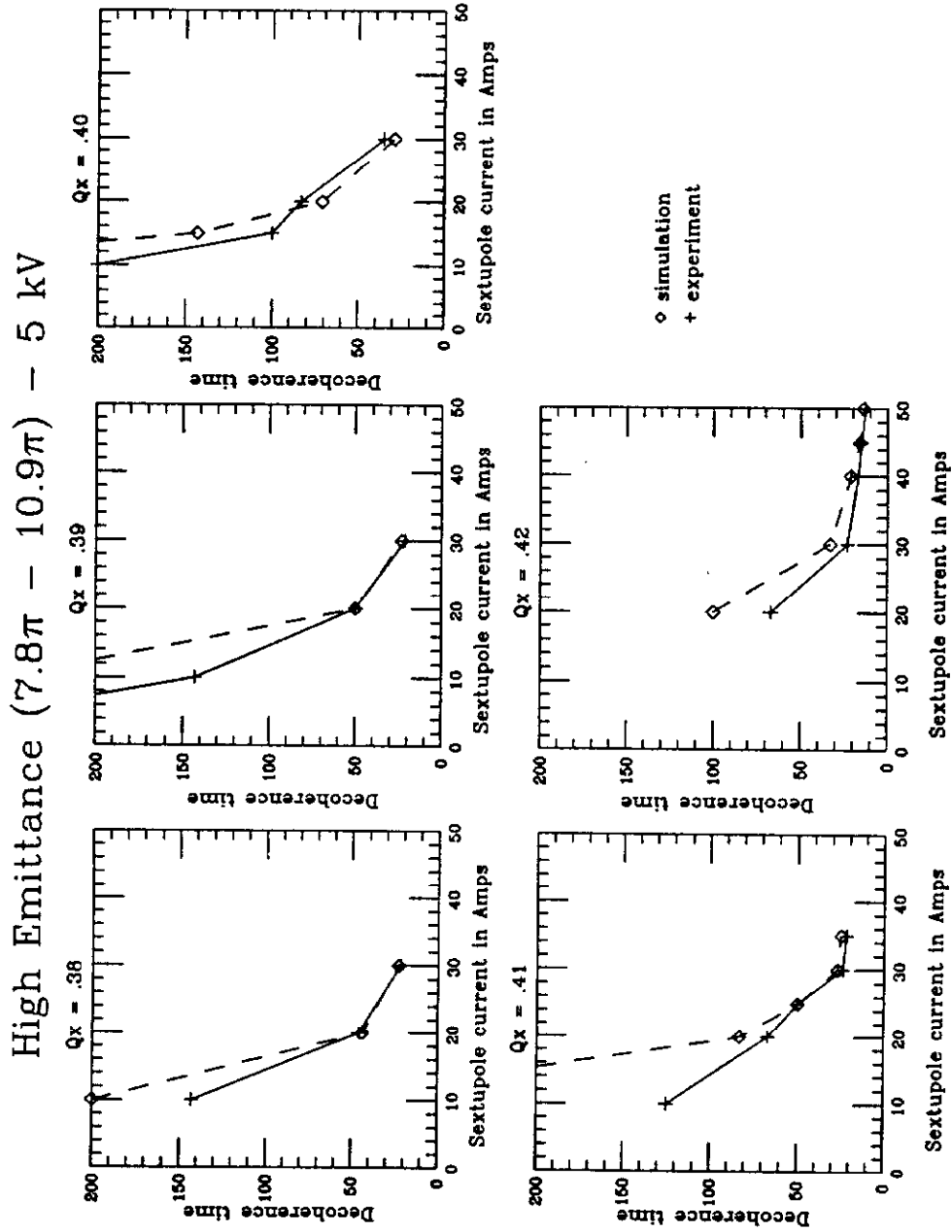


Figure 4.26: Decoherence time versus sextupole strength, high emittance, 5kV kick.

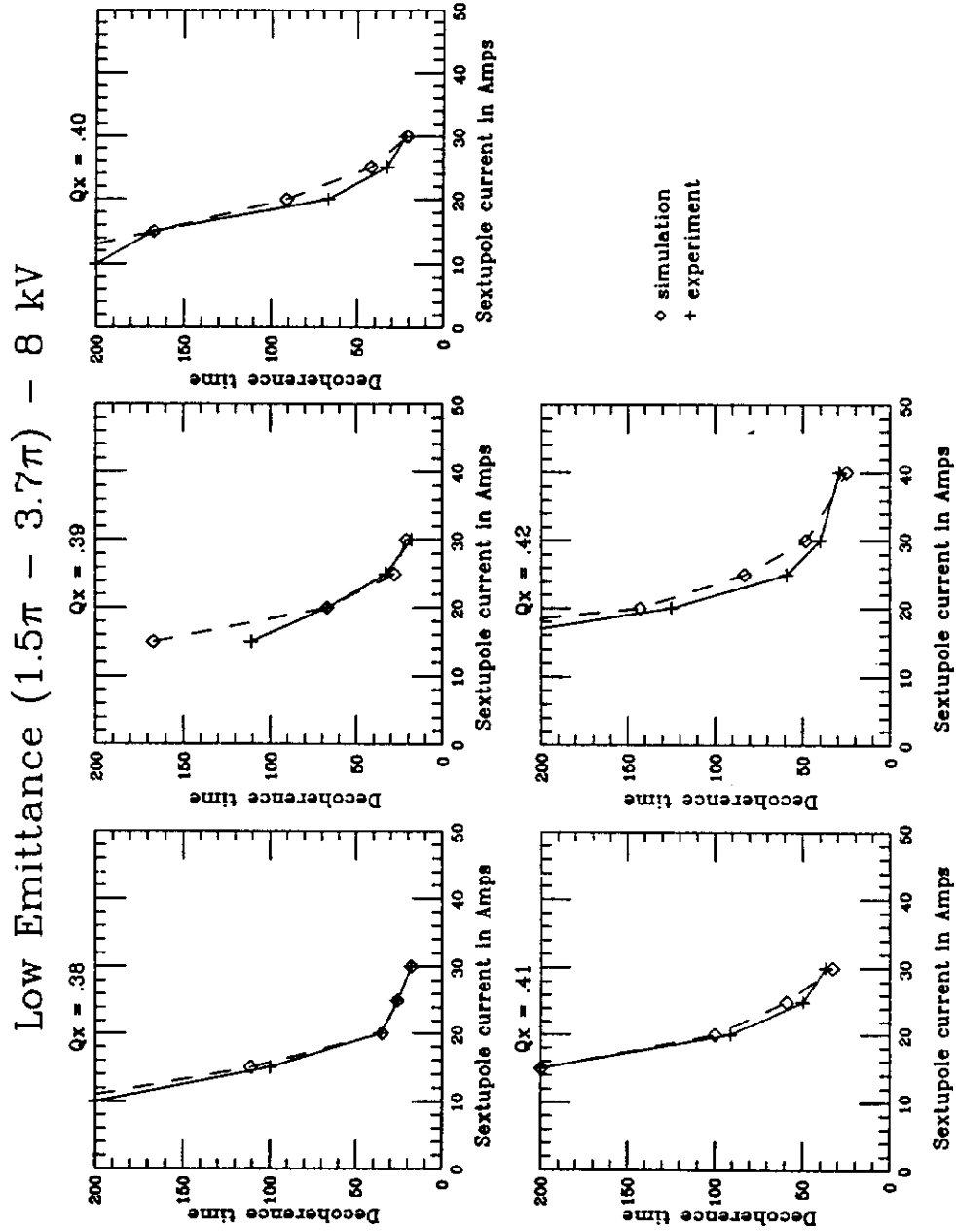


Figure 4.27: Decoherence time versus sextupole strength, low emittance, 8 kV kick.

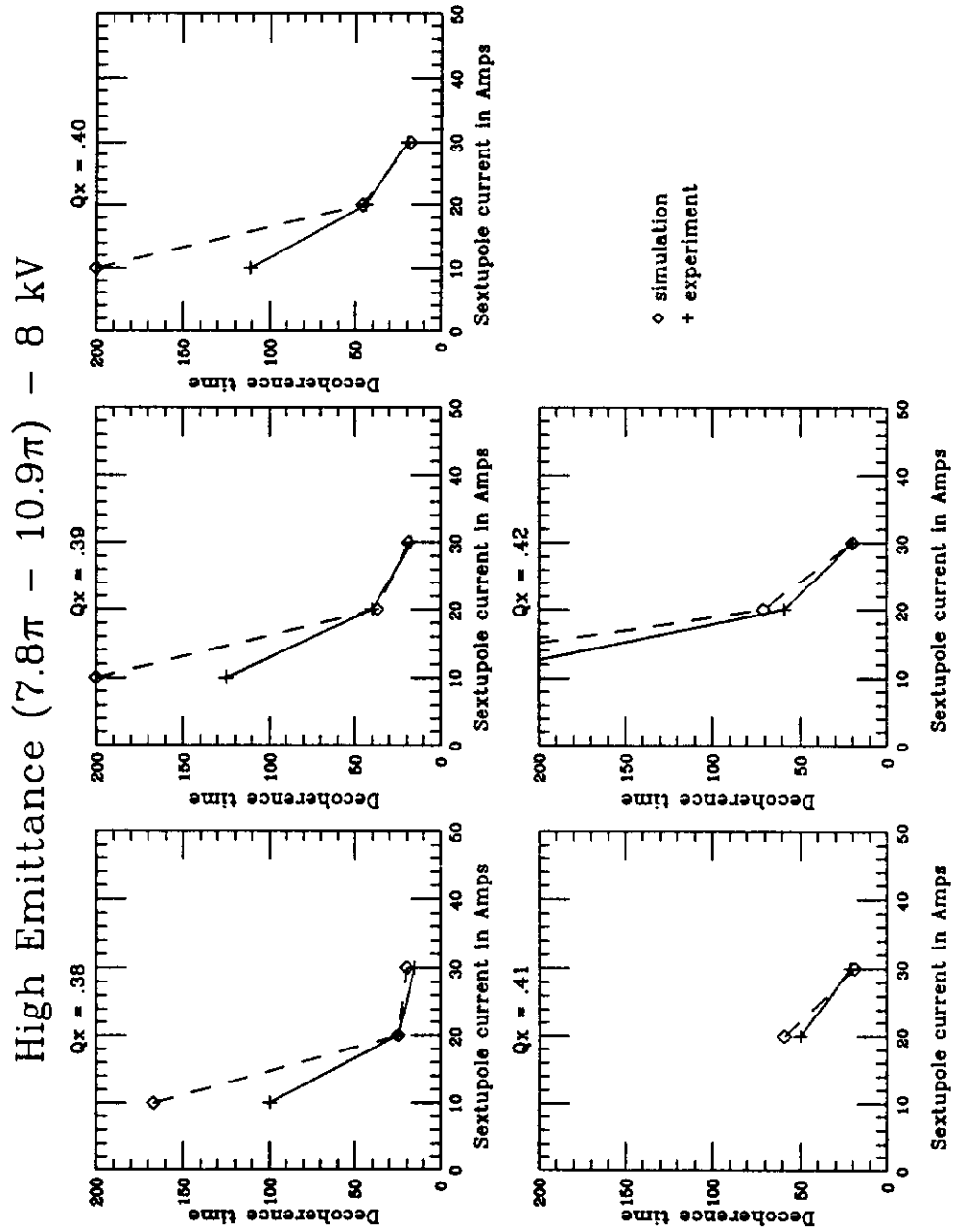


Figure 4.28: Decoherence time versus sextupole strength, high emittance, 8 kV

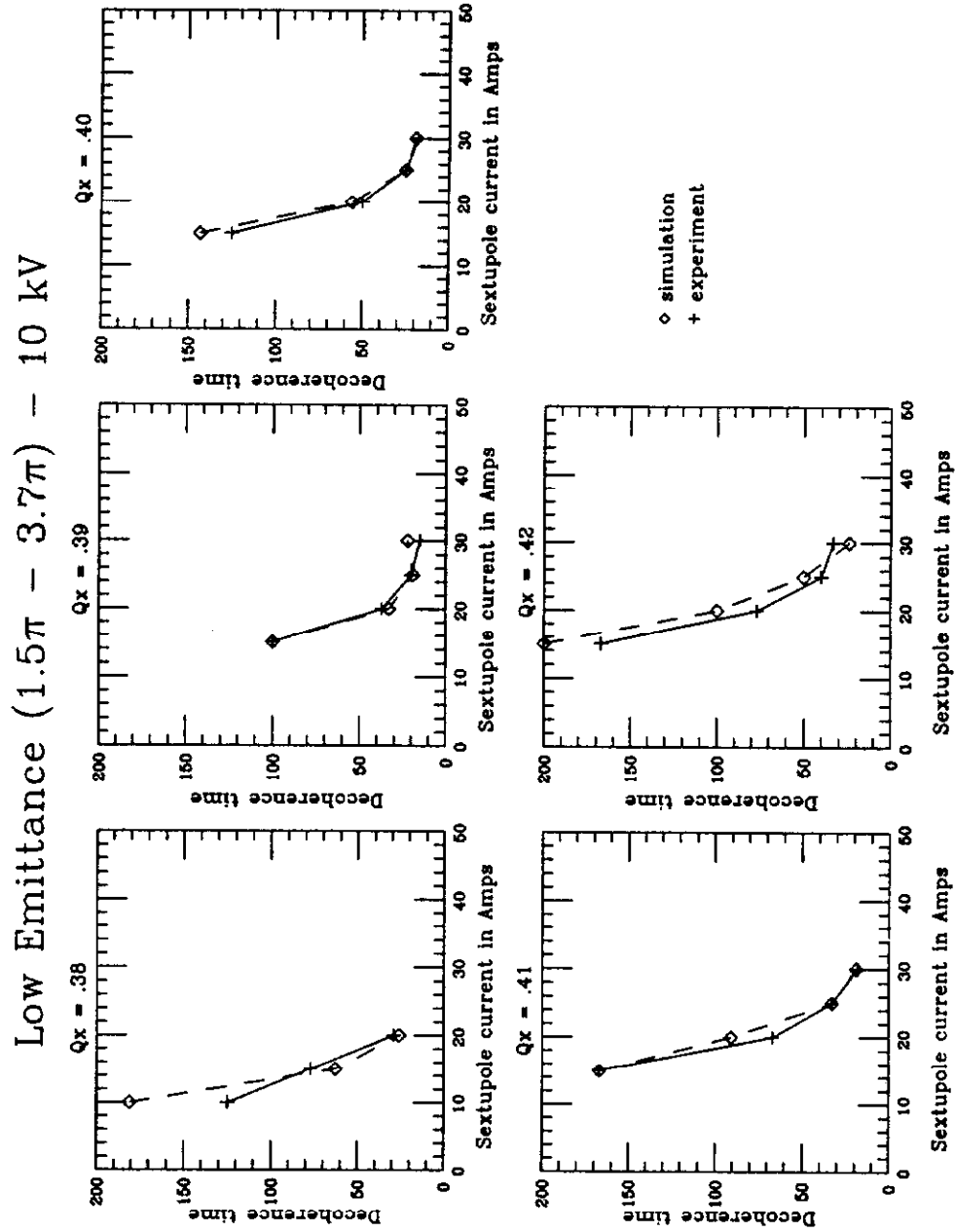


Figure 4.29: Decoherence time versus sextupole strength, low emittance, 10 kV

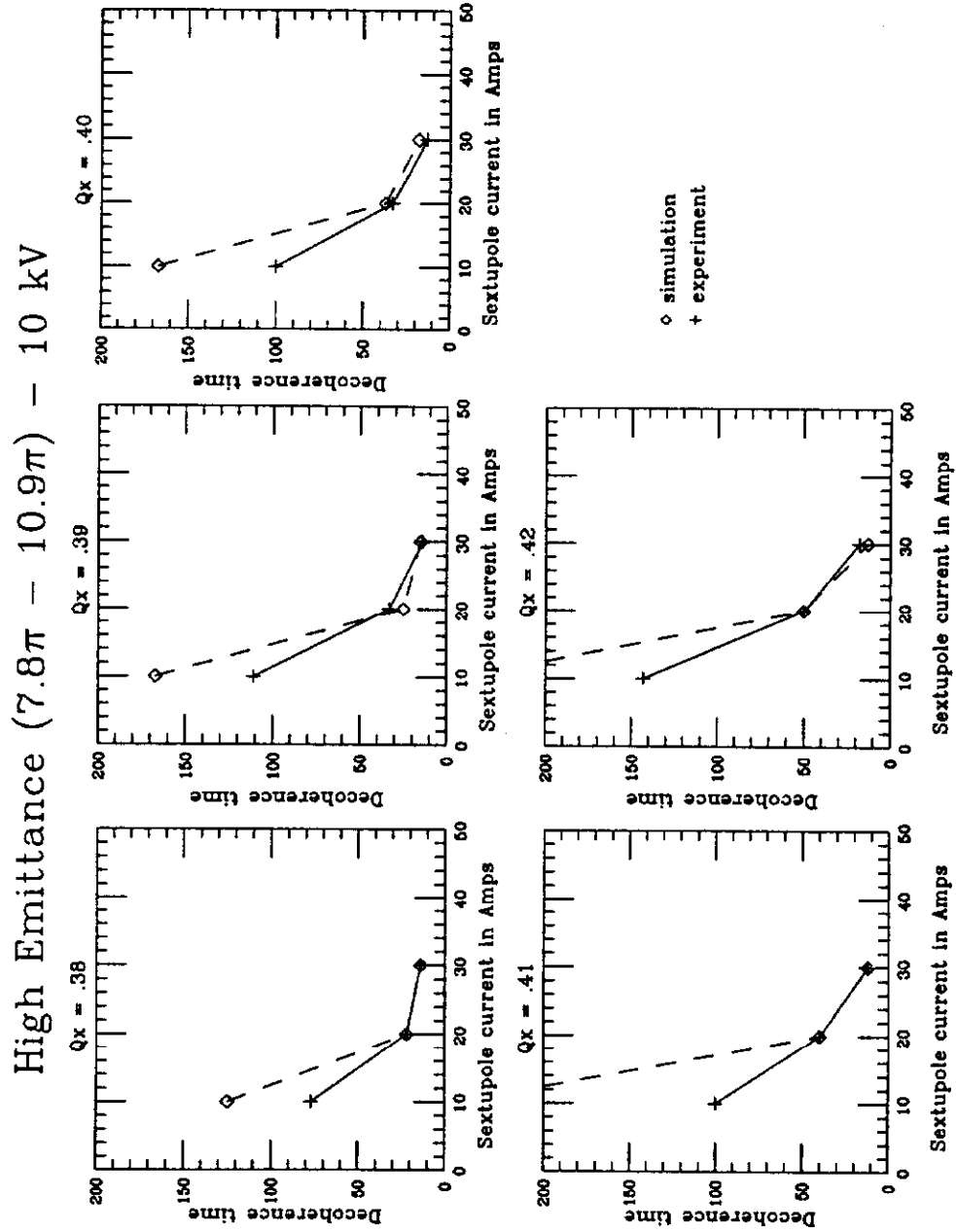


Figure 4.30: Decoherence time versus sextupole strength, high emittance, 10 kV

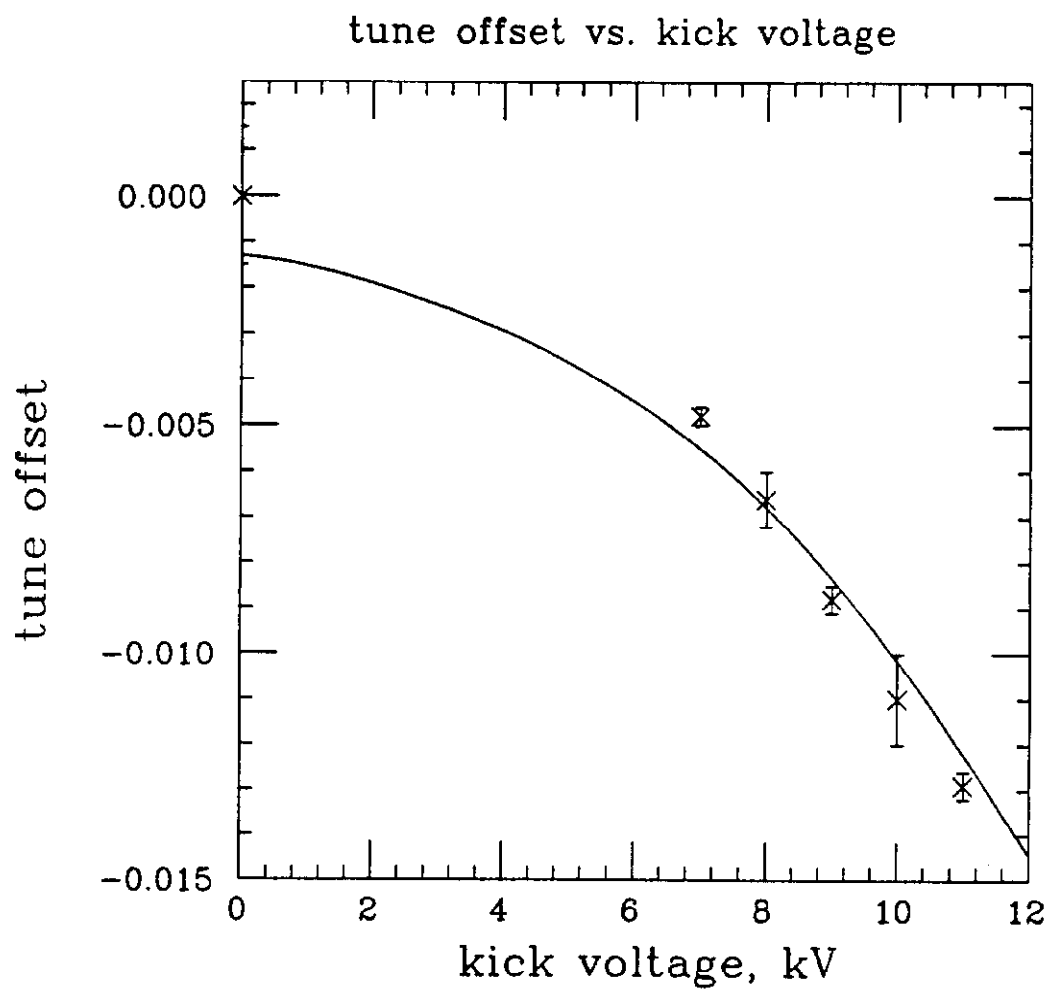


Figure 4.31: Experimental data illustrating the dependence of tune on the amplitude. The smooth curve is a fit to the data.

Sext Strength (Amps)	$\Delta\nu$	
	Perturbation	Single particle tracking
10	5.098×10^{-4}	.00050
20	2.039×10^{-3}	.0020
30	4.588×10^{-3}	.0050

Table 4.3: Amplitude-dependent tuneshift as calculated from perturbation theory and from single particle tracking. The agreement between the two methods of calculation is remarkably good.

the beam outside the stable region limited by the ‘separatrix’. Hence, even though most of the beam is kicked inside the dynamic aperture when the sextupole excitation is 30 amperes at a tune of 19.39 and a kick of 5 kV, the opposite is true for the same conditions but a kick of 10 kV as Fig. 4.32 illustrates. It is shown later (Chapter VII) that the stable area decreases with the increase of the magnitude of nonlinearities. Particles kicked outside the separatrix will eventually get lost. Furthermore, the fraction of the beam which survives for each set of accelerator conditions is of importance, especially in explaining certain discrepancies between calculations and observations. Hence it is of interest to calculate the fraction of surviving beam after the kick, for a variety of conditions and compare it with the recordings of the Tevatron intensity monitor I.45. The results are displayed in Fig. 4.33. The two different symbols employed for the experimental data distinguish between more and less reliable measurements. The source of this uncertainty is related to the calibration of the intensity monitor signals [44]. General agreement between simulation and observation has been established.

Before this chapter is concluded, I would like to stress the success of tracking calculations in predicting the values of the smear and the tune in the near-linear region of the phase space. This conclusion enhances the confidence in nonlinear

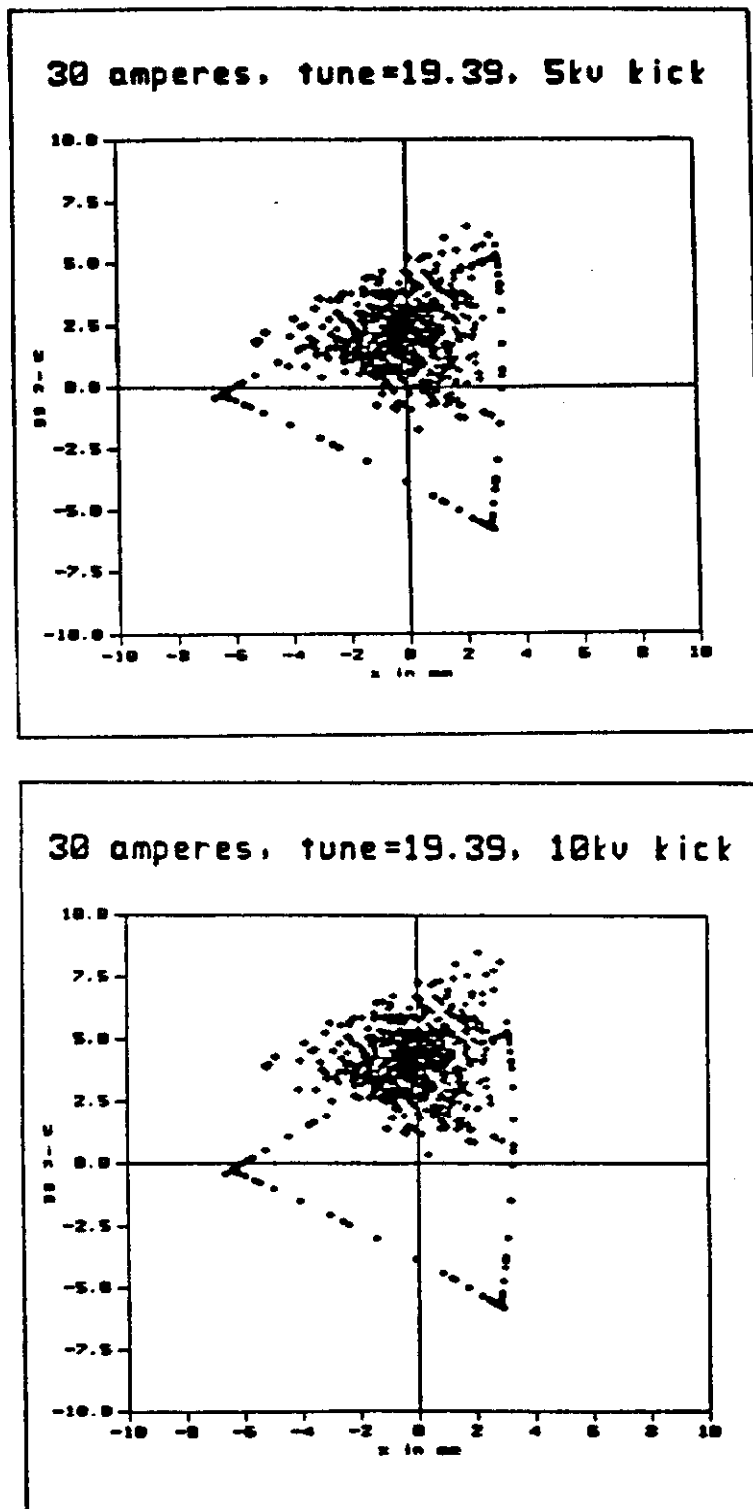


Figure 4.32: Simulation of two experimental conditions in phase space at kicker location immediately after beam deflection. The dotted line represents the limit of stability. The dots represent the particle distribution.

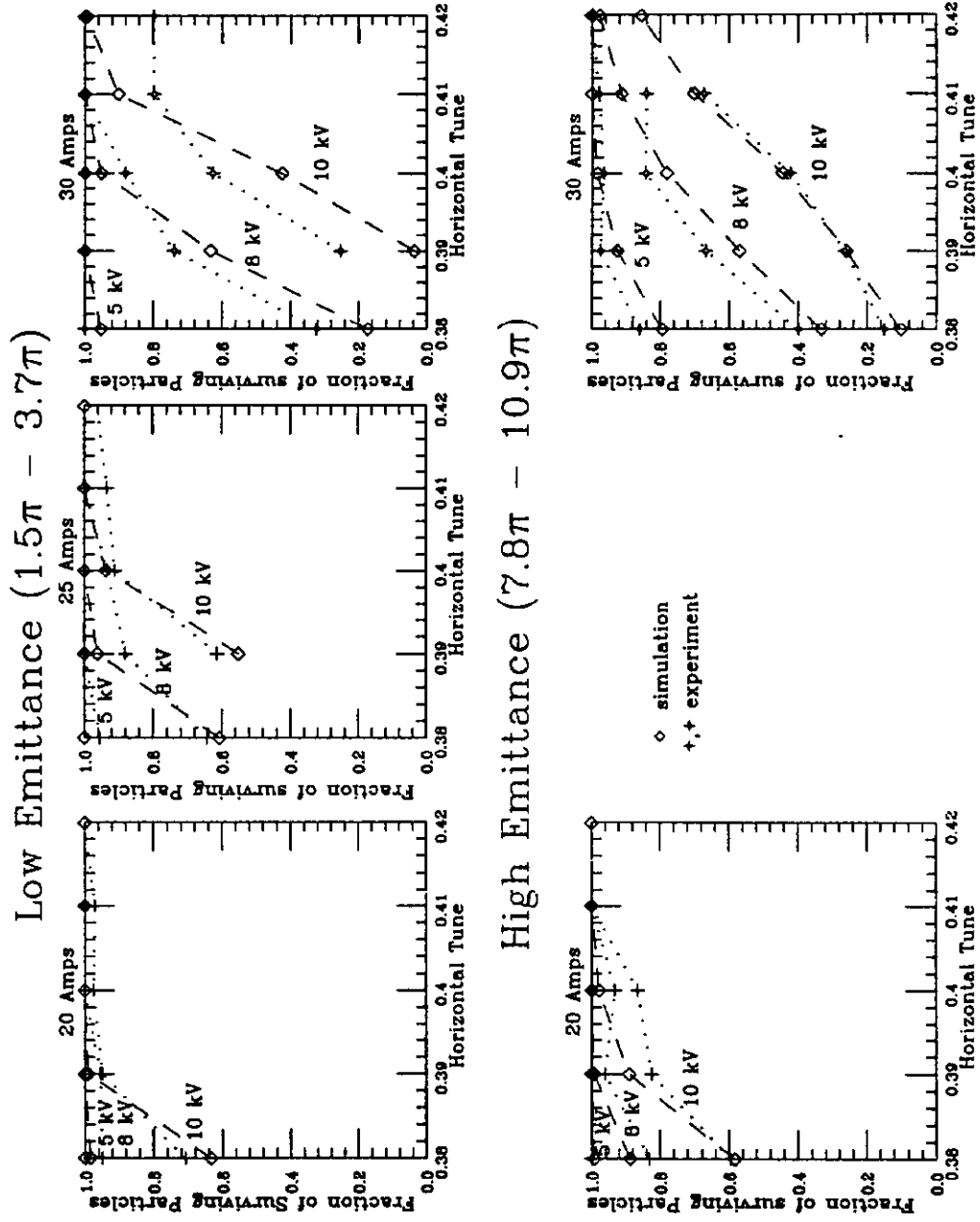


Figure 4.33: Fraction of surviving particles as a function of the horizontal tune.

tracking calculations in predicting the performance of future accelerators. It is also important to notice that one can rely on perturbation theory to describe the motion in this particular region (for small amplitudes); a technique which saves computing time and allows for more generality.

CHAPTER V

THE INJECTION EXPERIMENT

The Experiment

This experiment addresses the question of correlating the smear with routine accelerator performance such as injection efficiency and particle lifetime. The experimental technique used involved setting up the Tevatron with the sixteen strong sextupoles powered to excitations of 0, 15, 30, 40, 45 and 50 amperes. Beam was then injected both onto the closed orbit and off the closed orbit by 1.5 mm. The injection of the beam with a steering error was produced by a deflection kicker. The magnitude of the kick was 4 kV. Fig. 5.1(a) displays first-turn data at a horizontal tune of 19.42 and 0 sextupole excitation, while the beam was matched onto the closed orbit. Fig. 5.1(b) shows again first-turn data taken under the same accelerator conditions, except that a steering error was introduced. In Fig. 5.1(c) the difference of these two orbits is displayed, which is an oscillation with amplitude of 1.5 mm.

At each sextupole setting the orbit was smoothed and the tune adjusted to the desired value. The experiment was performed at tunes of 19.38 and 19.42. The recorded data include

1. First-turn position monitor data
2. Closed orbit data recorded 50 msec after injection

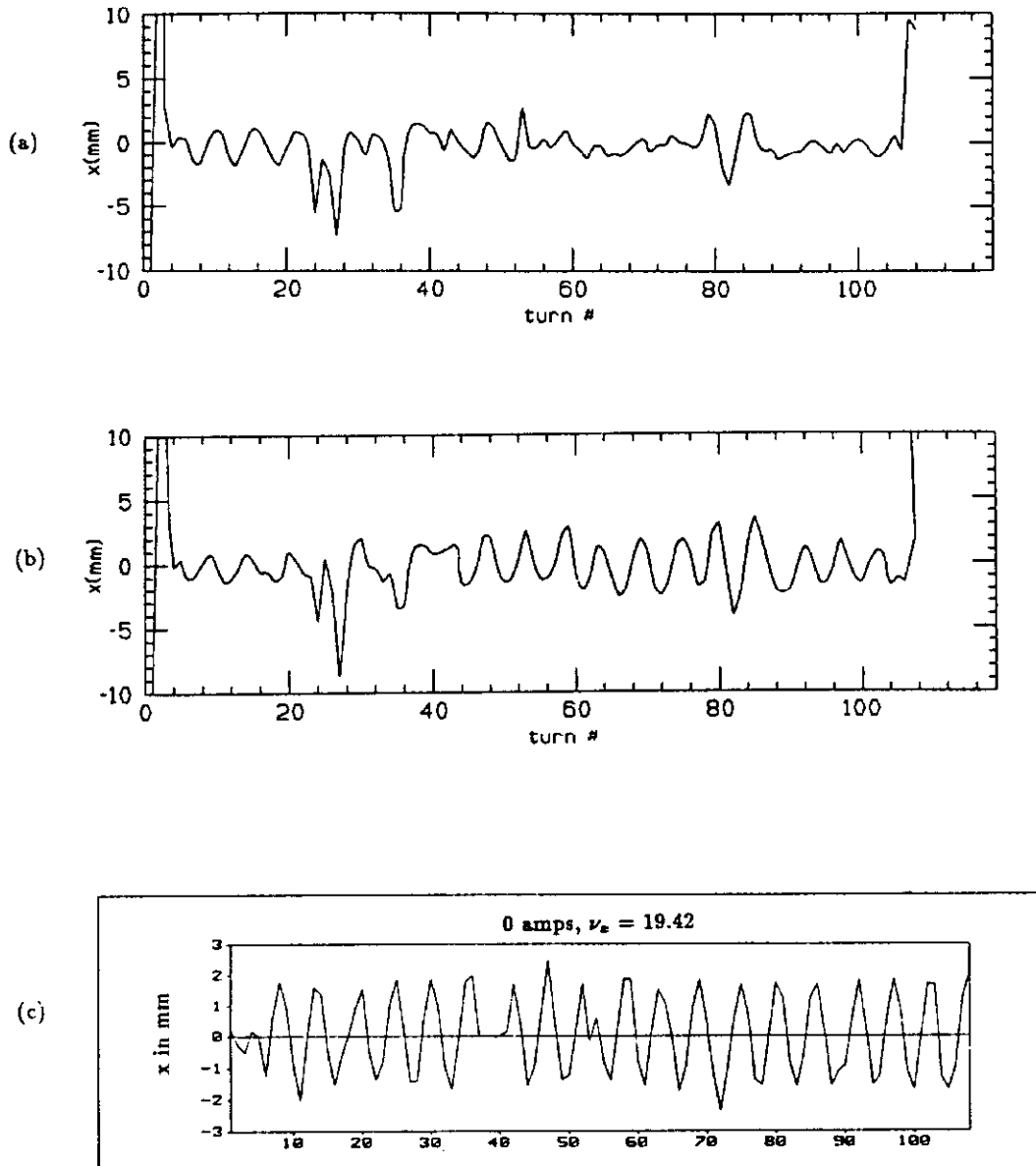


Figure 5.1: First-turn data taken with the sextupoles turned off, (a) without, (b) with a steering error of 4 kV, and (c) their difference.

3. Turn-by-turn data at injection recorded by two BPM's at HE24 and HE26
4. Flying wire data at injection at HC48, HA17 and VC48
5. Flying wire data at the same locations as above, but 9 seconds after injection
6. Beam intensity versus time.

Results

Typical datasets, results of the analysis and their interpretation are presented for each of the six sets of data recorded during the injection experiment.

First-turn position monitor data are studied first. Fig. 5.2 displays the difference between first-turn data taken by injecting the beam on the closed orbit and off of the closed orbit. The sextupole excitation was 45 amperes and the tune 19.42. In order to determine the effect of a strongly nonlinear environment on the first turn after injection, Fig. 5.1(c) and Fig. 5.2 are overlayed. The result is Fig. 5.3. Obviously the first turn orbit changed by less than a millimeter between sextupole strengths of 0 and 45 amperes. The same result holds true for tune of 19.38 and for the other sextupole settings.

Closed orbit data (also called display frame data in the Fermilab jargon) recorded 50 msec after injection onto the closed orbit are shown in Fig. 5.4(a). The tune here was 19.42 and the strong sextupoles were turned off. Fig. 5.4(b) displays closed orbit data taken under the same conditions, but now the beam is injected with a steering error. The difference of the two orbits is plotted in Fig. 5.4(c). It is worth noticing that there is no sign of the steering error at injection on the display frame. The closed orbit is taken late enough (a few hundred turns after injection) for the beam to decohere and average very close to zero.

Fig. 5.4(d) displays a difference of two closed orbits—injected with and without a steering error—in the presence of sextupoles excited at 45 amperes. The tune is

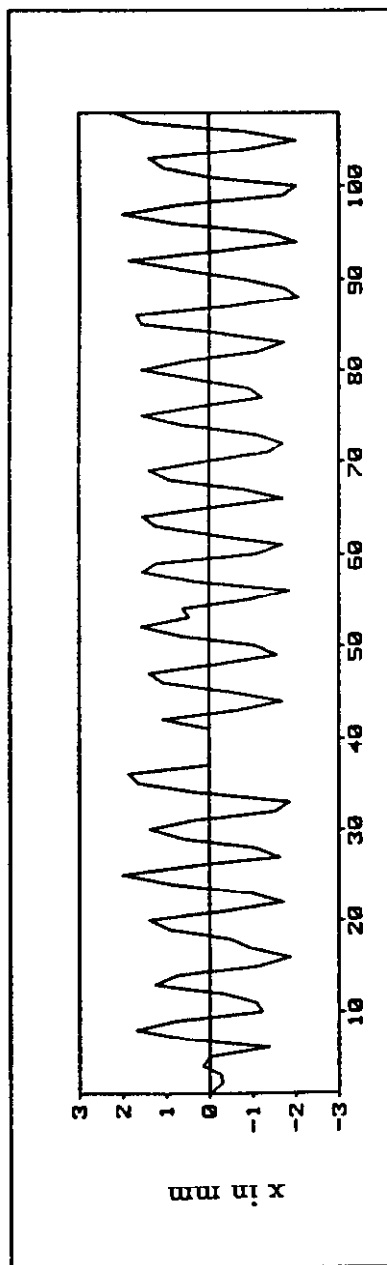


Figure 5.2: Difference between first-turn data taken by injecting the beam on the closed orbit and off the closed orbit. The sextupole excitation is 45 amps.

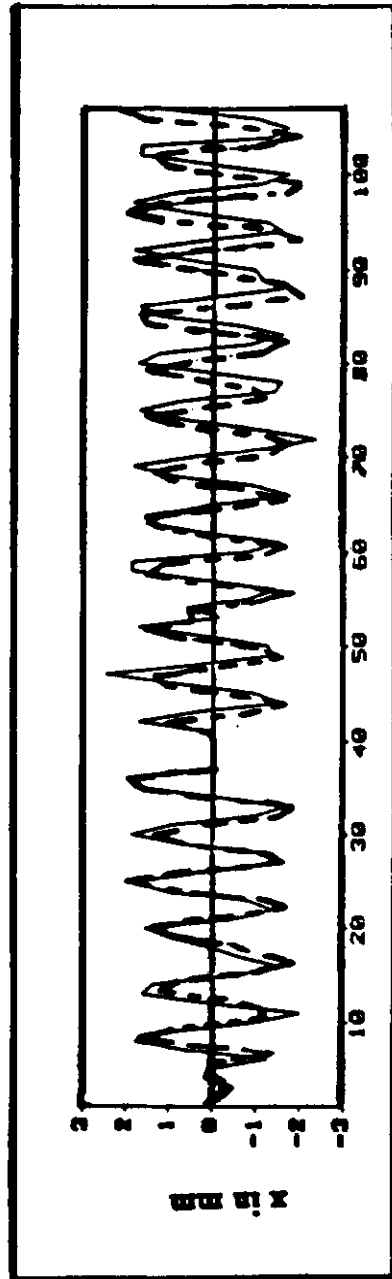


Figure 5.3: Overlay of Fig. 5.1(c) and Fig. 5.2.

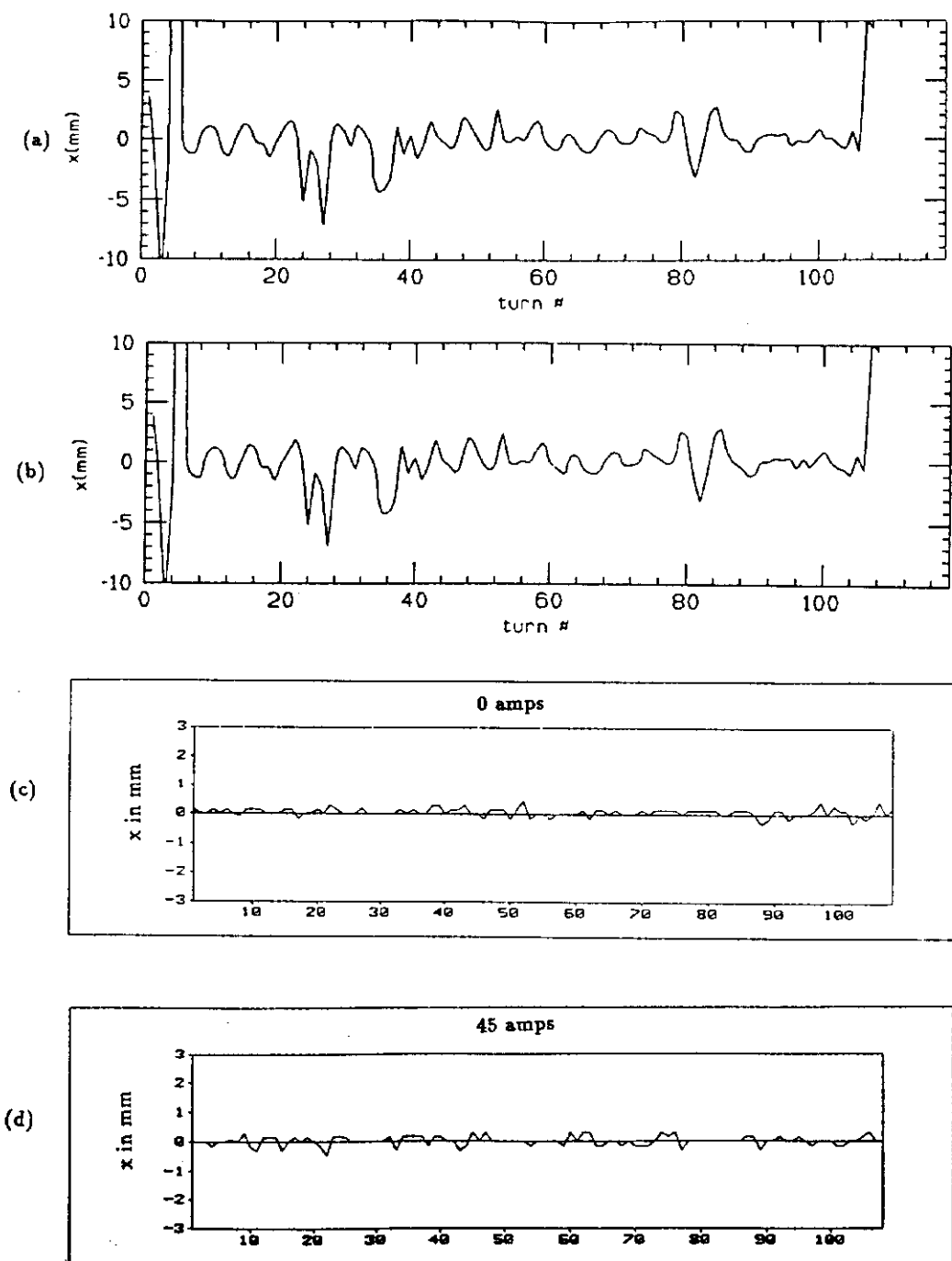


Figure 5.4: Display frame data, at 0 amps and a tune of 19.42, (a) without and (b) with a steering error. The difference is illustrated in (c). Another such difference, with the sextupoles powered to 45 amps is illustrated in (d).

again 19.42. There is practically no difference between Fig. 5.4(c) and Fig. 5.4(d).

Turn-by-turn data at injection were recorded for 1024 turns by two horizontal BPM's at HE24 and HE26. No significant deterioration was observed as the sextupole excitations advanced from 0 to 50 amperes.

Hence the conclusion that can be drawn from the above three items is that injection diagnosis and correction functioned satisfactorily up to the largest sextupole settings for a typical injection offset of 1.5 mm.

The Tevatron flying wires were flown at HC48, VC48 and HA17, .25 seconds after injection and 9 seconds later. All three wire profiles revealed significant beam losses at high sextupole current. An interesting pattern shown in Fig. 5.5 occurred at HC48 and VC48 but not at HA17, namely the 'tails' of the beam profiles. This pattern is present only at the profiles taken at 5.35 seconds and only at high sextupole currents. It is due to DC beam losses occurring at the C48 location. By the time of the second fly—14.35 seconds—the particles outside the RF buckets have been spread completely around the machine leaving no trace on the new profiles.

The last quantity recorded in the injection experiment was the beam intensity as a function of time. Fig. 5.6 is a summary of the observations. The fractional beam loss in the first five seconds after injection is plotted as a function of sextupole excitation. The four curves represent injection onto the closed orbit and injection 1.5 mm off of the closed orbit at two different values of the horizontal tune. In each case, there was apparently a threshold sextupole current above which loss was found. Much of the loss was slow as shown in Fig. 5.7, which is a typical plot of the beam intensity in the Main Ring and Tevatron. Here the sextupole excitation was 45 amperes and the machine tune was 19.42. The transfer of the beam from the Main Ring to the Tevatron took place at 5.1 seconds.

In an attempt to understand this slow loss of particles it was found that the time structure of the early loss, as seen on the scintillation counters associated with the

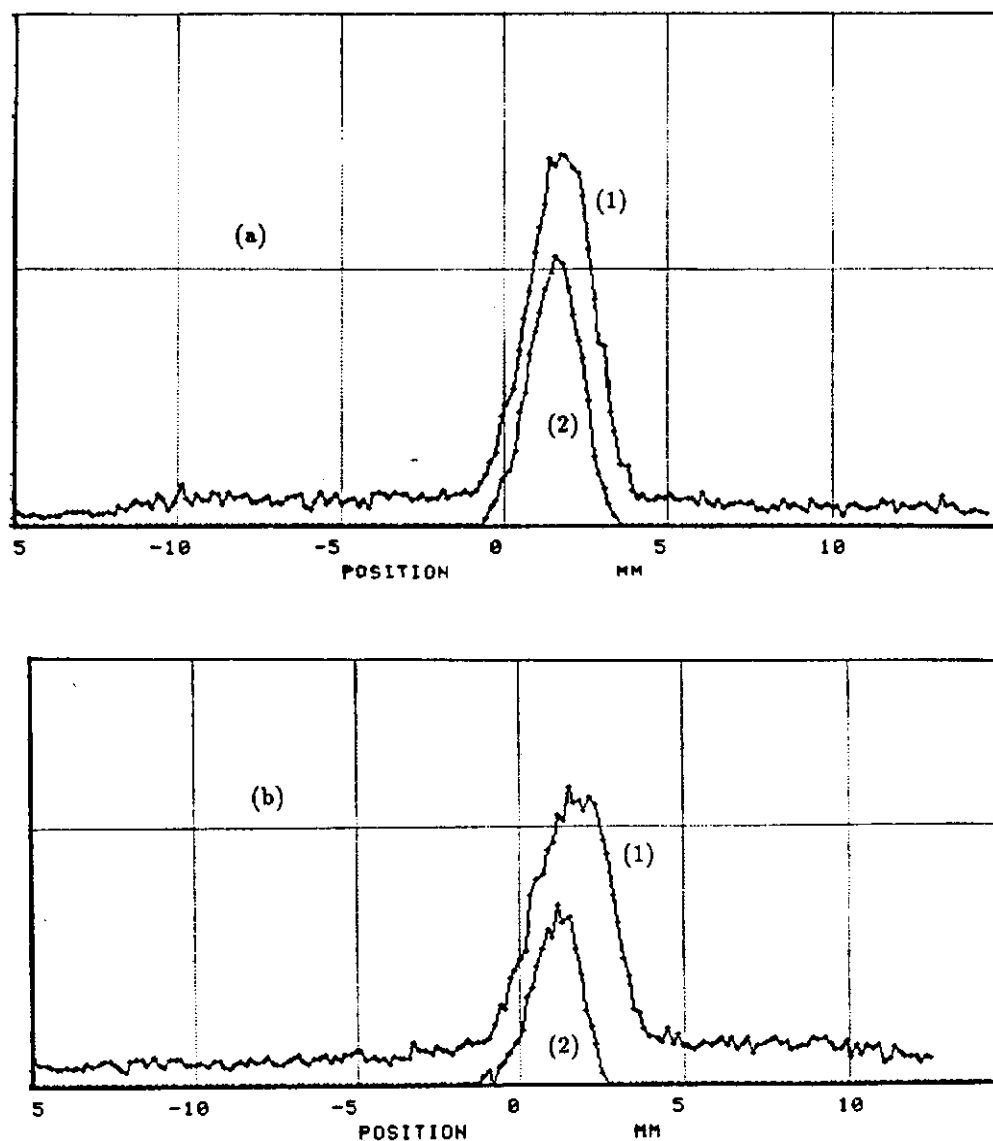


Figure 5.5: Flying wire data from the Tevatron at C48. The sextupole excitation was 45 amps and the tune 19.38. In (a) there was no steering error; in (b) there was a steering error of 4 kV. Profiles (1) were taken .25 secs after injection, and profiles (2) were taken 9 secs later.

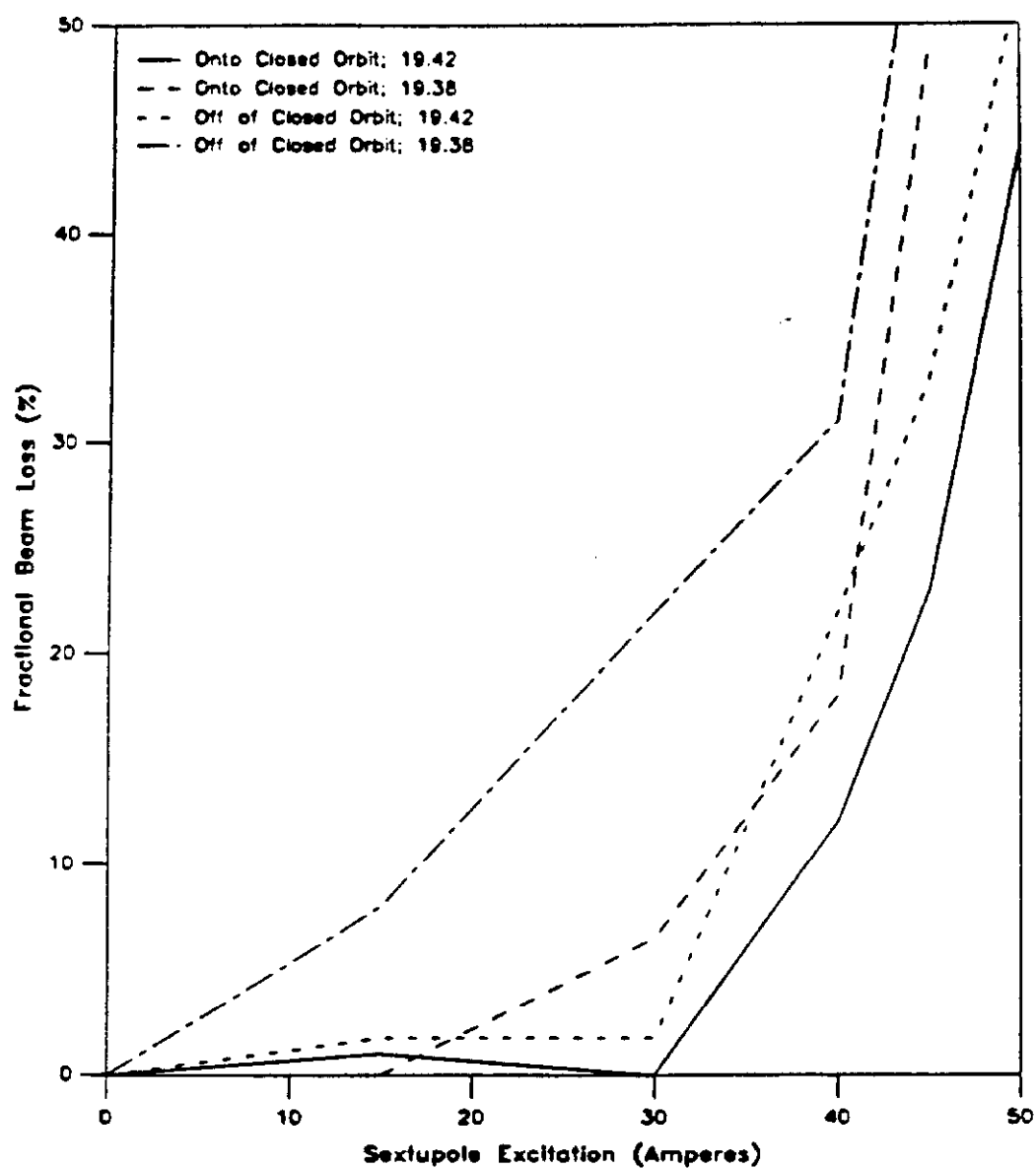


Figure 5.6: Fraction of beam lost between injection into the Tevatron and 5 secs later, versus sextupole excitation.

Beam Intensity vs. Time for 45 Amps, tune = 19.42

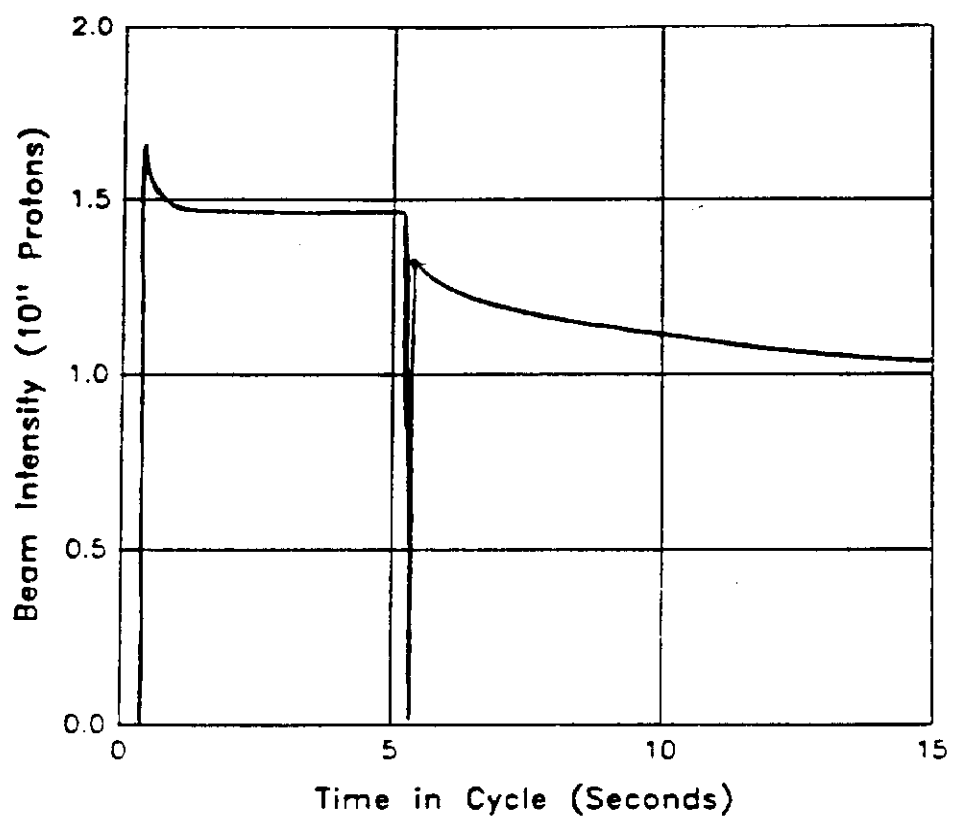


Figure 5.7: Beam intensity in the Main Ring and Tevatron as a function of time for a sextupole excitation of 45 amps and a tune of 19.42.

flying wires, contains a component at the synchrotron frequency: the difference in time, between the two major peaks of Fig. 5.8 is approximately 15 msec, which corresponds to about 70 Hz. This was a hint that the longitudinal motion may play a role. The slow loss issue was investigated further with the RF cavities turned off this time. Further detuning of the cavities was accomplished by turning off the water heaters. The heaters are used to adjust the physical dimensions of the cavities and thus their resonant frequency. Fig. 5.9 summarizes the new results: a dramatic reduction of the losses was achieved by turning the RF off; cooling the cavities effected further reduction of the losses. However much more effort is needed in order to understand the underlying mechanism causing these phenomena.

It was demonstrated experimentally—in one degree of freedom—that short time scale accelerator performance like injection efficiency and particle lifetime, are not influenced significantly by the presence of strong nonlinearities in the machine, hence allowing a safe diagnosis and correction of injection problems.

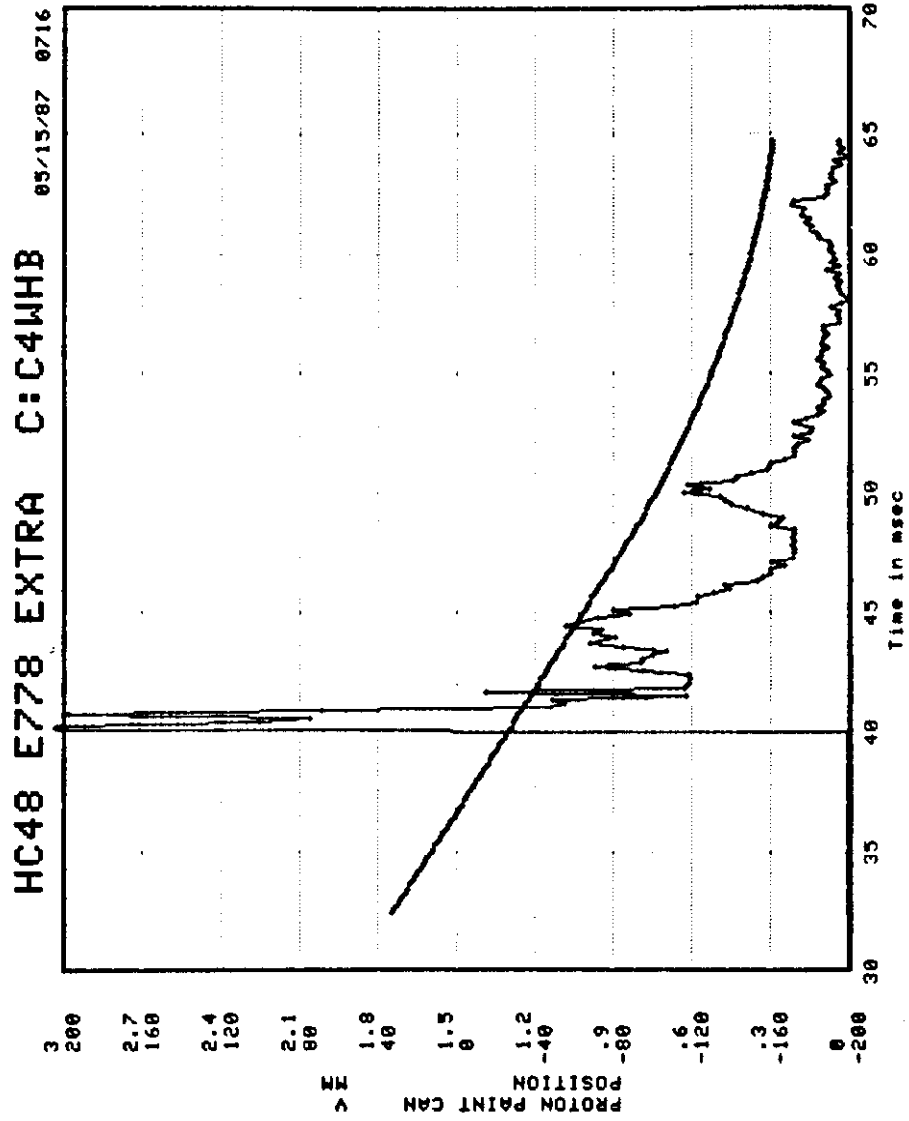


Figure 5.8: Plot obtained from the scintillation counters associated with the flying wires, illustrating that the time structure of the losses contains a component at the synchrotron frequency.

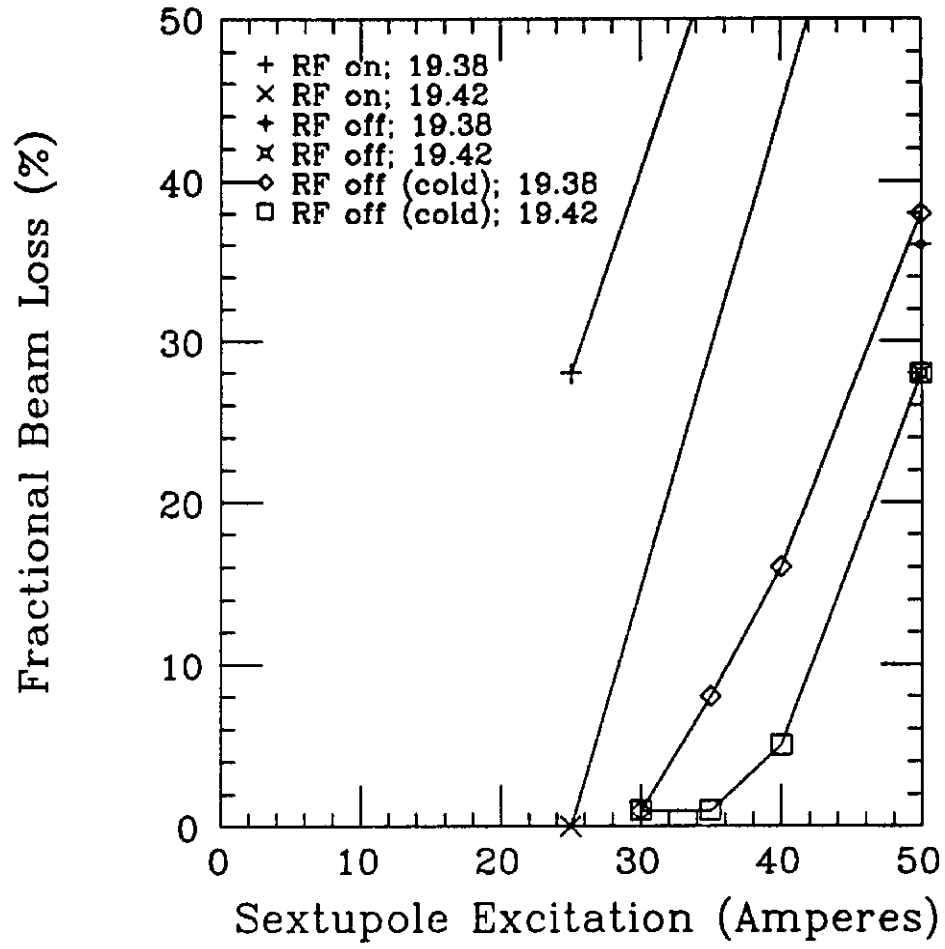


Figure 5.9: Summary of the results on the losses after the RF was turned off, and the cavities cooled.

CHAPTER VI

RESONANCE ISLANDS

In the resonance island experiment the existence of stable nonlinear resonance islands was demonstrated by directly observing particles captured into them. The ‘capture efficiency’ was measured as well as other characteristics of the islands such as their amplitudes and phases, which determine their location in phase space. Although particle trapping was observed on the 3/8 and 5/13 resonance islands, systematic data taking was restricted to the 2/5 resonance.

This chapter is structured as follows. First, the results obtained in Chapter II are used to derive expressions for the island width and the island tune. In the following section tracking calculations will be employed to first demonstrate the existence of the 2/5 islands and then estimate the various quantities of interest. The experimental observations will be laid out next, followed by a description of the analysis techniques employed to extract information out of the data. The results of the calculations and the analysis of the experimental data conclude this chapter.

Island Width and Island Tune

The calculation of Chapter II led to the following expression for the 2/5 resonance Hamiltonian,

$$H_4(a, I) = \nu I + cI^2 + \epsilon_0 I^{5/2} \cos [(5a - 97\theta) + \phi_0] \quad (6.1)$$

with

$$\epsilon_0 = \sqrt{\epsilon_1^2 + \epsilon_2^2} \quad (6.2)$$

and

$$\phi_0 = \arctan\left(-\frac{\epsilon_2}{\epsilon_1}\right). \quad (6.3)$$

ϵ_1 and ϵ_2 were defined by Eqs (2.101) and (2.102).

To derive the expressions for the island width and the island tune, I follow the traditional technique [17,16]. A canonical transformation to a rotating system in phase space with the generating function:

$$F_2 = \left(a - \frac{97}{5}\theta + \frac{\phi_0}{5}\right) I_1 \quad (6.4)$$

leads to

$$\Psi = \frac{1}{5}(5a - 97\theta + \phi_0), \quad (6.5)$$

$$I = I_1 \quad (6.6)$$

and

$$H_5(\Psi, I_1) = \delta I_1 + c I_1^2 + \epsilon_0 I_1^{5/2} \cos(5\Psi), \quad (6.7)$$

with

$$\delta = \nu - \frac{97}{5}. \quad (6.8)$$

The Hamiltonian has been put in a form explicitly independent of the “time” variable θ ; thus it is a constant of the motion.

The fixed points of the motion, where the trajectories are stationary, can be obtained by the conditions:

$$\frac{\partial H_5}{\partial I_1} = \frac{\partial H_5}{\partial \Psi} = 0 \quad (6.9)$$

which imply

$$\sin 5\Psi_0 = 0 \quad (6.10)$$

and

$$\delta + 2cI_0 + \frac{5}{2}\epsilon_0 I_0^{3/2} \cos(5\Psi_0) = 0. \quad (6.11)$$

For $\sin 5\Psi_0$, $\cos 5\Psi_0 = \pm 1$ and for different signs of $\cos 5\Psi_0$ the characteristics of the fixed points are different. It can be shown [19] that those angles corresponding to $\cos 5\Psi_0 = 1$ are stable fixed points (SFP) while those with $\cos 5\Psi_0 = -1$ are unstable fixed points (UFP). Both stable and unstable fixed points are shown in Fig. 6.1.

The boundaries of the stable islands are formed by curves joining the unstable fixed points. They are called *separatrices* and their equation can be easily found by the fact that the Hamiltonian is a constant on the curve. Setting the constant value of the Hamiltonian equal to its value at the unstable fixed point, I_u , one gets,

$$\delta I_1 + cI_1^2 + \epsilon_0 I_1^{5/2} \cos 5\Psi = \delta I_u + cI_u^2 - \epsilon_0 I_u^{5/2}. \quad (6.12)$$

The action I_u , of the unstable fixed points satisfies the equation

$$\delta + 2cI_u - \frac{5}{2}\epsilon_0 I_u^{3/2} = 0, \quad (6.13)$$

as can be easily seen from Eq. (6.11). Hence given ϵ_0 , c and δ , I_u can be computed and the constant value of the Hamiltonian can be found. Then one can draw the separatrices given by Eq. (6.12). This is illustrated in Fig. 6.1. In this particular case, the various coefficients are calculated as follows. The parameter c of the detuning term cI_1^2 , is calculated with the use of Eq. (2.100). For the E778 sextupole configuration with sextupole excitation of 25 amperes and a tune of 19.415, c is calculated to be

$$c = -47.21 \text{ mm}^{-1}. \quad (6.14)$$

The calculation of ϵ_0 is relatively straightforward with the warning that formula (2.32) holds true *only* for $0 < \theta < 2\pi$. For the above experimental conditions, ϵ_0 turns out to be

$$\epsilon_0 = 18.30 \text{ mm}^{-3/2}. \quad (6.15)$$

Finally one can calculate I_u , which satisfies the equation (6.13). This is a cubic equation in $I_u^{1/2}$ so it can be easily solved. For the above values of c and ϵ_0 , the

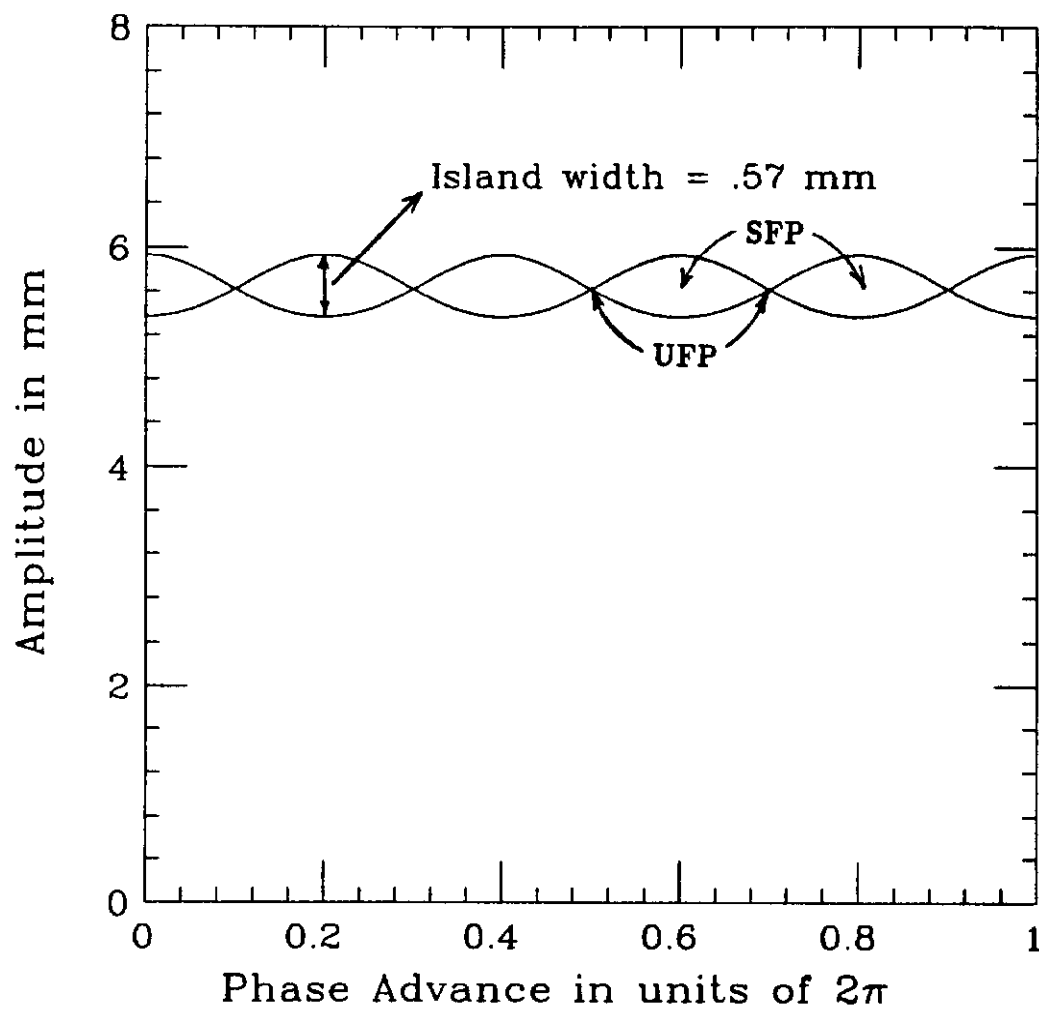


Figure 6.1: Contours of the Hamiltonian describing motion under the action of a fifth-order resonance. The sextupole excitation is 25 amperes and the initial tune 19.415.

physically acceptable solution is

$$I_u = 1.6 \times 10^{-4} \text{ mm.} \quad (6.16)$$

Then the amplitude of the unstable fixed points is calculated to be

$$\mathcal{A}_u = 5.66 \text{ mm.} \quad (6.17)$$

From Fig. 6.1 one can extract the island width being the maximum separation in amplitude of the two separatrices. It turns out to be

$$\Delta a_w|_{\text{figure}} = .57 \text{ mm.} \quad (6.18)$$

However one can actually derive an expression for the island width [15,17]. This calculation is demonstrated next.

If I_r is the resonance action defined by

$$\nu + 2cI_r = \frac{97}{5}, \quad (6.19)$$

then Eq. (6.12) can be written in the form

$$cI_1^2 - 2cI_1I_r + \epsilon_0 I_1^{5/2} \cos 5\Psi = cI_u^2 - 2cI_uI_r - \epsilon_0 I_u^{5/2}. \quad (6.20)$$

Expanding for I_1 close to I_u gives the difference of the amplitude between I_1 and I_u ,

$$(I_1 - I_u)^2 \simeq \frac{2\epsilon_0 I_u^{5/2} (1 - \cos 5\Psi)}{2c}. \quad (6.21)$$

From here the maximum separation or the island half width is

$$\Delta I = 2\sqrt{\frac{\epsilon_0 I_u^{5/2}}{2c}}. \quad (6.22)$$

Using the values of ϵ_0 , c and I_u given by Eqs (6.15), (6.14) and (6.16) respectively, one finds that the island width as calculated from Eq. (6.22) is

$$\Delta a_w|_{\text{formula}} = .56 \text{ mm,} \quad (6.23)$$

in remarkable agreement with Eq. (6.18). The conclusion from this agreement is that the approximation used in the derivation of Eq. (6.22) is very accurate.

The island tune Q_I can also be expressed in terms of the coefficients ϵ_0 and c and the resonance action I_r . In order to derive an expression for Q_I [17], I need to see the Hamiltonian in the vicinity of I_r , that is, around the center of the island. For this, the Hamiltonian (6.7) is expressed in terms of p , where

$$I_1 = p + I_r, \quad (6.24)$$

and

$$H = cp^2 + \epsilon_0 I_r^{5/2} \cos 5\Psi, \quad (6.25)$$

where constant terms have been dropped.

The equations of motion in (Ψ, p) coordinates are

$$\dot{\Psi} = \frac{\partial H}{\partial p} = 2cp \quad (6.26)$$

and

$$\dot{p} = -\frac{\partial H}{\partial \Psi} = 5\epsilon_0 I_r^{5/2} \sin 5\Psi. \quad (6.27)$$

Combination of the two equations gives

$$\ddot{\Psi} - 10\epsilon_0 c I_r^{5/2} \sin 5\Psi = 0 \quad (6.28)$$

or

$$\ddot{\Psi} + 10\epsilon_0 |c| I_r^{5/2} \sin 5\Psi = 0. \quad (6.29)$$

This is the familiar equation of motion for a pendulum. When the amplitude is small, the small amplitude oscillation frequency Q_I can be obtained from (6.29) by approximating

$$\sin 5\Psi \simeq 5\Psi. \quad (6.30)$$

This yields the island tune,

$$Q_I^2 = 5^2 (2|c|) \epsilon_0 I_r^{5/2}. \quad (6.31)$$

Substituting c and ϵ_0 from Eqs (6.14) and (6.15), and solving (6.19) for I_r , one finds that

$$Q_I = 4.9 \times 10^{-5} \mathcal{A}_r^{5/2}, \quad (6.32)$$

where \mathcal{A}_r is the resonance amplitude, measured from the origin of the phase space. The coefficient 4.9×10^{-5} is expressed in $\text{mm}^{-5/2}$.

Simulation

Single and multi-particle tracking calculations were performed to study the resonance island region of the nonlinear phase space, using mainly EVOL and occasionally TEAPOT and ART.

Single particle tracking provides a clear picture of the location, size and configuration of the 5 islands, an action-angle representation of which is displayed in Fig. 6.2. To obtain this particular figure, the base tune was set equal to 19.415, the sextupole excitation being 25 amperes. In principle the transformations derived in Chapter II can be used to map the actual shape of the islands of Fig. 6.2. The kick amplitude was 5.25 mm.

From Fig. 6.2 one can see that the average resonance amplitude A_r is approximately

$$A_r|_{tr} \simeq 5.95 \text{ mm} \quad (6.33)$$

in reasonable agreement with the calculation above (Eq. (6.17)). In order to compare the island widths as derived from the two methods, one must first define the island width from tracking calculation, in Fig. 6.2. If the island width is defined as the average island width over the five islands then

$$\Delta a_w|_{tr} \simeq .41 \text{ mm}. \quad (6.34)$$

The discrepancy between the two approaches in the determination of the island width is not very surprising. The Hamiltonian used to derive the island width does not de-

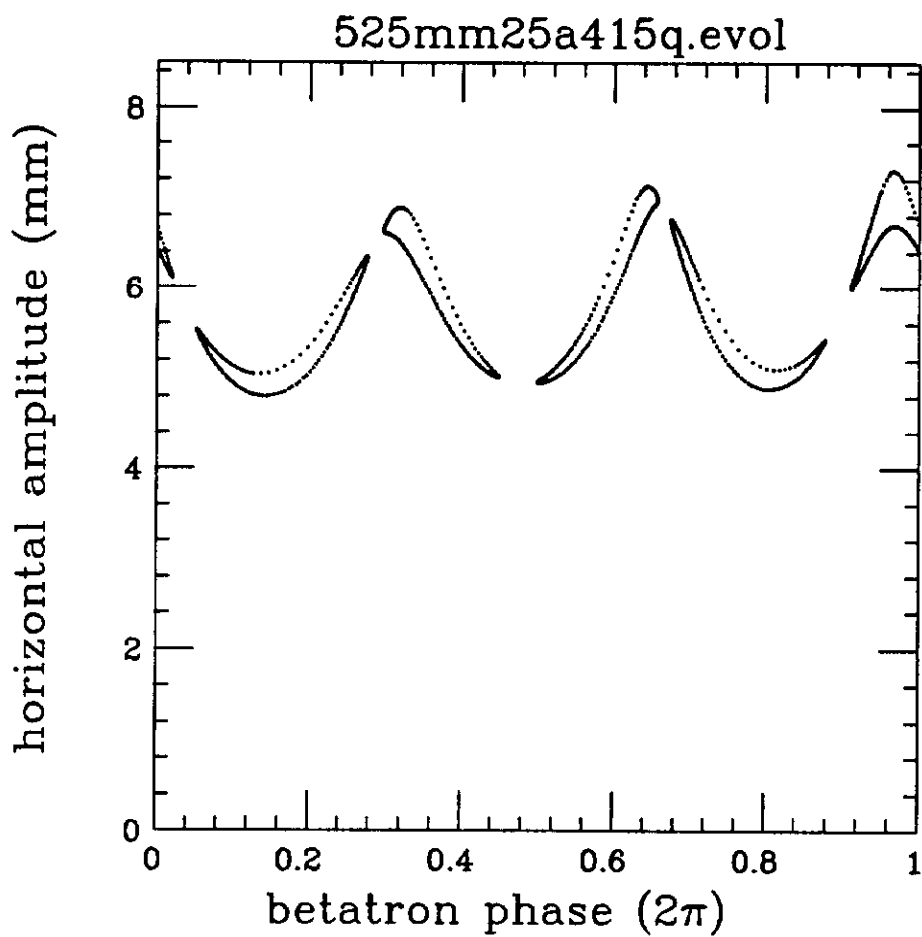


Figure 6.2: Action-angle representation of single particle tracking using EVOL. The sextupole excitation is 25 amperes, the kick amplitude is 5.25 mm and the initial tune 19.415.

scribe the experimental situation accurately. In E778 a strong third integer resonance driving term distorts the phase space to a triangular shape on which the five islands are superimposed. To account for this fact, the correct Hamiltonian must include an extra term of the form

$$\cos(3a - 58\theta). \quad (6.35)$$

However it is not clear how to calculate the island width in the presence of two resonances. So instead, the single resonance approximation was used, which places the five islands on a circle in phase space around the origin.

When the beam is kicked to an appropriate amplitude, some of the protons are captured on the stable islands, provided that the sextupoles are turned on to give resonant islands. Fig. 6.3 illustrates the relative position of the beam right after the kick with respect to the 5 stable islands. Fig. 6.4 is a magnified view of the previous plot to observe how the beam size is distributed through the area of the island. This particular beam has an emittance of 3π mm-mrad and hence its σ is .56 mm.

The next logical step is to perform multi-particle simulation in order to create the link between the above description and the actual observation. For the simulation, a 3π mm-mrad beam was used and for each of 4 values of the kick amplitude - 8, 9, 10, 11 kV - a scan in tune was performed to maximize the fraction of particles captured in stable islands. Table 6.1 contains all cases simulated with EVOL. The simulated data were analyzed and quantities such as the capture efficiency and the phases of the 5 islands were extracted. The results of this analysis are presented in the last section of this chapter. Before this though, the experimental aspect of this study will be discussed next.

The Experiment

The first aim of the resonance island experiment was to demonstrate the existence of the stable nonlinear resonance islands. Capture of particles into stable islands

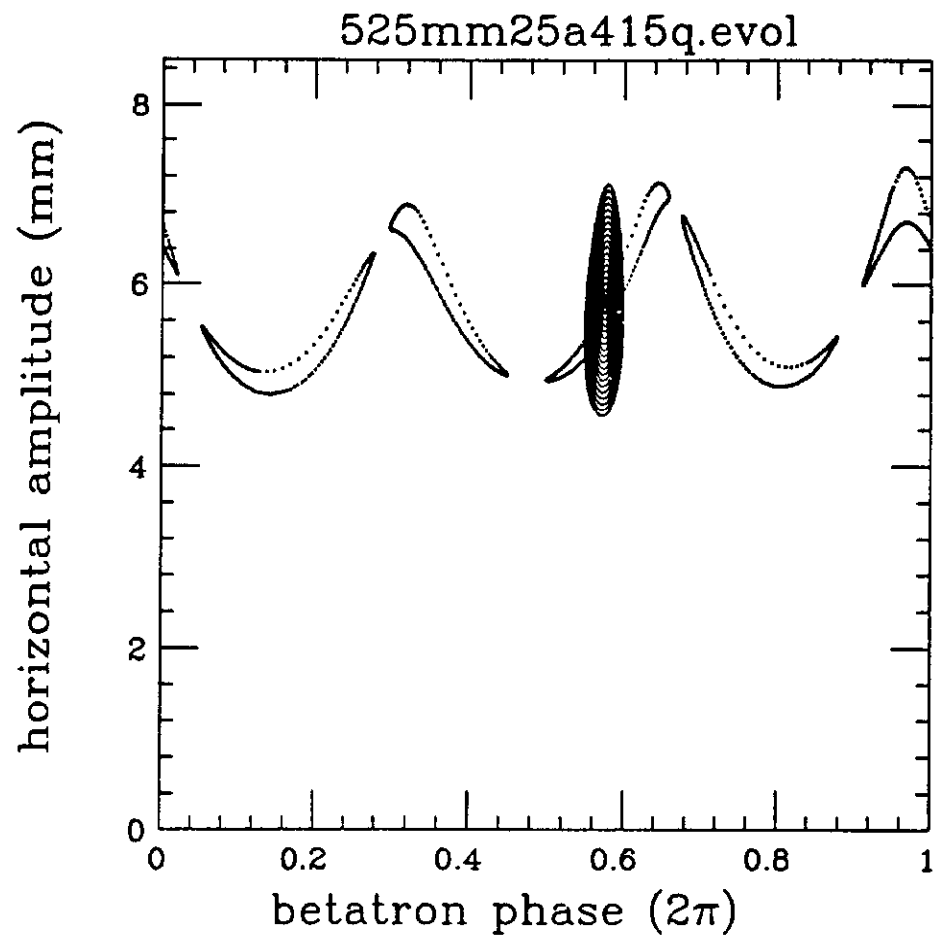


Figure 6.3: Relative position of the kicked beam with respect to the five stable islands.

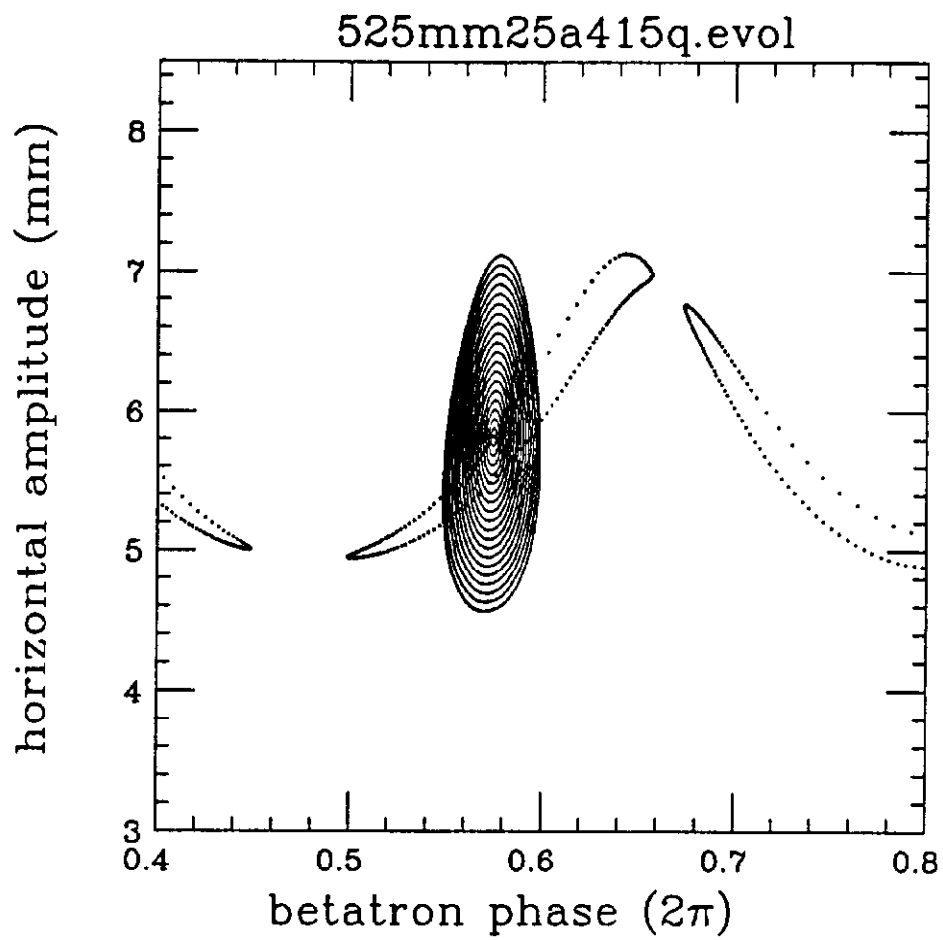


Figure 6.4: A magnified view of the previous plot.

8 kV (3.6 mm)		9 kV (4.05 mm)		10 kV (4.5 mm)		11 kV (4.95 mm)	
Q_0	Capt Eff	Q_0	Capt Eff	Q_0	Capt Eff	Q_0	Capt Eff
19.404	.0137	19.406	.0215	19.409	.0561	19.412	.0956
19.405	.0231	19.407	.0400	19.410	.0815	19.413	.1203
19.406	.0405	19.408	.0623	19.411	.1048	19.414	.1434
19.407	.0554	19.409	.0826	19.412	.1198	19.415	.1517
19.408	.0648	19.410	.0920	19.413	.1203	19.416	.1465
19.409	.0650	19.411	.0912	19.414	.1084	19.417	.1323
19.410	.0557	19.412	.0779	19.415	.0899	19.418	.1107
19.411	.0388	19.413	.0569	19.416	.0682	19.419	.0855
19.412	.0265	19.414	.0386	19.417	.0472	19.420	.0597

Table 6.1: A summary of multiparticle EVOL simulation performed for the study of the resonance islands.

manifests itself by the absence of decoherence. Recall that the average fractional part of the tunes of the particles captured into the islands locks onto $2/5$. Hence the decoherence is defeated and the signal from the centroid of the beam is observable over many seconds, in Fig. 6.5 for example. Such signals have been observed to persist for about a minute (corresponding to a million turns).

Fourier analysis of the signal yields a value of

$$\nu = .400010 \pm .000005, \quad (6.36)$$

consistent with $2/5$. Fig. 6.6 is a raw data plot of x_1 versus x_2 for approximately 4000 turns starting right before the kicker fired. The uncaptured part of the beam decoheres within the first few turns while the captured part forms the 5 stable islands. Fig. 6.7 displays the same dataset for some thousands of turns taken after some seconds and the 5 islands are clearly visible. At last, if one joins the successive points of the above

tape14.021

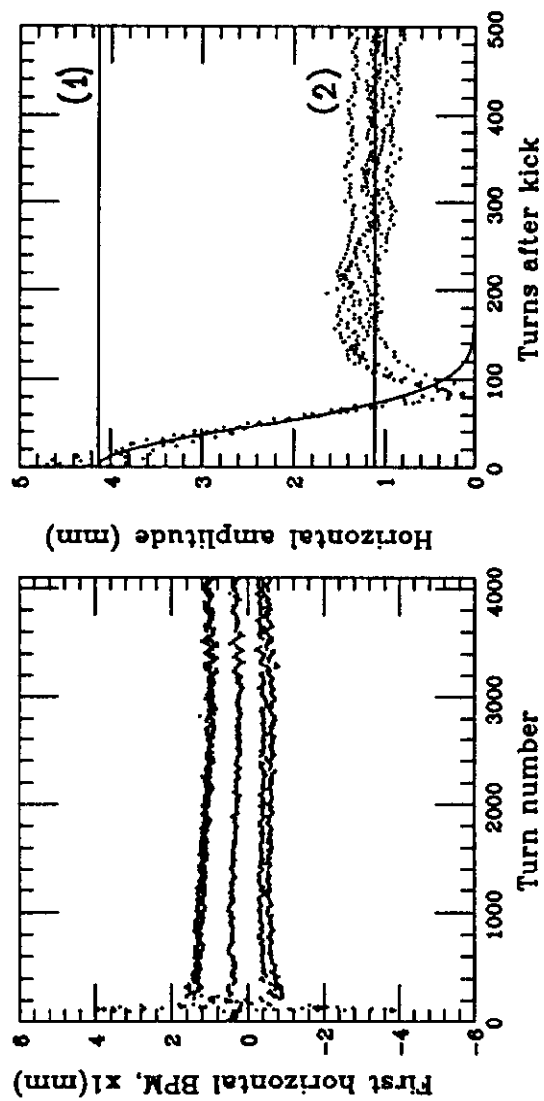


Figure 6.5: Raw BPM turn-by-turn output, for (a) 4000 turns and (b) 500 turns, with sextupole strength of 25 amps. The capture efficiency is given by amplitude (2) / amplitude (1).

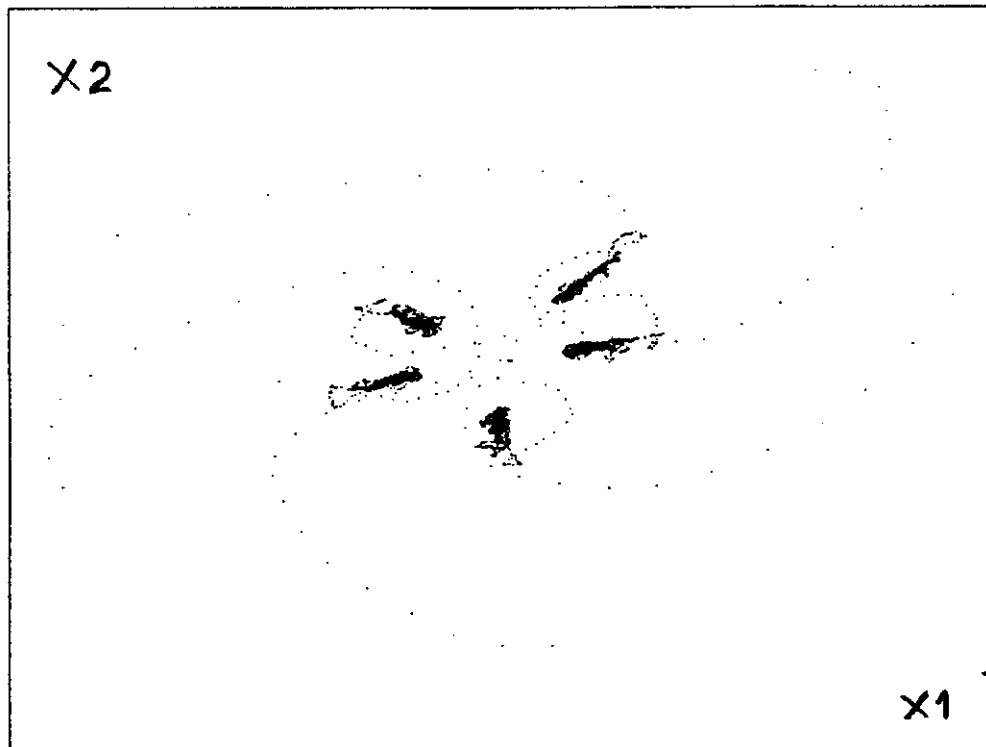


Figure 6.6: Experimental phase space plot, for 4000 turns, starting right before the kick.

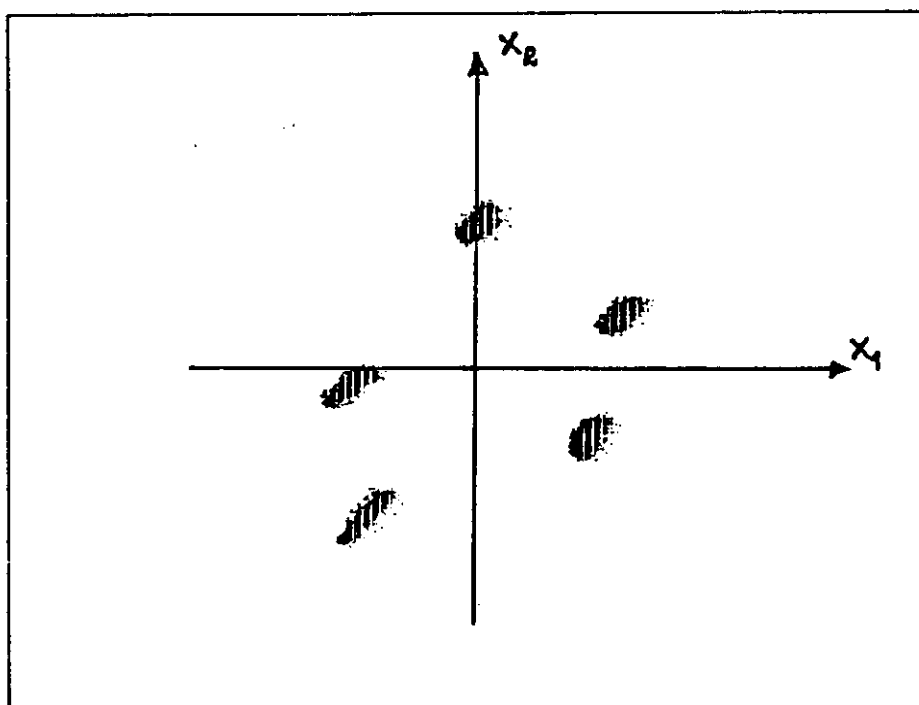


Figure 6.7: Experimental phase space plot of the same data as in Fig. 6.6, taken some seconds later.

plot by straight lines one obtains the plot of Fig. 6.8. Notice that the point lands on every second island, confirming the $2/5$ identification.

The second aim of this experiment was to quantify the observations and compare them with prediction. For this, the capture efficiency was defined as the fraction of the non-decohering charge surviving 500 turns, well after the decoherence of uncaptured particles and before appreciable decay has occurred. In Fig. 6.5 the capture efficiency is given by the ratio of the amplitude (2) over the amplitude (1). The capture efficiency depends on the relation between the beam size and the island size, as well as on the angular orientation of the islands in phase space. In order to study the capture efficiency experimentally the kick amplitude was kept fixed and the base tune was varied. It is shown in the last section, that the capture efficiency becomes appreciable when the kick amplitude is approximately equal to the resonance amplitude. Measurements were taken at different values of the kick amplitude and Table 6.2 summarizes the different conditions at which data were recorded. After a brief description of the analysis tools in the next section, I shall conclude this chapter with the presentation of the results.

Analysis

If persistent signal analysis has been requested by the user in TEVEX.CMD, then in addition to the analysis described in Chapter IV, the following aspects are examined and information is reported.

The user specifies the range of data, after decoherence, over which the persistent signal analysis takes place. First TEVEX calculates the average value of the amplitude of the persistent signal and finds the minimum and maximum values of the amplitude in this region. Furthermore, TEVEX calculates the persistent fraction which is defined as the ratio of the average of the persistent amplitude over the kick amplitude. This quantity was called capture efficiency earlier. The persistent frac-

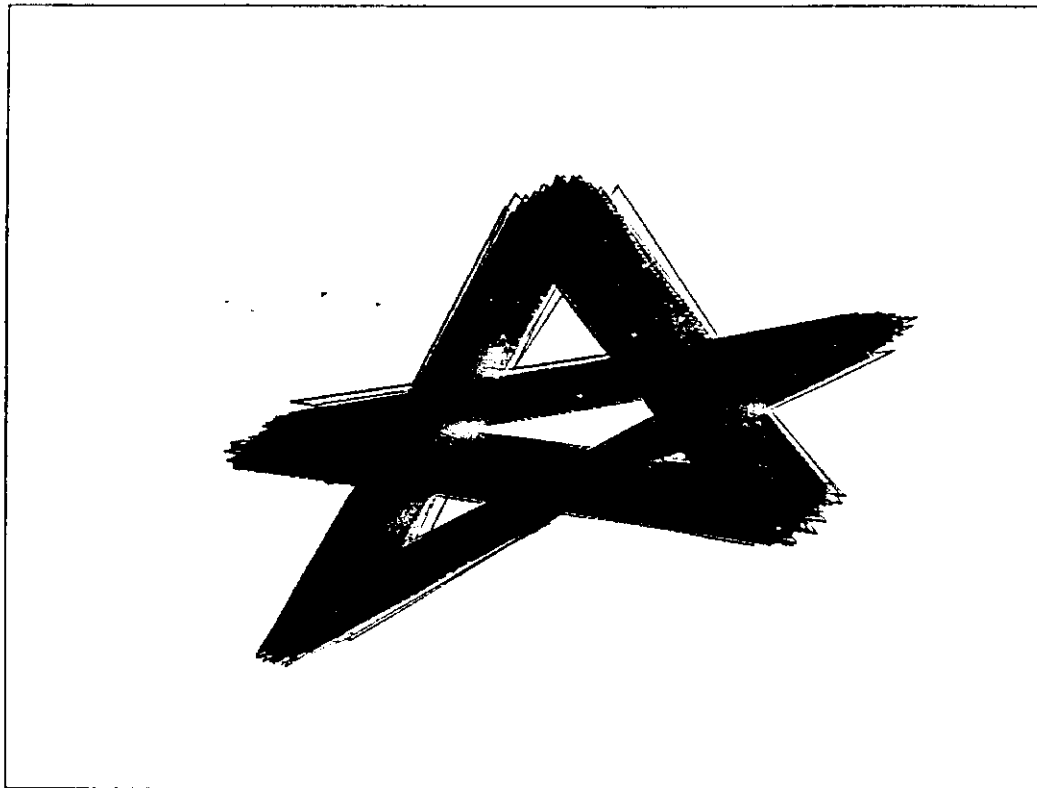


Figure 6.8: A different representation of the data of the previous plot where successive points are now joined by straight lines. This plot confirms the $2/5$ identification.

kV	Q _{eo}	PerF	A _{init}	(SD) _φ	(SD) _{Amp}	φ ₁	Amp ₁	φ ₂	Amp ₂	φ ₃	Amp ₃	φ ₄	Amp ₄	φ ₅	Amp ₅
8	.438	.056	3.32	.062	.049	.078	.207	.224	.258	.343	.177	.570	.138	.918	.142
8	.436	.103	3.31	.030	.052	.027	.358	.227	.431	.381	.330	.584	.322	.869	.260
8	.434	.106	3.28	.038	.084	.023	.322	.245	.399	.409	.349	.588	.358	.840	.312
8	.434	.091	3.32	.044	.082	.024	.294	.224	.342	.383	.326	.583	.293	.835	.250
8	.440	.029	3.42	.078	.027	.089	.113	.216	.156	.314	.106	.490	.064	.954	.061
8	.439	.045	3.32	.068	.032	.063	.194	.198	.222	.293	.139	.552	.068	.920	.130
8	.437	.079	3.03	.078	.071	.029	.265	.189	.248	.422	.145	.631	.284	.829	.252
8	.435	.134	3.24	.024	.059	.017	.468	.216	.490	.398	.398	.601	.430	.858	.380
8	.435	.103	3.23	.021	.102	.010	.353	.237	.351	.423	.293	.608	.369	.863	.301
8	.437	.074	3.33	.053	.080	.026	.231	.238	.317	.376	.259	.562	.232	.849	.183
8	.436	.094	3.30	.060	.092	.004	.293	.239	.364	.383	.295	.607	.332	.856	.260
9	.436	.223	3.77	.011	.068	.003	.840	.234	.935	.400	.811	.595	.888	.853	.732
9	.438	.204	3.67	.021	.082	.003	.782	.215	.859	.387	.652	.600	.792	.854	.662
9	.434	.110	3.58	.036	.087	.010	.414	.205	.421	.385	.355	.610	.386	.830	.400
9	.435	.188	3.66	.020	.077	.018	.696	.231	.697	.411	.635	.611	.733	.832	.688
9	.437	.220	3.65	.044	.205	.026	.725	.240	.929	.405	.818	.585	.951	.811	.598
9	.437	.184	3.66	.010	.050	.003	.684	.219	.742	.403	.587	.600	.759	.845	.605
9	.439	.124	3.62	.013	.034	.001	.429	.229	.515	.395	.413	.594	.506	.842	.379
9	.440	.113	3.80	.015	.044	.018	.418	.230	.543	.373	.416	.579	.454	.860	.313
10	.440	.269	4.13	.005	.048	.003	1.165	.217	1.354	.369	1.021	.585	1.114	.856	.892
10	.440	.263	4.10	.006	.046	.007	1.076	.221	1.256	.382	1.005	.584	1.176	.842	.875
10	.438	.228	4.08	.009	.061	.002	.878	.228	1.106	.383	.924	.579	1.044	.832	.707
10	.436	.198	3.97	.023	.106	.020	.704	.239	.866	.400	.725	.612	.875	.821	.761
10	.442	.146	4.11	.010	.040	.001	.586	.219	.748	.359	.590	.569	.622	.844	.440
11	.440	.357	4.33	.007	.090	.023	1.494	.223	1.646	.397	1.399	.598	1.791	.829	1.390
11	.440	.401	4.10	.007	.071	.017	1.714	.209	1.807	.386	1.347	.596	1.895	.833	1.453
11	.436	.143	4.10	.061	.159	.040	.635	.171	.571	.408	.332	.645	.708	.818	.676
11	.436	.197	4.36	.043	.206	.010	.818	.211	.969	.395	.702	.615	1.020	.821	.790
11	.436	.102	4.20	.085	.159	.026	.378	.238	.478	.409	.379	.613	.507	.824	.408
11	.438	.261	4.22	.014	.093	.035	1.005	.232	1.211	.390	.984	.608	1.217	.821	1.089

Table 6.2: A summary of the experimental conditions at which data were taken for the study of the nonlinear resonance islands.

tion, the kick amplitude, the average amplitude of the persistent signal, the minimum and maximum amplitudes in this region, are then recorded in the output.

Next TEVEX finds the average values of the phase advance and the amplitude of each of the 5 islands, as well as their standard deviations. The output includes the phase advance, amplitude, standard deviation of the phase and standard deviation of the amplitude for each of the 5 islands, ordered in ascending phase. Fig. 6.9 is a typical TEVEX output including results of persistent signal analysis. Fig. 6.10 is the corresponding graphical output of TEVEX.

Results

The results of the analysis of the simulated and the experimental data are presented here. First a plot that was done - using EVOL - for reference purposes is presented. For each value of the kick amplitude A_k , a scan was done through the various tune values until the capture efficiency was maximized. In Fig. 6.11 the kick amplitude as a function of the base tune which maximizes the captured fraction is plotted. This scan was done for a single particle (which in a sense is equivalent to 0π emittance beam) and for a beam of emittance 3π mm-mrad.

Fig. 6.12 came from single particle EVOL tracking [46]. It illustrates the island tune Q_I as a function of the resonance amplitude A_r . Tracking shows that the relation between these two fundamental quantities of the resonance island structure is

$$Q_I = 3.8 \times 10^{-5} A_r^{5/2}. \quad (6.37)$$

Recall that perturbation calculation predicts that

$$Q_I = 4.9 \times 10^{-5} A_r^{5/2} \quad (6.38)$$

in very good agreement with the tracking results.

Next, in Fig. 6.13, EVOL's prediction on the phases of the 5 islands is presented for various horizontal tunes. The various symbols correspond to different kick amplitudes.

```

>>> THE FOLLOWING PARAMETERS ARE SET IN tevex.cmd <<<
----- Input file format parameters -----
format, #headers, initial noise      = 0 12 0.20000
----- Fast pass default values -----
BATCH FAST level nt(st,fs,ff,fi) next = F F 3 0 40 40 1 0
infiles : 5kv15a.files
----- Input and output filters -----
FILTER, qmin, qmax                    = F 0.00050 0.00500
----- Persistent signal analysis -----
PERSIG npsmin npsmax                  = T 300 500
----- Discrete Fourier Transform parameters -----
DODFT, dftL, dftR, dftMIN, dftMAX    = F 0.35000 0.45000 0.00000 1.10000
Max harmonic, Q1/2 choice, threshold = 3 1 1 0.10000
----- Slow Phase Parameters -----
Nstrob, Numer, Norder, DftTol        = 1 2 5 0.10000
----- Idealised lattice parameters -----
beta(x1,y1,x2,y2), phase per cell    = 99.64 28.36 94.83 29.94 67.84
alpha(x1,y1,x2,y2)                   = -1.900 0.530 -1.900 0.530
----- Test data parameters -----
BPM LSB, 1st & last particles         = 0.00000 1 100
----- Fitting control parameters -----
manual ctrl, max iters, iters/write   = 1 2000 -2000
initial & shake factors, tolerance     = 1.50000 0.99000 0.200-11
----- Graphical output control -----
XlvT, AXvT, AXvFIX, SvT, QXvT, FITvT = T T T T T T
Horizontal file:[e778.apr17]10kv30a.98h *****

FILE 98 10KV,30 AMPS, CX = +10, NUXUP 04/17/87 1652
Detector 1 = T:HPE24 Data Timing: 29.9980
Detector 2 = T:HPE26 Data Timing: 29.9980
T:HPE24 T:HPE26
13360 12591 12087 14136 8224 13873 12853
12576 19248 11350 12339 16672
20557 11347 17164 8280 8253
12587 11312 20000 22613 20565
29.99800 29.99800
-1.93081 -1.33278
0 0

First data line : 1 -2.24000 -1.63000 0.00000 0.00000
Real data starts: 97 -3.66000 -5.90000 0.00000 0.00000

LEVEL = 3 *****

Tracking data appears to start on turn 97 and finish on turn 1024
ntstrt, ntfini, ntfinf, ntfini= 97 1 150 1

NTFIN Ax mm. SMEAR Qx Xoff(1,2) mm. BetaX(1,2) m. Fix d. Rdec
103 3.7967 0.0564 0.41994 -2.0993 -1.4919 100.01 94.48 67.239 0.9770-01
104 3.9271 0.0543 0.42265 -2.1168 -1.5478 98.53 95.90 69.700 0.8230-01
105 4.2861 0.0651 0.42341 -2.1782 -1.4883 98.82 95.61 73.957 0.5010-01
106 4.1281 0.0623 0.41993 -2.1596 -1.4982 99.60 94.67 74.242 0.4430-01
107 3.7871 0.0604 0.42081 -2.1104 -1.4884 98.14 96.28 74.677 0.5060-01
108 3.9144 0.0582 0.42294 -2.0867 -1.4729 98.20 96.22 74.034 0.4760-01
109 4.1096 0.0602 0.42240 -2.1232 -1.5190 98.63 97.76 73.441 0.3860-01

145 1.6175 0.0602 0.42477 -2.0627 -1.4731 97.71 96.70 72.847 0.2920-01
146 1.5486 0.0602 0.42449 -2.0555 -1.4770 97.90 96.52 73.065 0.2910-01
147 1.5822 0.0620 0.42501 -2.0775 -1.4780 98.82 95.61 73.262 0.2880-01
148 1.6389 0.0667 0.42472 -2.0464 -1.4615 99.70 94.78 72.631 0.2840-01
149 1.4135 0.0663 0.42486 -2.0523 -1.4674 99.67 94.80 72.481 0.2840-01
150 1.4121 0.0667 0.42492 -2.0462 -1.4544 99.15 95.30 72.282 0.2820-01

Min(X1,X2), max(X1,X2), <X1>, <X2> (mm) = -5.9000 2.6800 -2.0737 -1.4911
X Amplitude: min, max (mm) = 0.0138 4.7947

The largest non-noisy phase discontinuity was
Turn Amp(mm) Old fi(2pi) New fi(2pi) Old<slowfi> New<slowfi> Dsfi(adjusted)
104 3.980 0.1742 0.6164 0.9332 1.0581 0.0161

PERSISTENCE: AmpFrac Akick Apersist Ampsmin Ampsmax
0.0811 4.0524 0.3288 0.0138 0.6829

Measured island locations. Typical SDs, (Fi,A): 0.245 0.153
Island ID: 4 2 5 3 1
<Fix> : 0.307 0.317 0.300 0.306 0.373
<Ax> [mm]: 0.338 0.334 0.320 0.320 0.332
SD of Fix: 0.244 0.222 0.254 0.249 0.261
SD of Ax : 0.153 0.157 0.149 0.161 0.155
EXIT with only summary graphics *****

```

Figure 6.9: Typical TEVEX output including the persistent signal analysis.

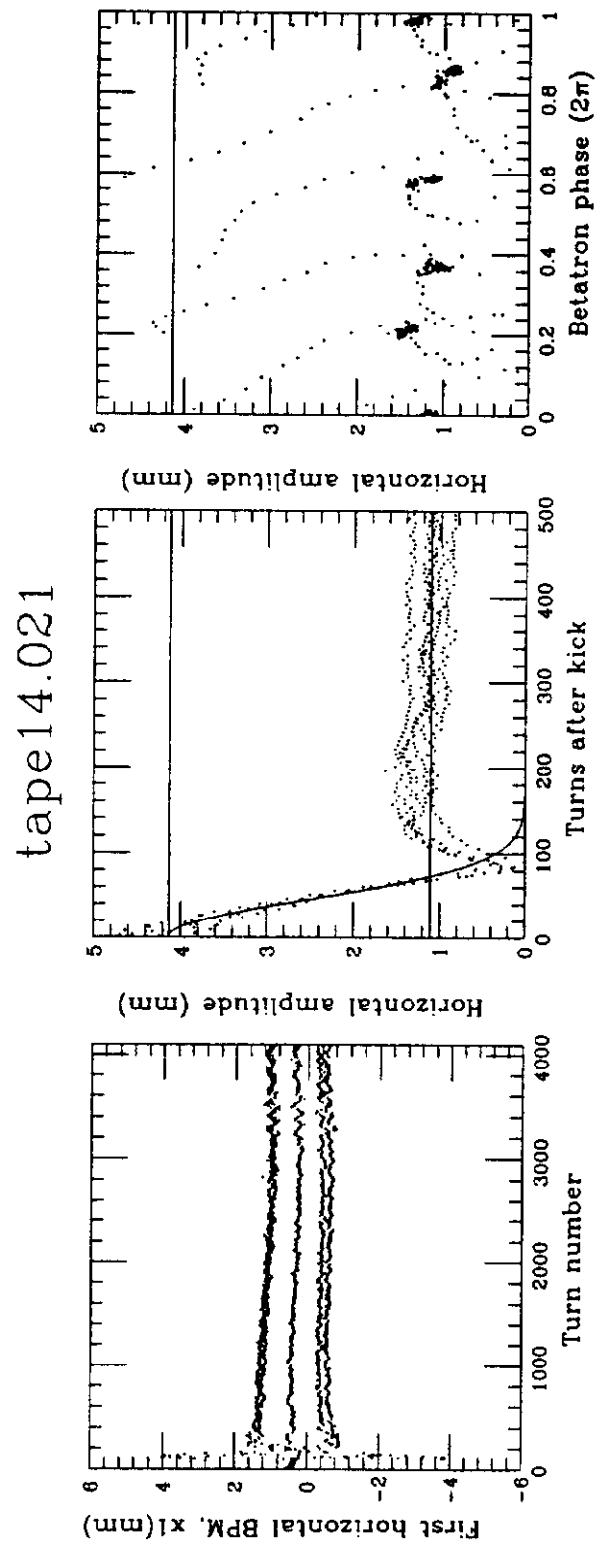


Figure 6.10: Typical graphical output of TEVEX in the case of persistent signal analysis.

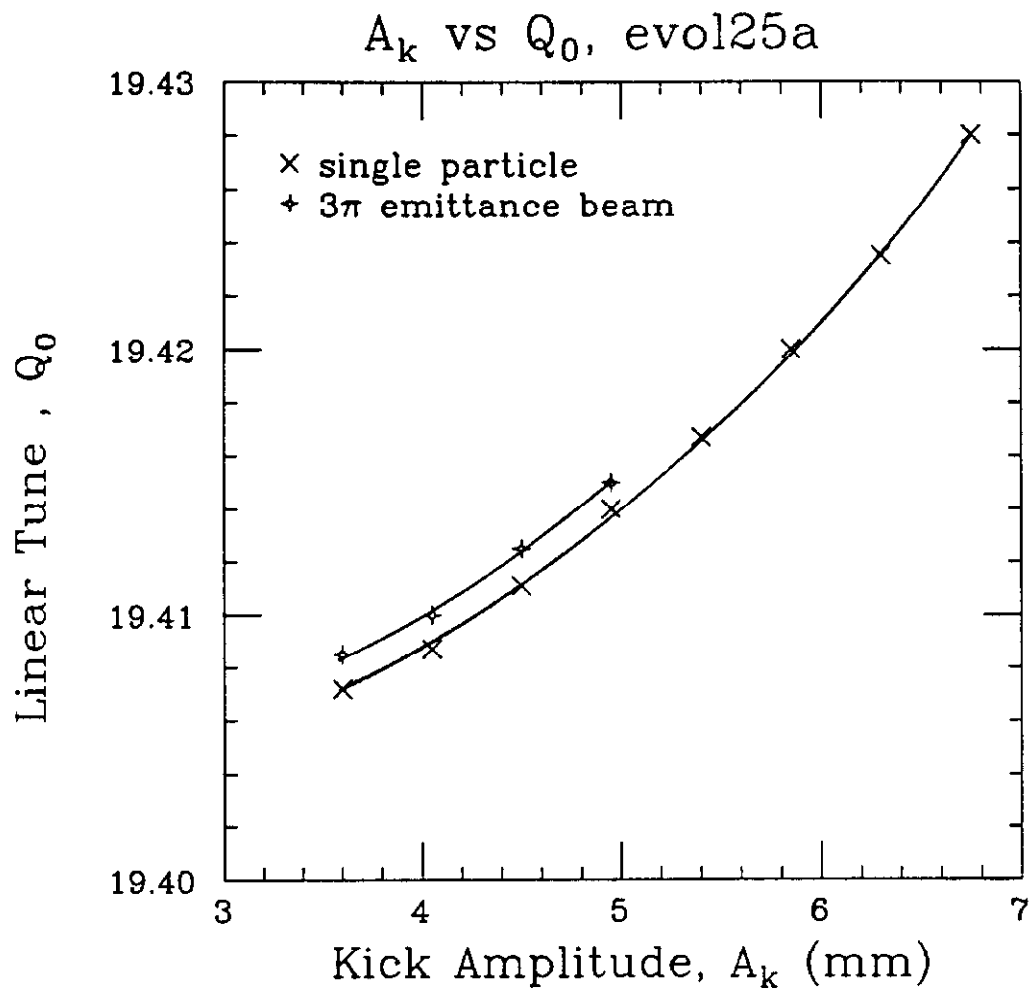


Figure 6.11: Kick amplitude versus base tune, corresponding to maximum capture efficiency. Data have been obtained from EVOL simulations.

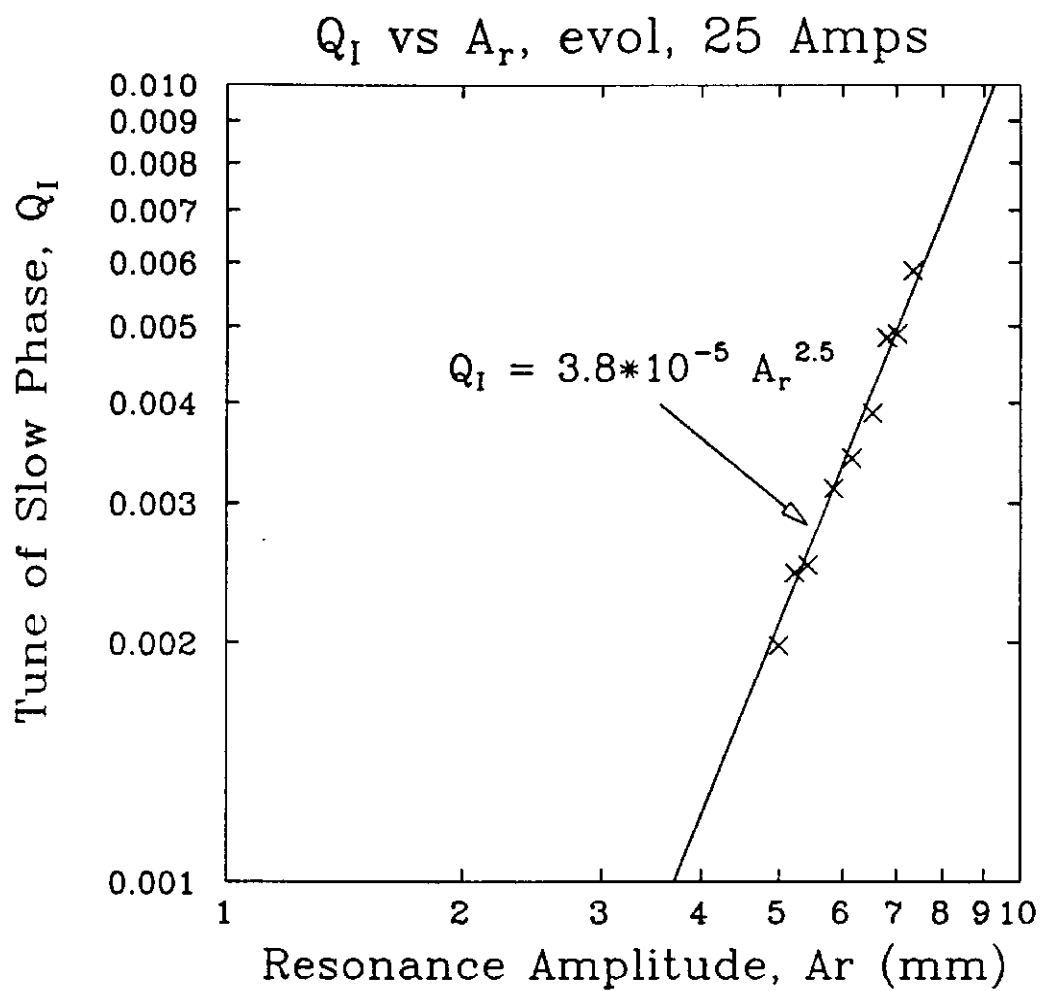


Figure 6.12: Island tune versus resonance amplitude, from single particle EVOL tracking.

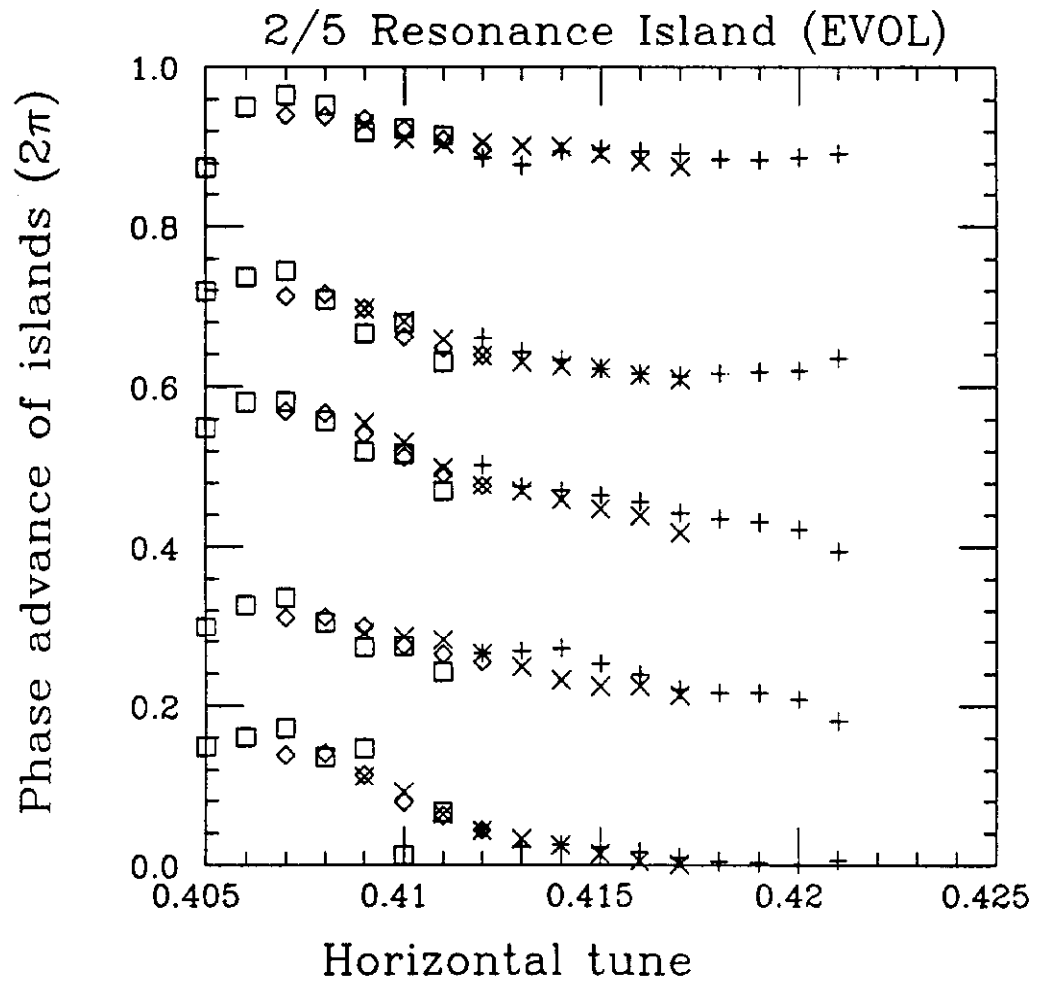


Figure 6.13: Phases of the five islands versus tune as predicted from EVOL.

This plot is to be compared with Fig. 6.14 which displays the same information as derived from the analysis of the experimental data. Notice here that the 5 islands are not symmetrically distributed around the center of the phase space. Furthermore, the phase difference of an island between experiment and simulation is not the same for all 5 islands.

At last, one of the most important measurable quantities associated with the resonance islands, namely the capture efficiency is plotted. Fig. 6.15 illustrates the capture efficiency as a function of the horizontal tune for various kick amplitudes — 8, 9, 10 and 11 kV. These are multi-particle tracking results. As expected, one observes the classical resonance response when the kick amplitude is approximately equal to the resonance amplitude. The experimental data, for a kick of 9 kV or an amplitude of 4.05 mm, are displayed in Fig. 6.16. The curve through the experimental points is a guide to the eye. The different symbols differentiate a coarse scan and a fine scan.

The maximum persistent response is plotted against the kick voltage in Fig. 6.17 for both experimental and tracking data. The dashed line is a theoretical fit to the data. There is obviously a factor of 2 difference between prediction and reality. This discrepancy is due to the sensitivity of the calculation to the lattice function errors, particularly phase and beta function errors. To demonstrate the effect of an error on the relative location of the kicked beam with respect to the island, five plots similar to Fig. 6.4 are given. All these plots illustrate part of the five islands (phase advance between $.4 \times 2\pi$ and $.8 \times 2\pi$) corresponding to sextupole strength of 25 amperes and a tune of 19.415. Furthermore, two kicked beams superimposed on one of the islands are also shown. One of the beams has been kicked with no known errors, while the second one has been kicked in the presence of some error. Specifically, the error in Fig. 6.18 originates from the fact that the sextupole SF22 was turned off when the second (left) beam was kicked. In Fig. 6.19, sextupole SF26 was turned off, leading to a somewhat different relative displacement of the two beams, and in Fig. 6.20

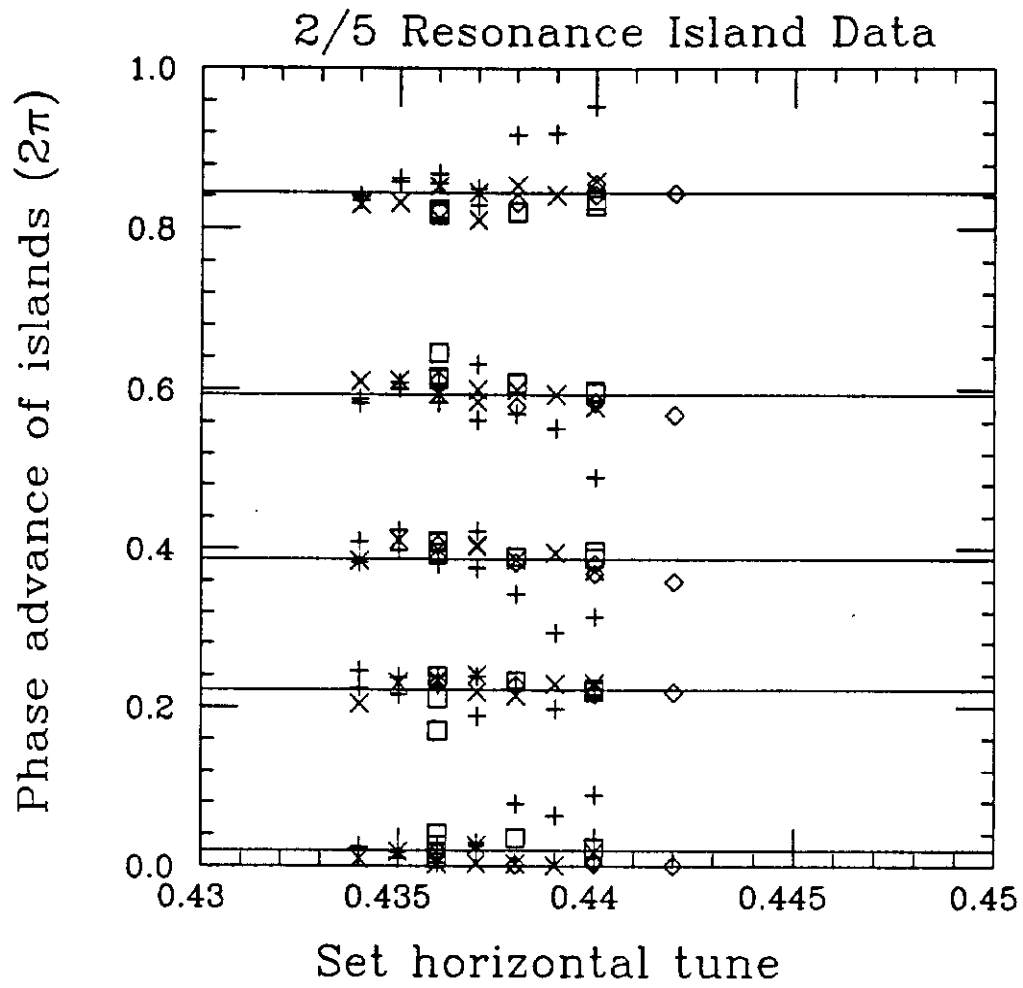


Figure 6.14: Phases of the five islands from experimental data.

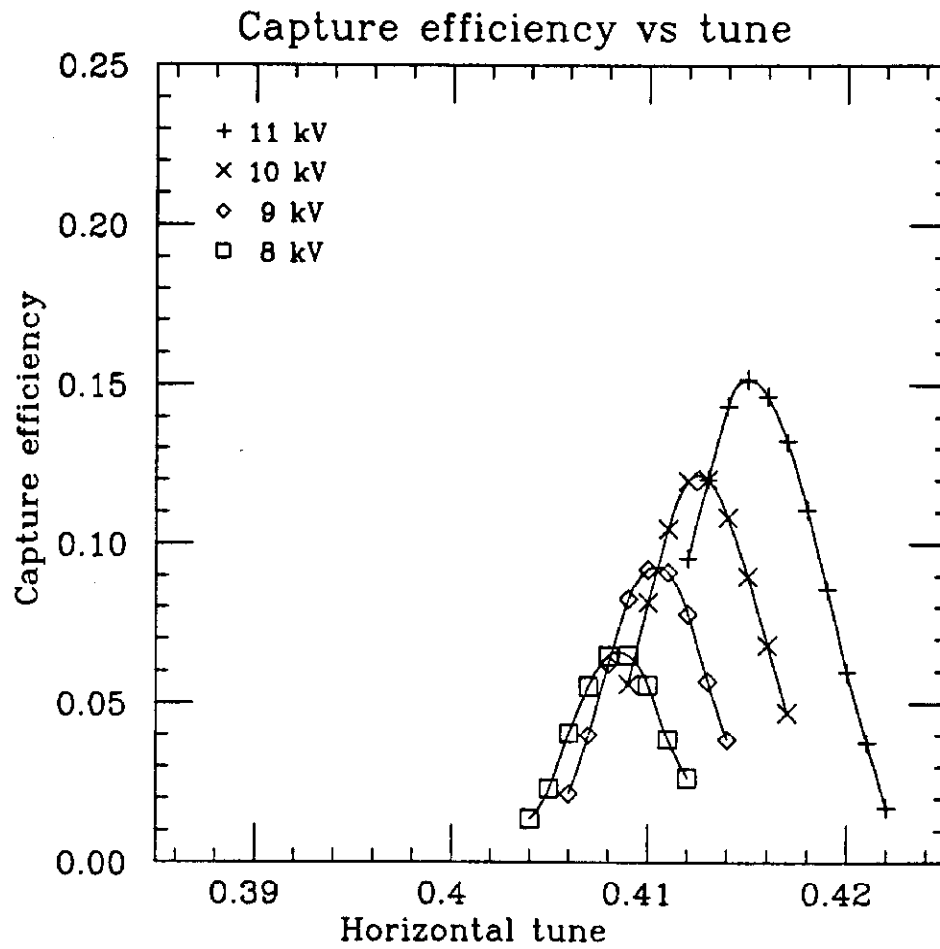


Figure 6.15: Capture efficiency versus tune using EVOL, for 4 different kick amplitudes.

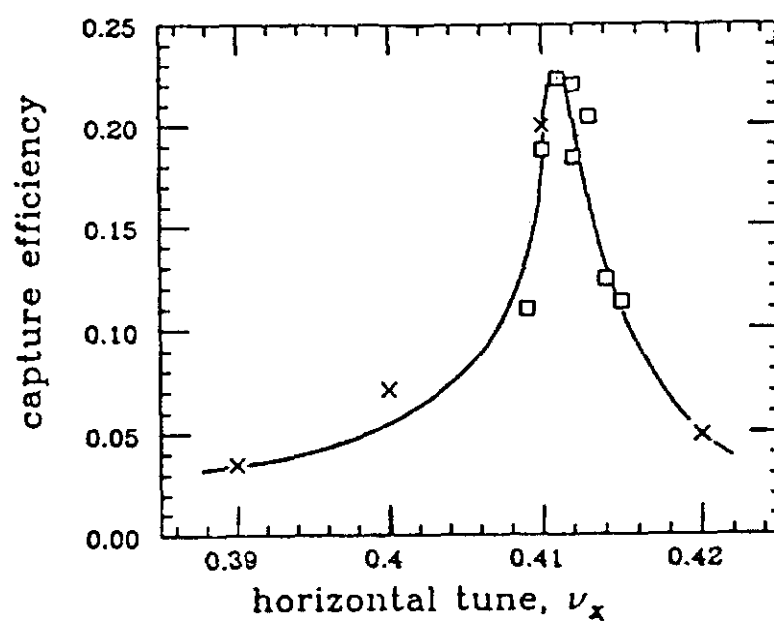


Figure 6.16: Resonant response of the capture fraction as a function of the tune. The curve only guides the eye. The different symbols differentiate a course and a fine scan.

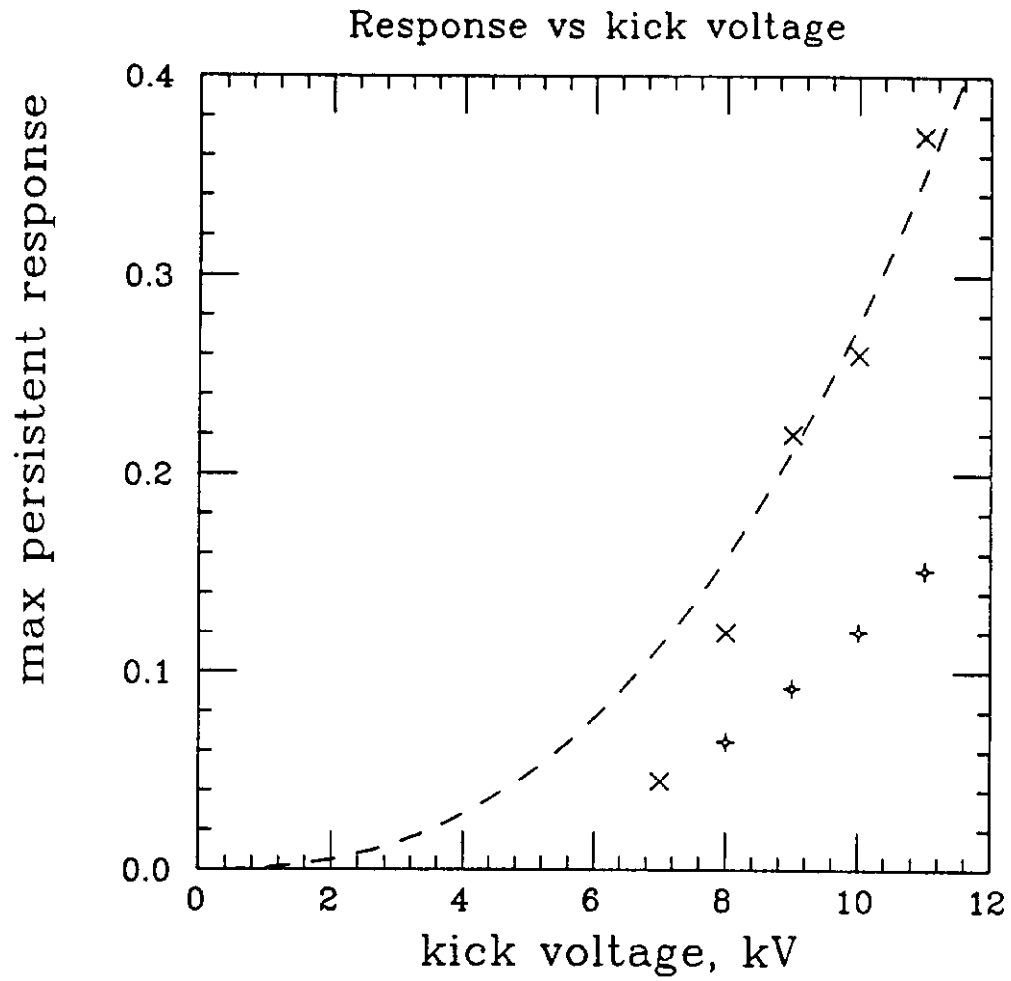


Figure 6.17: Maximum persistent response versus kick amplitude, for the experimental data (crosses) and from simulated data (rhombs). The dashed line is a theoretical fit to the data.

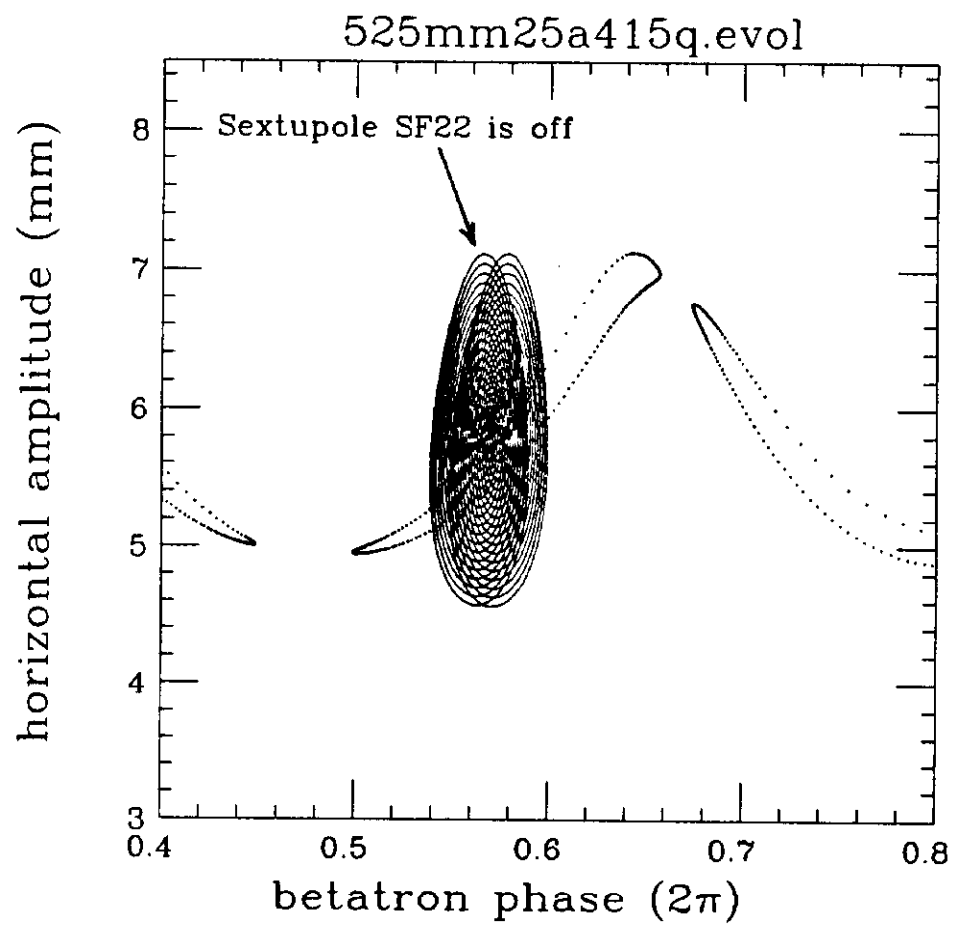


Figure 6.18: The beam on the left has been kicked while sextupole SF22 was turned off.

sextupole SF28 was turned off. In Fig. 6.21 a phase error has been introduced. The relative phase advance between sextupoles SF38 and SC22 is different from the design phase advance by $.04 \times 2\pi$. Notice that the relative displacement of the two beams is, as expected, quite considerable. Finally, a phase error half as big as before, that is $.02 \times 2\pi$, combined with one of the sextupoles turned off (see Fig. 6.22) can lead to an effect of the same magnitude as that of Fig. 6.21.

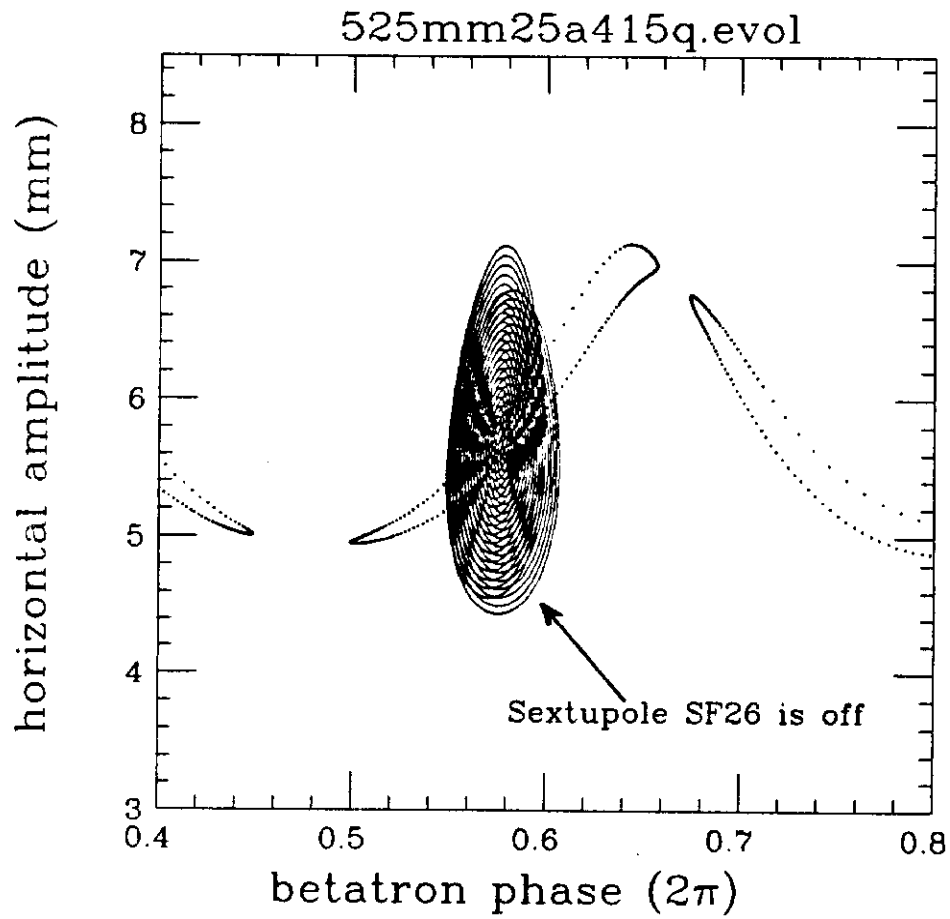


Figure 6.19: The beam on the right has been kicked while sextupole SF26 was turned off.

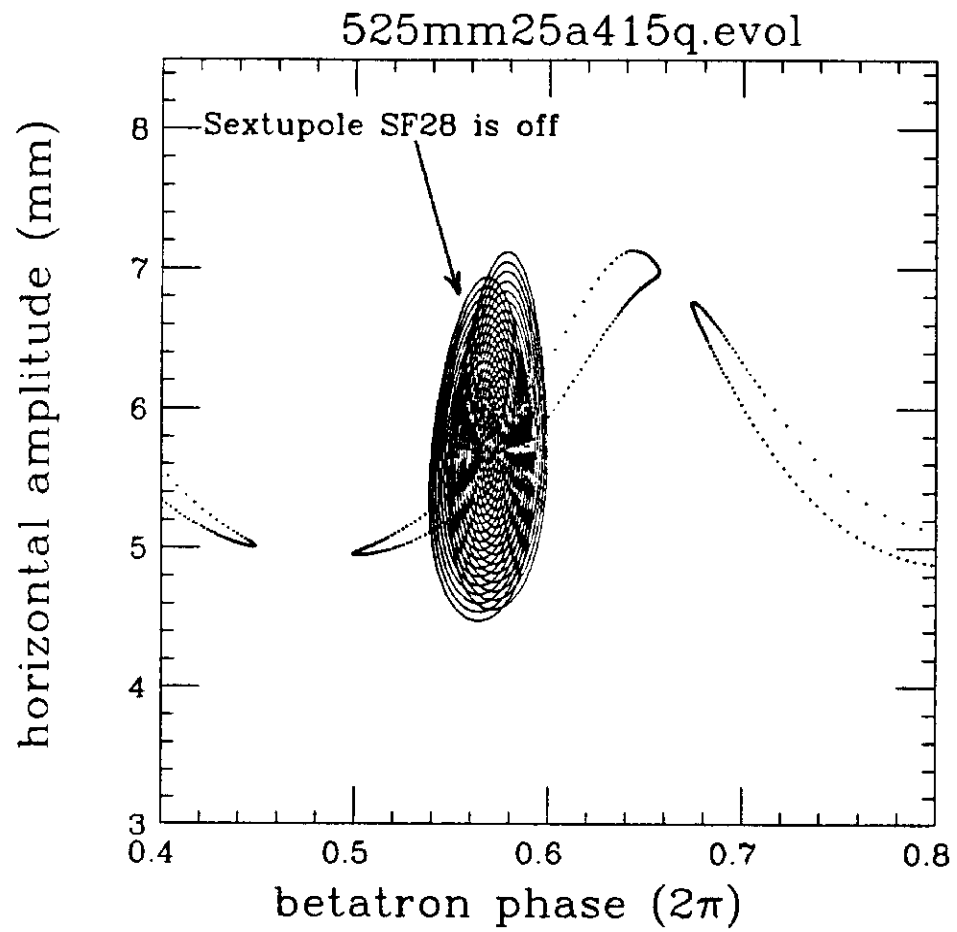


Figure 6.20: The beam on the left has been kicked while sextupole SF28 was turned off.

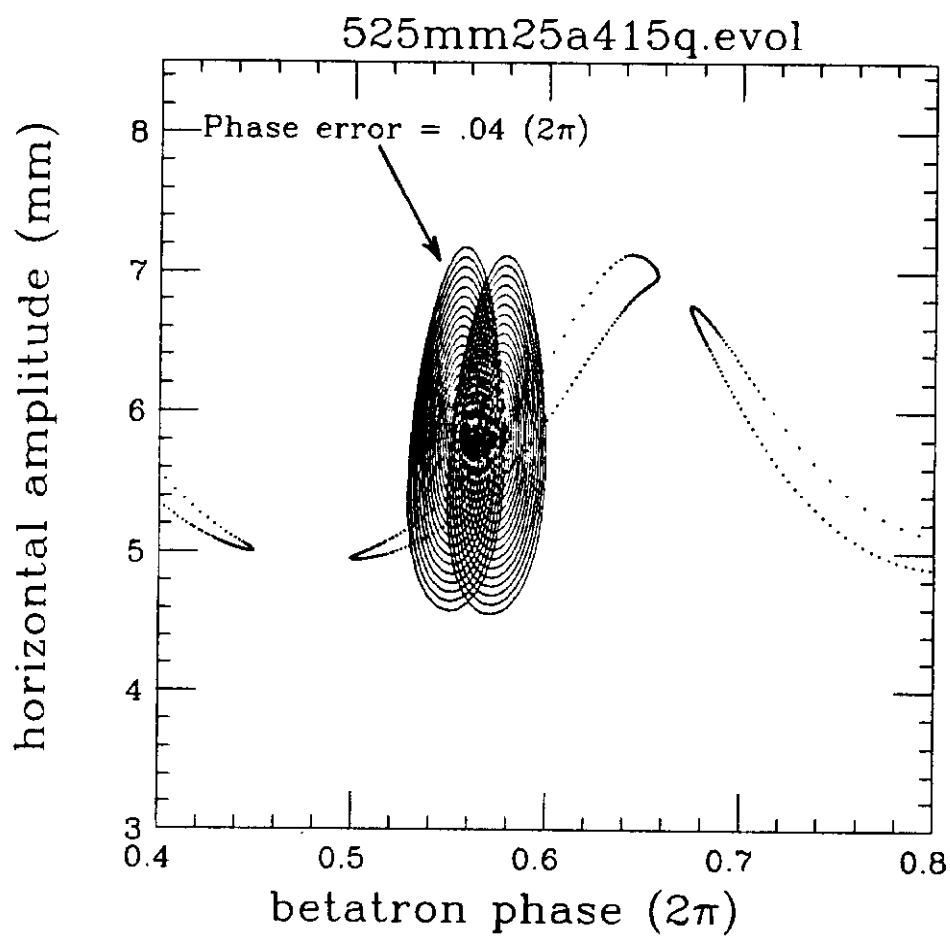


Figure 6.21: The beam on the left has been kicked in the presence of a phase error.

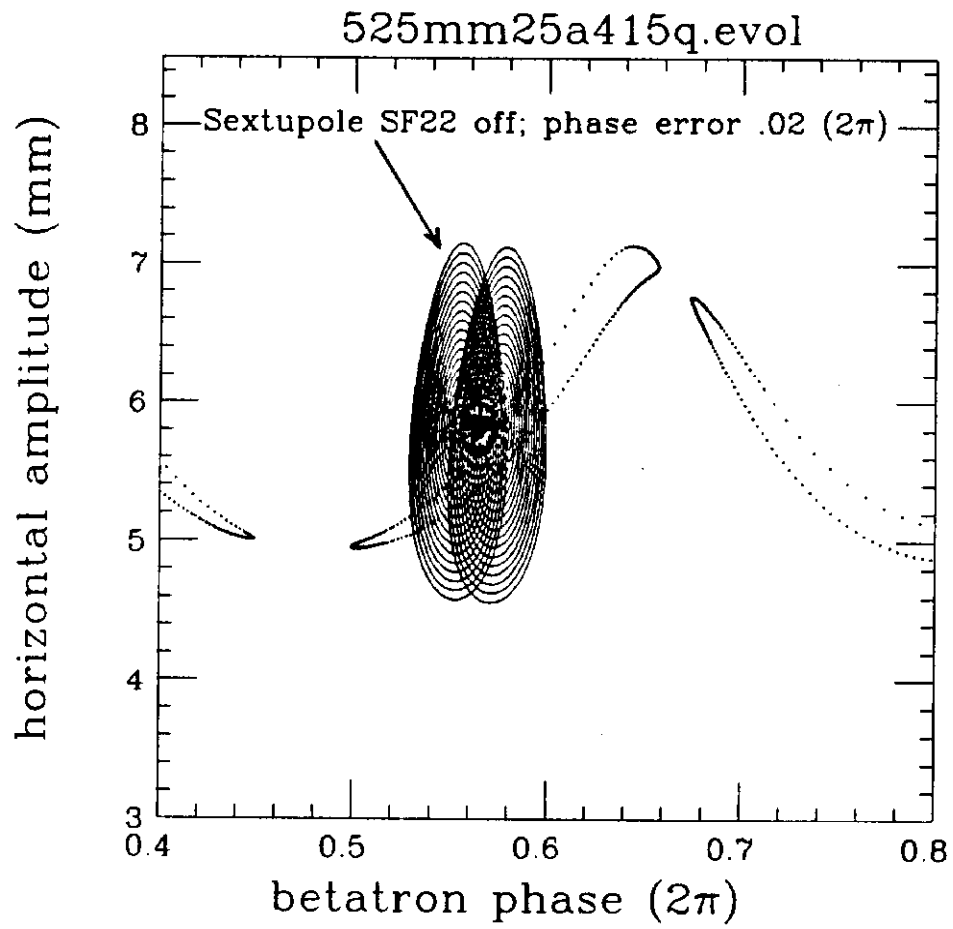


Figure 6.22: The beam on the left has been kicked in the presence of a phase error and of one of the sextupole (SF22) being turned off.

CHAPTER VII

THE DYNAMIC APERTURE EXPERIMENT

In the presence of nonlinearities the motion of a large-amplitude particle loses its regularity and becomes chaotic. Typical phase space trajectories close to the dynamic aperture are shown in Fig. 7.1. This plot was generated by computer simulation using TEAPOT.

Predictions on the size of the dynamic aperture for a given lattice configuration can be obtained from short-term—of the order of 500 turns— tracking of particles. The purpose of this experiment was to measure the dynamic aperture of the Tevatron in the presence of the sixteen strong sextupoles, for various sextupole excitations, and compare the experimental results with the short-term tracking calculations.

The Experiment

The basic experimental procedure consisted of intentionally increasing the horizontal emittance of the 150 GeV injected beam in the Tevatron until particles were lost. The beam ‘heating’ was done by introducing noise into the transverse damper system of the Tevatron. The beam size was then observed with the flying wires. Flying wire scans were usually made four times per cycle, at 32, 62, 82 and 102 seconds after injection. The beam intensity as a function of time is shown in Fig. 7.2. The

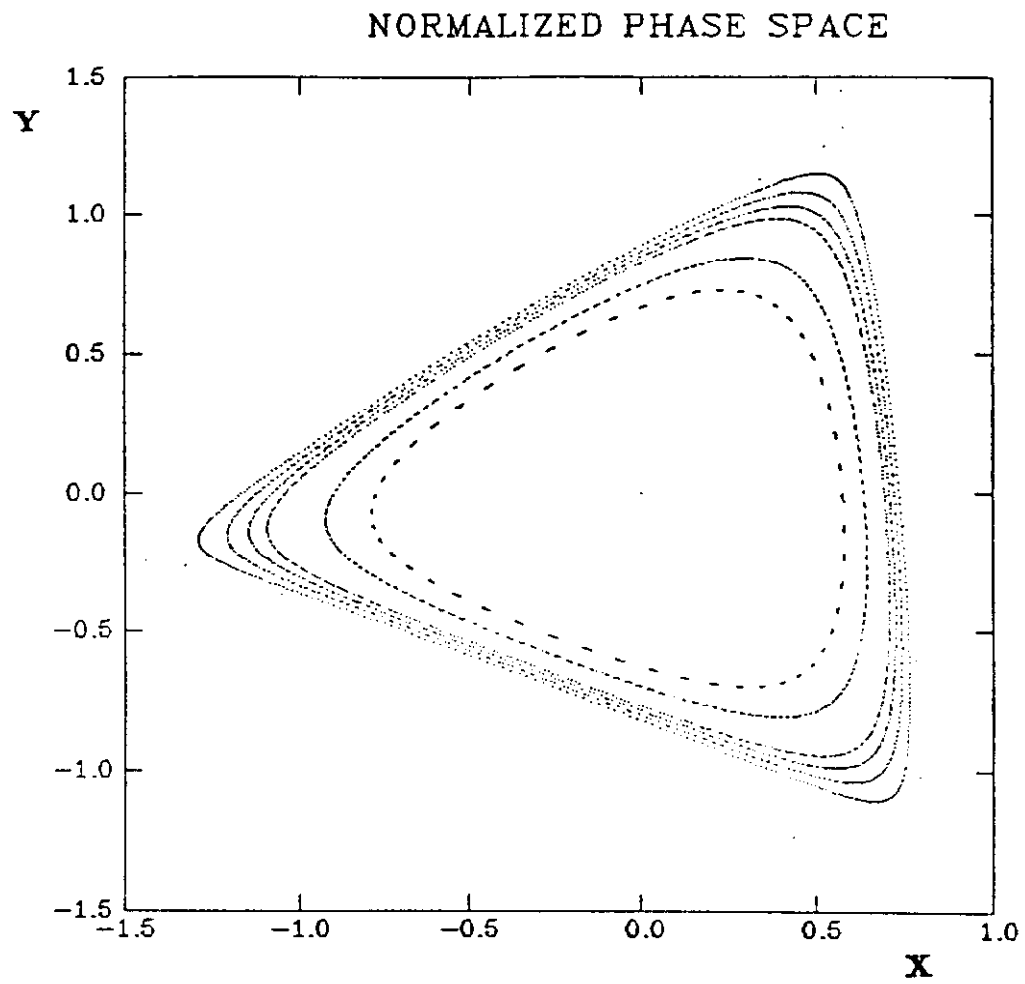


Figure 7.1: Phase space trajectories close to the dynamic aperture.

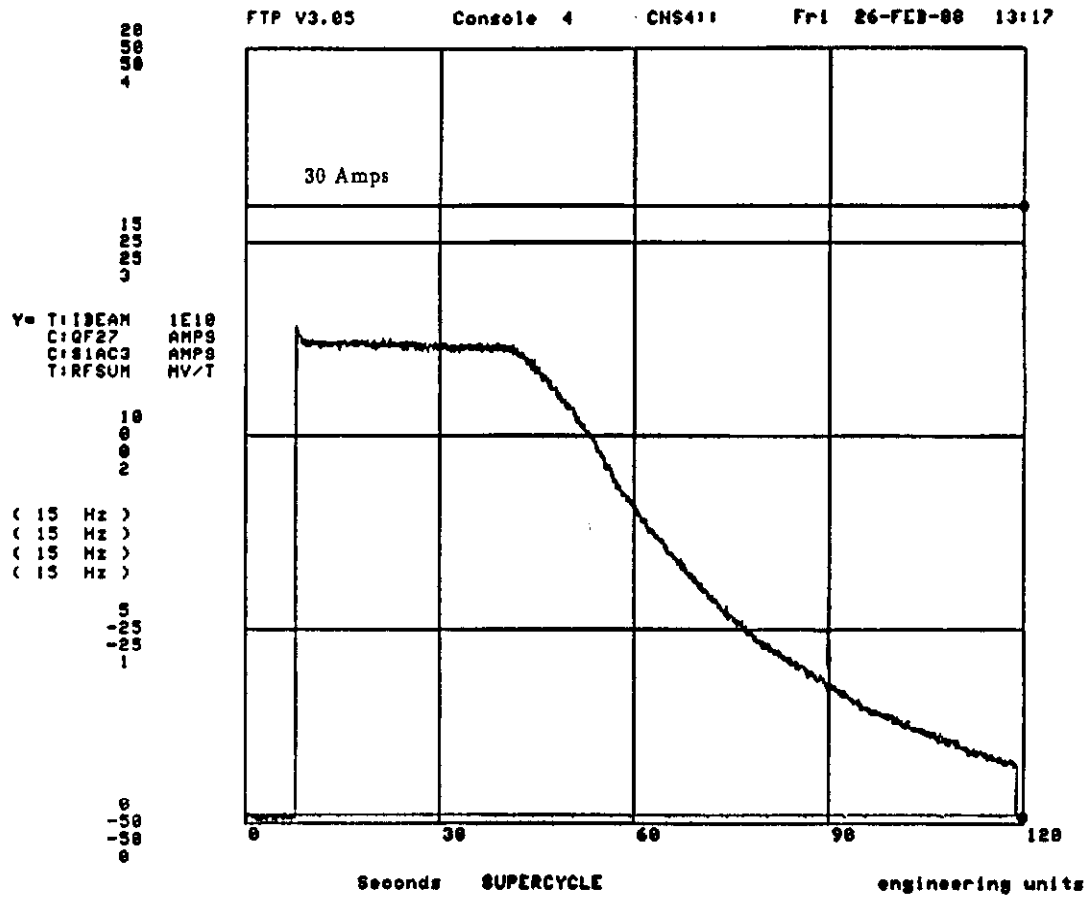


Figure 7.2: Beam intensity versus time for a sextupole excitation of 30 amps.

arrows indicate the times of the flying wire scans. In this case the sextupole strength was 30 amperes.

The horizontal tune of the fixed-target lattice was set at 19.3715 and the vertical tune was set at 19.46. In order to avoid confusion from longitudinal multi-bunch instability, the RF voltage was turned off and the RF cavities detuned. The energy spread, σ_E/E , was measured to be approximately 1.5×10^{-4} , hence the 20-bunch beam was observed to debunch and spread around the ring. By 32 seconds after injection, the beam distribution was fairly uniform as seen from the flying wire scans.

The noise-modulated damper-magnet was turned on at 32 seconds after injection. With no sextupole excitation, beam loss became apparent about 1 minute after turning on the dampers. With 30 amperes in the sextupoles however, beam loss began almost immediately, as shown in Fig. 7.2.

Analysis

Three flying wires were used—two in the horizontal and one in the vertical direction. The two horizontal wires were located at HA17 and HC48 while the vertical was located at VC48. The points of the two horizontal wires have quite different horizontal dispersion; HA17 has a dispersion of 5.04 meters, while HC48 has a dispersion of 1.9 meters. Fig. 7.3 displays a typical set of horizontal beam profiles from the flying wire HC48. The four different curves correspond to the four times the wires were flown within the cycle. Notice that the initially symmetric beam distribution develops eventually a left-right asymmetry. This is understood in the sense that computer simulations were capable of reproducing the asymmetry, as shown in Fig. 7.1. The pronounced triangularity of the same plot, which is actually present in all sextupole excitations, illustrates the dominance of the third-integer resonance.

The vertical-wire profiles revealed no qualitative or quantitative changes, indicating that the horizontal-vertical coupling was not appreciable in this experiment.

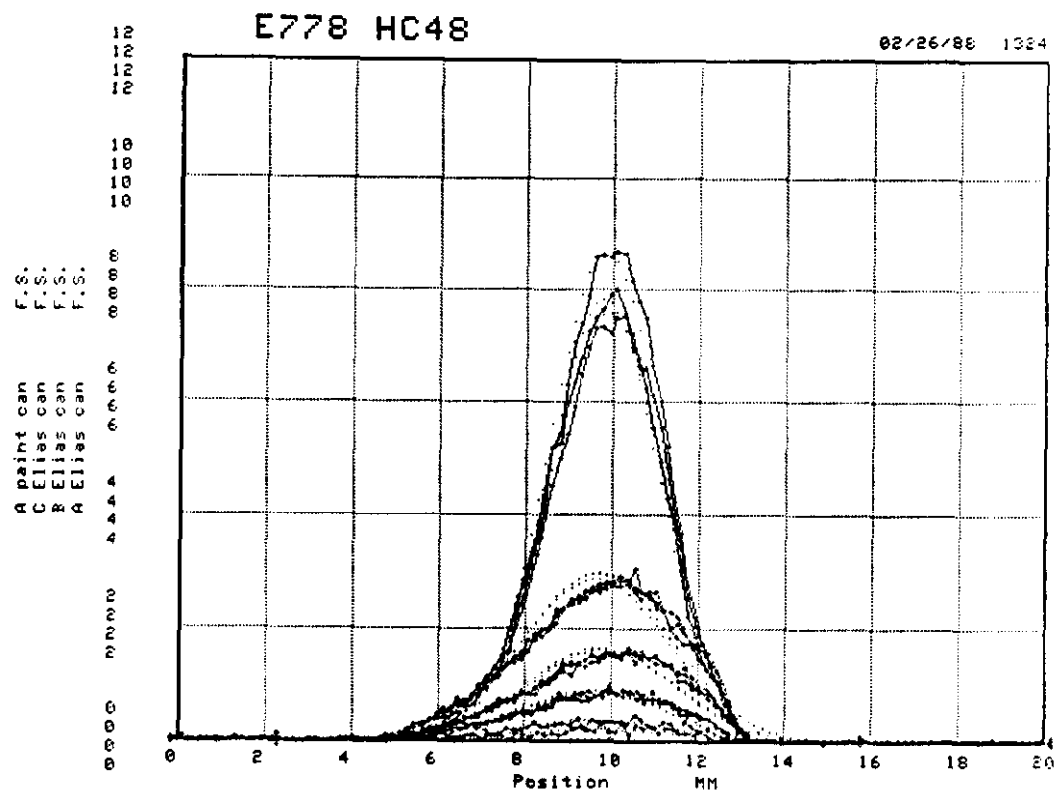


Figure 7.3: Beam profiles taken using the wire profile technique, at the location HC48.

The full-width at the base of the profile was used to measure the dynamic aperture.

Two different codes were employed to predict the dynamic aperture from tracking calculations. The first one, ART, used a simplified lattice which was perfectly linear except for the sixteen special sextupoles. A gaussian distribution of particles in energy with standard deviation $\sigma = 1.5 \times 10^{-4}$ was tracked and the dynamic aperture of the distribution was calculated after 500 turns. The second code, TEAPOT, used the complete fixed-target Tevatron lattice and included the effects of the chromaticity-correction sextupoles. It was found that both codes agreed very well in their predictions, so one can conclude that the chromaticity-correction sextupoles had a negligible effect on the aperture. The calculations were repeated for seven different values of the sextupole excitations: 0, 10, 15, 20, 25, 30 and 40 amperes. Further TEAPOT tracking calculations, done at 15 and 40 amperes in the 16 sextupoles, deemed unlikely that the sextupole component in the superconducting Tevatron dipoles had an effect on the dynamic aperture.

Results

The measured and the calculated dynamic apertures at the positions of the flying wires HC48 and HA17 are shown in Fig. 7.4 and Fig. 7.5 respectively. The agreement at high sextupole excitations is satisfactory. Two effects complicate the comparison between the data points and the curve. First, the calculations were limited to a few hundred turns whereas the data points were extracted after millions of turns. Hence the curve is really an upper bound. Second, an uncertainty in the closed orbit at the sixteen sextupoles affects the machine tune and thus the calculations of the dynamic aperture. A shift in the average closed orbit at the sixteen sextupoles of 0.25 mm will change the computed dynamic aperture by about 3.5 mm at each sextupole setting. This is roughly the deviation between the curve and the data at large sextupole currents.

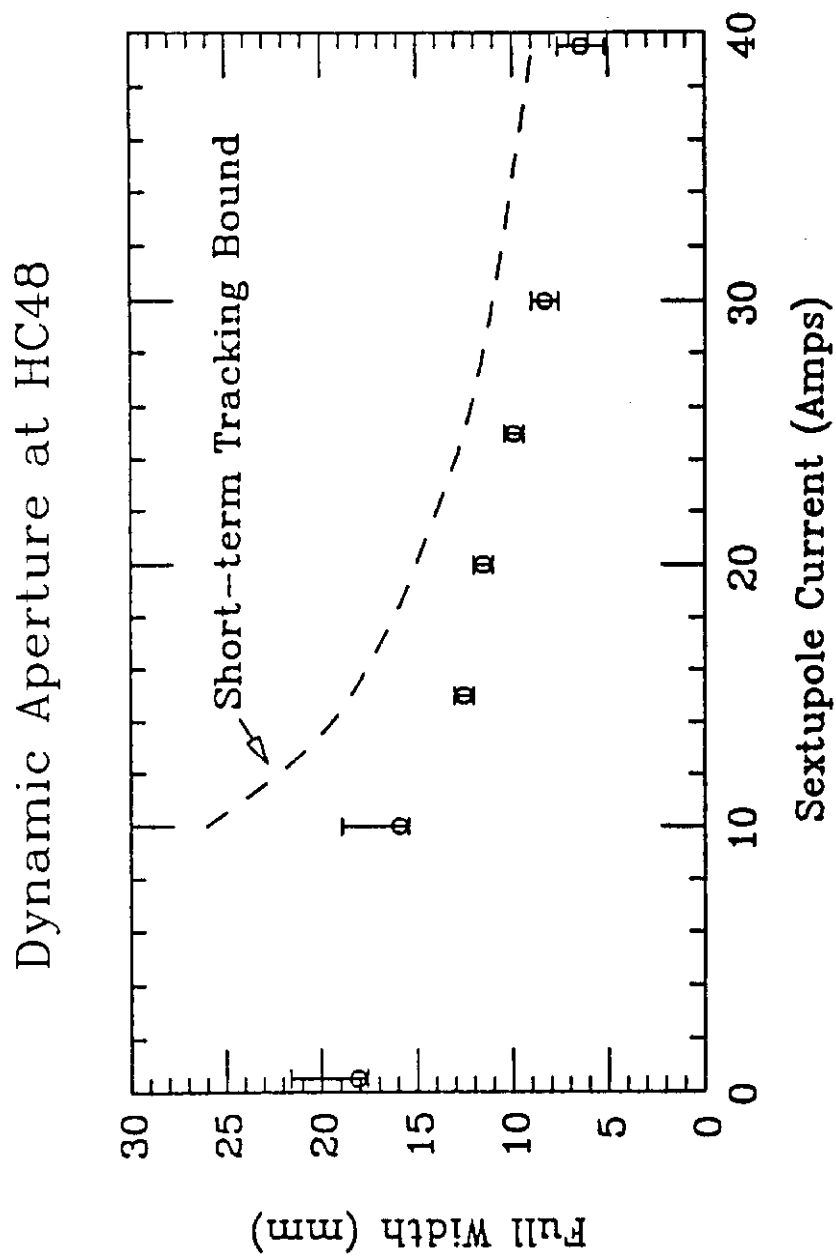


Figure 7.4: Dynamic aperture at HC48. The circles represent the experimental data points while the dashed line was obtained from tracking calculations using TEAPOT and ART.

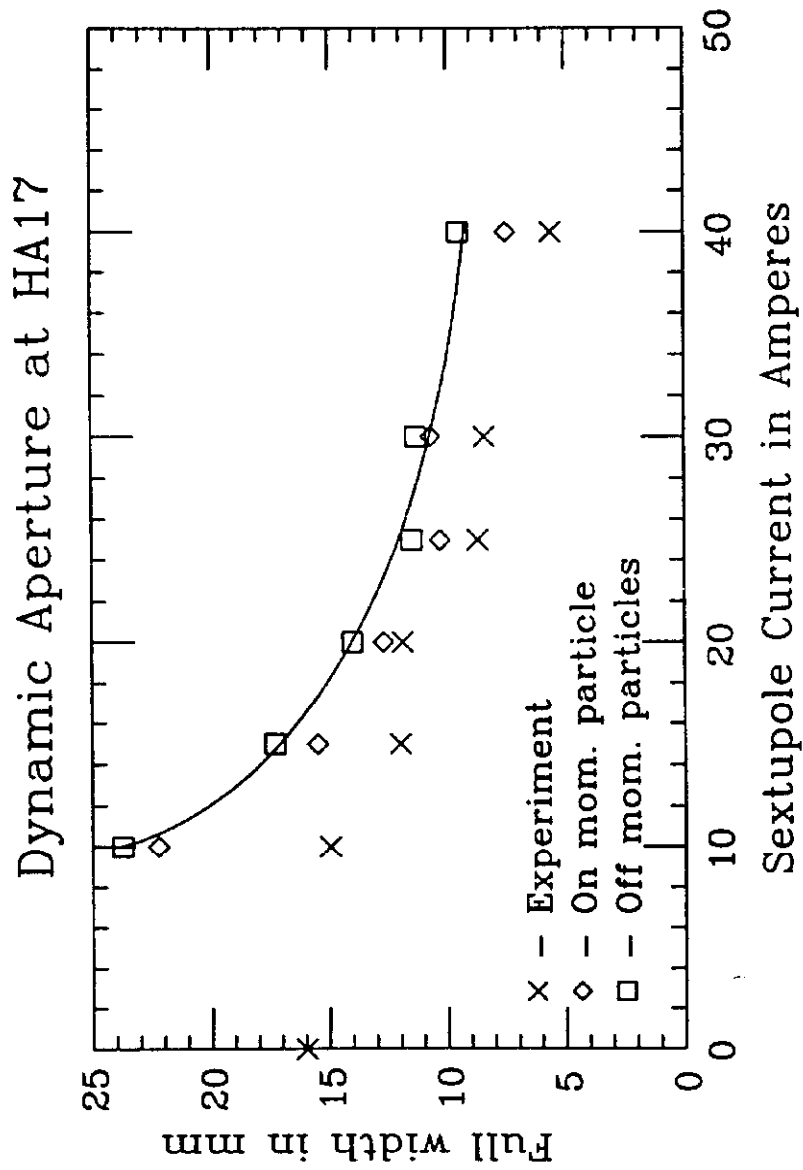


Figure 7.5: Dynamic aperture at HA17. The smooth curve is a fit to the simulated results for off-momentum particles.

Finally the deviation at low sextupole excitations is presumably due to a physical aperture, such as a septum magnet.

CHAPTER VIII

CONCLUDING REMARKS

A nonlinear dynamics experiment has been performed in the Tevatron. The various regions of the phase space have been studied in a three-fold way: experimentally, numerically and analytically.

The first purpose of this experiment was to confront the tracking calculations with experimental observations, in order to test their reliability. After confirming that the Tevatron was essentially linear, smear measurements were performed. From these data, the phase space motion of the centroid of the beam was tracked and quantities such as the smear and the tunes shift were extracted. Multi-particle nonlinear tracking calculations provided predictions of the same quantities. The agreement between experimental results and tracking calculations is excellent, over a wide range of conditions. One can conclude that tracking calculations, which are important in projecting the performance of future accelerators, are reliable.

Furthermore, perturbation theory, in the form of successive Moser transformations, was used to describe analytically this particular region of the phase space. The agreement between analytical predictions and observations is very good for the low current—low kicker amplitude data points, while it deteriorates as one moves to higher currents and kick amplitudes. As expected, nonlinearities of sufficiently low strength can be handled perturbatively.

The second purpose of E778 was to correlate phenomenological accelerator performance with the value of the smear. The first conclusion to be drawn from the injection experiment is that injection diagnosis and correction functioned satisfactorily up to the largest sextupole settings, for a typical injection offset of 1.5 mm. Recordings of the beam intensity as a function of time revealed significant slow losses above a threshold sextupole current. Turning the RF off reduced the losses significantly, while a further reduction was achieved by cooling the cavities.

In the resonance island experiment, E778 demonstrated the existence of stable nonlinear resonance islands by directly observing particles captured into them. Systematic data taking was restricted to the 2/5 resonance. The capture efficiency was measured and compared with simulated results. The factor of two discrepancy between calculation and observations can be explained in terms of the sensitivity of the measurements to phase errors primarily and beta functions errors.

Successive Moser transformations up to third order in the sextupole strength gave rise to the Hamiltonian describing a system under the influence of the 2/5 isolated resonance. An expression was then derived for the island width, which yielded a number reasonably close to single particle tracking prediction. The discrepancy is due to the assumption of an isolated resonance. The island tune, however, as predicted from the analytical calculation agrees very well with the single particle tracking calculation.

The agreement that has been established between calculation and observation, in the resonance island experiment, is worse than in the smear experiment. While in the smear experiment, quantities that vary linearly with the sextupole strength were studied, it is observables proportional to s^3 that were measured in the resonance island experiment. The latter measurements are much more sensitive to errors than the former ones, which explains the different degree of agreement.

In the dynamic aperture experiment, measurements of the dynamic aperture were compared with short-term tracking predictions and the agreement is satisfactory. The

conclusion is that it is generally hard to predict the dynamic aperture; calculations are mostly limited to a few hundred turns whereas data points are usually extracted after millions of turns.

Future plans on the continuation of E778 include the study of the following subjects. In one degree of freedom, a further study of the resonance islands will be attempted, both statically — observation of particle trapping and measurements of island width and island tune — and dynamically — exploration of the stability of the islands under tune modulation [47].

Furthermore the smear measurements will be repeated with different sextupole configurations and hence different values of the smear and the tuneshift.

With the one-degree-of-freedom study more or less completed, the next step is to proceed to the more realistic, and hence more relevant question of nonlinear behavior in two degrees of freedom. An attempt will be made to repeat the smear and the injection experiment, however extraction of the smear and tuneshift parameters from the data can not be as straightforward as in the one-degree-of-freedom case. Coupling between the two planes complicate the situation resulting in a non gaussian decoherence. Recall that the assumption of a gaussian decoherence was a critical element for the extraction of smear and tuneshift from the one-degree-of-freedom data. In two degrees of freedom, extraction of the same information may require a completely different approach, such as working with the Fourier spectra of the signals. A substantial offline effort will have to be put into this subject, before any conclusions can be drawn.

APPENDICES

APPENDIX A

Smear due to horizontal-vertical coupling

It is demonstrated that linear coupling introduces a smear of order $K^2/(\nu_x - \nu_y)^2$, where K is the coupling constant and ν_x, ν_y are the horizontal and vertical tunes respectively. The derivation follows that of Teng in reference [31]. Notice that this entire derivation is valid in the weak coupling approximation [32]: the whole treatment breaks down near the $\nu_x = \nu_y$ resonance.

The approximate coupled equations of motion are

$$x'' + \nu_x^2 x = Ky \quad (\text{A.1})$$

and

$$y'' + \nu_y^2 y = Kx, \quad (\text{A.2})$$

or

$$X'' = MX \quad (\text{A.3})$$

where

$$M = \begin{pmatrix} -\nu_x^2 & K \\ K & -\nu_y^2 \end{pmatrix}. \quad (\text{A.4})$$

Here x, y denote the horizontal and vertical displacement of the particle from the closed orbit. The prime denotes differentiation with respect to θ and

$$K = \frac{R^2}{B\rho} \left\langle \frac{\partial B_x}{\partial x} \right\rangle. \quad (\text{A.5})$$

These equations can be decoupled by diagonalizing M . The eigenvalues of M can be found easily,

$$\nu_u^2 = \nu_x^2 + aK \quad (\text{A.6})$$

and

$$\nu_v^2 = \nu_y^2 - aK, \quad (\text{A.7})$$

where

$$a \equiv \sqrt{1 + \xi^2} - \xi \quad (\text{A.8})$$

and

$$\xi \equiv \frac{\nu_x^2 - \nu_y^2}{2K}. \quad (\text{A.9})$$

The normal coordinates u and v are given by

$$u = x - ay \quad (\text{A.10})$$

and

$$v = ax + y \quad (\text{A.11})$$

and obey the decoupled equations

$$u'' + \nu_u^2 u = 0 \quad (\text{A.12})$$

and

$$v'' + \nu_v^2 v = 0. \quad (\text{A.13})$$

Consider now the special solution that corresponds to the case with x -motion only, i.e. $x = 1$, $x' = 0$, $y = y' = 0$ at $\theta = 0$. This is

$$x = \frac{1}{1 + a^2} (\cos \nu_u \theta + a^2 \cos \nu_v \theta) \quad (\text{A.14})$$

$$y = \frac{a}{1 + a^2} (\cos \nu_v \theta - \cos \nu_u \theta). \quad (\text{A.15})$$

Define $\bar{\nu}$ and μ such that

$$\nu_u = \bar{\nu} + \frac{\mu}{2} \quad (\text{A.16})$$

and

$$\nu_v = \bar{\nu} - \frac{\mu}{2}; \quad (\text{A.17})$$

that is,

$$\bar{\nu} \equiv \frac{\nu_u + \nu_v}{2} \quad (\text{A.18})$$

and

$$\mu \equiv \nu_u - \nu_v. \quad (\text{A.19})$$

Then (A.14) and (A.15) become

$$x = \left(\cos \frac{\mu}{2} \theta \right) \cos \bar{\nu} \theta - \left(\frac{1 - a^2}{1 + a^2} \sin \frac{\mu}{2} \theta \right) \sin \bar{\nu} \theta \quad (\text{A.20})$$

and

$$y = \left(\frac{2a}{1 + a^2} \sin \frac{\mu}{2} \theta \right) \sin \bar{\nu} \theta. \quad (\text{A.21})$$

Hence x and y are amplitude-modulated oscillations. The amplitudes of the x and y oscillations, \mathcal{A}_x and \mathcal{A}_y , are given by

$$\mathcal{A}_x^2 = \frac{1}{(1 + a^2)^2} (1 + a^4 + 2a^2 \cos \mu \theta) \quad (\text{A.22})$$

and

$$\mathcal{A}_y^2 = \frac{2a^2}{(1 + a^2)^2} (1 - \cos \mu \theta). \quad (\text{A.23})$$

Then the smear in the horizontal direction due to coupling, s_{cx} , is given by

$$s_{cx} = \frac{\sqrt{\langle \mathcal{A}_x^2 \rangle - \langle \mathcal{A}_x \rangle^2}}{\langle \mathcal{A}_x \rangle}, \quad (\text{A.24})$$

where \mathcal{A}_x is given by Eq. (A.22).

The calculation of the smear s_{cx} will be done in the weak coupling approximation, i.e., to lowest nonvanishing order in $K/(\nu_x - \nu_y)$.

Notice that

$$a \equiv \sqrt{1 + \xi^2} - \xi \simeq \frac{K}{\nu_x - \nu_y} \quad (\text{A.25})$$

in the weak coupling approximation. So \mathcal{A}_x can be expanded in powers of a . The result is

$$\mathcal{A}_x = 1 - a^2(1 - \cos \mu\theta) + \frac{3a^4}{2}(1 - \cos \mu\theta) + \dots \quad (\text{A.26})$$

From here one gets

$$\langle \mathcal{A}_x \rangle = 1 - a^2 + \frac{5a^4}{4} + \dots, \quad (\text{A.27})$$

$$\langle \mathcal{A}_x \rangle^2 = 1 - 2a^2 + \frac{7a^4}{2} + \dots \quad (\text{A.28})$$

and

$$\langle \mathcal{A}_x^2 \rangle = 1 - 2a^2 + 4a^4 + \dots \quad (\text{A.29})$$

So,

$$s_{cx} \sim a^2 \sim \frac{K^2}{(\nu_x - \nu_y)^2}. \quad (\text{A.30})$$

APPENDIX B

Derivation of the expression for the amplitude

Let a_{x1} and a_{x2} be the amplitudes of the betatron oscillations at the location of the two BPMs. Also let β_{x1} , β_{x2} and $(\phi - \delta)$, $(\phi + \delta)$ denote the beta functions and the phases at the two BPMs. The phase ϕ is defined as the phase advance in the middle of the two BPMs while $\delta = \phi_{\text{cell}}/2$. If a_x is defined to be the geometric mean of a_{x1} and a_{x2} then one can prove that

$$a_x^2 = c_{11}x_1^2 + c_{12}x_1x_2 + c_{22}x_2^2, \quad (\text{B.1})$$

where c_{11} , c_{12} and c_{22} are defined by

$$c_{11} = \frac{1}{\sin^2(\phi_{\text{cell}})} \sqrt{\frac{\beta_{x2}}{\beta_{x1}}}, \quad (\text{B.2})$$

$$c_{22} = \frac{1}{\sin^2(\phi_{\text{cell}})} \sqrt{\frac{\beta_{x1}}{\beta_{x2}}}, \quad (\text{B.3})$$

$$c_{12} = -2 \frac{\cos(\phi_{\text{cell}})}{\sin^2(\phi_{\text{cell}})}. \quad (\text{B.4})$$

The displacements of the centroid of the beam from the closed orbit at the two BPMs, x_1 and x_2 are given by

$$x_1 = a_{x1} \cos(\phi - \delta) \quad (\text{B.5})$$

and

$$x_2 = a_{x2} \cos(\phi + \delta). \quad (\text{B.6})$$

Since $a_x^2 = a_{x1}a_{x2}$, a_{x1}, a_{x2} can be expressed in terms of a_x as follows

$$a_{xi} = \frac{a_x \sqrt{\beta_{xi}}}{(\beta_{x1}\beta_{x2})^{1/4}} \quad i = 1, 2. \quad (\text{B.7})$$

Hence

$$x_1 = \frac{a_x \sqrt{\beta_{x1}}}{(\beta_{x1} \beta_{x2})^{1/4}} \cos(\phi - \delta), \quad (\text{B.8})$$

$$x_2 = \frac{a_x \sqrt{\beta_{x2}}}{(\beta_{x1} \beta_{x2})^{1/4}} \cos(\phi + \delta); \quad (\text{B.9})$$

from these two equations the above expression for the amplitude a_x will be derived.

First ϕ is eliminated from the expressions for x_1 and x_2 . Eqs (B.8) and (B.9) give

$$\frac{x_1}{\sqrt{\beta_{x1}}} - \frac{x_2}{\sqrt{\beta_{x2}}} = \frac{a_x}{(\beta_{x1} \beta_{x2})^{1/4}} [\cos(\phi - \delta) - \cos(\phi + \delta)] \quad (\text{B.10})$$

or

$$\frac{x_1}{\sqrt{\beta_{x1}}} - \frac{x_2}{\sqrt{\beta_{x2}}} = \frac{a_x}{(\beta_{x1} \beta_{x2})^{1/4}} 2 \sin \phi \sin \delta. \quad (\text{B.11})$$

Solving for $\sin \phi$, one gets

$$\sin \phi = \frac{(\beta_{x1} \beta_{x2})^{1/4}}{2a_x \sin \delta} \left[\frac{x_1}{\sqrt{\beta_{x1}}} - \frac{x_2}{\sqrt{\beta_{x2}}} \right]. \quad (\text{B.12})$$

Substituting $\sin \phi$ from (B.12) into (B.8) and then solving for $\cos \phi$ leads to,

$$\cos \phi = \frac{(\beta_{x1} \beta_{x2})^{1/4}}{2a_x \cos \delta} \left[\frac{x_1}{\sqrt{\beta_{x1}}} + \frac{x_2}{\sqrt{\beta_{x2}}} \right]. \quad (\text{B.13})$$

By squaring (B.12) and (B.13) and summing one gets the desired expression for the amplitude

$$a_x^2 = \frac{1}{\sin^2(\phi_{\text{cell}})} \sqrt{\frac{\beta_{x2}}{\beta_{x1}}} x_1^2 - 2 \frac{\cos(\phi_{\text{cell}})}{\sin^2(\phi_{\text{cell}})} x_1 x_2 + \frac{1}{\sin^2(\phi_{\text{cell}})} \sqrt{\frac{\beta_{x1}}{\beta_{x2}}} x_2^2 \quad (\text{B.14})$$

or

$$a_x^2 = c_{11} x_1^2 + c_{12} x_1 x_2 + c_{22} x_2^2. \quad (\text{B.15})$$

APPENDIX C

Derivation of the expression for the phase advance

The displacements from the closed orbit at the two BPMs are

$$x_1 = \frac{a_x \sqrt{\beta_{x1}}}{(\beta_{x1} \beta_{x2})^{1/4}} \sin(\phi - \delta) \quad (\text{C.1})$$

and

$$x_2 = \frac{a_x \sqrt{\beta_{x2}}}{(\beta_{x1} \beta_{x2})^{1/4}} \sin(\phi + \delta). \quad (\text{C.2})$$

Let z_1, z_2 be defined as

$$z_i = \frac{x_i}{\sqrt{\beta_{xi}}} \quad i = 1, 2. \quad (\text{C.3})$$

Then

$$z_{1,2} = \frac{a_x}{(\beta_{x1} \beta_{x2})^{1/4}} \sin(\phi \pm \delta) \quad (\text{C.4})$$

and

$$\frac{(z_1 + z_2)/\cos \delta}{(z_2 - z_1)/\sin \delta} = \frac{[\sin(\phi - \delta) + \sin(\phi + \delta)] \sin \delta}{[\sin(\phi + \delta) - \sin(\phi - \delta)] \cos \delta} = \tan \phi. \quad (\text{C.5})$$

Hence

$$\phi = \arctan \left(\frac{(z_1 + z_2)/\cos \delta}{(z_2 - z_1)/\sin \delta} \right). \quad (\text{C.6})$$

APPENDIX D

Derivation of decoherence due to nonlinearity

Let a and ϕ be the amplitude and phase of the betatron oscillation at a given point in the accelerator. The amplitude a is defined as $\sqrt{\beta\epsilon}/\sigma_x$, where ϵ is the Courant-Snyder invariant and σ_x is the rms beam size. Then the displacement x is

$$x = a\sigma_x \cos(2\pi\nu n + \phi),$$

where n is the turn number. ϕ is the phase advance at $n = 0$.

The transverse distribution of particles in the beam, expressed in terms of x and x' is

$$\rho(x, x') dx dx' = \frac{\beta}{2\pi\sigma_x^2} e^{-\frac{1}{2\sigma_x^2}[x^2 + (\alpha x + \beta x')^2]} dx dx'$$

and in amplitude-angle coordinates

$$dx dx' = \frac{1}{\beta} a \sigma_x^2 da d\phi,$$

thus

$$\rho(a, \phi) da d\phi = \frac{1}{2\pi} a e^{-\frac{a^2}{2}} da d\phi.$$

Suppose now that at $n = 0$ the beam is kicked by an angle $\Delta x'$. This kick corresponds to a shift in amplitude of magnitude $a_0 = \beta\Delta x'/\sigma_x$, and the new distribution function becomes

$$\begin{aligned} \rho(a, \phi) &= \frac{1}{2\pi} a e^{-\frac{(\vec{a} - \vec{a}_0)^2}{2}} \\ &= \frac{1}{2\pi} a e^{-\frac{(a^2 + a_0^2 - 2aa_0 \cos \phi)}{2}}. \end{aligned}$$

Assuming a quadratic tune dependence on amplitude

$$\nu = \nu_0 - \mu a^2$$

one finds that the phase shift $\Delta\phi(a, n)$ of a particle of amplitude a is

$$\Delta\phi(a, n) = 2\pi\Delta\nu n = -2\pi\mu a^2 n.$$

The centroid of the beam after n turns, $\bar{x}(n)$, is

$$\begin{aligned}\bar{x}(n) &= \int x(a, \phi, n) \rho(a, \phi) da d\phi \\ &= \frac{1}{2\pi} \sigma_x \int_0^\infty da a^2 e^{-\frac{(a^2 + a_0^2)}{2}} \int_0^{2\pi} d\phi \cos [2\pi\nu_0 n + \Delta\phi(a, n) + \phi] e^{aa_0 \cos \phi} \\ &= \frac{\sigma_x}{2\pi} \int_0^\infty da a^2 e^{-\frac{(a^2 + a_0^2)}{2}} \int_0^{2\pi} d\phi [\cos(2\pi\nu_0 n + \Delta\phi) \cos \phi \\ &\quad - \sin(2\pi\nu_0 n + \Delta\phi) \sin \phi] e^{aa_0 \cos \phi} \\ &= \frac{\sigma_x}{2\pi} \int_0^\infty da a^2 e^{-\frac{a^2 + a_0^2}{2}} \cos(2\pi\nu_0 n - 2\pi\mu a^2 n) \int_0^{2\pi} d\phi \cos \phi e^{aa_0 \cos \phi} \\ &\quad - \frac{\sigma_x}{2\pi} \int_0^\infty da a^2 e^{-\frac{a^2 + a_0^2}{2}} \sin(2\pi\nu_0 n - 2\pi\mu a^2 n) \int_0^{2\pi} d\phi \sin \phi e^{aa_0 \cos \phi}.\end{aligned}$$

With the use of the identity

$$e^{r \cos \phi} = \sum_{m=-\infty}^{\infty} e^{im\phi} I_m(r)$$

the above formula becomes

$$\begin{aligned}\bar{x}(n) &= \frac{\sigma_x}{2\pi} \int_0^\infty da a^2 e^{-\frac{a^2 + a_0^2}{2}} \cos(2\pi\nu_0 n - 2\pi\mu a^2 n) \sum_m I_m(aa_0) \int_0^{2\pi} d\phi \cos \phi e^{im\phi} \\ &\quad - \frac{\sigma_x}{2\pi} \int_0^\infty da a^2 e^{-\frac{a^2 + a_0^2}{2}} \sin(2\pi\nu_0 n - 2\pi\mu a^2 n) \sum_m I_m(aa_0) \int_0^{2\pi} d\phi \sin \phi e^{im\phi}.\end{aligned}$$

But

$$\sum_m I_m(aa_0) \int_0^{2\pi} d\phi e^{im\phi} \cos \phi = \pi [I_1(aa_0) + I_{-1}(aa_0)] = 2\pi I_1(aa_0)$$

and

$$\sum_m I_m(aa_0) \int_0^{2\pi} d\phi e^{im\phi} \sin \phi = \pi i [I_1(aa_0) - I_{-1}(aa_0)] = 0.$$

Hence

$$\begin{aligned}
 \bar{x}(n) &= \sigma_x \int_0^\infty da a^2 e^{-\frac{a^2 + a_0^2}{2}} \cos(2\pi\nu_0 n - 2\pi\mu a^2 n) I_1(aa_0) \\
 &= \sigma_x e^{-\frac{a_0^2}{2}} \operatorname{Re} \left\{ e^{i2\pi\nu_0 n} \int_0^\infty da a^2 e^{-a^2(1/2 + i2\pi\mu n)} I_1(aa_0) \right\} \\
 &= \sigma_x e^{-\frac{a_0^2}{2}} \operatorname{Re} \left\{ e^{i2\pi\nu_0 n} \int_0^\infty da a^2 e^{-a^2(1/2 + i2\pi\mu n)} (-i) J_1(iaa_0) \right\},
 \end{aligned}$$

where the relation between I_m and J_m has been used

$$I_m(z) = i^{-m} J_m(iz).$$

Now one can evaluate the last integral above with the use of formula 6.631.4 from Gradshteyn and Ryzhik

$$\int_0^\infty x^{\nu+1} e^{-\alpha x^2} J_\nu(\beta x) dx = \frac{\beta^\nu}{(2\alpha)^{\nu+1}} e^{-\beta^2/4\alpha}.$$

In this case $\nu = 1$, $\alpha = 1/2 + i2\pi\mu n$ and $\beta = ia_0$ and so,

$$\begin{aligned}
 \bar{x}(n) &= \sigma_x e^{-\frac{a_0^2}{2}} \operatorname{Re} \left\{ e^{i2\pi\nu_0 n} \frac{a_0}{(1 + i4\pi\mu n)^2} \exp \left[-\frac{(ia_0)^2}{2 + i8\pi\mu n} \right] \right\} \\
 &= \sigma_x e^{-\frac{a_0^2}{2}} \operatorname{Re} \left\{ e^{i2\pi\nu_0 n} \frac{a_0}{(1 + i\theta)^2} \exp \left[\frac{a_0^2}{2(1 + i\theta)} \right] \right\},
 \end{aligned}$$

where θ is defined as follows

$$\theta = 4\pi\mu n.$$

So

$$\begin{aligned}
 \bar{x}(n) &= \sigma_x \exp \left(\frac{a_0^2}{2} \right) a_0 \operatorname{Re} \left\{ \frac{(1 - i\theta)^2}{(1 + \theta)^2} \exp(i2\pi\nu_0 n) \exp \left[\frac{a_0^2}{2} \frac{(1 - i\theta)}{(1 + \theta^2)} \right] \right\} \\
 &= \frac{\sigma_x a_0}{(1 + \theta^2)^2} \exp \left[-\frac{a_0^2}{2} \frac{\theta^2}{1 + \theta^2} \right] \left[(1 - \theta^2) \cos \left(2\pi\nu_0 n - \frac{a_0^2}{2} \frac{\theta}{1 + \theta^2} \right) \right. \\
 &\quad \left. + 2\theta \sin \left(2\pi\nu_0 n - \frac{a_0^2}{2} \frac{\theta}{1 + \theta^2} \right) \right] \\
 &= \sigma_x \bar{a}(n) \left[\frac{1 - \theta^2}{1 + \theta^2} \cos \left(2\pi\nu_0 n - \frac{a_0^2}{2} \frac{\theta}{1 + \theta^2} \right) + \frac{2\theta}{1 + \theta^2} \sin \left(2\pi\nu_0 n - \frac{a_0^2}{2} \frac{\theta}{1 + \theta^2} \right) \right] \\
 &= \sigma_x \bar{a}(n) \cos \left(2\pi\nu_0 n - \frac{a_0^2}{2} \frac{\theta}{1 + \theta^2} - 2\arctan\theta \right),
 \end{aligned}$$

where the decoherence factor $A(n)$ is given by

$$A(n) = \frac{1}{1 + \theta^2} \exp \left[-\frac{a_0^2}{2} \frac{\theta^2}{1 + \theta^2} \right]$$

and the amplitude of the centroid $\bar{a}(n)$ is

$$\bar{a}(n) = a_0 A(n).$$

Hence the decoherence factor $A(n)$ is

$$A(n) = \frac{1}{1 + (4\pi\mu n)^2} \exp \left[-\frac{1}{2} (4\pi\mu n a_0)^2 \frac{1}{1 + (4\pi\mu n)^2} \right].$$

For small kicks, $a_0 \ll 1$,

$$A(n) \simeq \frac{1}{1 + (4\pi\mu n)^2},$$

while for a kick much greater than the beam size, $a_0 \gg 1$

$$A(n) \simeq e^{-\frac{1}{2} (4\pi\mu n a_0)^2}.$$

Hence the decoherence rate R , defined by (4.37) is given by

$$R = 4\pi\mu a_0. \tag{D.1}$$

APPENDIX E

TEVEX Subroutines

A. RDCMD

1. Subroutine RDCMD first opens the output file TEVEX.OUT (unit 7) which will develop to a record of the data analysis.
2. Next it opens the input file TEVEX.CMD and reads the following information.

2a. Input control parameters

a1. *ifmt* specifies the input format to be read. Six different formats have been considered. For E778 ASCII files, *ifmt*=0. For E778 shared memory data, *ifmt*=1. For EVOL data, *ifmt*=2. For TPOT-TeVbpm data, *ifmt*=3. For TEAPOT data, *ifmt*=4 and for camac 5 (resonant BPM) data, *ifmt*=5.

a2. *ihead* is the number of header lines stripped off the input files. *Ihead*=8 or 12 for E778 ASCII files, *ihead*=16 for EVOL data, *ihead*=7 for TEAPOT data, and *ihead* could be anything for the remaining cases.

a3. *bnoise*, expressed in mm, determines the lowest bound for the real data to start, e.g., *bnoise*=0.2.

2b. Fast pass default values

- b1. *batch*, logical variable. If it is true the input filenames are read from INFILS.
- b2. *fast*, logical variable. If it is true, it invokes the default values in the array,
- b3. *ifast(1-6)*, instead of prompting the user. All the above are to be used for a fast pass through the data.
- b4. *infiles* contains the BATCH input filenames.

2c. Filtering input and output data

- c1. *filtre*, logical variable. If it is true, it filters tune values from *qmin* to *qmax* from both horizontal position raw data and from the intensity data.
- c2. *qmin* is the lower limit of the filtered range.
- c3. *qmax* is the upper limit of the filtered range.

2d. Persistent signal analysis

- d1. *persig*, logical variable. If it is true, it turns the persistent signal analysis on.
- d2. *npsmin* is the lower limit of a post-decoherence range where the persistent signal analysis will be done.
- d3. *npsmax* is the upper limit of the range for persistent signal analysis.

2e. Discrete Fourier transform parameters

- e1. *dodft*, logical variable. If it is true, it turns the discrete Fourier transform (DFT) analysis on.
- e2. *fl/ft* are the left and right margins for the DFT plots.

- e3. *ftmin* is the lower bound for the DFT plots. If $FTMIN > 0.0$ a logarithmic scale is used.
- e4. *ftmaz* is the upper vertical bound of the DFT plot.
- e5. *maxpar* is the maximum harmonic order plotted.
- e6. *iq1/iq2* specify which of the following three ways to define the horizontal/vertical tunes to use for Q_1/Q_2 , in the harmonic analysis. Hence, if $IQ1/IQ2 = 0$, the ratio of the number of phase space turns over the number of machine turns is used. If $IQ1/IQ2 = 1$ the highest peak in the DFT is used, and if $IQ1/IQ2 = 2$ the second highest peak in the DFT is employed.
- e7. *senhar* denotes the threshold DFT response to signify a harmonic peak.

2f. Slow phase parameters

- f1. *nstrob*. On some graphs only every NSTROB'th turn is plotted.
- f2. *numer/norder*. The resonance tune is $Q_{res} = NUMER/NORDER$.
- f3. *dfitol* denotes the tolerance for the BPM glitches and/or phase discontinuities and it is expressed in units of 2π .

2g. Idealised lattice parameters

- g1. *beta*(x_1, y_1, x_2, y_2) are the design values of the horizontal and vertical beta functions at the position of the two BPMs, HF42 and HF44.
- g2. *ficell* is the phase advance per cell in degrees.
- g3. *alfa*(x_1, y_1, x_2, y_2) are the design alphas at the position of the monitors.

2h. Test data parameters

- h1. *bitsiz* is the assumed bit size of the BPMs.
- h2. *npstrt/npfin* are the start and finish particles whose coordinates are summed.

2i. Fitting control

- i1. *man*. This parameter assumes only two values, 0 or 1. If it is 0(1) it turns off (on) some manual control of the optimization.
- i2. *itmz* is the maximum number of HYDRA steps before quitting.
- i3. *itw* is the number of HYDRA steps per write.
- i4. *pfin* multiplies single coordinates of the initial matrix.
- i5. *pfac* is the multiplier used when shaking up the solution.
- i6. *ftol* is the goal tolerance.

2j. Graphical output control

- j1. *x1vt* is true if data from the first BPM are plotted versus turn number (uses NSKIP).
- j2. *axvt* is true if the amplitude is plotted versus turn number.
- j3. *axvfix* is true if amplitude is plotted versus phase.
- j4. *svt* is true if smear is plotted versus last turn number fitted.
- j5. *qxvt* is true if tune is plotted versus last turn number fitted.
- j6. *fitvt* is true if the fitted parameters are plotted versus last turn number fitted.

3. The next function of RDCMD is to do logic initialization. In particular, it opens the file INFILS if BATCH is true, it initializes the logarithmic scale if FTMIN

< 0.0 and it initializes the shared memory if $IFMT = 1$.

4. Finally it writes on the screen and in `TEVEX.OUT` the values of all the parameters contained in `TEVEX.CMD`.

B. FORM0

Subroutine `FORM0` reads the data from the 1987 E778 ASCII files.

1. `FORM0` prompts the user for input filename with “Enter horizontal turn-by-turn filename for input” and “Enter vertical input filename”. The input file with the horizontal data is unit 8 while the vertical data are in unit 9.
2. Next, the first `IHEAD` lines from the files are discarded and `FORM0` reads the recordings of the two horizontal and two vertical BPMs, x_1 , x_2 and y_1 , y_2 for `NTMX` turns. The parameter `NTMX` belongs to the parameter list file of `TEVEX`, `TEVEX-PAR.H`, and has been set equal to 4096. If there are no vertical data, which is the case through out this whole work, y_1 and y_2 are set equal to zero.
3. The first turn of significant data is determined next, as the turn number with corresponding position larger than `BNOISE`. If such a turn does not exist error messages and instructions follow.
4. Finally the first line of data together with the line where real data start ($x > \text{BNOISE}$) are recorded in `TEVEX.OUT` as well as on the screen.

C. FORM1

`FORM1` reads data from the shared memory.

1. First `FORM1` warns the user that a batch job cannot be submitted with shared memory data.
2. A second warning is that there is no capability of analyzing vertical data at this point. A future upgrade will remove this problem.
3. The answer to the question “Enter data input name” provides `FORM1` with the

horizontal data filename, e.g. TAPE3.43.

4. The search for the first turn of significant data, MINNT, is done using the BNOISE criterion.
5. FORM1 also finds the last turn of significant data, MAXNT.
6. The first and the last turn of significant data are recorded on TEVEX.OUT and on the screen.

D. FORM2

FORM2 reads simulated data from EVOL.

1. FORM2 first gets the input filename from the user.
2. The first IHEAD lines are discarded.
3. The current and the horizontal and vertical positions at the location of the two monitors are read for every turn. The units of the above quantities are mm.
4. The first and the last turn of data are recorded in TEVEX.OUT and are displayed on the screen.

F. FORM4

FORM4 reads simulated data from TEAPOT.

1. The input filename is supplied by the user.
2. The first IHEAD lines are stripped off.
3. The horizontal position x , and the angle of deflection x' , as well as the vertical position y , and the angle y' , are read for every turn.
4. The above information is translated into horizontal and vertical positions at the location of the two monitors.
5. The first line of data is recorded in TEVEX.OUT and on the screen.

G. FORM5

FORM5 reads data recorded by camac 5, the resonant Tevatron BPMs. This format can only be used on the SUN Workstations.

H. NOLOW

Subroutine NOLOW filters the tune values from QMIN to QMAX from the raw position and intensity data.

1. Key constants are set-up first.
2. Filter BPM data, find and measure "synchrotron" tunes and amplitudes with the use of FILTER and PKPWR.

I. PARAMS

The function of this subroutine is to get the fitting level and the fitting do-loop parameters.

1. At this point TEVEX presents four options to the user:

"Level controls the raw BPM data conversion

Level = 0 use raw data

Level = 1 only subtract average closed orbit offsets

Level = 2 fit BPM betas, phases and closed orbit offsets

Level = 3 as 2 and fit for gaussian decoherence

Enter the level chosen (eg 3): "

2. Once the choice has been made, the chosen level is recorded on TEVEX.OUT.

3. The first turn number for the range of interest is specified next as follows: TEVEX informs the user of the range of significant data. If the chosen level is the third one, then the analysis has to start from the first turn of significant data. If the chosen level is other than 3 and FAST is true, then the starting value has already been specified

in TEVEX.CMD. A third possibility is to supply the value by hand, by answering the appropriate question. The starting turn number must be between the first turn of significant data and the last turn minus 10.

4. The do-loop variables for the last turn number in the range of interest are specified here. If FAST is true, the range values have been chosen in TEVEX.CMD. Otherwise the user supplies the numbers by hand by answering the appropriate questions.

5. Finally, a check of the last turn do-loop range values concludes the function of PARAMS. The criteria for correct values are that the starting turn number of the final do-loop must be greater or equal to the starting turn of the analysis plus 5, and it must also be less than the last turn of the analysis. Also the increment must be positive. At last, the difference between the final do-loop turn number and the initial one, must be greater than the increment for the do-loop to start.

J. STATS

STATS finds the averages and the limits of the digitized data in the range between the first turn for the analysis and the starting value for the last turn do-loop. Specifically it calculates $\langle x_1 \rangle$, $\langle x_2 \rangle$, $\langle y_1 \rangle$, $\langle y_2 \rangle$ and x_{\min} , x_{\max} , y_{\min} , y_{\max} .

K. PREPRO

This subroutine prepares the fitting vectors, PSOLX and PSOLY.

1. If the chosen level is 0 then the components of the fitting vector PSOLX are:

$$\begin{aligned} \text{psolx}(1) &= 0 \\ \text{psolx}(2) &= 0 \\ \text{psolx}(3) &= \frac{\phi_{\text{cell}}}{2} \\ \text{psolx}(4) &= \sqrt{\frac{\beta_{x1}}{\beta_{x2}}} \\ \text{psolx}(5) &= 0 \end{aligned}$$

and

$$\text{ndimx} = 0.$$

Similar equations hold true for the vertical direction. Recall that ϕ_{cell} is the design value of the phase advance per cell, and β_{x1}, β_{x2} are the design values of the horizontal beta functions at the two monitors.

2. If the analysis level is 1 then PSOLX becomes:

$$\begin{aligned}\text{psolx}(1) &= \langle x_1 \rangle \\ \text{psolx}(2) &= \langle x_2 \rangle \\ \text{psolx}(3) &= \frac{\phi_{\text{cell}}}{2} \\ \text{psolx}(4) &= \sqrt{\frac{\beta_{x1}}{\beta_{x2}}} \\ \text{psolx}(5) &= 0\end{aligned}$$

and

$$\text{ndimx} = 0$$

Again similar equations can be written for the vertical direction.

3. If the level is equal to 2 then:

$$\begin{aligned}\text{psolx}(1) &= \langle x_1 \rangle \\ \text{psolx}(2) &= \langle x_2 \rangle \\ \text{psolx}(3) &= \frac{\pi \phi_{\text{cell}}}{360} \\ \text{psolx}(4) &= \sqrt{\frac{\beta_{x1}}{\beta_{x2}}} \\ \text{psolx}(5) &= 0\end{aligned}$$

and

$$\text{ndimx} = 4$$

and the same for y .

4. Finally if the level equals 3 then PSOLX is:

$$\begin{aligned}\text{psolx}(1) &= \langle x_1 \rangle \\ \text{psolx}(2) &= \langle x_2 \rangle \\ \text{psolx}(3) &= \frac{\pi \phi_{\text{cell}}}{360} \\ \text{psolx}(4) &= \sqrt{\frac{\beta_{x1}}{\beta_{x2}}} \\ \text{psolx}(5) &= \frac{0.1}{(n_{cf} - n_i)^2}\end{aligned}$$

and

$$\text{ndimx} = 5,$$

where n_{cf} is the final turn of the calculations and n_i is the turn number where data start.

APPENDIX F

E778 Hardware

The second run of E778 required more and higher precision data than the first run, and the limited machine time available implied highly efficient data taking, monitoring and logging. Hence a many-turn beam data acquisition and analysis system was constructed [29].

From the Tevatron beam position pickups, the signals were directed to two front end electronics. The first, the standard Fermilab BPM front end, gave direct horizontal (HF42 and HF44), vertical (VF43 and VF45) and intensity (I45) signals. The second was a peak-sensing circuit which gave less noisy signals.

The signals were digitized with two LeCroy 6810 5-Mhz, 12-bit transient digitisers, each with .5 Megasamples of onboard memory. The camac-based LeCroy modules were controlled by a Sun 3/140 workstation via the Sun's VME backplane and a CES CBD/8210 camac branch driver. Fig. F.1 illustrates the cabling from the BPMs — located at the service building F4 — to the Sun 3/140 (Fig), also located at F4.

Control and data flow to the main control room (MCR) workstation (Myrtle) were through the Suns' ethernet links. (See Figs F.2 and F.3. In F0, the cable from the Schottky rack to cables 13 and 14 is RG58.)

Information such as kicker voltages, tune settings, sextupoles currents etc, was fed to the system from the Tevatron control system through a serial link. Data context information and comments were logged to a disk fifo buffer and to cartridge tape for

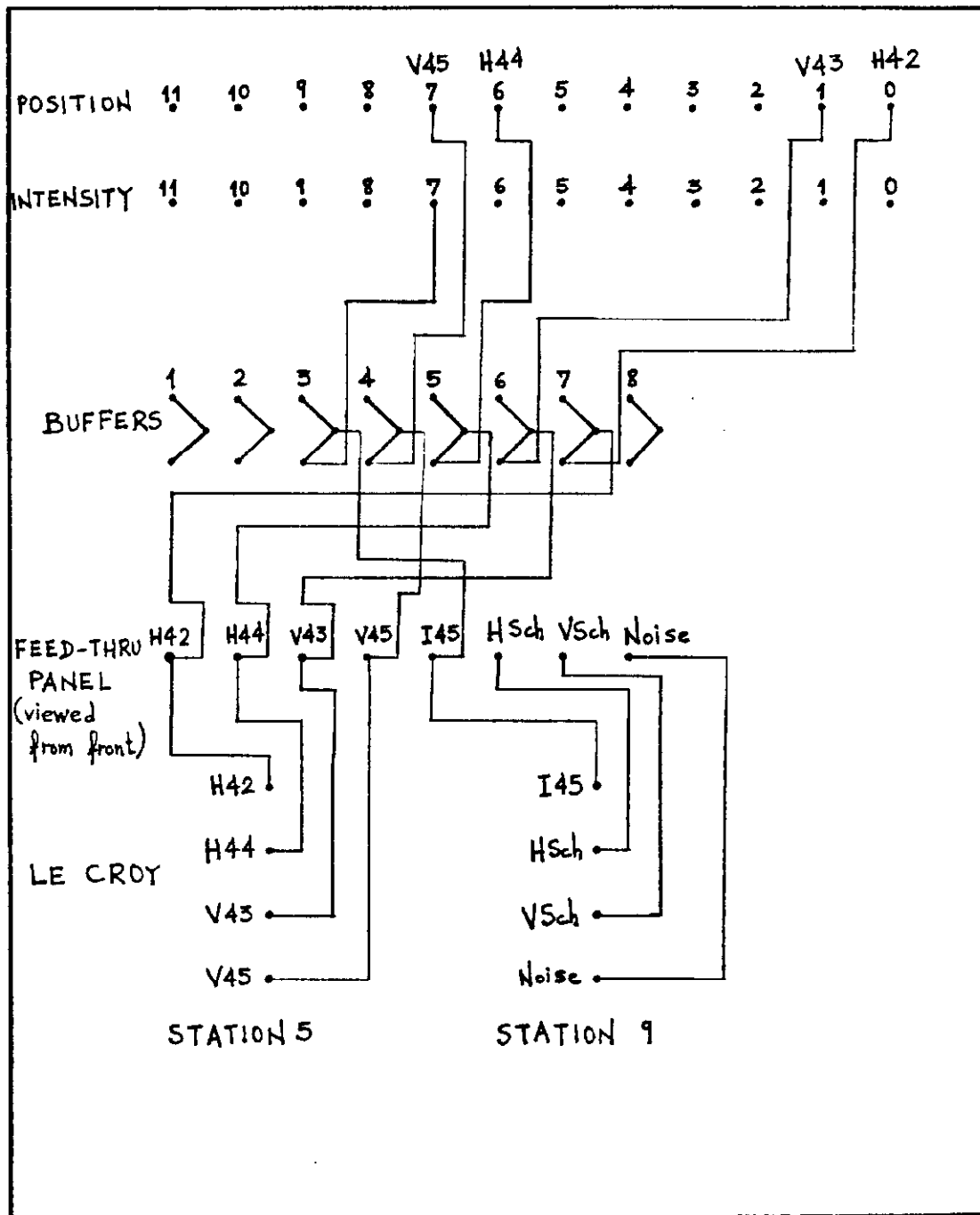


Figure F.1: Tevatron F4 to Sun 3/140 (Fig) cabling.

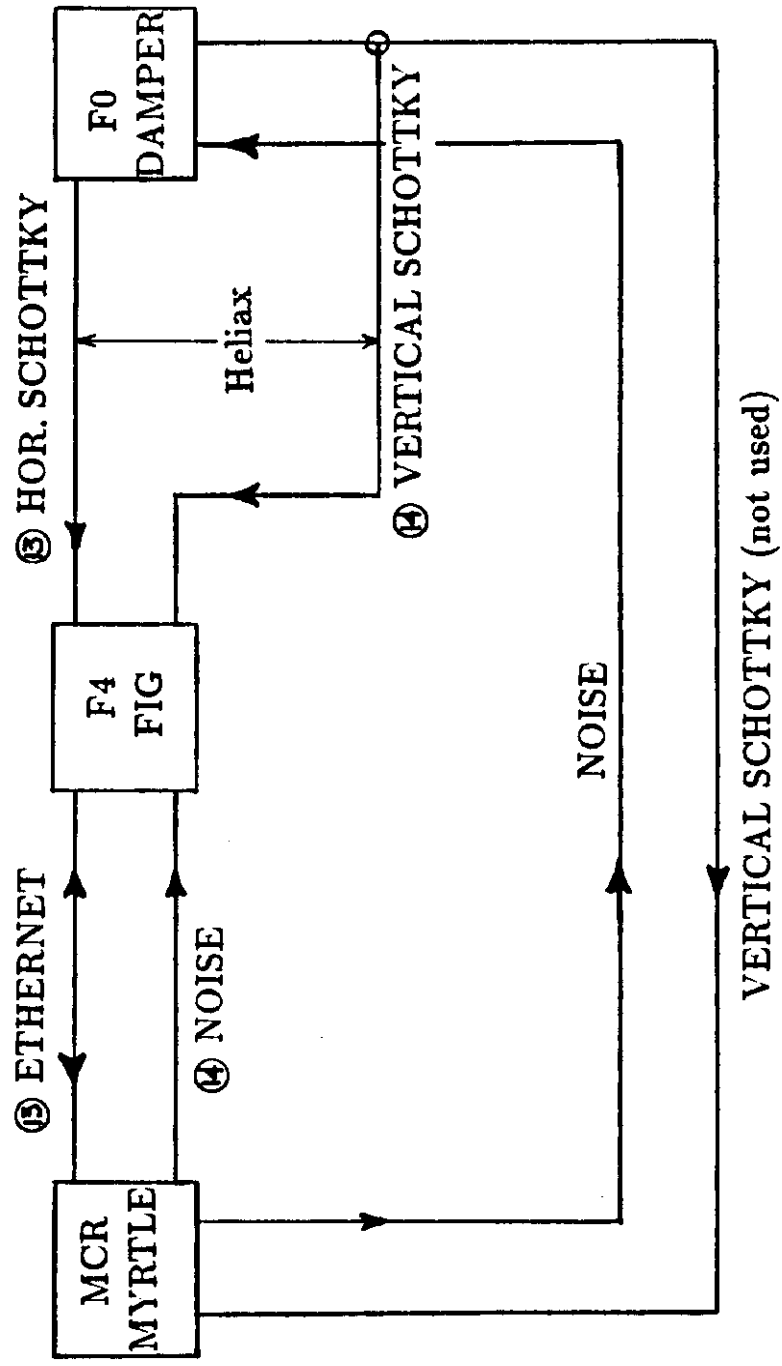


Figure F.2: Links among the Suns and the Schottky and noise devices.

CEILING OF F4

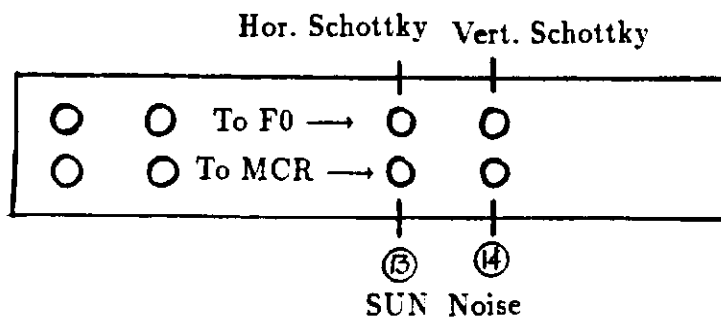


Figure F.3: Part of the ceiling of the service building F4.

long term storage. More details on the hardware of this structure, as well as the software — almost entirely written in C — can be found in reference [29].

BIBLIOGRAPHY

BIBLIOGRAPHY

- [1] SSC Central Design Group, Conceptual Design of the Superconducting Super Collider, SSC-SR-2020, March 1986.
- [2] A. W. Chao et al., A Progress Report on Fermilab Experiment E778. An Experimental Study of the SSC Magnet Aperture Criterion, FN-471, SSC-156, January 1988.
- [3] A. W. Chao et al., Experimental Investigation of Nonlinear Dynamics in the Fermilab Tevatron, Physical Review Letters, pg. 2752, December 12, 1988.
- [4] N. Merminga et al., An Experimental Study of the SSC Magnet Aperture Criterion, Fermilab-Conf-88/94-E, presented at the EPAC, Rome, June 7-11, 1988.
- [5] J. M. Peterson et al., Dynamic Aperture Measurements at the Tevatron, presented at the EPAC, Rome, June 7-11, 1988.
- [6] D. A. Edwards and M. J. Syphers, An Overview of Experiment E778, submitted to the Proceedings of the ICFA Workshop on 'Aperture-Related Limitations of the Performance and Beam Lifetime in Storage Rings,' Lugano, Switzerland, April 1988.
- [7] A. W. Chao et al., An Experimental Study of the SSC Magnet Aperture Criterion, original proposal submitted on October 17, 1986.
- [8] Frank T. Cole, Nonlinear Transformations in Action-Angle Variables, Fermilab Report, TM-179, June 13, 1969.
- [9] R. Talman, Nonlinear Perturbation of a Cyclic Accelerator Lattice; Exact and Approximate Solutions, Cornell LNS Report, Ithaca, (1976).
- [10] A. Dragt, Phys. Pub. 85-004, University of Maryland, (1984).
- [11] E. D. Courant and H. S. Snyder, Theory of the Alternating-Gradient Synchrotron, Annals of Physics:3, 1-48 (1958).
- [12] D. A. Edwards, An Introduction to Circular Accelerators (BNL/SUNY Summer School, 1983), AIP Conference Proceedings No. 127 (1985).
- [13] D. A. Edwards and M. J. Syphers, An Introduction to the Physics of Particle Accelerators, AIP Conference Proceedings No. 184 (1988).

- [14] S. G. Peggs, Hamiltonian Theory of the E778 Nonlinear Dynamics Experiment, SSC-175, April 1988.
- [15] Leo Michelotti, Introduction to the Nonlinear Dynamics Arising from Magnetic Multipoles, (Fermilab Summer School, 1984), AIP Conference Proceedings 153 (1987).
- [16] R. D. Ruth, Single-Particle Dynamics in Circular Accelerators, (SLAC Summer School, 1985), AIP Conference Proceedings 153 (1987).
- [17] E. D. Courant, R. D. Ruth, W. T. Weng, Stability in Dynamical Systems I, (BNL/SUNY Summer School, 1983), AIP Conference Proceedings No.127 (1985).
- [18] E. J. N. Wilson, Nonlinear Resonances, CERN Accelerator School Proceedings, CERN 87-03, 21 April 1987
- [19] N. Merminga and K.-Y. Ng, 2/5 Resonance Islands Generated by Sextupoles, Fermilab Report, FN-506, February 1989.
- [20] T. L. Collins, Distortion Functions, Fermilab Internal Report 84/114, October 23, 1984.
- [21] N. Merminga, K.-Y. Ng, Hamiltonian Approach to Distortion Functions, Fermilab Report FN-493, August 1988.
- [22] K.-Y. Ng, Derivation of Collins' Formulæ for Beam-Shape Distortion due to Sextupoles Using Hamiltonian Method, Fermilab Report TM-1281, October 1984.
- [23] K.-Y. Ng, Distortion Functions, Lecture given in KEK Oho '87 High Energy Accelerator Seminars, August 1987.
- [24] J. Moser, Nach. Akad. Wiss. Gottingen, IIA, NO. 6, 87 (1955).
- [25] Leo Michelotti, Deprit's Algorithm, Green's Functions, and Multipole Perturbation Theory, Particle Accelerators, Vol. 19, pp. 205-210 (1986).
- [26] Leo Michelotti, private communication.
- [27] Leo Michelotti, The Physics of Phase Space, Y. S. Kim and W. W. Zachary, Springer-Verlag, 1987.
- [28] D. Edwards, R. Johnson and F. Willeke, Tests of Orbital Dynamics using the Tevatron, Particle Accelerators, Vol. 17 (1985)
- [29] S. Peggs, C. Saltmarsh and R. Talman, Million Revolution Accelerator Beam Instrument for Logging and Evaluation, SSC-169, March 1988.
- [30] E778 Logbook, page 106, February 1988.

- [31] Lee C. Teng, Skew-Quadrupole Field and Horizontal-Vertical Coupling in the Main Ring, Fermilab Report, TM-382, July 21, 1972.
- [32] Leo Michelotti, private communication.
- [33] Application Program of Fermilab's Controls System, (page T130)
- [34] E778 Logbook, page 96, February 1988.
- [35] E778 Logbook, page 142, February 1988.
- [36] E778 Logbook, page 136, February 1988.
- [37] N. Merminga and K. Y. Ng, Analytical Expressions for the Smear due to Non-linear Multipoles, Fermilab Report, FN-505, February 1989.
- [38] S. R. Mane, N. Merminga and D. A. Edwards, Decoherence of Kicked Particle Beams Using Different Formalisms, submitted to the 1989 Particle Accelerator Conference, Chicago, March 20-23, 1989.
- [39] Modifications of TEVEX has been done by Tong Chen and Merminga.
- [40] R. E. Meller et al., Decoherence of Kicked Beams, SSC-N-360, May 1987.
- [41] L. Schachinger and R. Talman, TEAPOT: A Thin Element Accelerator Program for Optics and Tracking, Particle Accelerators 22, 35 (1987).
- [42] ART, a code written by N. Merminga.
- [43] S. Peggs, Hadron Collider Behavior in the Nonlinear Numerical Model EVOL, Particle Accelerators, Vol. 17, pp. 11-50, (1985).
- [44] Lia Merminga, Rod Gerig and Steve Peggs, On the Calibration of Tevatron Beam Position and Intensity Monitors Used in E778, Fermilab Report TM-1532, SSC-N-510, May 1988.
- [45] W. H. Press, B. P. Flannery, S. A. Teukolsky, W. T. Vetterling, Numerical Recipes, page 292.
- [46] This plot was made with simulated data generated by Tong Chen.
- [47] S. G. Peggs and R. M. Talman, Nonlinear Problems in Accelerator Physics, Annual Reviews of Nuclear Science 1986. 36:287-325 or SSC-61, February 1986.